# TRANSPORT AND FIRST-PRINCIPLES STUDY OF NOVEL THERMOELECTRIC MATERIALS

by

**Hang Chi**

A dissertation submitted in partial fulfillment
of the requirements for the degree of
Doctor of Philosophy
(Physics)
in The University of Michigan
2014

**Doctoral Committee:**

**Professor Ctirad Uher, Chair**
**Professor Roy Clarke**
**Professor Rachel S. Goldman**
**Professor Massoud Kaviany**
**Assistant Professor Lu Li**
**Associate Professor Anton Van der Ven**

## DEDICATION

TO MY WIFE NAN, MY PARENTS,

AND

THE UHER RESEARCH GROUP

# ACKNOWLEDGEMENTS

I wish to express my most sincere gratitude to my advisor Professor Ctirad Uher for the guidance in life, career, and fundamental transport physics. I have been honored and enjoyed working *with* him and sharing all the fun as a creative experimental physicist.

I want to thank my mentors: Professors Massoud Kaviany, Manos Kioupakis, and Anton Van der Ven who have taught me theoretical simulations; Professors Roy Clarke, Rachel Goldman, Lu Li, Qiang Li, Petr Lošťák, Donald T. Morelli, Jamie Phillips, Ferdinand Poudeu, and Xinfeng Tang who have provided supports for my experiments.

I also have the privilege of sharing the lab/office with my talented fellow colleagues: Lynn Endicott, Si Hui, Hyoungchul Kim, Wei Liu, Alex Page, Xianli Su, Hui Sun, John C. Thomas, Guoyu Wang, Tao Ying, and Sarah Zhou among many others. Without their support, my research life would have been much less enjoyable.

Finally and most importantly, I would like to thank my wife Nan and my family, for their understanding, hope and love that make more sense of my work.

My thesis work has been supported as part of the Center for Solar and Thermal Energy Conversion, an Energy Frontier Research Center funded by the U.S. Department of Energy, Office of Science, Office of Basic Energy Sciences under Award Number DE-SC0000957.

## TABLE OF CONTENTS

**DEDICATION** ........ **ii**

**ACKNOWLEDGEMENTS** ........ **iii**

**LIST OF FIGURES** ........ **vi**

**LIST OF TABLES** ........ **xiv**

**LIST OF APPENDICES** ........ **xv**

**ABSTRACT** ........ **xvi**

**CHAPTER 1 INTRODUCTION** ........ **1**

**CHAPTER 2 THERMO-GALVANOMAGNETIC TRANSPORT** ........ **12**

**CHAPTER 3 EXPERIMENTAL AND *AB-INITIO* TECHNIQUES** ........ **23**

**CHAPTER 4 ADVANCED THERMOELECTRICS GOVERNED BY A SINGLE PARABOLIC BAND** ........ **31**

**CHAPTER 5 CONFIGURING PNICOGEN RINGS IN SKUTTERUDITES FOR LOW PHONON CONDUCTIVITY** ........ **47**

**CHAPTER 6 OBSERVATION OF PHONON DRAG AND TUNING ITS TEMPERATURE DOMAIN IN THIN FILMS** ........ **64**

**CHAPTER 7 FINE TUNING THE FERMI LEVEL IN BISMUTH TELLURIDE VIA THALLIUM DOPING** ........ **84**

**CHAPTER 8 LOW-TEMPERATURE STRUCTURAL AND TRANSPORT ANOMALIES IN DICOPPER SELENIDE** ........ **103**

**CHAPTER 9 CONCLUDING REMARKS AND OUTLOOK** ........ **115**

**APPENDICES** ........................................................................ **118**

**REFERENCE** ........................................................................ **149**

# LIST OF FIGURES

Figure 1.1 The Seebeck effect in a thermocouple. 6

Figure 1.2 The Peltier effect. 9

Figure 4.1 (a) First Brillouin zone showing the three-fold degenerated ($N_v$ = 3) electron pockets at X. (b) Schematic representation of the band structure (electron energy $\varepsilon$ vs. wave vector $k$). The valence band (VB) is at Γ while the convergence of the light and heavy conduction bands (LCB and HCB) located at X point results in the doubled valley degeneracy ($N_v$ = 6) at all temperatures of interest. 32

Figure 4.2 Temperature dependent electrical conductivity $\sigma$ of $Mg_2(Si_{0.3}Sn_{0.7})_{1-y}Bi_y$. 33

Figure 4.3 Experimental data (symbols) and theoretical results (lines) based on the single parabolic band (SPB) model for the Seebeck coefficient $\alpha$. 33

Figure 4.4 The Pisarenko plot (Seebeck coefficient $\alpha$ vs. Hall density $n_H$) at 300 K with a fixed density-of-states effective mass $m_d^*$ reflects a single parabolic nature of the band structure invariant of doping. 34

Figure 4.5 Temperature dependent Hall density $n_H$ of $Mg_2(Si_{0.3}Sn_{0.7})_{1-y}Bi_y$. 36

Figure 4.6 The relationship between $n_H$ and the actual Bi concentration, while the dashed line presents the theoretical prediction assuming that one Bi atom donates one electron to the structure. 36

Figure 4.7 Temperature dependent Hall mobility $\mu_H$ of $Mg_2(Si_{0.3}Sn_{0.7})_{1-y}Bi_y$. 37

Figure 4.8 The theoretical fitting of $\mu_H$ for the $y$ = 0.010 and 0.025 samples indicates that acoustic phonon (AP) scattering dominates at high temperatures over alloy scattering (AS). ........ 39

Figure 4.9 Plots of $\mu_H$ verse $n_H$ at 295 K, 473 K and 673 K, respectively. The $\mu_H$ data show no significant deterioration upon increasing $n_H$, implying an excellent electronic performance. ........ 39

Figure 4.10 Temperature dependent power factor ($PF$) of $Mg_2(Si_{0.3}Sn_{0.7})_{1-y}Bi_y$. ........ 41

Figure 4.11 The predicted $PF$ based on the single parabolic band (SPB) model, in agreement with the experimental data. ........ 42

Figure 4.12 Temperature dependent thermal conductivity $\kappa$. ........ 43

Figure 4.13 Temperature dependent lattice thermal conductivity $\kappa_L$. Note the significant bipolar effect at elevated temperatures, especially for samples with low doping levels. . 43

Figure 4.14 Temperature dependent figure of merit $ZT$ of $Mg_2(Si_{0.3}Sn_{0.7})_{1-y}Bi_y$. ........ 45

Figure 4.15 The predicted $ZT$ based on the SPB model (lines) are in accord with the experimentally determined $ZT$ (symbols). ........ 45

Figure 5.1 DFT formation energies of 340 calculated configurations of $CoSb_{3-m-n}Ge_mTe_n$. Configurations featured with CD $Ge_2Te_2$ rings (solid points) have considerably lower energy than those without CD $Ge_2Te_2$ rings (open circles). ........ 50

Figure 5.2 Formation energies of $CoSb_{3(1-x)}Ge_{1.5x}Te_{1.5x}$. Two typical structures are illustrated at $x$ = 0.5. The solid red line is the 5th-order Redlich-Kister polynomial fit to the lower bound of formation energies. ........ 50

Figure 5.3 A typical crystal structure (left) of $CoSb_{3(1-x)}Ge_{1.5x}Te_{1.5x}$ at $x$ = 0.5 which mixes variety of rings (right) of $Sb_4$ and CD $Ge_2Te_2$ (or $Te_2Ge_2$). The cubic unit cell contains 32 atoms. The tilting of rings gives rise to the formation of corner-shared octahedra, which create large cages centering at (0, 0, 0) and (1/2, 1/2, 1/2). ............................................ 51

Figure 5.4 The phase diagram of $CoSb_{3(1-x)}Ge_{1.5x}Te_{1.5x}$. The miscibility gap without coherency strain (solid, black) becomes significantly suppressed by the presence of coherency strain (dashed, red). ........................................................................................ 53

Figure 5.5 XRD pattern of various $CoSb_{3(1-x)}Ge_{1.5x}Te_{1.5x}$ samples. ................................. 53

Figure 5.6 (a) Composition dependence of the mean square displacement for individual atoms (ADP) in atomic-substituted $CoSb_{3(1-x)}Ge_{1.5x}Te_{1.5x}$ and filled $Ba_yCo_4Sb_{12}$. (b) Projected phonon dispersion curves for $x$ = 0.5 and $y$ = 0.5 using DFT. Atomistic configurations of each vibration mode for filler and double substitution are also given. Blue sphere represents the Co atom. Green sphere represents the Ba filler atom. (c) Atomistic configurations showing a pnicogen ring and octahedron consisting of substituted atoms ($x$ = 0.5). Red arrows show the large displacement of each Ge atom.. 56

Figure 5.7 Calculated phonon dispersion curves and density-of-states: (a) $x$ = 0, (b) 0.5, (c) $y$ = 0.5, and (d) a hybrid filled-substituted structure ($x$ = 0.5 and $y$ = 0.5). The site-projected density-of-states are also shown. ..................................................................... 57

Figure 5.8 Variations of the predicted lattice thermal conductivity of $CoSb_{3(1-x)}Ge_{1.5x}Te_{1.5x}$, (a) concentration dependence at $T$ = 500 K, and (b) temperature dependence for several compositions. Our experimental results (using the Wiedemann-Franz law) and the results of the point-defect model and NEAIMD are shown. The minimum conductivity $\kappa_{min}$ (~ 0.37 W/m-K) for the amorphous $CoSb_3$ phase [86] is also shown. ................................. 59

Figure 6.1 Temperature dependent hole concentration $p$ of ZnTe:N MBE thin films with various doping levels. ........................................................................................................ 67

Figure 6.2 Temperature dependent Hall mobility $\mu_H$ of ZnTe:N MBE thin films with various doping levels. ........................................................................................ 67

Figure 6.3 Temperature dependent electrical resistivity $\rho$ of ZnTe:N MBE thin films with various doping levels. ........................................................................................ 68

Figure 6.4 PL spectra at 20 K of pure ZnTe and ZnTe:N MBE thin films with various doping levels. ........................................................................................................ 69

Figure 6.5 Seebeck coefficient of ZnTe:N from 150 K to 300 K. ................................... 70

Figure 6.6 The effective mass $m^*$ of ZnTe:N from 150 K to 300 K. .............................. 70

Figure 6.7 Pisarenko plot at 300 K indicating $\alpha$ vs. $p$ relation follows the single parabolic band model. ................................................................................................................ 71

Figure 6.8 Temperature dependent Seebeck coefficient $\alpha$ of ZnTe:N MBE thin films with various doping levels. ........................................................................................ 73

Figure 6.9 The correlation between the Seebeck coefficient peak (~ 13 K) and an electrical resistivity plateau, suggesting that phonon-drag leaves an imprint on the temperature profile of the electrical resistivity. ............................................................. 73

Figure 6.10 Temperature dependent Seebeck coefficient for $Bi_2Te_3$ single crystal, 9 nm $Bi_2Te_3$ films on $BaF_2$ (111), and sapphire (0001) substrates. .......................................... 78

Figure 6.11 The lattice thermal conductivity of bare $BaF_2$ substrate, bare sapphire substrate, and the $Bi_2Te_3$ single crystal, which is obtained by subtracting the electron contribution from the total thermal conductivity via the Wiedemann-Franz law............ 78

Figure 6.12 Temperature dependence of the Seebeck coefficients (left axis) for two 9 nm films grown on sapphire substrates with thickness of 0.5 mm and 0.1 mm, respectively. The lattice thermal conductivities (right axis) of two substrates are also shown. ............ 80

Figure 6.13 Temperature dependent Seebeck coefficient (normalized to the value at 200 K) for $Bi_2Te_3$ single crystal and films with different thickness on sapphire (0001) substrate. The dashed vertical line and arrow indicate the phonon-drag peak position for films and the single crystal, respectively. ........................................................................ 82

Figure 7.1 Crystal structure of (a) $Bi_2Te_3$ and (b) $TlBiTe_2$ with repeating ($Te^1$–Bi–$Te^2$–Bi–$Te^1$) and (Te–Bi–Te–Tl) layers, respectively. Defected form of $TlBiTe_2$ represented by (Te–Bi–Te–Tl–$V_{Te}^{\bullet\bullet}$) + 2$e$ includes an atomic plane of Te vacancies, has nearly identical in-plane lattice parameters as $Bi_2Te_3$, shares the same space group, and donates electrons necessary to explain transport properties. ........................................................ 85

Figure 7.2 XRD patterns of powders made from Tl-doped $Bi_2Te_3$ single crystals, matching the $Bi_2Te_3$ standard (JCPDS 82-0358), with arrows indicating additional peaks of the $TlBiTe_2$ phase. ........................................................................................... 87

Figure 7.3 (a) HRTEM image and (b) SAED pattern taken from the $x = 0.30$ sample. The distance of the neighboring lattice fringes in (a) is 0.323 nm, in agreement with the $(\bar{1}14)$ lattice spacing for $TlBiTe_2$. ........................................................................ 88

Figure 7.4 XPS analysis performed on various Tl-doped $Bi_2Te_3$ surfaces either perpendicular to the $c$-axis ($\perp c$, i.e. the basal plane) or parallel to the $c$-axis ($// c$) showing core levels for (a) Bi 4$f$, $\perp c$; (b) Te 3$d$, $\perp c$; (c) Tl 4$f$, $\perp c$; (d) Bi 4$f$, $// c$; (e) Te 3$d$, $// c$; (f) Tl 4$f$, $// c$. ........................................................................................ 90

Figure 7.5 Temperature dependent electrical resistivity $\rho$ for Tl-doped $Bi_2Te_3$ single crystals. The inset is a sketch of the band structure (binding energy $E_B$ v.s. wave vector $k$) along the Γ-K direction, where Fermi level $E_F$ for various $x$ are indicated by horizontal dashed lines. With increasing amount of Tl, the $E_F$ is shifted continuously from the valence band (VB) into the conduction band (CB)........................................................ 92

Figure 7.6 Temperature dependent Seebeck coefficient $\alpha$ for Tl-doped $Bi_2Te_3$ single crystals. ........................................................................................................ 92

Figure 7.7 Temperature dependent Hall coefficients $R_H$ from 2 K to 300 K................... 96

Figure 7.8 Temperature dependent carrier density defined as $n = 1/(e R_H)$, where $e$ is the elementary charge and positive (negative) $n$ stands for hole (electron). ......................... 96

Figure 7.9 Temperature dependent Hall mobility defined as $\mu_H = R_H/\rho$. The inset is $\mu_H$ vs. $T$ plotted on a log-log scale indicating the $T^{-3/2}$ acoustic phonon temperature dependence at temperatures near the ambient. ........................................................................ 97

Figure 7.10 The temperature dependence thermal conductivity $\kappa$ for Tl-doped $Bi_2Te_3$ single crystals.............................................................................................................. 98

Figure 7.11 The temperature dependence of thermoelectric figure of merit $ZT$ for Tl-doped $Bi_2Te_3$ single crystals. ........................................................................... 98

Figure 7.12 The lattice thermal conductivity $\kappa_L$ of Tl-doped $Bi_2Te_3$ single crystals, with the dashed line indicating the numerical fitting result of the Debye-Callaway model for (a) $x = 0$, (b) $x = 0.01$, (c) $x = 0.05$, (d) $x = 0.10$, (e) $x = 0.20$, and (f) $x = 0.30$, which documents a generally enhanced point defect scattering of phonons upon increasing the content of Tl................................................................................................... 100

Figure 8.1 Projected (along the monoclinic *b*-axis) *ab inito* ground state structure of $Cu_2Se$ formed by repeating sextuple layers of Se-Cu-Cu-Cu-Cu-Se............................. 105

Figure 8.2 The calculated phonon band structure and density of states ($D_p$) indicate the proposed structure is dynamically stable. ..................................................................... 107

Figure 8.3 The electronic band structure and density of states ($D_e$) calculated using HSE hybrid functional suggests that $Cu_2Se$ is a semiconductor with band gap $E_g = 1.03$ eV. 107

Figure 8.4 (a) Simulated SAED pattern along the zone axis [011] of the monoclinic phase and the $[101]_{fcc}$ with the diffractions from the fcc structure labeled as squares. (b) The experimental SAED pattern along the [011] zone axis of the monoclinic phase. .......... 107

Figure 8.5 Reduced total scattering XRD structure function, $F(Q) = Q[S(Q)-1]$, where $S(Q)$ is the total scattering structure function and $Q$ is the momentum transfer, in 100-300 K range (main panel). Temperature evolution of the normalized intensity around (400) reflection in cubic notation, marked with an arrow in the upper left inset ($Q \sim 4.3$ Å$^{-1}$). This region is sensitive to subtle structural changes, and evidences the $\alpha$□ to $\alpha$ superstructure transition at around 175 K, as denoted by a vertical dashed line (upper right inset). Red symbols denote the evolution with temperature of the intensity peaked at $Q \sim 4.362$ Å$^{-1}$, while the blue symbols show the evolution of the intensity peaked at $Q \sim 4.436$ Å$^{-1}$. ........................................................................................................ 109

Figure 8.6 Low-temperature electrical resistivity $\rho$ and Hall coefficient $R_H$ of stoichiometric $Cu_2Se$, showing an anomalies at 100–150 K, where $\rho$ measurements overlap upon either warm up or cool down in the temperature. .................................... 109

Figure 8.7 Low-temperature Hall density $p$ and Hall mobility $\mu_H$ of stoichiometric $Cu_2Se$. ........................................................................................................................ 110

Figure 8.8 Magnetoresistance profile (as a function of magnetic field intensity) of $Cu_2Se$ at various temperatures (1.8–30 K) indicating evolution of weak antilocalization behavior as the temperature is lowered to 1.8 K. ........................................................................ 111

Figure 8.9 Theoretical fitting to differential magnetoconductance using a modified HLN model at 1.8 K. ........ 112

Figure 8.10 Theoretical fitting to differential magnetoconductance using a modified HLN model at 9 K. ........ 112

Figure 8.11 the fitting parameters showing a power law behavior (~ $T^{-0.83}$) of the quantum interference length. ........ 113

# LIST OF TABLES

Table 2-1 Thermo-galvanomagnetic transport coefficients. ........................................... 15

Table 2-2. Transport coefficients in degenerate semiconductors .................................... 21

Table 4-1 Transport parameters of $Mg_2(Si_{0.3}Sn_{0.7})_{1-y}Bi_y$ ($0 \leq y \leq 0.04$) at 300 K: Seebeck coefficient $\alpha$ (μV K$^{-1}$), Hall density $n_H$ ($10^{20}$ cm$^{-3}$), Hall mobility $\mu_H$ (cm$^2$ V$^{-1}$ s$^{-1}$), reduced Fermi level $\eta$ ($= E_F/k_BT$), Hall factor $r_H$, and the density-of-states effective mass $m_d^*$ (in units of the electron rest mass $m_e$). ...................................................................... 34

Table 5-1 Calculated properties of $CoSb_3$ and $CoGe_{1.5}Te_{1.5}$. The literature results for $CoSb_3$ are also listed. $T_D$, $\gamma_G$, $B$, $c_{ij}$, and $c_v$ are the Debye temperature, the Grüneisen parameter, bulk modulus, elastic constant, and specific heat capacity. ........................... 56

Table 6-1 Typical transport coefficients of various ZnTe:N thin films at 300 K, including nitrogen concentration [$N$] from SIMS measurement, Hall coefficient $R_H$, hole concentration $p$, electrical resistivity $\rho$, Seebeck coefficient $\alpha$, thermoelectric power factor $PF$, Hall mobility $\mu_H$, and effective mass $m^*$. ....................................................... 66

Table 7-1 Binding energies $E_B$ in eV observed by XPS. ................................................. 90

Table 7-2 Lattice thermal conductivity fitting parameters for $Bi_{2-x}Tl_xTe_3$ single crystals. ......................................................................................................................... 101

# LIST OF APPENDICES

APPENDIX A ADDITIONAL NOTES ON TRANSPORT COEFFICIENT ............... 118

APPENDIX B PUBLICATION LIST ............................................................................ 147

# ABSTRACT

## TRANSPORT AND FIRST-PRINCIPLES STUDY
## OF NOVEL THERMOELECTRIC MATERIALS

by

Hang Chi

Chair: Ctirad Uher

Thermoelectric materials can recover waste industrial heat and convert it to electricity as well as provide efficient local cooling of electronic devices. The efficiency of such environmentally responsible and exceptionally reliable solid state energy conversion is determined by the dimensionless figure-of-merit $ZT = \alpha^2\sigma T/\kappa$, where $\alpha$ is the Seebeck coefficient, $\sigma$ is the electrical conductivity, $\kappa$ is the thermal conductivity, and $T$ is the absolute temperature. The goal of the thesis is to (i) illustrate the physics to achieve high $ZT$ of advanced thermoelectric materials and (ii) explore fundamental structure and transport properties in novel condensed matter systems, via an approach combining comprehensive experimental techniques and state-of-the-art first-principles simulation methods.

Thermo-galvanomagnetic transport coefficients are derived from Onsager's reciprocal relations and evaluated via solving Boltzmann transport equation using Fermi-Dirac statistics, under the relaxation time approximation. Such understanding provides insights on enhancing *ZT* through two physically intuitive and very effective routes: (i) improving power factor $PF = \alpha^2\sigma$ and (ii) reducing thermal conductivity $\kappa$, as demonstrated in the cases of $Mg_2Si_{1-x}Sn_x$ solid solution and Ge/Te double substituted skutterudites $CoSb_{3(1-x)}Ge_{1.5x}Te_{1.5x}$, respectively. Motivated by recent theoretical predictions of enhanced thermoelectric performance in highly mismatched alloys, ZnTe:N molecular beam epitaxy (MBE) films deposited on GaAs (100) substrates are carefully examined, which leads to a surprising discovery of significant phonon-drag thermopower (reaching 1–2 mV $K^{-1}$) at ~ 13 K. Further systematic study in $Bi_2Te_3$ MBE thin films grown on sapphire (0001) and/or $BaF_2$ (111) substrates, reveal that the peak of phonon drag can be tuned by the choice of substrates with different Debye temperatures. Moreover, the detailed transport and structure studies of $Bi_{2-x}Tl_xTe_3$ single crystals demonstrate that thallium doping leads to a bulk insulating state for such a topological insulator, which opens an avenue for further investigations of transport phenomena related to surface states. Finally, using the combined theoretical and experimental approaches, a new layered transition metal dichalcogenide type of ground state of $Cu_2Se$ is proposed, which exhibits extraordinary weak anti-localization type of magnetoresistance at liquid helium temperatures.

# CHAPTER 1

# INTRODUCTION

## 1.1 Irreversible thermodynamics

Suppose a steady-state system can be considered as a collection of small volume elements, each of which is in “local equilibrium” described by its own thermodynamic variables. We apply to such an element the fundamental thermodynamic relation [1, 2]

$$dU = TdS - pdV + \mu dN, \tag{1.1}$$

where all quantities are defined in the element, $U$ is the internal energy, $T$ is the absolute temperature, $S$ is the entropy, $p$ is the pressure, $V$ is the volume, $\mu$ is the electrochemical potential energy per particle, and $N$ is the number of particles. The $\mu dN$ term can be replaced by $\sum_i \mu_i dN_i$ if multiple species (indexed by $i$) contribute to the internal energy. The electrochemical potential energy $\mu$ is the combination of a chemical potential energy $\mu_c$, and an electric potential energy $\mu_e$,

$$\mu = \mu_c + \mu_e = \mu_c + q\varphi_e, \tag{1.2}$$

where $\mu_c$, in general, depends weakly on temperature and strongly on the particle (carrier) concentration, $q$ is the charge of the carrier [$+e$ ($-e$) for hole (electron) and elementary charge $e = 1.602\times10^{-19}$ C], and $\varphi_e$ is the ordinary electrostatic potential. Electrochemical potential energy $\mu$ is the driving force for particle (electric) current flow in the presence of (i) gradient in chemical potential energy $\mu_c$ (resulting from gradient in temperature and/or carrier concentration) and/or (ii) gradient in electrostatic potential (i.e., electric field). In practice, when measuring voltage difference $\Delta V$ across a sample, one actually measures the electrochemical potential energy difference $\Delta\mu$ per unit carrier charge $q$ between the two ends of the sample, $\Delta V = \Delta\mu/q$. If there is no gradient in temperature or carrier concentration, the measured voltage equals $\Delta\varphi_e$, as one would normally expect.

Assuming insignificant thermal expansion and other mechanical effects (neglecting the $-pdV$ term) and normalizing Eq. (1.1) by the element volume $V$, we have

$$Tds = du - \mu dn, \tag{1.3}$$

where $s$ is the entropy density, $u$ is the internal energy density, and $n$ is the particle number density in the element. The total internal energy $U$, entropy $S$, and particle number $N$ of the whole system are

$$U = \int u d\tau, \, S = \int s d\tau, \, N = \int n d\tau. \tag{1.4}$$

The increment rate of $s$ is determined by the corresponding continuum equation

$$\frac{\partial s}{\partial t} = -\nabla \cdot \boldsymbol{J}_s + \Theta, \tag{1.5}$$

where $\boldsymbol{J}_s$ is the entropy current density, and $\Theta$ is the rate of production of entropy per unit volume in the element. The increment rate of total entropy in the system is then

$$\frac{dS}{dt} = \frac{d}{dt}\int s d\tau = \int \frac{\partial s}{\partial t} d\tau = \int \left[ -\nabla \cdot \boldsymbol{J}_s + \Theta \right] d\tau. \tag{1.6}$$

Using Gauss's theorem,

$$\frac{dS}{dt} = -\oint \boldsymbol{J}_s \cdot d\boldsymbol{\sigma} + \int \Theta d\tau, \tag{1.7}$$

where, on the right hand side of the equation, the first term denotes the amount of entropy that flows into the system per unit time through the system boundary from the external environment, and the second term characterizes the rate of production of entropy in the system due to internal causes.

It is this internal $\Theta$ that helps to identify the proper "currents" and "forces" used in Onsager's reciprocal relations [1]. Let $\alpha_i$ be a set of measurable internal parameters describing the irreversible processes in the system. Assume the macroscopic empirical laws (e.g., Ohm's law of electrical conduction, Fick's law of diffusion) governing these processes can be expressed in linear kinetic equations

$$\frac{\partial \alpha_i}{\partial t} = \sum_j L_{ij} \gamma_j, \tag{1.8}$$

where

$$\gamma_j \equiv \frac{\partial s}{\partial \alpha_j}, \tag{1.9}$$

are measures of the deviation from the equilibrium state, since in equilibrium $s$ is a maximum and $\gamma_j$ are zero. The kinetic coefficients $L_{ij}$ are measures of the interference of the $j$th "force" $\gamma_j$ on the $i$th "current" $\partial \alpha_i / \partial t$. They are functions of the state of the system that depend on temperature, composition, and applied magnetic fields. Furthermore, Onsager's theorem states that

$$L_{ij}(\boldsymbol{B}) = L_{ji}(-\boldsymbol{B}). \tag{1.10}$$

Dropping the $\alpha_j$ independent $-\nabla \cdot \boldsymbol{J}_s$ term in Eq. (1.5),

$$\Theta = \left.\frac{\partial s}{\partial t}\right|_{\text{internal}} = \sum_j \frac{\partial s}{\partial \alpha_j} \frac{\partial \alpha_j}{\partial t} = \sum_j \gamma_j \frac{\partial \alpha_j}{\partial t}, \tag{1.11}$$

through which the proper "forces" $\gamma_j$, and "currents" $\partial \alpha_j / \partial t$ can be conveniently identified.

We now introduce, in accordance with the thermodynamic relations, the particle number current density $\boldsymbol{J}_n$, the electric current density

$$\boldsymbol{J}_e = q\boldsymbol{J}_n, \tag{1.12}$$

the heat current density

$$\boldsymbol{J}_q = T\boldsymbol{J}_s, \tag{1.13}$$

and the internal energy current density

$$\boldsymbol{J}_u = \boldsymbol{J}_q + \mu\boldsymbol{J}_n. \tag{1.14}$$

Conservation laws similar to Eq. (1.5) hold for $\boldsymbol{J}_n$ ($\boldsymbol{J}_e$) and $\boldsymbol{J}_u$, with no presence of sources,

$$\frac{\partial n}{\partial t} + \nabla \cdot \boldsymbol{J}_n = 0, \frac{\partial u}{\partial t} + \nabla \cdot \boldsymbol{J}_u = 0. \tag{1.15}$$

Combining Eq. (1.3) and Eq. (1.15), we have

$$\frac{\partial s}{\partial t} = \frac{1}{T}\frac{\partial u}{\partial t} - \frac{\mu}{T}\frac{\partial n}{\partial t} = -\nabla \cdot \left(\frac{\boldsymbol{J}_q}{T}\right) + \nabla\frac{1}{T} \cdot \boldsymbol{J}_q - \frac{1}{T}\nabla\mu \cdot \boldsymbol{J}_n, \tag{1.16}$$

where, by comparison with Eq. (1.5),

$$\Theta = \nabla\frac{1}{T} \cdot \boldsymbol{J}_q - \frac{1}{T}\nabla\mu \cdot \boldsymbol{J}_n. \tag{1.17}$$

We have thus identified the "forces" $-\frac{1}{T}\nabla\mu$ and $\nabla\frac{1}{T}$ with "currents" $\boldsymbol{J}_n$ and $\boldsymbol{J}_q$.

## 1.2 Thermoelectric phenomena

We can consider the thermoelectric effects with one-dimensional (1D) primary currents. The phenomena of interest are the electrical conduction (Joule heating), the heat conduction (Fourier's law), Seebeck effect, Peltier effect, and Thomson effect.

The kinetic equations governing thermoelectrics are

$$\begin{aligned} \boldsymbol{J}_n &= L_{11}\left(-\frac{1}{T}\nabla\mu\right) + L_{12}\left(\nabla\frac{1}{T}\right), \\ \boldsymbol{J}_q &= L_{21}\left(-\frac{1}{T}\nabla\mu\right) + L_{22}\left(\nabla\frac{1}{T}\right). \end{aligned} \tag{1.18}$$

Noting that in the absence of applied magnetic fields, Onsager's theorem states

$$L_{21} = L_{12}, \tag{1.19}$$

we have

$$\begin{aligned} \boldsymbol{J}_n &= L_{11}\left(-\frac{1}{T}\nabla\mu\right) + L_{12}\left(\nabla\frac{1}{T}\right), \\ \boldsymbol{J}_q &= L_{12}\left(-\frac{1}{T}\nabla\mu\right) + L_{22}\left(\nabla\frac{1}{T}\right). \end{aligned} \tag{1.20}$$

In practice, however, electric current density $\boldsymbol{J}_e$ and temperature gradient $\nabla T$ are more conveniently to control, thus the following sets of equations are often useful:

$$\begin{aligned} \nabla\mu &= -\frac{T}{qL_{11}}\boldsymbol{J}_e - \frac{L_{12}}{TL_{11}}\nabla T, \\ \boldsymbol{J}_q &= \frac{L_{12}}{qL_{11}}\boldsymbol{J}_e - \frac{D}{T^2L_{11}}\nabla T, \\ D &\equiv L_{11}L_{22} - L_{12}^2 = \det\begin{bmatrix} L_{11} & L_{12} \\ L_{12} & L_{22} \end{bmatrix}. \end{aligned} \tag{1.21}$$

### 1.2.1 Electrical conductivity

The isothermal ( $\nabla T = 0$ ) electrical conductivity $\sigma$ is defined as the electric current density $\boldsymbol{J}_e$ per unit electrochemical potential gradient $\boldsymbol{E} = -\nabla\mu/q$,

$$\sigma = \frac{\boldsymbol{J}_e}{\boldsymbol{E}} = \frac{q^2L_{11}}{T}. \tag{1.22}$$

### 1.2.2 Thermal conductivity

The thermal conductivity $\kappa$ is defined as the heat current density $\boldsymbol{J}_q$ per unit temperature gradient $-\nabla T$, with no electric current flow ( $\boldsymbol{J}_e = 0$ ),

$$\kappa = \frac{\boldsymbol{J}_q}{-\nabla T} = \frac{D}{T^2 L_{11}}. \tag{1.23}$$

### 1.2.3 Seebeck effect

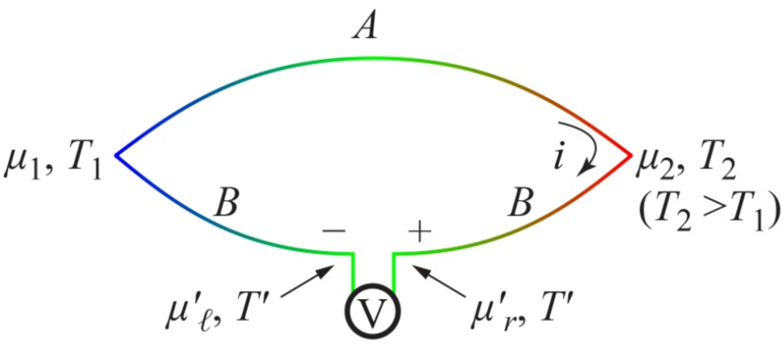

Figure 1.1 The Seebeck effect in a thermocouple.

The Seebeck effect originally refers to the production of an electromotive force (e.m.f.) in a thermocouple under the open circuit condition. Consider a thermocouple composed by materials *A* and *B*, with junctions at temperatures $T_1$ and $T_2$ ($T_2 > T_1$) , as schematically shown in Figure 1.1. Let an "ideal voltmeter" (which allows no passage of electricity, but offers no resistance to the heat flow) be inserted in *B* leg at a point at which the temperature is $T'$. From Eq. (1.21), for either conductor with $\boldsymbol{J}_e = 0$,

$$\nabla \mu = -\frac{L_{12}}{TL_{11}} \nabla T \equiv -S_J \nabla T, \tag{1.24}$$

where

$$S_J \equiv L_{12} / TL_{11}, \tag{1.25}$$

is the entropy per particle, carried on the particle current density $\boldsymbol{J}_n$ when flowing in a given temperature distribution, as is evident in the expression of $\boldsymbol{J}_s$ in terms of $\boldsymbol{J}_n$ and $\nabla T$ ,

$$\boldsymbol{J}_s = \frac{1}{T}\boldsymbol{J}_q = \frac{L_{12}}{qTL_{11}}\boldsymbol{J}_e - \frac{D}{T^3 L_{11}}\nabla T = \frac{S_J}{q}\boldsymbol{J}_e - \frac{1}{T}\kappa\nabla T = S_J \boldsymbol{J}_n - \frac{1}{T}\kappa\nabla T, \tag{1.26}$$

i.e.,

$$\boldsymbol{J}_q = TS_J \boldsymbol{J}_n - \kappa \nabla T. \tag{1.27}$$

Thus,

$$\begin{aligned} \mu_2 - \mu_1 &= -\int_{T_1}^{T_2} S_J^A dT, \\ \mu_2 - \mu_r' &= -\int_{T'}^{T_2} S_J^B dT, \\ \mu_\ell' - \mu_1 &= -\int_{T_1}^{T'} S_J^B dT. \end{aligned} \tag{1.28}$$

Eliminating $\mu_1$ and $\mu_2$,

$$\mu_r' - \mu_\ell' = \int_{T_1}^{T_2} \left( S_J^B - S_J^A \right) dT. \tag{1.29}$$

The voltage is

$$V = \frac{1}{q}\left( \mu_r' - \mu_\ell' \right) = \frac{1}{q} \int_{T_1}^{T_2} \left( S_J^B - S_J^A \right) dT. \tag{1.30}$$

The relative Seebeck coefficient, or thermoelectric power, of the thermocouple, $\alpha_{AB}$, is defined as the change in voltage per unit change in temperature difference. The sign of $\alpha_{AB}$ is chosen as positive if the voltage increment is such as to drive the (transient) current *i* from *A* to *B* at the hot junction. Then

$$\alpha_{AB} \equiv \frac{\partial V}{\partial T_2} = \frac{1}{q}\left[ S_J^B (T_2) - S_J^A (T_2) \right] \equiv \alpha_B - \alpha_A, \tag{1.31}$$

where the quantities $\alpha_A = S_J^A / q$ and $\alpha_B = S_J^B / q$ are referred to as the absolute Seebeck coefficients, or thermoelectric powers, of materials *A* and *B*, respectively.

Consistent with the above mentioned definition, the absolute Seebeck coefficient $\alpha$ can also be introduced as the electrochemical potential gradient $\boldsymbol{E}$ ($= -\nabla\mu/q$) per unit temperature gradient $\nabla T$ [3], under the open circuit condition ($\boldsymbol{J}_e = 0$),

$$\alpha = \frac{\boldsymbol{E}}{\nabla T} = \frac{-\nabla \mu / q}{\nabla T} = \frac{L_{12}}{qTL_{11}} = \frac{S_J}{q}. \tag{1.32}$$

Recall from Eq. (1.26),

$$\boldsymbol{J}_s = \frac{1}{T}\boldsymbol{J}_q = \alpha \boldsymbol{J}_e - \frac{1}{T}\kappa \nabla T, \tag{1.33}$$

suggests that the absolute Seebeck coefficient $\alpha$ is the entropy current density per unit electric current density.

Using $\sigma$, $\kappa$, and $\alpha$ derived so far, the kinetic coefficients can be expressed as

$$\begin{aligned} L_{11} &= \frac{T}{q^2}\sigma, \\ L_{12} &= \frac{T^2}{q}\alpha\sigma, \\ L_{22} &= T^3\alpha^2\sigma + T^2\kappa. \end{aligned} \tag{1.34}$$

Hence the kinetic equations are,

$$\begin{aligned} \boldsymbol{J}_n &= \frac{T\sigma}{q^2}\left(-\frac{1}{T}\nabla\mu\right) + \frac{T^2\alpha\sigma}{q}\left(\nabla\frac{1}{T}\right), \\ \boldsymbol{J}_q &= \frac{T^2\alpha\sigma}{q}\left(-\frac{1}{T}\nabla\mu\right) + \left(T^3\alpha^2\sigma + T^2\kappa\right)\left(\nabla\frac{1}{T}\right), \end{aligned} \tag{1.35}$$

and

$$\begin{aligned} \nabla\mu &= -\frac{q}{\sigma}\boldsymbol{J}_e - q\alpha\nabla T, \\ \boldsymbol{J}_q &= T\alpha\boldsymbol{J}_e - \kappa\nabla T. \end{aligned} \tag{1.36}$$

Note that $\boldsymbol{J}_e = \sigma(-\nabla\mu/q) - \alpha\sigma\nabla T$ suggests that both electric field ( $-\nabla\mu/q$ ) and thermal gradient ( $\nabla T$ ) can lead to an electric current flow.

### 1.2.4 Peltier effect

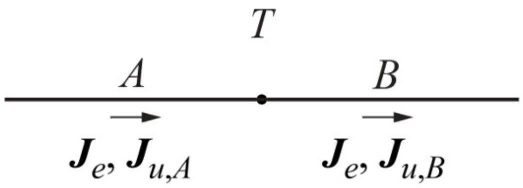

Figure 1.2 The Peltier effect.

The Peltier effect refers to the evolution of heat accompanying the flow of an electric current $\boldsymbol{J}_e$ across an isothermal junction of two materials $A$ and $B$, as shown in Figure 1.2. The internal energy flow will be discontinuous across the junction, and the energy difference appears as "Peltier heat" at the junction. We have $\boldsymbol{J}_u = \boldsymbol{J}_q + \mu\boldsymbol{J}_n$, and since both $\mu$ and $\boldsymbol{J}_n$ are continuous across the junction it follows that the discontinuity in $\boldsymbol{J}_u$ is equal to the discontinuity in $\boldsymbol{J}_q$.

$$\boldsymbol{J}_{u,B} - \boldsymbol{J}_{u,A} = \boldsymbol{J}_{q,B} - \boldsymbol{J}_{q,A}. \tag{1.37}$$

Under the isothermal condition, in either conductor,

$$\boldsymbol{J}_q = T\alpha\boldsymbol{J}_e, \tag{1.38}$$

whence

$$\boldsymbol{J}_{q,B} - \boldsymbol{J}_{q,A} = T(\alpha_B - \alpha_A)\boldsymbol{J}_e, \tag{1.39}$$

The Peltier coefficient $\pi_{AB}$ is defined as the heat current density which must be supplied to the junction per unit electric current $\boldsymbol{J}_e$ passed from $A$ to $B$,

$$\pi_{AB} = \frac{\boldsymbol{J}_{q,B} - \boldsymbol{J}_{q,A}}{\boldsymbol{J}_e} = T(\alpha_B - \alpha_A) = T\alpha_{AB}, \tag{1.40}$$

which is historically known as the Second Kelvin Relation of thermoelectrics.

The "absolute" Peltier coefficient of a material can be obtained from Eq. (1.36),

$$\boldsymbol{J}_q = T\alpha\boldsymbol{J}_e - \kappa\nabla T, \tag{1.41}$$

where, on the right hand side of the equation, the second term is the heat current density due to Fourier heat conduction, and the first term is the Peltier heat current density

$$\boldsymbol{J}_{q\pi} = T\alpha\boldsymbol{J}_e. \tag{1.42}$$

Thus,

$$\pi = T\alpha. \tag{1.43}$$

### 1.2.5 Thomson effect

The Thomson effect refers to the evolution of heat as a steady-state electric current $\boldsymbol{J}_e$ traverses a temperature gradient $\nabla T$ in a material. The increment rate of internal energy density

$$\frac{\partial u}{\partial t} = -\nabla\cdot\boldsymbol{J}_u = -\nabla\cdot\left(\boldsymbol{J}_q + \mu\boldsymbol{J}_n\right) = -\nabla\cdot\boldsymbol{J}_q - \nabla\mu\cdot\boldsymbol{J}_n, \tag{1.44}$$

since $\nabla\cdot\boldsymbol{J}_n = 0$ for a steady-state current. In terms of $\boldsymbol{J}_e$ and $\nabla T$, we have

$$\frac{\partial u}{\partial t} = -\nabla\cdot\left(T\alpha\boldsymbol{J}_e - \kappa\nabla T\right) + \left(\frac{1}{\sigma}\boldsymbol{J}_e + \alpha\nabla T\right)\cdot\boldsymbol{J}_e = -T\boldsymbol{J}_e\cdot\nabla\alpha + \nabla\cdot\left(\kappa\nabla T\right) + \frac{1}{\sigma}\boldsymbol{J}_e^2, \tag{1.45}$$

where, on the right hand side of the equation, the third term $\boldsymbol{J}_e^2/\sigma$ represents the liberated Joule heat, the second term is due to heat conduction (turns out to be zero [1]), and the first term

$$q_T \equiv -T\boldsymbol{J}_e\cdot\nabla\alpha = -T\frac{d\alpha}{dT}\boldsymbol{J}_e\cdot\nabla T, \tag{1.46}$$

is the liberating rate of Thomson heat per unit volume. The Thomson coefficient $\tau$ is defined as the ratio of $q_T$ to the product $-\boldsymbol{J}_e\cdot\nabla T$ ,

$$\tau = T\frac{d\alpha}{dT}. \tag{1.47}$$

Taking derivative with respect to $T$ on the Second Kelvin Relation,

$$\frac{d\pi_{AB}}{dT} = (\alpha_B - \alpha_A) + T\left(\frac{d\alpha_B}{dT} - \frac{d\alpha_A}{dT}\right), \tag{1.48}$$

which leads to the First Kelvin Relation:

$$\frac{d\pi_{AB}}{dT} + (\tau_A - \tau_B) = \alpha_B - \alpha_A. \tag{1.49}$$

## 1.3 The figure of merit *ZT*

Efficiency of a thermoelectric material is evaluated based on its dimensionless figure of merit defined as $ZT = \alpha^2\sigma T/\kappa$, where $\alpha$ is the Seebeck coefficient, $\sigma$ is the electrical conductivity, $\kappa$ is the thermal conductivity, and $T$ is the absolute temperature. Since transport parameters are interdependent, it is a challenging task to maximize the figure of merit. In the theoretical evaluation of transport properties, a variety of models are used, among them the most popular one is the single parabolic band (SPB) model. Its appeal stems from its mathematical simplicity and readily available relevant formulae, offering an excellent initial evaluation of electronic properties of thermoelectric materials. However, applying the SPB model in more quantitative studies often requires extra attention and care because the band structure of the existing materials is rarely strictly parabolic.

# CHAPTER 2

# THERMO-GALVANOMAGNETIC TRANSPORT

The interplay of temperature gradients and electromagnetic fields in solids has lead to a variety of thermo-galvanomagnetic effects [4-8], the spirit of which is still generating curiosities in contemporary condensed matter physics [9-12]. In this chapter, I will describe the transport effects using thermodynamic arguments [1, 2, 13] and obtain Onsager's kinetic coefficients [14, 15] by solving the Boltzmann transport equation under the relaxation time approximation with Fermi-Dirac statistics. These formula are crucial in understanding the transport behavior of novel thermoelectric materials.

## 2.1 Thermo-galvanomagnetic phenomena

We now expand the analyses from CHAPTER 1 to describe simultaneous electric current and heat current with applied magnetic fields, when various new effects appear. If we consider a system in which a magnetic field $\boldsymbol{B} = B_z \hat{e}_z$ is applied along the $z$ axis and in which the currents and gradients are constrained in the isotropic $x$-$y$ plane, we still have

$$\varTheta = \nabla \frac{1}{T} \cdot \boldsymbol{J}_q - \frac{1}{T} \nabla \mu \cdot \boldsymbol{J}_n . \tag{2.1}$$

In its component form,

$$\varTheta = \nabla_x \frac{1}{T} \cdot J_{q,x} + \nabla_y \frac{1}{T} \cdot J_{q,y} - \frac{1}{T} \nabla_x \mu \cdot J_{n,x} - \frac{1}{T} \nabla_y \mu \cdot J_{n,y} . \tag{2.2}$$

Thus the kinetic equations become

$$
\begin{aligned}
J_{n,x} &= L_{11}\left(-\frac{1}{T}\nabla_x\mu\right)+L_{12}\left(\nabla_x\frac{1}{T}\right)+L_{13}\left(-\frac{1}{T}\nabla_y\mu\right)+L_{14}\left(\nabla_y\frac{1}{T}\right),\\
J_{q,x} &= L_{21}\left(-\frac{1}{T}\nabla_x\mu\right)+L_{22}\left(\nabla_x\frac{1}{T}\right)+L_{23}\left(-\frac{1}{T}\nabla_y\mu\right)+L_{24}\left(\nabla_y\frac{1}{T}\right),\\
J_{n,y} &= L_{31}\left(-\frac{1}{T}\nabla_x\mu\right)+L_{32}\left(\nabla_x\frac{1}{T}\right)+L_{33}\left(-\frac{1}{T}\nabla_y\mu\right)+L_{34}\left(\nabla_y\frac{1}{T}\right),\\
J_{q,y} &= L_{41}\left(-\frac{1}{T}\nabla_x\mu\right)+L_{42}\left(\nabla_x\frac{1}{T}\right)+L_{43}\left(-\frac{1}{T}\nabla_y\mu\right)+L_{44}\left(\nabla_y\frac{1}{T}\right).
\end{aligned}
\tag{2.3}
$$

Basic symmetry considerations of $L_{ij}$, due to the isotropy in the $x$-$y$ plane, require that

$$
\begin{aligned}
L_{31} &= -L_{13}, L_{32} = -L_{14}, L_{33} = L_{11}, L_{34} = L_{12},\\
L_{41} &= -L_{23}, L_{42} = -L_{24}, L_{43} = L_{21}, L_{44} = L_{22},
\end{aligned}
\tag{2.4}
$$

where $L_{11}$, $L_{12}$, $L_{21}$, and $L_{22}$ are even functions of the magnetic field, and $L_{13}$, $L_{14}$, $L_{23}$, and $L_{24}$ are odd functions of the magnetic field. According to Onsager's theorem,

$$
L_{21}(\boldsymbol{B}) = L_{12}(-\boldsymbol{B}) = L_{12}(\boldsymbol{B}), L_{23}(\boldsymbol{B}) = L_{32}(-\boldsymbol{B}) = -L_{14}(-\boldsymbol{B}) = L_{14}(\boldsymbol{B}),
\tag{2.5}
$$

we have

$$
\begin{aligned}
J_{n,x} &= L_{11}\left(-\frac{1}{T}\nabla_x\mu\right)+L_{12}\left(\nabla_x\frac{1}{T}\right)+L_{13}\left(-\frac{1}{T}\nabla_y\mu\right)+L_{14}\left(\nabla_y\frac{1}{T}\right),\\
J_{q,x} &= L_{12}\left(-\frac{1}{T}\nabla_x\mu\right)+L_{22}\left(\nabla_x\frac{1}{T}\right)+L_{14}\left(-\frac{1}{T}\nabla_y\mu\right)+L_{24}\left(\nabla_y\frac{1}{T}\right),\\
J_{n,y} &= -L_{13}\left(-\frac{1}{T}\nabla_x\mu\right)-L_{14}\left(\nabla_x\frac{1}{T}\right)+L_{11}\left(-\frac{1}{T}\nabla_y\mu\right)+L_{12}\left(\nabla_y\frac{1}{T}\right),\\
J_{q,y} &= -L_{14}\left(-\frac{1}{T}\nabla_x\mu\right)-L_{24}\left(\nabla_x\frac{1}{T}\right)+L_{12}\left(-\frac{1}{T}\nabla_y\mu\right)+L_{22}\left(\nabla_y\frac{1}{T}\right),
\end{aligned}
\tag{2.6}
$$

with only six independent coefficients: $L_{11}$, $L_{12}$, $L_{22}$, $L_{13}$, $L_{14}$, and $L_{24}$. More discussion of the kinetic coefficient matrix **L** (Table 2-1) and its sub-matrices $\mathbf{L}_{i;j}$ [Eq. (2.7)] can be found in APPENDIX A.

Considering that the electric current $\boldsymbol{J}_e$ ($\equiv q\boldsymbol{J}_n$) and temperature gradient $\nabla T$ are easier to control in practice, we express $\nabla\mu$ and $\boldsymbol{J}_q$ in terms of $\boldsymbol{J}_e$ and $\nabla T$,

$$
\begin{aligned}
\nabla_x \mu &= -\frac{TL_{11}}{q \det \mathbf{L}_{13;13}} J_{e,x} - \frac{\det \mathbf{L}_{13;14}}{T \det \mathbf{L}_{13;13}} \nabla_x T + \frac{TL_{13}}{q \det \mathbf{L}_{13;13}} J_{e,y} - \frac{\det \mathbf{L}_{12;13}}{T \det \mathbf{L}_{13;13}} \nabla_y T, \\
J_{q,x} &= \frac{\det \mathbf{L}_{13;14}}{q \det \mathbf{L}_{13;13}} J_{e,x} - \frac{\det \mathbf{L}_{134;134}}{T^2 \det \mathbf{L}_{13;13}} \nabla_x T + \frac{\det \mathbf{L}_{12;13}}{q \det \mathbf{L}_{13;13}} J_{e,y} + \frac{\det \mathbf{L}_{123;134}}{T^2 \det \mathbf{L}_{13;13}} \nabla_y T, \\
\nabla_y \mu &= -\frac{TL_{13}}{q \det \mathbf{L}_{13;13}} J_{e,x} + \frac{\det \mathbf{L}_{12;13}}{T \det \mathbf{L}_{13;13}} \nabla_x T - \frac{TL_{11}}{q \det \mathbf{L}_{13;13}} J_{e,y} - \frac{\det \mathbf{L}_{13;14}}{T \det \mathbf{L}_{13;13}} \nabla_y T, \\
J_{q,y} &= -\frac{\det \mathbf{L}_{12;13}}{q \det \mathbf{L}_{13;13}} J_{e,x} - \frac{\det \mathbf{L}_{123;134}}{T^2 \det \mathbf{L}_{13;13}} \nabla_x T + \frac{\det \mathbf{L}_{13;14}}{q \det \mathbf{L}_{13;13}} J_{e,y} - \frac{\det \mathbf{L}_{134;134}}{T^2 \det \mathbf{L}_{13;13}} \nabla_y T,
\end{aligned}
\tag{2.7}
$$

where the somewhat cumbersome notation of $\mathbf{L}_{i;j}$ are sub-matrices constructed by keeping the *i*- rows and the *j*-columns of **L**.

The thermo-galvanomagnetic transport effects can be defined under two types of boundary conditions, namely (i) the isothermal condition, where temperature gradient in the direction perpendicular to the primary current is zero, and (ii) the adiabatic condition, in contrast, where no transverse heat is allowed to flow. A recipe of how to specify the correct boundary condition is given in APPENDIX A.

Let *x* axis be the direction of the primary electric current density $J_{e,x}$ and/or heat current density $J_{q,x}$, we introduce all the 14 thermo-galvanomagnetic effects: electrical conductivity (2), thermal conductivity (2), Seebeck coefficient (2), Peltier coefficient (2), Hall coefficient (2), Nernst coefficient (2), Ettingshausen coefficient (1), and Righi-Leduc coefficient (1). The Ettingshausen effect and Righi-Leduc effect can only be observed adiabatically, while the other effects can be measured under both isothermal and adiabatic conditions. Since we only have 6 independent kinetic coefficients, 8 (= 14 – 6) relations are expected among these transport coefficients.

We now summarize these transport coefficients in Table 2-1, while detailed derivations can be found in APPENDIX A.

Table 2-1 Thermo-galvanomagnetic transport coefficients.

| Coefficient | Definition | Boundary Condition | Expression |
|---|---|---|---|
| Electrical conductivity | $\sigma = \frac{J_{e,x}}{E_x}$ | $J_{e,y} = 0, \nabla_x T = 0, \nabla_y T = 0$ (isothermal) | $\sigma_i = \frac{q^2}{T} \frac{\det \mathbf{L}_{13;13}}{L_{11}}$ |
| | | $J_{e,y} = 0, \nabla_x T = 0, J_{q,y} = 0$ (adibatic) | $\sigma_a = \frac{q^2}{T} \frac{\det \mathbf{L}_{134;134}}{\det \mathbf{L}_{12;12}}$ |
| Thermal conductivity | $\kappa = \frac{J_{q,x}}{-\nabla_x T}$ | $J_{e,y} = 0, J_{e,x} = 0, \nabla_y T = 0$ (isothermal) | $\kappa_i = \frac{1}{T^2} \frac{\det \mathbf{L}_{134;134}}{\det \mathbf{L}_{13;13}}$ |
| | | $J_{e,y} = 0, J_{e,x} = 0, J_{q,y} = 0$ (adibatic) | $\kappa_a = \frac{1}{T^2} \frac{\det \mathbf{L}}{\det \mathbf{L}_{134;134}}$ |
| Seebeck | $\alpha = \frac{E_x}{\nabla_x T}$ | $J_{e,y} = 0, J_{e,x} = 0, \nabla_y T = 0$ (isothermal) | $\alpha_i = \frac{1}{qT} \frac{\det \mathbf{L}_{13;14}}{\det \mathbf{L}_{13;13}}$ |
| | | $J_{e,y} = 0, J_{e,x} = 0, J_{q,y} = 0$ (adibatic) | $\alpha_a = \frac{1}{qT} \frac{\det \mathbf{L}_{134;234}}{\det \mathbf{L}_{134;134}}$ |
| Peltier | $\pi = \frac{J_{q,x}}{J_{e,x}}$ | $J_{e,y} = 0, \nabla_x T = 0, \nabla_y T = 0$ (isothermal) | $\pi_i = \frac{1}{q} \frac{\det \mathbf{L}_{13;14}}{\det \mathbf{L}_{13;13}}$ |
| | | $J_{e,y} = 0, \nabla_x T = 0, J_{q,y} = 0$ (adibatic) | $\pi_a = \frac{1}{q} \frac{\det \mathbf{L}_{134;234}}{\det \mathbf{L}_{134;134}}$ |
| Hall | $R_H = \frac{E_y}{J_{e,x} B_z}$ | $J_{e,y} = 0, \nabla_x T = 0, \nabla_y T = 0$ (isothermal) | $R_{H,i} = \frac{T}{q^2 B_z} \frac{L_{13}}{\det \mathbf{L}_{13;13}}$ |
| | | $J_{e,y} = 0, \nabla_x T = 0, J_{q,y} = 0$ (adibatic) | $R_{H,a} = \frac{T}{q^2 B_z} \frac{-\det \mathbf{L}_{12;23}}{\det \mathbf{L}_{134;134}}$ |

| Coefficient (cont'd) | Definition | Boundary Condition | Expression |
|---|---|---|---|
| Nernst | $N = \frac{E_y}{-\nabla_x T B_z}$ | $J_{e,y} = 0, J_{e,x} = 0, \nabla_y T = 0$ (isothermal) | $N_i = \frac{1}{qTB_z} \frac{\det \mathbf{L}_{12;13}}{\det \mathbf{L}_{13;13}}$ |
| | | $J_{e,y} = 0, J_{e,x} = 0, J_{q,y} = 0$ (adibatic) | $N_a = \frac{1}{qTB_z} \frac{-\det \mathbf{L}_{134;124}}{\det \mathbf{L}_{134;134}}$ |
| Ettingshausen | $P = \frac{-\nabla_y T}{J_{e,x} B_z}$ | $J_{e,y} = 0, \nabla_x T = 0, J_{q,y} = 0$ (adiabatic) | $P = \frac{T^2}{qB_z} \frac{\det \mathbf{L}_{12;13}}{\det \mathbf{L}_{134;134}}$ |
| Righi-Leduc | $L = \frac{-\nabla_y T}{-\nabla_x T B_z}$ | $J_{e,y} = 0, J_{e,x} = 0, J_{q,y} = 0$ (adibatic) | $L = \frac{1}{B_z} \frac{\det \mathbf{L}_{134;123}}{\det \mathbf{L}_{134;134}}$ |

RELATIONS

(Bridgman) $TN_i = \kappa_i P$ .

(Kelvin) $\pi_i = T\alpha_i$ , $\pi_a = T\alpha_a$ .

(Putley) $\sigma_i^{-1} - \sigma_a^{-1} = B_z^2 P N_i$ , $\kappa_i - \kappa_a = -B_z^2 \kappa_i L^2$ , $\alpha_i - \alpha_a = -B_z^2 N_i L$ , $N_i - N_a = L\alpha_i$ , $R_{H,i} - R_{H,a} = P\alpha_i$ .

KINETIC COEFFICIENTS

$$\mathbf{L} \equiv \begin{bmatrix} L_{11} & L_{12} & L_{13} & L_{14} \\ L_{12} & L_{22} & L_{14} & L_{24} \\ -L_{13} & -L_{14} & L_{11} & L_{12} \\ -L_{14} & -L_{24} & L_{12} & L_{22} \end{bmatrix}$$

## 2.2 Boltzmann transport equation

In order to evaluate the kinetic coefficients $L_{ij}$, we solve the Boltzmann transport equation (BTE) with the relaxation time approximation,

$$\frac{\partial f}{\partial t}+\boldsymbol{v}\cdot\frac{\partial}{\partial \boldsymbol{r}}f+\frac{q}{m_s^*}\left(\boldsymbol{E}+\boldsymbol{v}\times\boldsymbol{B}\right)\cdot\frac{\partial f}{\partial \boldsymbol{v}}=-\frac{f-f_0}{\tau}. \tag{2.8}$$

In BTE, $f$ is the distribution function of electron perturbed from its equilibrium $f_0$ ( $\left|f-f_0\right| << f_0$ ) by small electric field, temperature and/or concentration (chemical potential) gradient. The equilibrium Fermi-Dirac distribution of electron $f_0$ is given by

$$f_0=\frac{1}{e^{(\varepsilon-\mu_c)/k_BT}+1}, \tag{2.9}$$

where energy $\varepsilon$ and $\mu_c$ are measured from the band edge [conduction (valence) band minimum (maximum) $E_C$ ($E_V$) for electron (hole)]. This reference system essentially sets $E_C$ ($E_V$) = 0 at different locations (although the absolute value measured from a global reference system varies at different location). The same quantum state $\boldsymbol{k}$ = ($k_x$, $k_y$, $k_z$) has the same energy at different locations,

$$\varepsilon(\boldsymbol{k})=\tilde{\varepsilon}(\boldsymbol{k})-E_C=\frac{\hbar^2}{2m_s^*}\left(k_x^2+k_y^2+k_z^2\right), \tag{2.10}$$

where $m_s^*$ is the effective mass for a single carrier in a single band/valley. The relaxation time $\tau$ generally depends on energy,

$$\tau=\tau_0\varepsilon^r. \tag{2.11}$$

For steady state, $\partial f/\partial t \sim 0$, an *ad hoc* solution of $f$ is given by

$$f=f_0-\boldsymbol{v}\cdot\boldsymbol{C}(\varepsilon)\frac{\partial f_0}{\partial \varepsilon}. \tag{2.12}$$

Assuming all electric fields and temperature gradients are in the $x$, $y$ plane and the applied magnetic field is in $z$ axis $\boldsymbol{B} = B_z \hat{e}_z$, we have (Section A.4 of APPENDIX A),

$$f = f_0 - \left(v_x C_x + v_y C_y\right)\frac{\partial f_0}{\partial \varepsilon}, \tag{2.13}$$

where

$$\begin{aligned}
C_x &= \frac{\alpha + \gamma \cdot \beta}{1+\gamma^2}, C_y = \frac{\beta - \gamma \cdot \alpha}{1+\gamma^2}, \\
\alpha &\equiv -\tau\left(\nabla_x \mu + \frac{\varepsilon - \mu_c}{T}\nabla_x T\right), \\
\beta &\equiv -\tau\left(\nabla_y \mu + \frac{\varepsilon - \mu_c}{T}\nabla_y T\right), \\
\gamma &\equiv \frac{q\tau}{m_s^*}B_z = \pm\omega_c\tau,\ \omega_c \equiv \frac{eB_z}{m_s^*}.
\end{aligned} \tag{2.14}$$

The number of electron per unit volume with energy between $\varepsilon$ and $\varepsilon + d\varepsilon$ is

$$dn = fD(\varepsilon)d\varepsilon, \tag{2.15}$$

where the density of states per unit volume $D(\varepsilon)$ for a three dimensional (3D) crystal is,

$$D(\varepsilon) = \frac{4\pi\left(2m_d^*\right)^{3/2}}{h^3}\varepsilon^{1/2}, \tag{2.16}$$

where $h = 6.626\times10^{-34}$ J s is the Planck constant, $m_d^* = N_v^{2/3} m_s^*$ is the density-of-states effective mass with $N_v$ fold degeneracy. Details of $D(\varepsilon)$ are given in Section A.4 of APPENDIX A. The electron number current density $J_{n,x}$ is given by, noting $m_s^* v_x^2/2 = \varepsilon/3$,

$$\begin{aligned}
J_{n,x} &= \int_{\varepsilon=0}^{\infty} v_x f D(\varepsilon)d\varepsilon = \int_{\varepsilon=0}^{\infty} v_x\left[f_0 - \left(v_x C_x + v_y C_y\right)\frac{\partial f_0}{\partial \varepsilon}\right]D(\varepsilon)d\varepsilon \\
&= -\int_{\varepsilon=0}^{\infty} v_x^2 C_x \frac{\partial f_0}{\partial \varepsilon}D(\varepsilon)d\varepsilon = \frac{2}{3m_s^*}\int_{\varepsilon=0}^{\infty}\frac{\partial f_0}{\partial \varepsilon}D(\varepsilon)\varepsilon\left(-C_x\right)d\varepsilon,
\end{aligned} \tag{2.17}$$

the kinetic energy current density $J_{\varepsilon,x}$ is

$$J_{\varepsilon,x} = \frac{2}{3m_s^*}\int_{\varepsilon=0}^{\infty}\frac{\partial f_0}{\partial\varepsilon}D(\varepsilon)\varepsilon^2(-C_x)d\varepsilon, \tag{2.18}$$

the total energy current density $J_{u,x}$ is

$$J_{u,x} = \frac{2}{3m_s^*}\int_{\varepsilon=0}^{\infty}\frac{\partial f_0}{\partial\varepsilon}D(\varepsilon)(\varepsilon + q\varphi_e)\varepsilon(-C_x)d\varepsilon, \tag{2.19}$$

and the heat current density $J_{q,x}$ (= $J_{u,x} - \mu J_{n,x} = J_{\varepsilon,x} - \mu_c J_{n,x}$) is given by

$$J_{q,x} = \frac{2}{3m_s^*}\int_{\varepsilon=0}^{\infty}\frac{\partial f_0}{\partial\varepsilon}D(\varepsilon)\varepsilon(\varepsilon - \mu_c)(-C_x)d\varepsilon. \tag{2.20}$$

Combining similar expressions along $y$ axis,

$$\begin{aligned}
J_{n,x} &= \frac{2}{3m_s^*}\int_{\varepsilon=0}^{\infty}\frac{\partial f_0}{\partial\varepsilon}D(\varepsilon)\varepsilon(-C_x)d\varepsilon,\\
J_{q,x} &= \frac{2}{3m_s^*}\int_{\varepsilon=0}^{\infty}\frac{\partial f_0}{\partial\varepsilon}D(\varepsilon)\varepsilon(\varepsilon - \mu_c)(-C_x)d\varepsilon,\\
J_{n,y} &= \frac{2}{3m_s^*}\int_{\varepsilon=0}^{\infty}\frac{\partial f_0}{\partial\varepsilon}D(\varepsilon)\varepsilon(-C_y)d\varepsilon,\\
J_{q,y} &= \frac{2}{3m_s^*}\int_{\varepsilon=0}^{\infty}\frac{\partial f_0}{\partial\varepsilon}D(\varepsilon)\varepsilon(\varepsilon - \mu_c)(-C_y)d\varepsilon.
\end{aligned} \tag{2.21}$$

Using the ***C*** coefficients, we have

$$\begin{aligned}
J_{n,x} &= L_{11}\left(-\frac{1}{T}\nabla_x\mu\right) + L_{12}\left(\nabla_x\frac{1}{T}\right) + L_{13}\left(-\frac{1}{T}\nabla_y\mu\right) + L_{14}\left(\nabla_y\frac{1}{T}\right),\\
J_{q,x} &= L_{12}\left(-\frac{1}{T}\nabla_x\mu\right) + L_{22}\left(\nabla_x\frac{1}{T}\right) + L_{14}\left(-\frac{1}{T}\nabla_y\mu\right) + L_{24}\left(\nabla_y\frac{1}{T}\right),\\
J_{n,y} &= -L_{13}\left(-\frac{1}{T}\nabla_x\mu\right) - L_{14}\left(\nabla_x\frac{1}{T}\right) + L_{11}\left(-\frac{1}{T}\nabla_y\mu\right) + L_{12}\left(\nabla_y\frac{1}{T}\right),\\
J_{q,y} &= -L_{14}\left(-\frac{1}{T}\nabla_x\mu\right) - L_{24}\left(\nabla_x\frac{1}{T}\right) + L_{12}\left(-\frac{1}{T}\nabla_y\mu\right) + L_{22}\left(\nabla_y\frac{1}{T}\right),
\end{aligned} \tag{2.22}$$

where

$$
\begin{aligned}
&L_{11}=\mathcal{K}_1, L_{12}=\mathcal{K}_2-\mu_c\mathcal{K}_1, L_{13}=\mathcal{H}_1, L_{14}=\mathcal{H}_2-\mu_c\mathcal{H}_1,\\
&L_{22}=\mathcal{K}_3-2\mu_c\mathcal{K}_2+\mu_c^2\mathcal{K}_1, L_{24}=\mathcal{H}_3-2\mu_c\mathcal{H}_2+\mu_c^2\mathcal{H}_1,
\end{aligned}
\tag{2.23}
$$

and

$$
\begin{aligned}
\mathcal{H}_i &\equiv \frac{2T}{3m_s^*}\int_{\varepsilon=0}^{\infty}\left(-\frac{\partial f_0}{\partial\varepsilon}\right)D(\varepsilon)\frac{\varepsilon^i\gamma\tau}{1+\gamma^2}d\varepsilon,\\
\mathcal{K}_i &\equiv \frac{2T}{3m_s^*}\int_{\varepsilon=0}^{\infty}\left(-\frac{\partial f_0}{\partial\varepsilon}\right)D(\varepsilon)\frac{\varepsilon^i\tau}{1+\gamma^2}d\varepsilon.
\end{aligned}
\tag{2.24}
$$

In the low field approximation, $\gamma \ll 1$,

$$
\begin{aligned}
\mathcal{H}_i &\overset{\gamma<<1}{\rightarrow} H_i \equiv \frac{2T}{3m_s^*}\int_{\varepsilon=0}^{\infty}\left(-\frac{\partial f_0}{\partial\varepsilon}\right)D(\varepsilon)\varepsilon^i\gamma\tau d\varepsilon\\
&=\frac{2T}{3m_s^*}\frac{4\pi\left(2m_d^*\right)^{3/2}}{h^3}\frac{qB_z}{m_s^*}\tau_0^2\left(i+2r+\tfrac{1}{2}\right)\left(k_BT\right)^{i+2r+\frac{1}{2}}F_{i+2r-\frac{1}{2}}(\eta),\\
\mathcal{K}_i &\overset{\gamma<<1}{\rightarrow} K_i \equiv \frac{2T}{3m_s^*}\int_{\varepsilon=0}^{\infty}\left(-\frac{\partial f_0}{\partial\varepsilon}\right)D(\varepsilon)\varepsilon^i\tau d\varepsilon\\
&=\frac{2T}{3m_s^*}\frac{4\pi\left(2m_d^*\right)^{3/2}}{h^3}\tau_0\left(i+r+\tfrac{1}{2}\right)\left(k_BT\right)^{i+r+\frac{1}{2}}F_{i+r-\frac{1}{2}}(\eta),
\end{aligned}
\tag{2.25}
$$

where the Fermi-Dirac integral $F_n(\eta)$ is defined as

$$
F_n(\eta)=\int_0^{\infty}f_0(\xi,\eta)\xi^n d\xi=\int_0^{\infty}\frac{1}{e^{\xi-\eta}+1}\xi^n d\xi,
\tag{2.26}
$$

where the reduced energy $\xi = \varepsilon/k_BT$, and the reduced chemical potential $\eta = \mu_c/k_BT$. In practice, $\eta$ is often referred to as the reduced Fermi level $\eta = E_F/k_BT$. Useful relations regarding the Fermi-Dirac integral are provided in Section A.4 of APPENDIX A.

We are now fully equipped to evaluate the thermo-galvanomagnetic transport coefficients (Table 2-1) for general degenerate semiconductors using Fermi-Dirac integrals. The results are summarized in Table 2-2. More details including expressions for two extreme cases, namely the non-degenerate limit and the highly degenerate (metallic) limit, are provided in Section A.4 of APPENDIX A.

Table 2-2. Transport coefficients in degenerate semiconductors

| Coefficient | Definition | General Formula | MFPIE<br>$\tau_0 = \ell\left(m^*/2\right)^{1/2}, r = -1/2$ |
|---|---|---|---|
| Carrier density | | $n = \frac{4\pi\left(2m_d^* k_B T\right)^{3/2}}{h^3} F_{\frac{1}{2}}(\eta)$ | |
| Hall coefficient | | $R_H = \frac{3}{2q}\frac{1}{n}\frac{\left(2r+\frac{3}{2}\right)}{\left(r+\frac{3}{2}\right)^2}\frac{F_{2r+\frac{1}{2}}(\eta)F_{\frac{1}{2}}(\eta)}{F_{r+\frac{1}{2}}^2(\eta)}$ | |
| Hall density | $n_H \equiv \frac{1}{qR_H}$ | $n_H = \frac{2}{3}\frac{\left(r+\frac{3}{2}\right)^2}{\left(2r+\frac{3}{2}\right)}\frac{F_{r+\frac{1}{2}}^2(\eta)}{F_{2r+\frac{1}{2}}(\eta)F_{\frac{1}{2}}(\eta)} n$ | |
| Electrical conductivity | | $\sigma = \frac{2}{3}\frac{nq^2\tau_0}{m_s^*}\left(r+\frac{3}{2}\right)\left(k_B T\right)^r \frac{F_{r+\frac{1}{2}}(\eta)}{F_{\frac{1}{2}}(\eta)}$ | $\sigma^{MFPIE} = N_v \frac{16\pi}{3}\frac{m_s^* q^2 \ell}{h^3} k_B T F_0(\eta)$ |
| Drift mobility | $\mu_d = \frac{\sigma}{nq}$ | $\mu_d = \frac{2}{3}\frac{q\tau_0}{m_s^*}\left(r+\frac{3}{2}\right)\left(k_B T\right)^r \frac{F_{r+\frac{1}{2}}(\eta)}{F_{\frac{1}{2}}(\eta)}$ | |
| Hall mobility | $\mu_H = R_H \sigma$ | $\mu_H = \frac{q}{m_s^*}\tau_0\left(k_B T\right)^r \frac{\left(2r+\frac{3}{2}\right)F_{2r+\frac{1}{2}}(\eta)}{\left(r+\frac{3}{2}\right)F_{r+\frac{1}{2}}(\eta)}$ | |
| Hall factor | $r_H = \frac{n}{n_H} = \frac{\mu_H}{\mu_d}$ | $r_H \equiv \frac{3}{2}\frac{\left(2r+\frac{3}{2}\right)}{\left(r+\frac{3}{2}\right)^2}\frac{F_{2r+\frac{1}{2}}(\eta)F_{\frac{1}{2}}(\eta)}{F_{r+\frac{1}{2}}^2(\eta)}$ | $r_H^{MFPIE} \equiv \frac{3}{4}\frac{F_{-\frac{1}{2}}(\eta)F_{\frac{1}{2}}(\eta)}{F_0^2(\eta)}.$ |
| Thermal conductivity | | $\kappa_e = \frac{2}{3}\frac{n\tau_0}{m_s^* T F_{\frac{1}{2}}(\eta)}\left(k_B T\right)^{r+2}\left[\left(r+\frac{7}{2}\right)F_{r+\frac{5}{2}}(\eta) - \frac{\left(r+\frac{5}{2}\right)^2 F_{r+\frac{3}{2}}^2(\eta)}{\left(r+\frac{3}{2}\right)F_{r+\frac{1}{2}}(\eta)}\right]$ | |

| Coefficient (cont'd) | Definition | General Formula | MFPIE $\tau_0 = \ell\left(m^*/2\right)^{1/2}, r = -1/2$ |
|---|---|---|---|
| Lorenz Number | $L = \frac{\kappa_e}{\sigma T}$ | $L = \left(\frac{k_B}{q}\right)^2 \left[\frac{\left(r+\frac{7}{2}\right)F_{r+\frac{5}{2}}(\eta)}{\left(r+\frac{3}{2}\right)F_{r+\frac{1}{2}}(\eta)} - \frac{\left(r+\frac{5}{2}\right)^2 F_{r+\frac{3}{2}}^2(\eta)}{\left(r+\frac{3}{2}\right)^2 F_{r+\frac{1}{2}}^2(\eta)}\right]$ | |
| Seebeck | | $\alpha = -\frac{k_B}{q}\left[\eta - \frac{\left(r+\frac{5}{2}\right)F_{r+\frac{3}{2}}(\eta)}{\left(r+\frac{3}{2}\right)F_{r+\frac{1}{2}}(\eta)}\right]$ | |
| Nernst | | $N = \frac{\tau_0 \left(k_B T\right)^{r+1}}{m_s^* T}\left[\frac{\left(2r+\frac{5}{2}\right)F_{2r+\frac{3}{2}}(\eta)}{\left(r+\frac{3}{2}\right)F_{r+\frac{1}{2}}(\eta)} - \frac{\left(r+\frac{5}{2}\right)\left(2r+\frac{3}{2}\right)F_{r+\frac{3}{2}}(\eta)F_{2r+\frac{1}{2}}(\eta)}{\left(r+\frac{3}{2}\right)^2 F_{r+\frac{1}{2}}^2(\eta)}\right]$ | |

# CHAPTER 3

# EXPERIMENTAL AND *AB-INITIO* TECHNIQUES

## 3.1 Sample preparation

There are three types of samples that I have used: polycrystalline samples prepared using chemical reaction and spark plasma sintering (SPS), single crystals grown via a modified Bridgman method, and thin films prepared by molecular beam epitaxy (MBE) techniques.

### 3.1.1 Polycrystalline samples

$Cu_2Se$ samples (CHAPTER 8) were prepared by melting 5N Cu and Se in a carbon-coated quartz tube at 1423 K for 24 hours under vacuum. The melt was slowly cooled down to 923 K in 50 hours and was kept at 923 K for a week, and finally being slowly cooled down to room temperature in 50 hours. The resulting ingots were ground into fine powders in an agate mortar and pestle sets and then sintered by SPS at around 850 K for about 10 min under a pressure of 40 MPa.

Skutterudite compounds (CHAPTER 5) were synthesized using high purity Sb (6N), Co (4N), Te (6N), and Ge (4N). Stoichiometric amounts of constituents were weighed in a glovebox under high-purity Ar to prepare $CoSb_{3(1-x)}Ge_{1.5x}Te_{1.5x}$ with $x = 0$, 0.17, 0.33, 0.50, and 1. The charge was sealed in a carbon-coated silica tube under the pressure of $10^{-3}$ Pa and then melted and kept at 1373 K for 30 hours. Subsequently, the ampoules with the melt were quenched in a supersaturated salt water bath, and ingots were annealed at 873 K for 7 days. The obtained material was ground into fine powder in a glovebox and sintered by SPS at 923 K (for $x = 0, 0.17, 1$) and 903K (for $x = 0.33, 0.50$) for 5 min under the pressure of 40 MPa.

$Mg_2(Si_{0.3}Sn_{0.7})_{1-y}Bi_y$ ($0 \leq y \leq 0.04$) solid solutions (CHAPTER 4) were prepared using high-purity elemental powders via a two-step solid state reaction (SSR) method (carried out at 873 K and 973 K for the first and second step, respectively), followed by an SPS process at 953 K under the pressure of 30 MPa. An 8% Mg excess over its stoichiometric amount in $Mg_2Si_{0.3}Sn_{0.7}$ was chosen to compensate for the evaporation loss of Mg during the synthesis, as well as to offer an optimized carrier density and electrical performance.

All ingots, after SPS, showed a very high density of 98+% of the theoretical value.

### 3.1.2 Single crystals

Single crystals of $Bi_2Te_3$ (CHAPTER 7) containing Tl, with the nominal concentration corresponding to $Bi_{2-x}Tl_xTe_3$ ($0 \leq x \leq 0.30$), were synthesized using a modified Bridgman method. First, we prepared $Tl_2Te_3$ from stoichiometric quantities of Tl and Te weighted under argon and then added appropriate amounts of Bi and Te. All elements were of 5N purity. The synthesis was done in well evacuated quartz ampoules with a tapered bottom. After annealing at 1090 K for 24 hours, single crystals were grown via lowering ampoules through a temperature gradient of 400 K/5 cm at a rate of 4.5 mm/hour. The resulting single crystals were easily cleavable along the hexagonal (0001) planes, i.e., perpendicular to the trigonal *c*-axis.

### 3.1.3 MBE films

$Bi_2Te_3$ thin films (CHAPTER 6) , with thickness spanning from 6 nm to 1000 nm, were deposited on insulating $BaF_2$ (111) and sapphire (0001) substrates by MBE using solid source effusion cells for Bi and Te.

ZnTe:N thin films (CHAPTER 6), with thickness of 1–2 μm, were grown on semi-insulating GaAs (100) substrate by MBE in Professor Jamie Phillips' lab, using solid source effusion cells for Zn and Te, and an electron cyclotron resonance plasma source for nitrogen incorporation.

## 3.2 Structure and chemical composition

### 3.2.1 X-ray diffraction

Powder X-ray diffraction (XRD) patterns ($2\theta$ 10° – 80°) of finely ground powders at room temperature were collected using a PANalytical X'Pert Pro type, a Rigaku Ultima IV, and/or a Scintag X1 X-Ray diffractometer with Cu K$\alpha$ radiation.

The temperature-dependent (100 K – 300 K) XRD were performed at the X17A beamline of the National Synchrotron Light Source at the Brookhaven National Laboratory in collaboration with Professor Qiang Li. Setup utilized cylindrical geometry with X-ray beam of 67.42 keV ($\lambda$ = 0.1839 Å), Perkin-Elmer image plate detector placed perpendicular to the primary beam path $d$ = 204.134 mm away from the Kapton capillary containing pulverized sample, and Oxford Cryosystem 700 for temperature control.

### 3.2.2 Secondary ion mass spectrometry

The amount of incorporated nitrogen atoms in selected ZnTe:N samples was characterized using secondary ion mass spectrometry (SIMS).

### 3.2.3 Electron microprobe analyzer

The actual chemical composition of samples were typically characterized on well-polished crystalline samples using a JXA-8230 SuperProbe Electron Probe Microanalyzer and/or a Cameca SX-100 Electron Microprobe Analyzer, equipped with wavelength dispersive x-ray spectrometers (WDS).

### 3.2.4 X-ray photoelectron spectroscopy

To verify the elements present in the samples and study their chemical states, X-ray photoelectron spectroscopy (XPS) analysis was performed in a Kratos Axis Ultra XPS system using a monochromatic Al source (K$\alpha$ = 1486.6 eV) with emission current 8 mA and anode voltage 15 kV at a vacuum pressure of $10^{-8}$–$10^{-9}$ Torr, where Cu was adopted as binding energy reference.

### 3.2.5 Transmission electron microscopy

A JEOL 3011 transmission electron microscope (TEM) operating at 300 kV and a JEOL 2010F TEM operating at 200 kV were used to analyze the detailed microstructure. Selected area electron diffraction (SAED) patterns were collected, with theoretical SAED patterns simulated by the CrystalKit software package. The chemical composition analyses were conducted using the energy dispersive spectrometry (EDS). The specimens were prepared by (1) conventional mechanical polishing and argon ion milling, and/or (2) *in situ* focused ion beam (FIB) lift-out method, performed in an FEI Helios 650 workstation.

## 3.3 Physical properties

### 3.3.1 Photoluminescence

Photoluminescence (PL) spectra of the ZnTe based MBE films were collected at 20 K using excitation from a He-Cd 325 nm laser, a grating spectrometer, lock-in amplification, and a photodiode detector.

### 3.3.2 Low-temperature transport properties

Low-temperature transport measurements were carried out over the temperature range of 2 K – 300 K. Electrical resistivity, Seebeck coefficient and thermal conductivity were determined using a longitudinal steady-state technique in a homemade cryostat equipped with a radiation shield.

Rectangular-shaped specimens were cut from the as-prepared polycrystalline ingots, single crystals, and thin films using a diamond saw or a spark erosion machine. For bulk samples, typical dimensions are $10 \times 3 \times 2$ mm$^3$ (2 mm along the trigonal *c*-axis in the case of $Bi_2Te_3$-based single crystals). For films grown on ~0.5 mm thick substrates, typical lateral dimensions are $10 \times 3$ mm$^2$ and the thickness of the film was determined by atomic force microscopy (AFM) and/or optical reflectance spectral measurements. Tiny indium contacts were soldered on to the sample. Silver epoxy contacts were also used on selected samples in order to double check the transport results and verify none of the observations were artifacts possibly induced by indium contacts becoming superconducting at low temperatures.

The base temperature of the sample holder is controlled via a Lakeshore 340 temperature controller. Thermal gradients were measured by fine Chromel-Au/Fe (0.07at%), with a small strain gauge serving as the heat source. Typical temperature difference between the hot and cold ends of the sample is 0.3 K above the liquid nitrogen temperature and around 0.1 K at the liquid helium temperature range. Different heater powers were supplied at various temperatures yielding consistent Seebeck and thermal conductivity readings. As Seebeck probes we used fine copper wires (25 μm in diameter) carefully calibrated to correct for the absolute thermopower of Cu. For measurements of the electrical resistivity, a dc current was passed along the length of each sample and the corresponding voltage was collected via a standard four-probe-technique using Keithley 2182A nanovoltmeters. Typical dc currents of ±10 mA (for bulk) and/or ±10 μA (for films) were used for the measurement, in order to avoid overheating the sample. Different currents at various temperatures were tried to confirm the ohmic nature of contacts and consistent electrical resistivity values.

Galvanomagnetic measurements were carried out in a Quantum Design MPMS system (magnetic field up to 5.5 T), with typical sample dimensions of $6\times2\times1$ mm$^3$, using a Linear Research ac bridge with 16 Hz excitation. Hall data were taken for both positive and negative magnetic fields to eliminate effects due to probe misalignment. The resistivity was also checked using the ac technique, which agrees with the data from dc measurement. The carrier concentration and the Hall mobility were then estimated from the Hall coefficient and the electrical resistivity. The uncertainties of electrical resistivity, Seebeck coefficient, Hall coefficient and thermal conductivity were estimated to be ±3%, ±2%, ±5%, and ±7%, respectively.

### 3.3.3 High-temperature transport properties

The electrical conductivity $\sigma$ and the Seebeck coefficient $\alpha$ in the range of 300 K – 823 K were acquired in a home built apparatus under the protective atmosphere of argon and/or in a commercial ZEM-1 apparatus (Ulvac Sinku-Riko) by a standard four-probe dc configuration. The thermal conductivity $\kappa$ of samples above room temperature was obtained through the formula of $\kappa = D \cdot Cp \cdot \rho_d$, where the thermal diffusivity $D$ was measured by the laser flash technique using an Anter Flashline 5000 and/or a Netzsch LFA-457 instrument, the heat capacity at constant pressure $Cp$ was obtained in a Netzsch, 404 Pegasus apparatus and/or a Q20 differential scanning calorimeter (TA Instruments), and the sample density $\rho_d$ at room temperature was determined by the Archimedes' method. Differential scanning calorimetry (DSC) measurements were performed in the Q20 differential scanning calorimeter. The high temperature Hall coefficient was measured from 300 K to 823 K using a homemade Hall probe system in an oven inserted in a 9 T Oxford air-bore superconducting magnet. The data were recorded using a Linear Research AC Resistance Bridge (LR-700) operated with a 16 Hz excitation frequency at magnetic fields of ±1 T. The room temperature longitudinal sound velocity $v_l$ was measured by an ultrasonic pulse echo method (Panametrics 5072PR) with a fundamental frequency of 20 MHz. The overall uncertainty of the electrical conductivity, the Seebeck coefficient, the thermal conductivity and the Hall coefficient were estimated to be about ±3%, ±2%, ±7%, and ±5% respectively.

## 3.4 Theoretical methodology

We explored low-energy configurations among all possible ways of arranging atoms on sites of an underlying lattice using density functional theory (DFT) calculations, guided by the cluster expansion (CE) method [16] as implemented by Professor Anton Van der Ven's team. DFT energies were obtained using the Vienna *ab initio* simulation package (VASP) [17] within the Perdew-Burke-Ernzerhof (PBE) parameterization of the generalized gradient approximation (GGA) for exchange and correlation [18] and using the projector augmented-wave (PAW) method [19, 20]. Formation energies were calculated relative to the thermodynamically stable end compounds. The electronic band structure and density of states ($D_e$) were calculated using more advanced Heyd-Scuseria-Ernzerhof (HSE06) hybrid functional [21, 22]. VASP and PHONON [23] codes were then used for the *ab initio* phonon calculations in collaboration with Professor Kaviany's group. The total energy and Hellmann-Feynman (HF) forces were found starting from the fully relaxed configuration, such that initial ionic forces were less than $10^{-5}$ eV/Å. The ionic displacements of 0.03 Å of selected atoms were sampled along the $x$, $y$, and $z$ directions. All phonon and thermodynamic properties were predicted using a fit of interatomic force constant tensors to the calculated HF forces. Diagonalization of the dynamical matrix yields the phonon dispersion, from which the density of states ($D_p$) and atomic displacement tensors were obtained. The trace of the diagonalized atomic displacement tensor is the atomic displacement parameter (ADP), a scalar measure of single-atom vibration amplitude based on finite-temperature phonon mode occupancy.

# CHAPTER 4

# ADVANCED THERMOELECTRICS GOVERNED BY A SINGLE PARABOLIC BAND

The well-known single parabolic band (SPB) model has been useful in providing insights into the understanding of transport properties of numerous thermoelectric materials. Especially, the coincidence of the band edges of two parabolic bands, a situation arising in $Mg_2Si_{1-x}Sn_x$ solids solutions when $x \sim 0.7$, naturally makes applicable the SPB approximation to evaluate all transport parameters. We demonstrate this on the case of Bi-doped $Mg_2Si_{0.3}Sn_{0.7}$ where the minima of the two conduction bands at the X-point of the Brillouin zone coincide. The combination of a large density-of-states effective mass $m_d^* \sim 2.6m_e$ arising from the enhanced valley degeneracy $N_v$, high mobility $\mu_d$ due to low deformation potential $E_d$ (8.77 – 9.43 eV), and ultra-low alloy scattering parameter $E_a$ (0.32 – 0.39 eV) leads to an outstanding power factor, $PF_{\max} \propto \left(m_d^*\right)^{3/2} \mu_d$, of up to 4.7 mW m$^{-1}$ K$^{-2}$ around 600 K. The specification and improved understanding of scattering parameters using the SPB model are important and instructive for further optimization of the thermoelectric performance of *n*-type $Mg_2Si_{0.3}Sn_{0.7}$.

## 4.1 $Mg_2Si_{1-x}Sn_x$ solid solutions

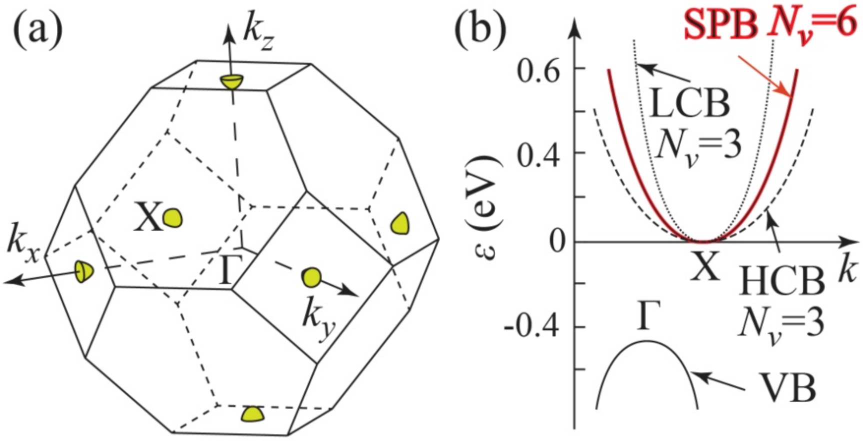

Figure 4.1 (a) First Brillouin zone showing the three-fold degenerated ($N_v = 3$) electron pockets at X. (b) Schematic representation of the band structure (electron energy $\varepsilon$ vs. wave vector $k$). The valence band (VB) is at Γ while the convergence of the light and heavy conduction bands (LCB and HCB) located at X point results in the doubled valley degeneracy ($N_v = 6$) at all temperatures of interest.

Among the most prospective novel thermoelectrics [24, 25] are $Mg_2Si_{1-x}Sn_x$ solid solutions that are environmentally friendly, inexpensive, and do not contain harmful and scarce lead and tellurium. Figure 4.1 illustrates the coincidence of the two parabolic conduction band minima (CBM) [26-28] when $x = 0.7$ ($Mg_2Si_{0.3}Sn_{0.7}$), a situation rarely encountered in other promising thermoelectric material systems such as $Bi_2Te_3$ [29-32], PbTe [33-35], skutterudite [36-39], half Heusler compounds [40, 41], and highly mismatched alloys [42, 43]. It offers a unique opportunity to evaluate transport phenomena using the SPB model that should be rigorously applicable in this case.

In this chapter, Bi-doped $Mg_2Si_{0.3}Sn_{0.7}$ solid solutions are adopted to evaluate the predictive power of the SPB model. In addition, the excellent electronic properties of $Mg_2(Si_{0.3}Sn_{0.7})_{1-y}Bi_y$ ($0 \leq y \leq 0.04$), having the origin in the conduction band convergence, are analyzed systematically.

## 4.2 The transport properties

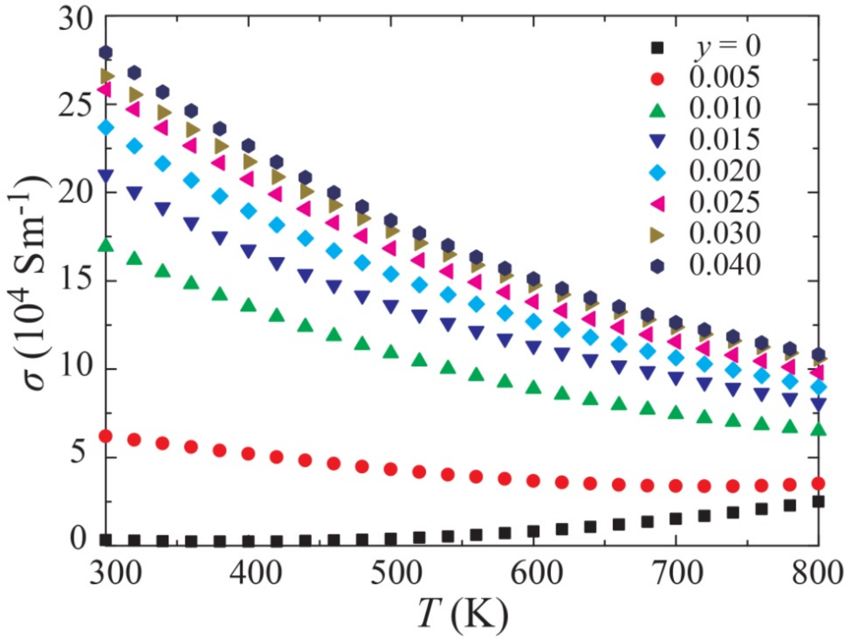

Figure 4.2 Temperature dependent electrical conductivity $\sigma$ of $Mg_2(Si_{0.3}Sn_{0.7})_{1-y}Bi_y$.

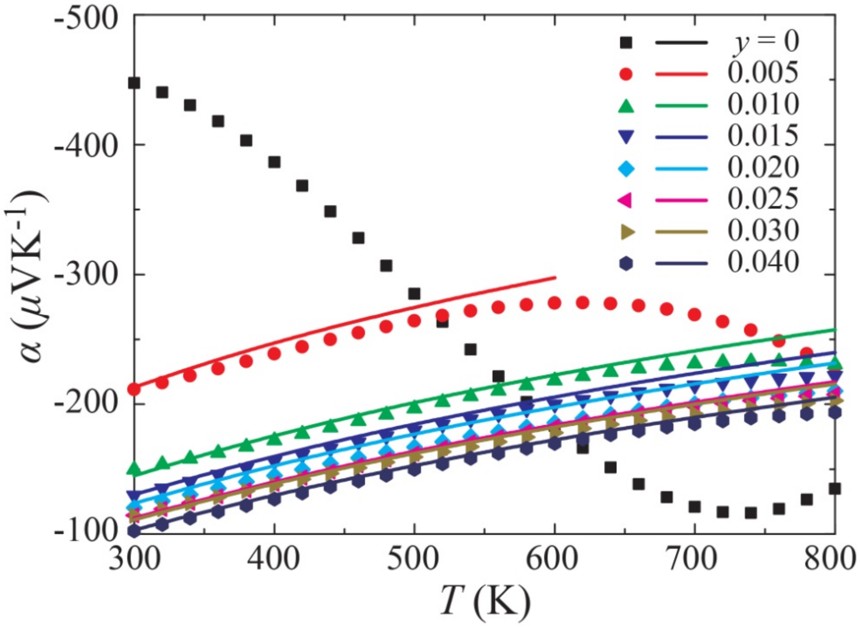

Figure 4.3 Experimental data (symbols) and theoretical results (lines) based on the single parabolic band (SPB) model for the Seebeck coefficient $\alpha$.

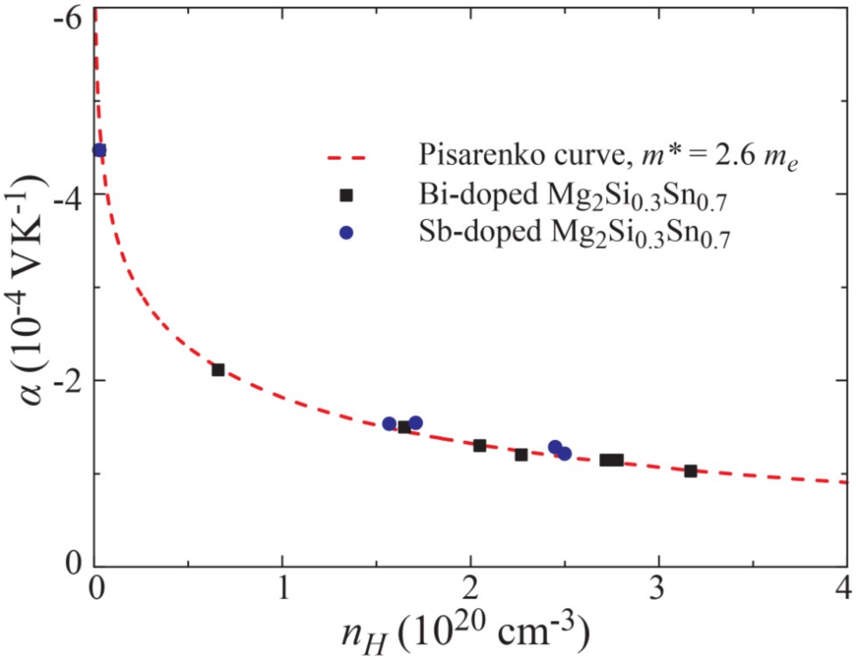

Figure 4.4 The Pisarenko plot (Seebeck coefficient $\alpha$ vs. Hall density $n_H$) at 300 K with a fixed density-of-states effective mass $m_d^*$ reflects a single parabolic nature of the band structure invariant of doping.

Table 4-1 Transport parameters of $Mg_2(Si_{0.3}Sn_{0.7})_{1-y}Bi_y$ ($0 \leq y \leq 0.04$) at 300 K: Seebeck coefficient $\alpha$ (μV K$^{-1}$), Hall density $n_H$ ($10^{20}$ cm$^{-3}$), Hall mobility $\mu_H$ (cm$^2$ V$^{-1}$ s$^{-1}$), reduced Fermi level $\eta$ (= $E_F/k_BT$), Hall factor $r_H$, and the density-of-states effective mass $m_d^*$ (in units of the electron rest mass $m_e$).

| $y$ | $\alpha$ | $n_H$ | $\mu_H$ | $\eta$ | $r_H$ | $m_d^*$ |
|---|---|---|---|---|---|---|
| 0 | -447 | 0.03 | 64 | -3.17 | 1.18 | 2.25 |
| 0.005 | -211 | 0.66 | 59 | -0.10 | 1.14 | 2.62 |
| 0.010 | -150 | 1.65 | 58 | 1.03 | 1.10 | 2.74 |
| 0.015 | -130 | 2.05 | 61 | 1.50 | 1.09 | 2.58 |
| 0.020 | -120 | 2.27 | 64 | 1.76 | 1.08 | 2.49 |
| 0.025 | -115 | 2.72 | 57 | 1.93 | 1.08 | 2.64 |
| 0.030 | -114 | 2.78 | 60 | 1.94 | 1.08 | 2.67 |
| 0.040 | -103 | 3.17 | 53 | 2.33 | 1.07 | 2.54 |

The temperature dependent electrical conductivity $\sigma$ of $Mg_2(Si_{0.3}Sn_{0.7})_{1-y}Bi_y$ is shown in Figure 4.2. While the $y = 0$ sample behaves as a typical intrinsic semiconductor, Bi-doping drives the system into a highly degenerate semiconducting regime for $y \geq 0.010$, with the Hall density $n_H$ on the order of $10^{20}$ cm$^{-3}$ (see Table 4-1 and Figure 4.5). As shown in Figure 4.3  and Table 4-1, the gradually decreasing magnitude of the Seebeck coefficient $\alpha$ with the increasing content of Bi maps well with the evolution of $\sigma$, reflecting the movement of the Fermi level $E_F$ well into the conduction band (CB).

In the SPB model, all galvanomagnetic transport coefficients can be obtained assuming an energy dependent relaxation time $\tau = \tau_0 \varepsilon^r$. The calculated $m_d^*$ at 300 K using a combination of the experimental $\alpha$ and $n_H$ have shown little variation among the samples (see Table 4-1). The $y = 0$ sample is understandably different as a result of its intrinsic transport nature. As illustrated in Figure 4.4 at 300 K, all Bi-doped samples (and also Sb-doped *n*-type $Mg_2Si_{0.3}Sn_{0.7}$) have fallen on the same Pisarenko line calculated using a fixed $m_d^* \sim 2.6 m_e$, which confirms that the converged CBs can be viewed as a doubly degenerate SPB with $N_v = 6$ (see Figure 4.1).

Furthermore, the temperature dependence of $\alpha$ (lines in Figure 4.3 ) predicted using the fixed room temperature value of the density-of-states effective mass $m_d^* = 2.6 m_e$ shows an excellent agreement with the experimental data at all temperatures. The deviations at the highest temperatures between the data and the SPB model are the consequence of the onset of intrinsic excitation of electrons through the band gap. The essentially constant value of $m_d^*$ at all temperatures and carrier densities verifies that the SPB model truly captures the key features of the conduction bands and can be used to characterize and predict all transport properties of *n*-type $Mg_2Si_{0.3}Sn_{0.7}$ solid solutions.

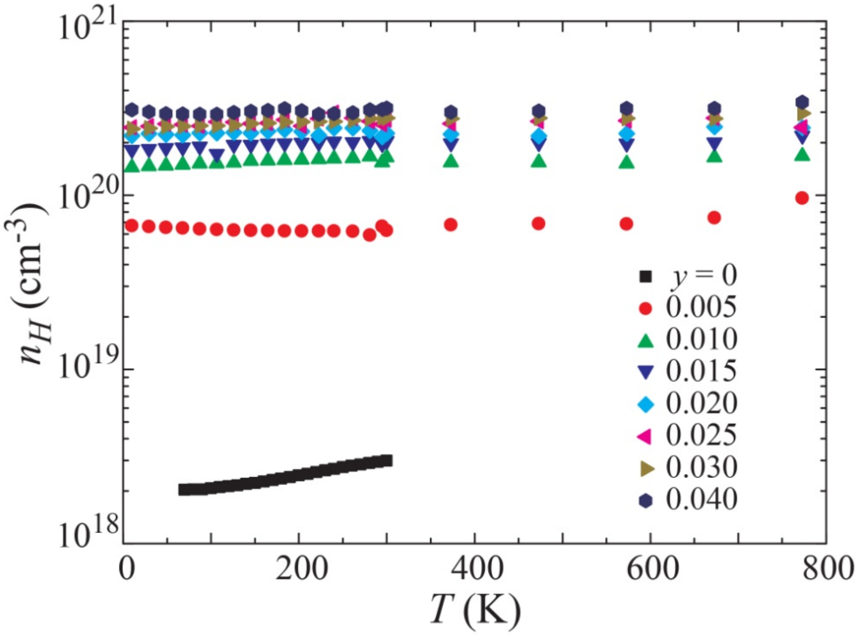

Figure 4.5 Temperature dependent Hall density $n_H$ of $Mg_2(Si_{0.3}Sn_{0.7})_{1-y}Bi_y$.

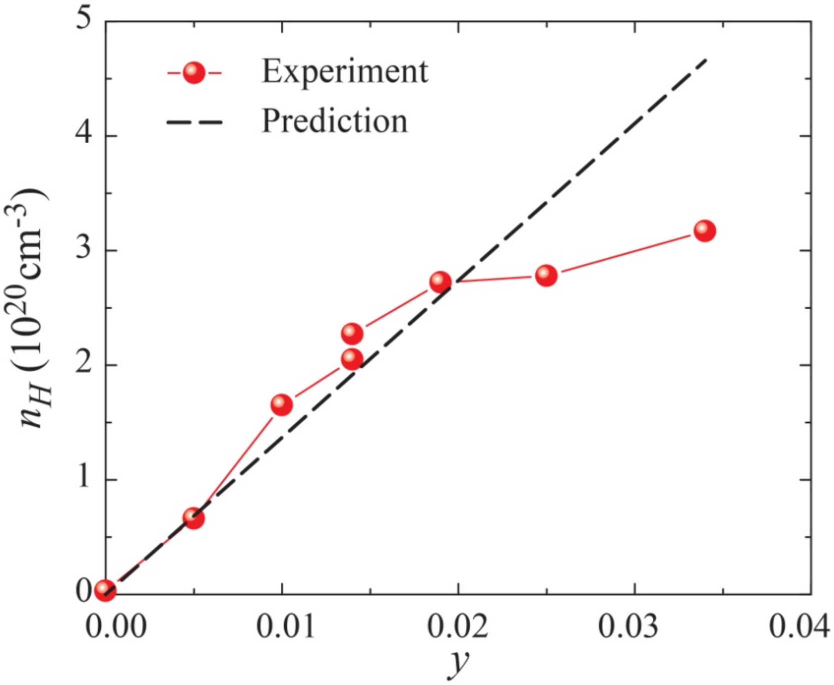

Figure 4.6 The relationship between $n_H$ and the actual Bi concentration, while the dashed line presents the theoretical prediction assuming that one Bi atom donates one electron to the structure.

The SPB nature of the *n*-type $Mg_2Si_{0.3}Sn_{0.7}$ thus offers a canonical testing ground for the transport study, which has rarely been so neatly accessible elsewhere. The carrier density as a function of Bi doping is depicted in Figure 4.5. A rather weak temperature dependence of the carrier density attests to a highly degenerate semiconductor. At low doping levels, see Figure 4.6, Bi is a single electron donor, specifically when the actual Bi content $y$ is lower than 0.020. However, the doping efficiency of Bi drops down rapidly with the further increase of Bi content which is associated with the limited solubility of Bi, indirectly confirmed by the indistinct lattice thermal conductivity $\kappa_L$ for $y \geq 0.020$, seen in Figure 4.13.

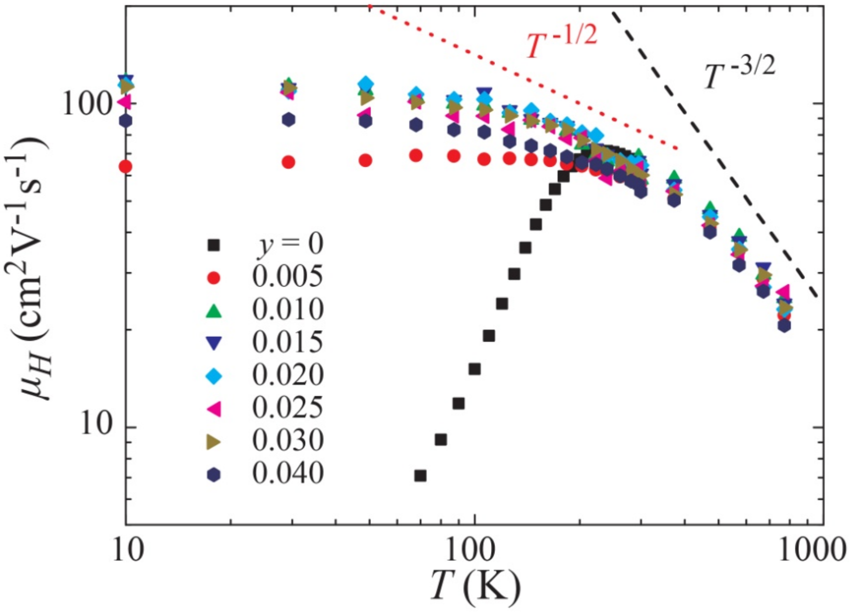

Figure 4.7 Temperature dependent Hall mobility $\mu_H$ of $Mg_2(Si_{0.3}Sn_{0.7})_{1-y}Bi_y$.

As shown in Figure 4.7, at high temperatures, acoustic phonons (AP) dominate the transport behavior, leading to a temperature dependence of $\mu_H^{AP} \propto T^{-3/2}$, while around ambient temperatures, alloy scattering (AS, $\mu_H^{AS} \propto T^{-1/2}$) appears to contribute relatively more significantly to the overall $\mu_H$. Indeed, as illustrated in Figure 4.8, typical weight of acoustic phonon scattering defined as $\Omega^{AP} = (1/\mu_H^{AP})/(1/\mu_H)$ has increased from ~ 60% at 295 K to ~ 80% at 673 K. The $\mu_H$ can be decomposed into its chief components (AP and AS) via the Matthiessen's rule:

$$\frac{1}{\mu_H} = \frac{1}{\mu_H^{AP}} + \frac{1}{\mu_H^{AS}}. \tag{4.1}$$

The mobility appropriate for acoustic phonon scattering is given by

$$\mu_H^{AP} = \frac{(8\pi)^{1/2} e\hbar^4 \rho_d v_l^2}{3E_d^2 (m_s^*)^{5/2} (k_B T)^{3/2}} \Psi_r(\eta), \tag{4.2}$$

where $e$ is the elementary charge, $\hbar$ is the reduced Planck constant, $k_B$ is the Boltzmann constant, $\rho_d$ is the density, $v_l$ ($5.29\times10^3$ m s$^{-1}$) is the longitudinal velocity of sound, and $E_d$ is the deformation potential describing the strength of the electron-phonon interaction. The single valley effective mass $m_s^*$ is related to $m_d^*$ via $m_d^* = N_v^{2/3} m_s^*$. Regarding alloy scattering, the relevant formula for the mobility is

$$\mu_H^{AS} = \frac{64 e\hbar^4 N_0}{9(2\pi)^{3/2} x(1-x) E_a^2 (m_s^*)^{5/2} (k_B T)^{1/2}} \Psi_r(\eta), \tag{4.3}$$

where $N_0$ is the number of atoms per unit volume, $x$ (= 0.7) is the Sn fraction in the solid solution of $Mg_2Si_{0.3}Sn_{0.7}$, and $E_a$ is the parameter characterizing the alloy potential fluctuation. The common factor $\Psi_r(\eta)$ is a scattering-mechanism-specific term (Section A.4 of APPENDIX A) determined by the reduced Fermi level $\eta$ (= $E_F/k_BT$) through a combination of the Hall factor $r_H$ and Fermi-Dirac integrals $F_n(\eta)$ and is taken to be identical for both AP and AS scattering processes ($r = -1/2$ as the mean-free path is assumed energy independent in both cases).

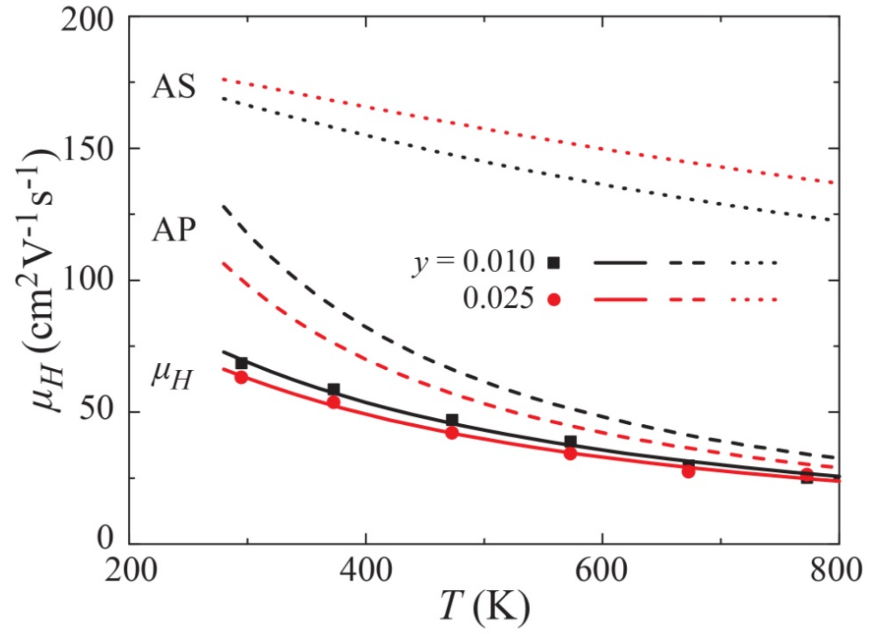

Figure 4.8 The theoretical fitting of $\mu_H$ for the $y$ = 0.010 and 0.025 samples indicates that acoustic phonon (AP) scattering dominates at high temperatures over alloy scattering (AS).

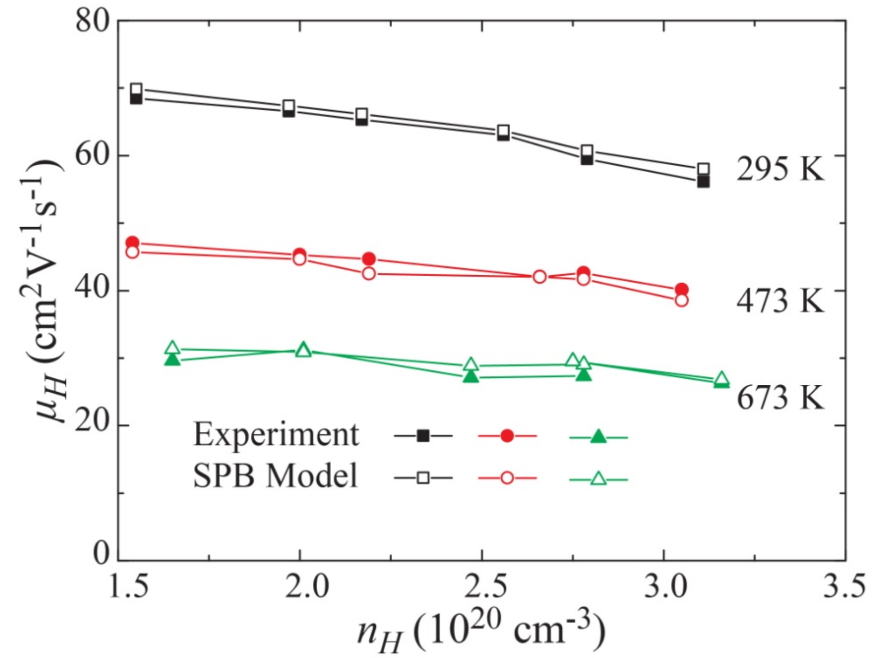

Figure 4.9 Plots of $\mu_H$ verse $n_H$ at 295 K, 473 K and 673 K, respectively. The $\mu_H$ data show no significant deterioration upon increasing $n_H$, implying an excellent electronic performance.

According to Eq. (4.2) and Eq. (4.3), $\mu_H^{AP}$ and $\mu_H^{AS}$ have a similar dependence on $m_s^*$ and the characteristic potentials $E_d$ and $E_a$. Fitting of $\mu_H$ vs. $T$ indicates (see Figure 4.8) that the model including $\mu_H^{AP}$ and $\mu_H^{AS}$ quantitatively characterizes the experimental $\mu_H$ and its temperature dependence. The values of $E_d$ (8.77–9.43 eV) and $E_a$ (0.32–0.39 eV) were then obtained. Literature values for potentials $E_d$ and $E_a$ for a range of semiconductors including $n$-type $Mg_2Si_{1-x}Sn_x$ [44, 45], the III-V compounds [46-49], $n$-type $Si_{1-x}Ge_x$ [50], $n$-type PbS [51], $PbSe_{1-x}Te_x$ [52, 53], and $n$-type $Cd_{1-x}Zn_xTe$ [54] are in the range of 5–35 eV and 0.6–2.0 eV, respectively. While the parameter $E_d$ of our $n$-type $Mg_2Si_{0.3}Sn_{0.7}$ is comparable to the lowest reported values, the alloy fluctuation parameter $E_a$ is apparently much smaller than the reported literature values. Although our $n$-type $Mg_2Si_{0.3}Sn_{0.7}$ possesses a much larger $m_s^*$ ($\approx$ 0.79 $m_e$) compared to the effective mass (0.07-0.60 $m_e$) for most of the above mentioned semiconductors, its reasonably large room temperature mobility of ~ 60 $cm^2\ V^{-1}\ s^{-1}$ is primarily due to the weak electron-phonon interaction (low $E_d$) and the rather limited effect on the mobility from the alloy disorder (ultra-low $E_a$). According to Brooks [50, 55], the parameter $E_a$ evaluates potential fluctuation in alloys caused by the alloy disorder, which is generally believed to be related to the band gap difference $\Delta E_g$ or the band edge difference (or the electron affinity difference $\Delta\chi$ in $n$-type materials) between the two end members in the alloy series. However, there are semiconductors such as the III-V compounds, $n$-type $Si_{1-x}Ge_x$ and $n$-type $Cd_{1-x}Zn_xTe$ where the discrepancy between $E_a$ and $\Delta E_g$ ($\Delta\chi$) is large, probably due to the fact that the band edges of these semiconductors do not have strictly the SPB character. In our research, the values of $E_a$ (0.32–0.39 eV) for $n$-type $Mg_2Si_{0.3}Sn_{0.7}$ are quite comparable to $\Delta E_g$ (~0.42 eV) [25-27] and/or $\Delta\chi$ (~0.19 eV) [56, 57] between

$Mg_2Si$ and $Mg_2Sn$. We ascribe such good agreement between $E_a$ and $\Delta E_g$ ($\Delta\chi$) to the fact that the electronic transport is very precisely described by the SPB model in the entire temperature range investigated. Roughly twice the value of $E_a$ (~0.7 eV) reported for $Mg_2Si_{0.45}Sn_{0.55}$ in the literature should be attributed to a non-uniform distribution of Si/Sn atoms (and thus extra scattering among different phases) as this composition falls in the range of the miscibility gap of the pseudo-binary phase diagram of $Mg_2Si$-$Mg_2Sn$ [25, 58, 59]. Moreover, a contributing factor to the low value of $E_a$ in our *n*-type $Mg_2Si_{0.3}Sn_{0.7}$ is a zero band offset between the light and heavy conduction bands (band convergence) while $Mg_2Si_{0.45}Sn_{0.55}$ has a finite offset (~ 0.1 eV) that may result in a certain amount of interband scattering [26, 27].

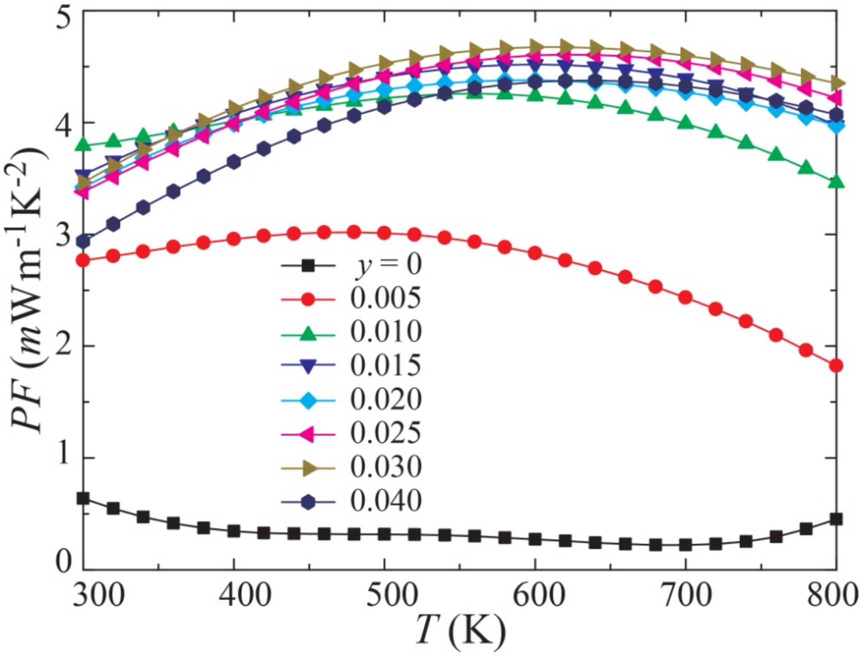

Figure 4.10 Temperature dependent power factor (*PF*) of $Mg_2(Si_{0.3}Sn_{0.7})_{1-y}Bi_y$.

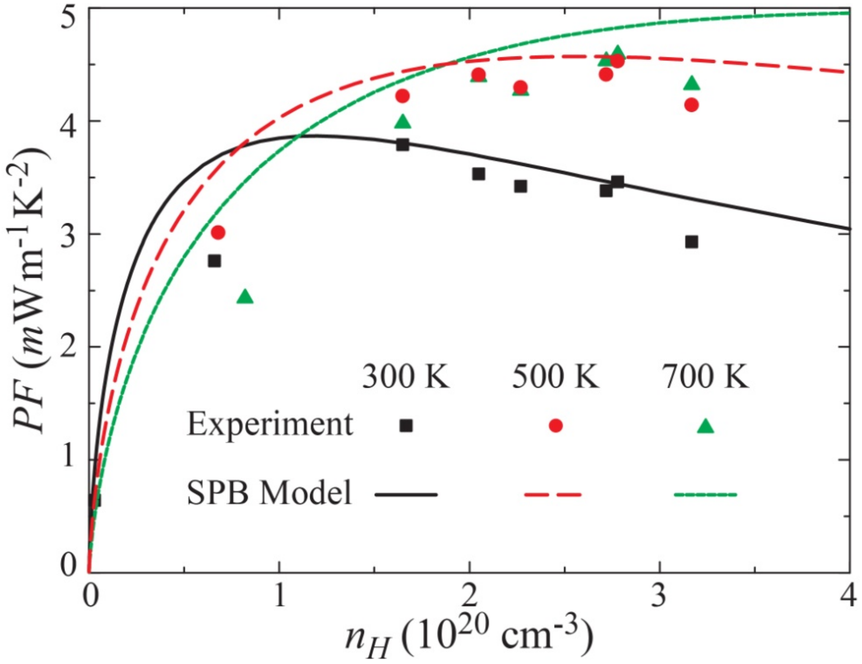

Figure 4.11 The predicted *PF* based on the single parabolic band (SPB) model, in agreement with the experimental data.

Thus, low values of $E_d$ and $E_a$, as well as the high Seebeck coefficient due to the conduction band convergence, lead to an outstanding power factor in $Mg_2(Si_{0.3}Sn_{0.7})_{1-y}Bi_y$ above 400 K, where values as high as 4.7 mW m$^{-1}$ K$^{-2}$ have been recorded for carrier concentrations of $2.05\times10^{20} \leq n_H \leq 2.78\times10^{20}$ cm$^{-3}$, as shown in Figure 4.10. Figure 4.11 displays plots of *PF* vs. $n_H$ calculated based on the SPB model at typical temperatures of 300 K, 500 K and 700 K. The agreement with the experimental data is good and even improves at high $n_H$ above $1.65\times10^{20}$ cm$^{-3}$, where the bipolar contribution interferes less with the data.

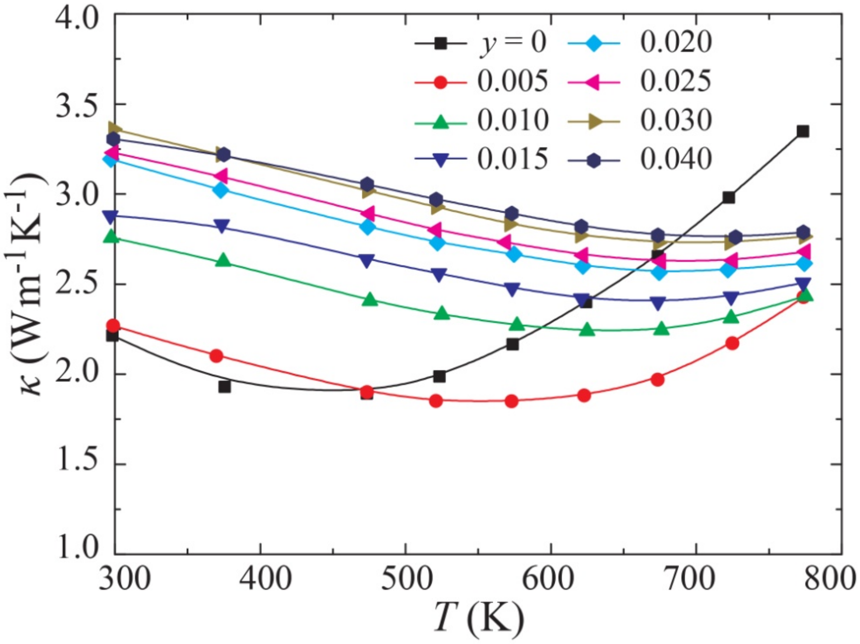

Figure 4.12 Temperature dependent thermal conductivity $\kappa$.

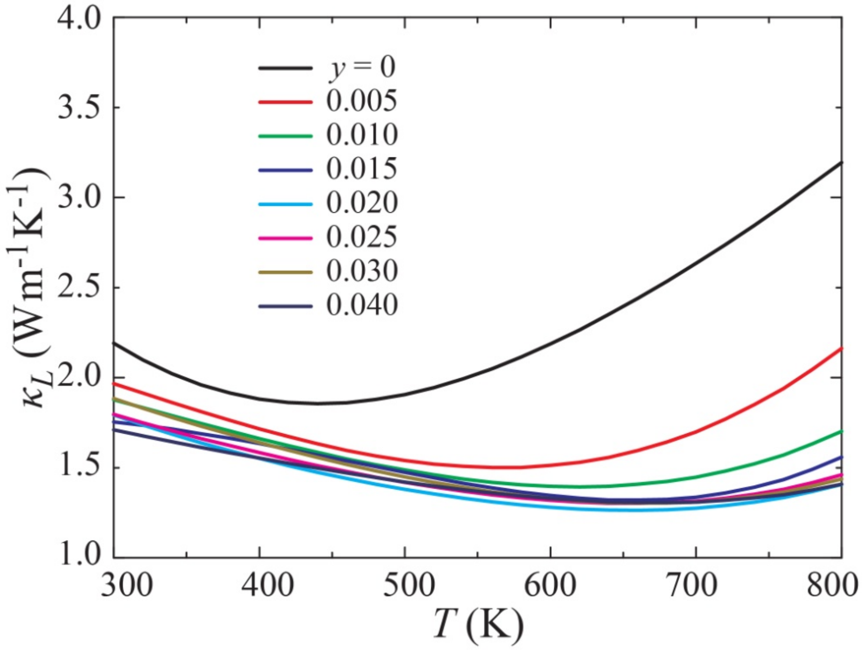

Figure 4.13 Temperature dependent lattice thermal conductivity $\kappa_L$. Note the significant bipolar effect at elevated temperatures, especially for samples with low doping levels.

The temperature dependent thermal conductivity $\kappa$ and the lattice thermal conductivity $\kappa_L$ (obtained via subtracting $\kappa_e = L\sigma T$ from $\kappa$ using the Wiedemann-Franz law, where $L$ is the Lorenz number) are shown in Figure 4.12 and Figure 4.13, respectively. The $\kappa_L$ derived in this way inevitably includes a contribution from the bipolar thermal conductivity $\kappa_b$ at high temperatures (sharp upturn on both $\kappa$ and $\kappa_L$). The $\kappa_e$ amounts for a large fraction of the total thermal conductivity as well as for its dependence upon doping by Bi. Bi-doping significantly decreases the $\kappa_L$ via strengthened point defect phonon scattering. This trend continues for samples with Bi content up to 0.020 at which point the lattice thermal conductivity of solid solutions becomes independent of the content of Bi. This reflects the limited ~2% solubility of Bi in the matrix. The lattice thermal conductivity $\kappa_L$ exhibits a nearly $T^{0.5}$ temperature dependence for all samples before the bipolar contribution $\kappa_b$ becomes significant. The deviation from the classical $T^{1}$ temperature dependence, expected from the usual phonon Umklapp interactions, indicates that point defects scattering still plays an important role in shaping the temperature profile of $\kappa_L$ at high temperatures. The ultimate value of $ZT$ (= $\alpha^2\sigma T/\kappa$) of $Mg_2(Si_{0.3}Sn_{0.7})_{1-y}Bi_y$ ~1.3 is limited by the intrinsic excitation processes which make a notable contribution above 700 K, see Figure 4.14. The averaged $ZT$ value in the range of 300–800 K is ~0.9. As shown in Figure 4.15, the predicted $ZT$ values (lines), calculated using the SPB model with $\kappa_L$ being an experimental parameter, are in excellent agreement with experimental results, especially at 300 K and 500 K. Deviations observed at 700 K or in the low $n_H$ region between the theory and the experiment are due to the interference of the bipolar effect which was not considered in the SPB model.

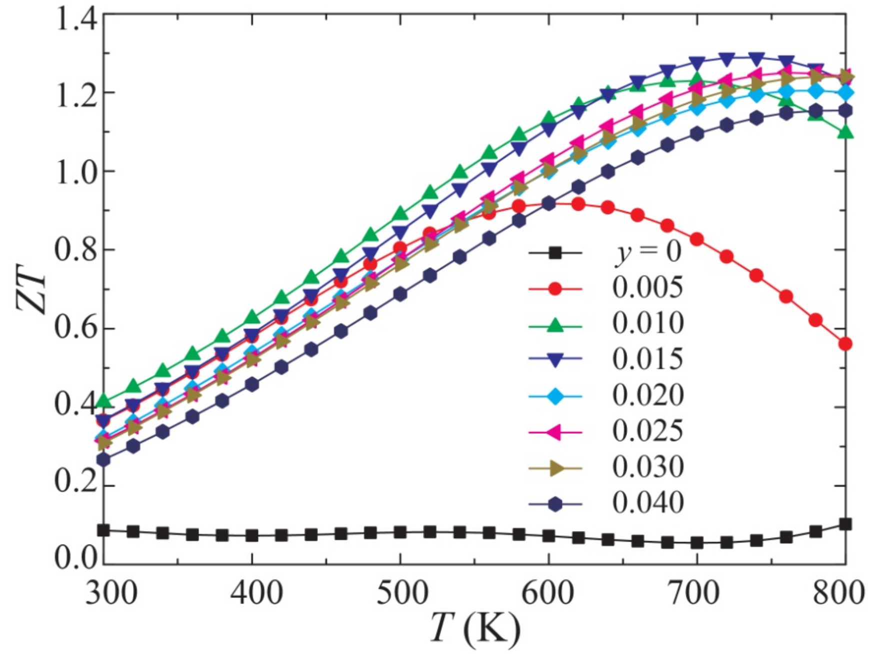

Figure 4.14 Temperature dependent figure of merit *ZT* of $Mg_2(Si_{0.3}Sn_{0.7})_{1-y}Bi_y$.

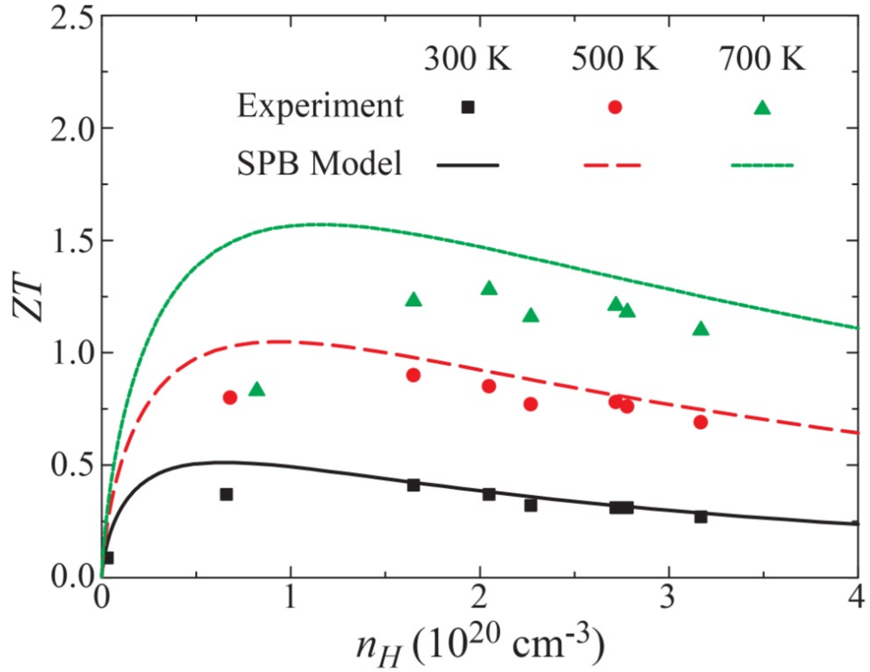

Figure 4.15 The predicted *ZT* based on the SPB model (lines) are in accord with the experimentally determined *ZT* (symbols).

The effort in determining the scattering parameters $E_d$ and $E_a$, as well as the clear physical interpretation of the scattering process at and above room temperature, is important and instructive for enhancing the carrier mobility of this material in the future. Moreover, the attempt to suppress the bipolar effect and further reduce the $\kappa_L$ through various routes, such as increasing the effective mass of the valence band edge and introducing *in-situ* formed nanostructures in the matrix of the bulk material, will be critical for further optimization of the figure of merit of *n*-type $Mg_2Si_{0.3}Sn_{0.7}$.

### 4.3 Summary

We have shown that $Mg_2Si_{0.3}Sn_{0.7}$ with converged conduction bands is an excellent testing ground for the SPB model. It offers an opportunity to precisely characterize and account for all thermal and electronic transport properties of *n*-type $Mg_2Si_{0.3}Sn_{0.7}$. The experimental study and theoretical modeling of Bi-doped $Mg_2Si_{0.3}Sn_{0.7}$ have revealed that the enhanced effective mass (due to doubled number of the carrier pockets $N_v$) together with the high $\mu_H$ (as a result of the low values of $E_d$ and $E_a$) yield an outstanding power factor and $ZT$ of ~1.3 at 700 K. Small values of $E_d$ of 8.77–9.43 eV indicate that the electron-phonon coupling is weak in *n*-type $Mg_2Si_{0.3}Sn_{0.7}$. In addition, a small $E_a$ of 0.32–0.39 eV in *n*-type $Mg_2Si_{1-x}Sn_x$ attests to its physical interpretation as being related to either the indirect band gap difference (~0.42 eV) or the electron affinity difference (~0.19 eV) between $Mg_2Si$ and $Mg_2Sn$. Further improvements in $ZT$s of *n*-type $Mg_2Si_{0.3}Sn_{0.7}$ are expected to be achieved by suppressing the bipolar effect and reducing the lattice thermal conductivity.

# CHAPTER 5

# CONFIGURING PNICOGEN RINGS IN SKUTTERUDITES FOR LOW PHONON CONDUCTIVITY

Dominant heat-carrying modes in skutterudites are associated with vibrations of the pnicogen rings. Apart from filling the structural cages with foreign species, disrupting the pnicogen ring structure by substitutional alloying should be an effective approach to reduce thermal conductivity. In this chapter we explore alloying configurations of pnicogen rings (Sb rings in the case of $CoSb_3$) that yield particularly low values of the thermal conductivity. We find that IV-VI double-substitution (replacing two Sb atoms with one atom each from the column IV and column VI elements to achieve an average charge of two Sb atoms) is a very effective approach. Our *ab initio* calculations, in combination with a cluster expansion, have allowed us to identify stable alloy configurations on the Sb rings. Subsequent molecular and lattice dynamics simulations on low energy configurations establish the range of atomic displacement parameters and values of the thermal conductivity. Theoretical results are in good agreement with our experimental thermal conductivity values. Combining both approaches of compensated double-substitution and filling of structural cages should be an effective way of improving the thermoelectric figure of merit of skutterudites.

## 5.1 Introduction

Filling structural cages in the $CoSb_3$ skutterudite crystal has proved to be an effective way of lowering lattice thermal conductivity [60, 61], making filled skutterudites one of the best novel thermoelectric (TE) materials for mid-temperature power generation applications [38, 62, 63]. An alternative approach to lowering thermal conductivity is to distort the near-square pnicogen (Sb) atomic rings, which are a characteristic feature of the skutterudite structure, thereby reducing the $\mathrm{Im}\overline{3}$ ( $T_h^5$ ) skutterudite space-group symmetry [64]. Since vibration modes involving Sb rings dominate the spectrum of heat-conducting phonons [65, 66], distortions of the rings should be particularly effective in disrupting heat transport. Ring deformation is easily accomplished via substitution of another species for Sb, with a historic focus on the *n*-type dopant Te [67]. Unfortunately, Te has a rather low solubility in $CoSb_3$ ($\leq 5\%$), and only weakly affects thermal conductivity. A charge-compensated alloy can be obtained by substitution of IV-VI species (e.g., Sn-Te [68] or Ge-Te [69, 70]), which has recently been shown to enhance Te solubility and, in the case of Ge-Te, imbalanced Ge/Te induces formation of finely dispersed Ge-Te-rich skutterudite nanodots in the Sb-rich matrix. The enhanced point-defect scattering and presence of nanoinclusions in these double-substituted skutterudites enabled them to attain a thermoelectric figure of merit (*ZT*) of 1.1, competitive with the best values for single-filled skutterudites. These exciting empirical findings reveal a compelling theoretical puzzle surrounding the role of pnicogen ring configuration in skutterudite heat transport.

In this chapter, I present a comprehensive theoretical analysis of the physical importance of pnicogen ring configuration on the thermal conductivity of the double-substituted skutterudite $CoSb_{3-m-n}Ge_mTe_n$. We use *ab initio* calculations to determine phase stability within $CoSb_{3-m-n}Ge_mTe_n$ and predict a strong energetic preference for short-range order of Ge and Te on pnicogen rings. While phase separation is predicted for charge-balanced $CoSb_{3(1-x)}Ge_{1.5x}Te_{1.5x}$, we find that it is sufficiently suppressed in the presence of coherency strains to make a solid solution experimentally accessible. New single-phase skutterudite samples of $CoSb_{3(1-x)}Ge_{1.5x}Te_{1.5x}$ have been successfully synthesized using the traditional melt-quench-anneal technique followed by spark plasma sintering (SPS). We explore the effect of the predicted short-range order of Ge and Te on lattice thermal conductivity and phonon dispersion of $CoSb_{3(1-x)}Ge_{1.5x}Te_{1.5x}$ solid solutions from first principles. Our thermal transport measurements support the idea that configurational disorder of pnicogen rings is an effective mechanism to reduce thermal conductivity in skutterudites.

## 5.2 Ground States, Phase Stability and Synthesis

Calculated formation energies of 340 ternary configurations of Ge, Te and Sb over the Sb sublattice are plotted in Figure 5.1, predicting that ternary solid solutions are thermodynamically unstable, with only two skutterudite phases globally stable: $CoSb_3$ and $CoGe_{1.5}Te_{1.5}$ ( $R\overline{3}$ ) [71]. Furthermore, the driving force for phase separation is minimized along the charge-compensated $CoSb_{3(1-x)}Ge_{1.5x}Te_{1.5x}$ tie-line connecting $CoSb_3$ and $CoGe_{1.5}Te_{1.5}$ [$x = 0$ and 1 in Figure 5.2]. The lowest energy configurations along the charge-compensated tie-line all contain counter-diagonal (CD) $Ge_2Te_2$ rings, as shown in Figure 5.3. As exemplified by the structures in Figure 5.2, all other ring configurations were found to result in substantially higher formation energies. Figure 5.3 shows a typical crystal structure with an energetically favorable ring configuration at $x = 0.5$.

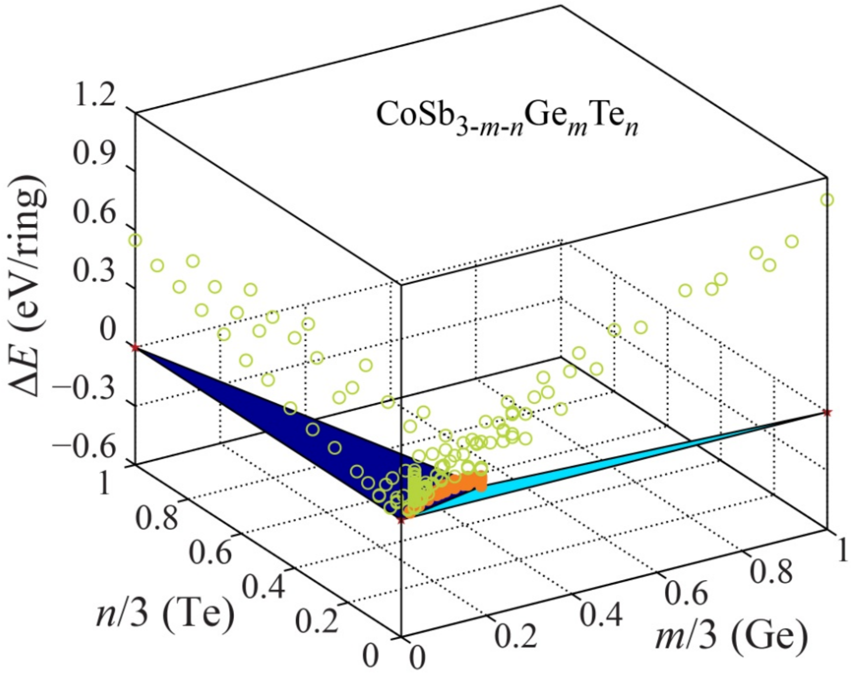

Figure 5.1 DFT formation energies of 340 calculated configurations of $CoSb_{3-m-n}Ge_mTe_n$. Configurations featured with CD $Ge_2Te_2$ rings (solid points) have considerably lower energy than those without CD $Ge_2Te_2$ rings (open circles).

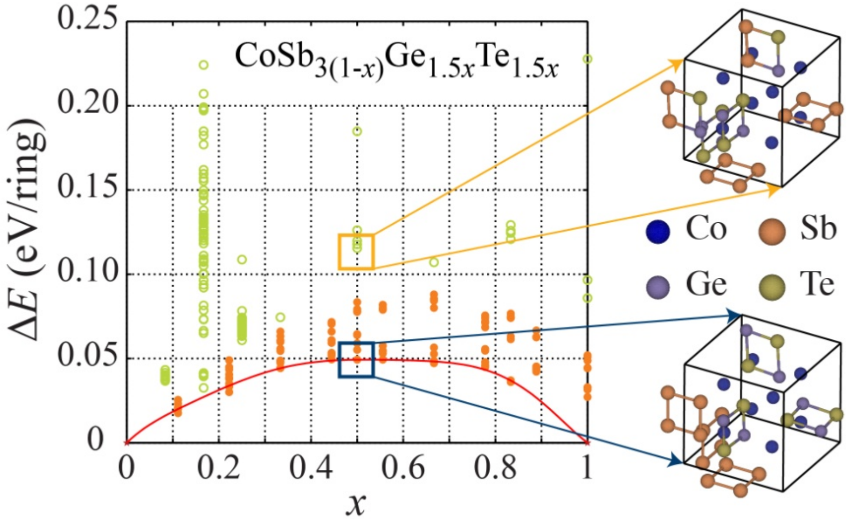

Figure 5.2 Formation energies of $CoSb_{3(1-x)}Ge_{1.5x}Te_{1.5x}$. Two typical structures are illustrated at $x = 0.5$. The solid red line is the 5th-order Redlich-Kister polynomial fit to the lower bound of formation energies.

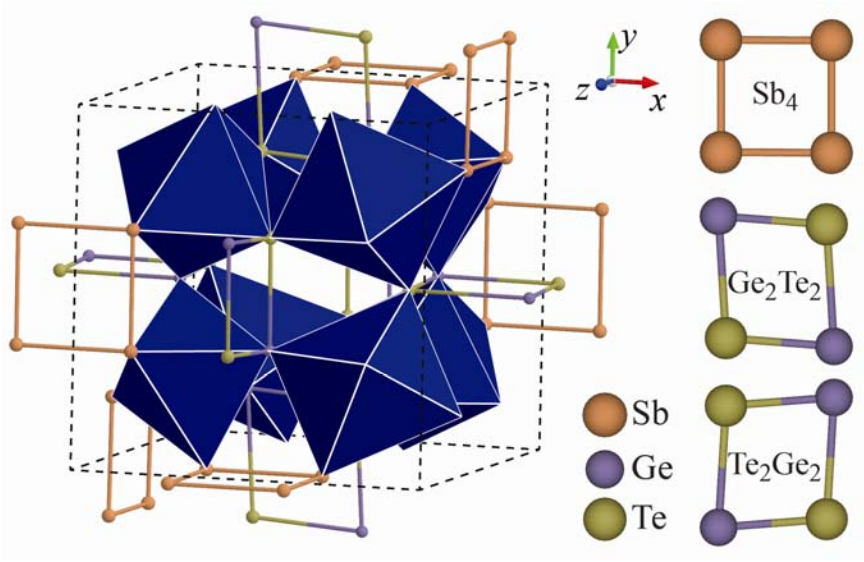

Figure 5.3 A typical crystal structure (left) of $CoSb_{3(1-x)}Ge_{1.5x}Te_{1.5x}$ at $x = 0.5$ which mixes variety of rings (right) of $Sb_4$ and CD $Ge_2Te_2$ (or $Te_2Ge_2$). The cubic unit cell contains 32 atoms. The tilting of rings gives rise to the formation of corner-shared octahedra, which create large cages centering at (0, 0, 0) and (1/2, 1/2, 1/2).

Calculated equilibrium lattice parameters of $CoSb_{3(1-x)}Ge_{1.5x}Te_{1.5x}$ exhibit a strong dependence on composition, with an ~11% decrease in volume from $x = 0$ to $x = 1$. The large strain energy penalties accompanying coherent phase coexistence therefore allow charge-compensated solid solutions to form as long as incoherent precipitation is suppressed. Such considerations have proved essential to the understanding of phase stability and high performance in other thermoelectric materials, including the well-known LAST alloy (i.e., $AgPb_mSbTe_{m+2}$) [72, 73].

Our DFT energy calculations for $CoSb_{3(1-x)}Ge_{1.5x}Te_{1.5x}$ indicate that it can be approximated as the pseudo-binary substitutional alloy $Co_{4/3}[Sb_4]_{(1-x)}[Ge_2Te_2]_x$, where $x$ measures the fraction of $Sb_4$ pnicogen rings that have been substituted with CD $Ge_2Te_2$ rings. Under this constraint, we constructed a free-energy model

$$g(x) = h(x) - Ts(x) \tag{5.1}$$

per pnicogen ring site, where $h(x)$ is the enthalpy and $s(x)$ is the entropy. The enthalpy was modeled by fitting a 5th order Redlich-Kister polynomial to the lower bound of DFT formation energies at 0K, resulting in an expression of the form

$$h(x) = x(1-x)\sum_{n=0}^{5} L_n (1-2x)^n, \tag{5.2}$$

where the $L_n$ are fitting parameters. The resulting enthalpy model is depicted alongside the first-principles formation energies in Figure 5.2. The entropy was calculated for an ideal solution of non-interacting $Sb_4$ and CD $Ge_2Te_2$ rings, accounting for the two degenerate orientations of a CD $Ge_2Te_2$ ring, depicted in Figure 5.3. The entropy term per ring-site is then

$$s(x) = \frac{S}{N} = \frac{1}{N} k_B \ln\left\{ \frac{N!}{(Nx)!\,[N(1-x)]!} \cdot 2^{Nx} \right\} \approx -k_B [x \ln(x/2) + (1-x)\ln(1-x)], \tag{5.3}$$

where the final expression is obtained for large $N$ from Stirling's approximation. The resulting total free energy model is

$$g(x) = x(1-x)\sum_{n=0}^{5} L_n (1-2x)^n + k_B T [x \ln(x/2) + (1-x)\ln(1-x)]. \tag{5.4}$$

Minimization of Eq. (5.4) allowing for the possibility of two-phase coexistence yields the temperature composition phase diagram of Figure 5.4 (black solid lines). The calculated phase diagram shows a miscibility gap below 600 K between $CoSb_3$ and $CoGe_{1.5}Te_{1.5}$ (which we respectively denote phase $\alpha$ and phase $\beta$). Any intermediate composition should result in a coexistence of the $\alpha$ phase and the $\beta$ phase in thermodynamic equilibrium.

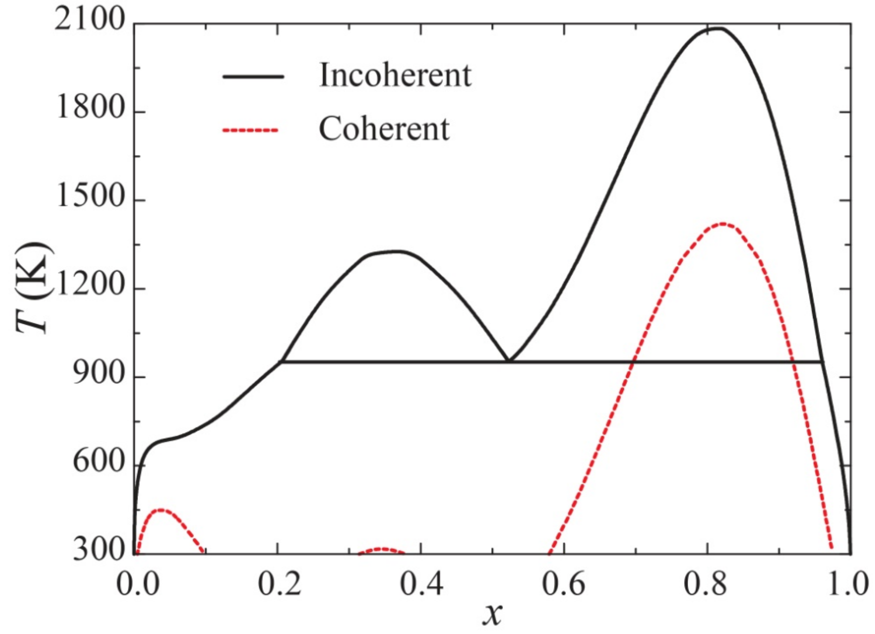

Figure 5.4 The phase diagram of $CoSb_{3(1-x)}Ge_{1.5x}Te_{1.5x}$. The miscibility gap without coherency strain (solid, black) becomes significantly suppressed by the presence of coherency strain (dashed, red).

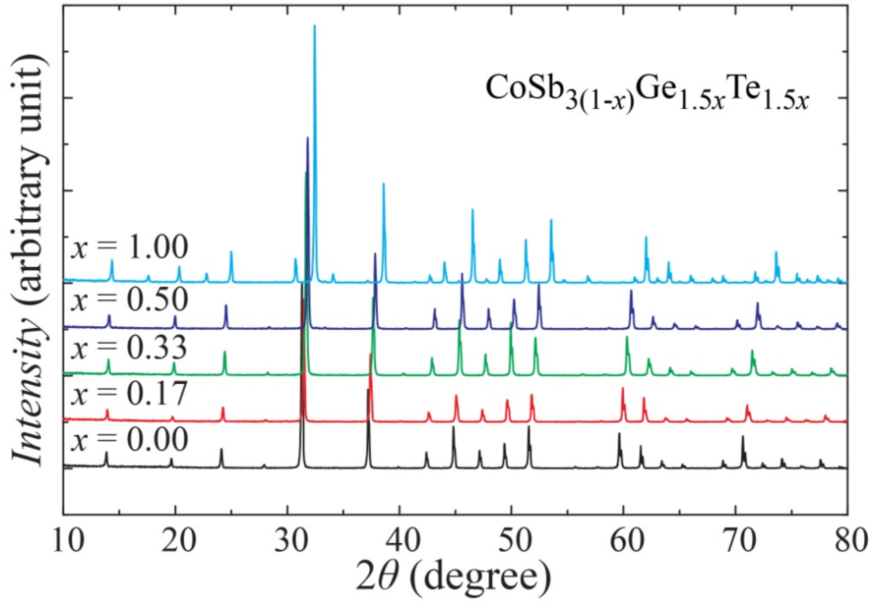

Figure 5.5 XRD pattern of various $CoSb_{3(1-x)}Ge_{1.5x}Te_{1.5x}$ samples.

The calculated phase diagram of Figure 5.4 (black solid lines) describes incoherent two-phase equilibrium. However, two-phase coexistence can also occur coherently whereby the continuity of crystal planes across the interface between the coexisting phases requires the phase with the larger lattice parameter to be compressed and the phase with the smaller lattice parameter to be stretched. An analysis of phase stability then requires an explicit treatment of the strain energy arising from coherent two-phase coexistence. In general, the strain energy due to coherent two-phase coexistence depends on the microstructure. One possible microstructure is as alternating layers of phase $\alpha$ and phase $\beta$ along a single crystallographic direction. Under additional simplifying assumptions (i.e. concentration independent elastic moduli and a lattice parameter variation with concentration that satisfies Vegard's law), the analysis of coherent two-phase equilibrium becomes straightforward and reduces to the application of a common tangent construction of strain modified homogeneous free energy [74-76].

Figure 5.4 also shows a phase diagram for coherent two-phase coexistence in $CoSb_{3(1-x)}Ge_{1.5x}Te_{1.5x}$, calculated using the free energy expression Eq. (5.4) and assuming (i) that the elastic constants are independent of the CD $Ge_2Te_2$ ring concentration (they were taken to be the average of each $c_{ij}$ for $CoSb_3$ and $CoGe_{1.5}Te_{1.5}$, as listed in Table 5-1), and (ii) that the lattice parameters obey Vegard's law. We found that the coherent phase diagram had a negligible dependence on the direction of two-phase separation and on whether plane strain or plane stress constraints in the plane perpendicular to two phase coexistence was used in the energy expression for the elastic strain energy.

As is clear in Figure 5.4, the miscibility gap is substantially suppressed by the strain energy penalty that emerges if phase separation occurs coherently. In the temperature range relevant to thermoelectric applications, this leads to a potentially large solid solution domain for Sb-rich and intermediate compositions (if incoherent precipitation can be suppressed). Coherent phase separation at Ge-Te-rich composition is still predicted to occur, however, in the temperature range of interest.

Following the predicted phase diagram, $CoSb_{3(1-x)}Ge_{1.5x}Te_{1.5x}$ with $x = 0$, 0.17, 0.33, 0.50, and 1, were synthesized. The experimental XRD patterns, as shown in Figure 5.5, confirm the existence of a solid solution. A transmission electron microscopy study showed no Ge-Te-rich nanodots, whose formation we ascribe to the rather more complicated thermodynamics of the imbalanced Ge/Te alloy.

## 5.3 Lattice Dynamics and Phonon Conductivity

Because our calculations predict pronounced short-range order of Ge and Te substituted on the pnicogen sublattice and the calculated phase diagram of our model system indicates that a range of compositions exhibiting such short-range order is accessible, we have focused our investigation of heat transport mechanisms on the charge-balanced $CoSb_{3(1-x)}Ge_{1.5x}Te_{1.5x}$ alloy.

Atomic displacement parameter (ADP) values of various low-energy configurations of $CoSb_{3(1-x)}Ge_{1.5x}Te_{1.5x}$ containing CD $Ge_2Te_2$ rings ($x = 0.25$, 0.5 and 1) are shown in Figure 5.6(a). Due to the strong covalent bonds of the rings, the ADPs of substitutional atoms are not expected to be large. Surprisingly, the calculated ADP of Ge is significantly larger than that of Sb for all three low-energy configurations considered at $x = 0.25$ and 0.5. For comparison, Figure 5.6(a) shows values for the Ba-filled skutterudite $Ba_yCo_4Sb_{12}$ at several values of $y$. The large ADP of the Ba filler atom, relative to most atoms on the pnicogen rings, indicates the rattling behavior of Ba. The rattling behavior of the Ba filler species is believed to cause a reduction in the lattice thermal conductivity of partially-filled skutterudites [37, 77, 78].

Table 5-1 Calculated properties of $CoSb_3$ and $CoGe_{1.5}Te_{1.5}$. The literature results for $CoSb_3$ are also listed. $T_D$, $\gamma_G$, $B$, $c_{ij}$, and $c_v$ are the Debye temperature, the Grüneisen parameter, bulk modulus, elastic constant, and specific heat capacity.

| | $T_D$ (K) | $\gamma_G$ | $B$ (GPa) | $c_{11}$ (GPa) | $c_{12}$ (GPa) | $c_{44}$ (GPa) | $c_v$ (J/mol-K) |
|---|---|---|---|---|---|---|---|
| $CoSb_3$ | 305.9 | 1.11 | 91.89 | 174.6 | 50.52 | 66.34 | 22.9 |
| $CoGe_{1.5}Te_{1.5}$ | 283.5 | 1.28 | 55.87 | 125.6 | 20.40 | 29.35 | 22.9 |
| $CoSb_3$ | 307[a, b] | 0.95[a] | 82[c] | 158[c] | - | 57[c] | - |

[a] from reference [[79]]
[b] from reference [[80]]
[c] from reference [[81]]

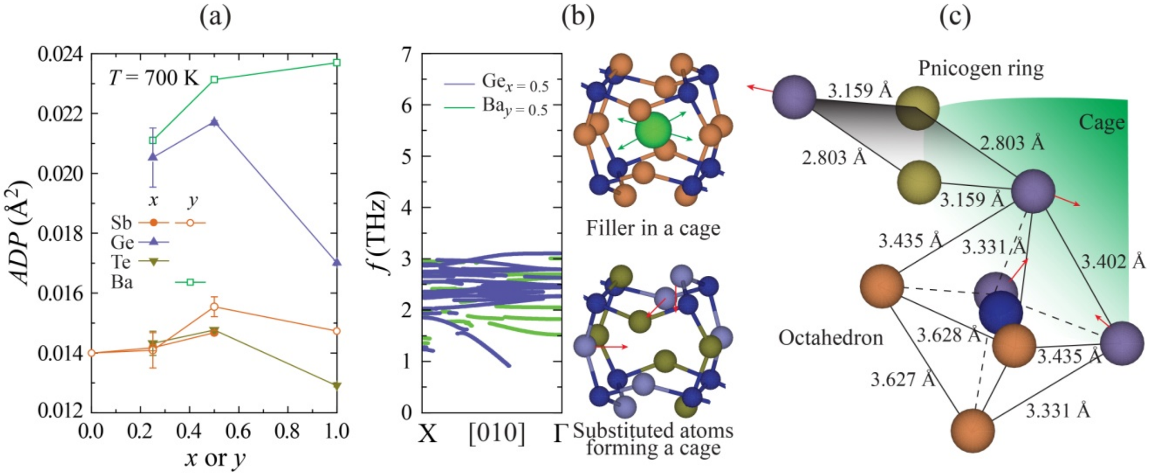

Figure 5.6 (a) Composition dependence of the mean square displacement for individual atoms (ADP) in atomic-substituted $CoSb_{3(1-x)}Ge_{1.5x}Te_{1.5x}$ and filled $Ba_yCo_4Sb_{12}$. (b) Projected phonon dispersion curves for $x = 0.5$ and $y = 0.5$ using DFT. Atomistic configurations of each vibration mode for filler and double substitution are also given. Blue sphere represents the Co atom. Green sphere represents the Ba filler atom. (c) Atomistic configurations showing a pnicogen ring and octahedron consisting of substituted atoms ($x = 0.5$). Red arrows show the large displacement of each Ge atom.

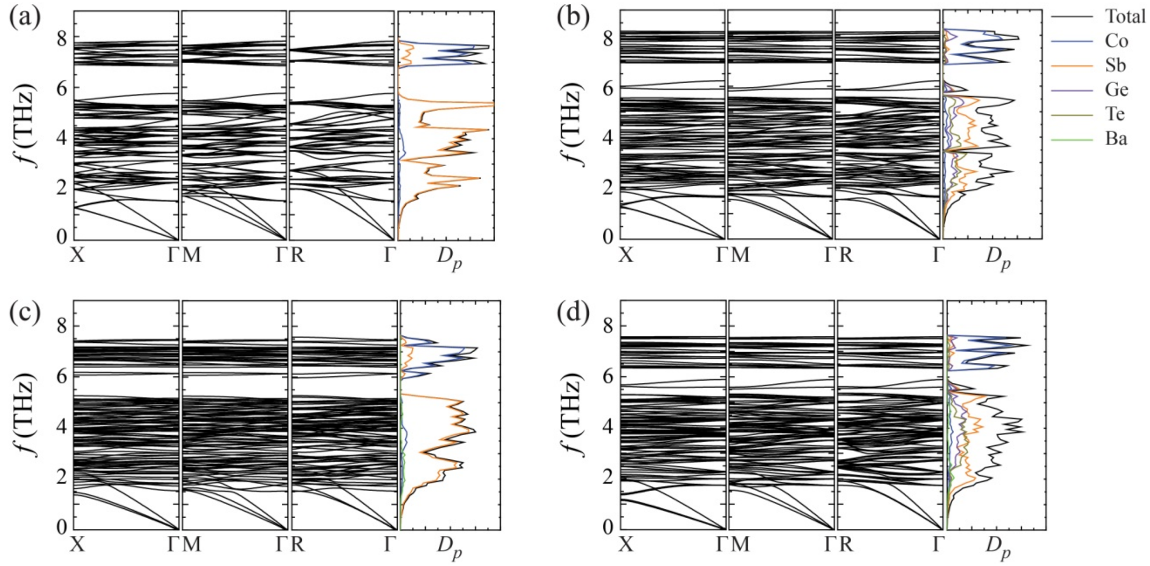

Figure 5.7 Calculated phonon dispersion curves and density-of-states: (a) $x = 0$, (b) 0.5, (c) $y = 0.5$, and (d) a hybrid filled-substituted structure ($x = 0.5$ and $y = 0.5$). The site-projected density-of-states are also shown.

While the Ge ADP is large for all compositions, it is maximized at $x = 0.5$ where it becomes comparable to that of a Ba filler atom. This suggests that Ge atoms on the CD $Ge_2Te_2$ ring could play a similar role as a rattler. As reported in Refs [37, 82, 83]. rattler species inhibit heat transport by both (i) reducing average vibrational frequencies via local bond-softening, and (ii) giving rise to low-frequency “guest” vibrational modes decoupled from the host crystal. In addition to having a large ADP, Ge exhibits similar projected phonon dispersion curves to those of Ba, as shown in Figure 5.6(b). Phonon modes arising predominantly from either Ba or Ge displacements show negligible dispersion, characteristic of local deformational modes with low group velocity. Note that full band structures and phonon density-of-states ($D_p$) of various $CoSb_{3(1-x)}Ge_{1.5x}Te_{1.5x}$ compounds are shown in Figure 5.7. In spite of this similarity to Ba filler, the collective modes of substituted Ge deform different segments of the skutterudite crystal structure and have different modal frequencies [i.e., Figure 5.6(b) for Ge and Ba show 2.27 and 1.52 THz at Γ; 1.24 and 1.45 THz at X]. Additionally, the dominant vibrational distortions of Ge responsible for its large ADP are along the diagonal of the CD $Ge_2Te_2$ rings, as illustrated in Figure 5.6(c). Collectively, this corresponds to a breathing mode (i.e., expansion/shrinkage) of the cage [Figure 5.6(b)]. We consider whether the distinct highly-displaced Ge modes and rattler modes of Ba can influence the phonon transport by simultaneously affecting different portions of the phonon spectrum. Our preliminary *ab-initio* calculations, as shown in Figure 5.7(d), show this hybrid skutterudite structure ($x$ = 0.5 and $y$ = 0.5, which is close to the filling limit [84]), will retain these distinct features. In particular, our results indicate mode flattening in specific direction (Ge at X; Ba at Γ), overall phonon downshift (Ba), and distinct softening induced in the guest vibrational mode frequencies.

Experimental measurements [85] on charge-balanced $CoSb_{3(1-x)}Ge_{1.5x}Te_{1.5x}$ solid solutions show a dramatic decrease in the thermal conductivity with increasing $x$, as shown in Figure 5.8(a). In fact, the minimum in the measured $\kappa_L$ near $x = 0.5$ coincides with the maximum of the calculated Ge ADP. The total measured thermal conductivity can be decomposed as $\kappa = \kappa_L + \kappa_e$, where $\kappa_L$ and $\kappa_e$ are the lattice and electronic thermal conductivity, respectively. An experimental value of $\kappa_L$ is calculated by approximating and subtracting $\kappa_e$ which, in turn, is determined from the Wiedemann-Franz law. Here $\kappa_e = L\sigma_e T$, where $\sigma_e$ is the measured electrical conductivity and $L$ is the Lorenz number, determined from the experimental Seebeck coefficient by assuming a single parabolic band [8]. The experimental value of $\kappa_L$ obtained in this way, which Figure 5.8(a) shows for several compositions at 500 K, quickly decreases with initial substitution before reaching a plateau at intermediate composition. The temperature dependence of $\kappa_L$, shown in Figure 5.8(b), exhibits a decreasing trend at all compositions.

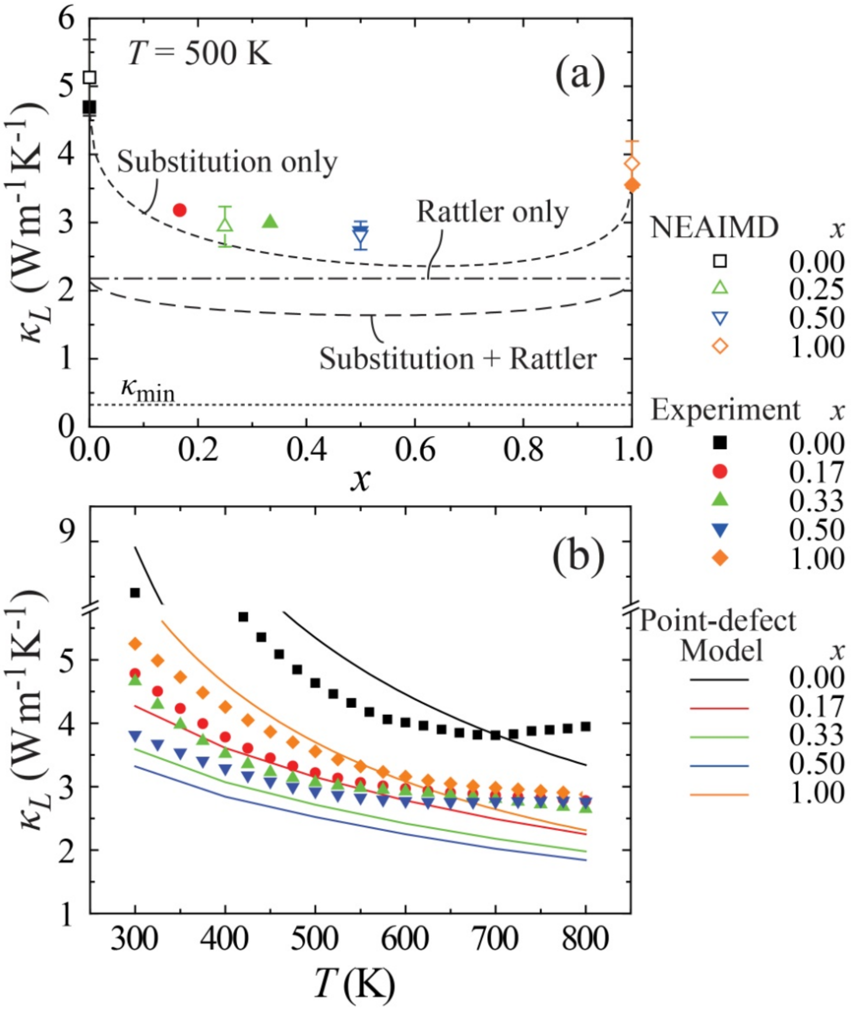

Figure 5.8 Variations of the predicted lattice thermal conductivity of $CoSb_{3(1-x)}Ge_{1.5x}Te_{1.5x}$, (a) concentration dependence at $T$ = 500 K, and (b) temperature dependence for several compositions. Our experimental results (using the Wiedemann-Franz law) and the results of the point-defect model and NEAIMD are shown. The minimum conductivity $\kappa_{min}$ (~ 0.37 W/m-K) for the amorphous $CoSb_3$ phase [86] is also shown.

In order to analyze the effect of pnicogen ring substitution on $\kappa_L$, we use experimentally- and DFT-parameterized analytical models for phonon-phonon and point-defect scattering [80, 86-90], as well as non-equilibrium *ab initio* molecular dynamics (NEAIMD) simulation [91].

Starting with $\kappa_L$ of $CoSb_3$ and $CoGe_{1.5}Te_{1.5,}$ which are dominated by phonon-phonon scattering, we add an analytical factor for point-defect scattering at intermediate alloy compositions [86, 88-90, 92]. Using the Matthiessen rule [92], the overall $\kappa_L$ with the inclusion of the point-defect scattering is $1/\kappa_L(x, T) = x/\kappa_L(0, T) + (1 - x)/\kappa_L(1, T) + 1/\kappa_{L,\mathrm{d}}$ [86, 93]. Here $\kappa_L(0, T)$ and $\kappa_L(1, T)$ are obtained from the Slack relation [92].

$$\kappa_L(T) = \frac{3.1\times10^4 \langle M\rangle \delta T_{D,\infty}^3}{T\langle \gamma_G^2\rangle N_c^{2/3}}, \tag{5.5}$$

where $<M>$ is the mean atomic weight in the primitive cell, $N_c$ is the number of atoms in a primitive cell, $\delta^3$ is the average volume per atom, $T_{\mathrm{D},\infty}$ is the Debye temperature and $\gamma_G$ is the Grüneisen parameter. For the $\kappa_{L,d}$, the point-defect scattering parameter $\Gamma_s$ including mass fluctuation and atomic displacement [89, 94-96] is

$$\Gamma_s = x(1-x)\left[\left(\frac{\Delta M}{M}\right)^2 + 3\gamma_G^2\left(\frac{\Delta R}{R}\right)^2\right], \tag{5.6}$$

where $M$ is the average atomic mass of the $CoSb_{3(1-x)}Ge_{1.5x}Te_{1.5x}$ alloy, $R$ is the average atomic radius, and $\gamma_\mathrm{G}$ is the Grüneisen parameter. The lattice thermal conductivity limited by the point defect scattering $\kappa_{L,d}$ is

$$\kappa_{L,d} = \frac{k_B}{4\pi u_{p,g,A}(a_1 CT)^{1/2}}, \tag{5.7}$$

where $CT$ is the relaxation time for phonon-phonon scattering including normal processes and Umklapp processes. Here $CT$ can be estimated from the experimentally-determined $\kappa_L(0, \mathrm{RT})$ of 8.3 W/m-K for $CoSb_3$. Using

$$CT = \frac{(6n)^{1/3} k_B}{2\pi^{4/3} \kappa_L(0)}, \tag{5.8}$$

where $n$ is the atomic number density, yields $CT = 4.758 \times 10^{-16}$ s.[86] The parameter $a_1$ is the coefficient for the Rayleigh point-defect scattering rate, given by

$$a_1 = \frac{V_c \Gamma_s}{4\pi u_{p,g,A}^3}, \tag{5.9}$$

where $V_c$ is the unit cell volume. To clarify this effect with a rattler, the analytical results for the partially-filled ($y = 0.5$) and for the hybrid structure (various $x$ with $y = 0.5$) are also shown in Figure 5.8(a). Here the overall $\kappa_L$ is given as $1/\kappa_{L,y=0.5}(x, T) = x/\kappa_{L,y=0.5}(0, T) + (1 - x)/\kappa_{L,y=0.5}(1, T) + 1/\kappa_{L,\mathrm{d}}$ [86, 93], assuming $\kappa_{L,y=0.5}(0, T)$ is equal to $\kappa_{L,y=0.5}(1, T)$. Here, $\kappa_{L,y=0.5}(0, T)$ is obtained from the classical MD results in Ref. [86]. Using this combined strategy we predict a further 33% reduction in $\kappa_L$ (much closer to the theoretical minimum, $\kappa_{\mathrm{min}}$, of an amorphous phase).

The lattice thermal conductivity using NEAIMD is computed as the ratio of an applied heat flux to the resulting temperature gradient,

$$\kappa_L = -\frac{\langle q(t) \rangle}{\langle dT/dz \rangle}, \tag{5.10}$$

where the brackets indicate time averages and $q(t)$ is the heat flux. The heat flux is imposed by dividing the simulation cell into sections of equal width, and exchanging kinetic energy between hot and cold sections. The temperature gradient along the $z$ axis is computed from the mean temperature of adjacent sections. For simulations we use the VASP code modified to perform NEAIMD -energy exchange [97, 98] as reported in Ref. [91]. The simulations are performed on supercells of 192 atoms (3×1×2) and 384 atoms (6×1×2), constructed as a solid-solution of pnicogen rings, based on the phase diagram of Figure 5.4. We equilibrate each simulation using equilibrium AIMD for 1 ps with a 0.5-fs time step. Equilibration is followed by 22 ps of NEAIMD using a 1-fs time step. This duration proved sufficiently long to obtain converged lattice thermal conductivity. Because the exchange of kinetic energy results in non-Newtonian dynamics in the hot and cold sections, only the linear portion of the temperature gradient is considered in calculating the lattice thermal conductivity.

The juxtaposition of the point-defect scattering model and our experimental measurements in Figure 5.8(a) and Figure 5.8(b) indicates favorable agreement between the two, suggesting that the reduction in $\kappa_L$ at intermediate substitution composition can largely be attributed to scattering from point-defects, which take the form of mass disorder and local atomic relaxations. Our analytical model does not account for the effect of bipolar carrier transport in our calculation of $\kappa_e$, likely resulting in overestimation of experimental $\kappa_L$ values at high temperature. As shown in Figure 5.8(a) and Figure 5.8(b) the NEAIMD prediction agrees with experimental and analytical results.

## 5.4 Summary

We have demonstrated that Ge/Te double substitution on pnicogen rings is an effective means of lowering the lattice thermal conductivity of skutterudites. Although comparable in magnitude to the effect of Ba filling, Ge/Te substitution targets vibrational modes that are qualitatively different from those of Ba fillers. We therefore expect that a combination of filling and substitutional double-doping is likely to act in a complementary manner in suppressing thermal conductivity. This combined strategy should therefore lead to even lower total skutterudite thermal conductivity and higher *ZT* values than have been realized using either strategy in isolation.

# CHAPTER 6

# OBSERVATION OF PHONON DRAG AND TUNING ITS TEMPERATURE DOMAIN IN THIN FILMS

Highly mismatched alloys have been predicted to exhibit enhanced thermoelectric properties. In this chapter, I first present the electronic transport properties (Hall effect, electrical resistivity, and Seebeck coefficient) of one such system, nitrogen-doped ZnTe epitaxial layers on GaAs (100). Fermi-Dirac statistics was used to analyze the transport parameters of ZnTe:N films assuming a single parabolic band. The power factor demonstrates a measurable improvement with increasing nitrogen concentration.

More importantly/surprisingly, significant phonon-drag thermopower reaching 1.5–2.5 mV $K^{-1}$ was observed. At low temperatures, in reasonably pure conductors subjected to a thermal gradient, charge carriers are swept (dragged) by out of equilibrium phonons, giving rise to a large contribution to the Seebeck coefficient called phonon drag. We further demonstrate a spectacular influence of substrate phonons on charge carriers in thin films of $Bi_2Te_3$.We show that one can control and tune the position and magnitude of the phonon-drag peak over a wide range of temperatures by depositing thin films on substrates with vastly different Debye temperatures. Our experiments also provide a way to study the nature of the phonon spectrum in thin films, which is rarely probed but clearly important for a complete understanding of thin film properties and the interplay of the substrate and films.

## 6.1 The electronic properties of ZnTe:N films

ZnTe is a direct wide band gap (2.27 eV at 300 K [99]) II-VI semiconductor with zincblende crystal structure, utilized in optoelectronic applications including green light emitting diodes [100] and solar cells [101]. Recently, highly mismatched alloys (HMAs) of II-VI compounds, formed by alloying isovalent constituents with vastly different electronegativities (e.g., $ZnSe_{1-x}O_x$) have been proposed as candidate materials for promising thermoelectric performance [42]. The optimistic prediction is based on an assumption that such materials would possess an enhanced power factor defined as $PF = \alpha^2\sigma$, where $\alpha$ is the Seebeck coefficient or thermopower, and $\sigma$ is the electrical conductivity. Practically, however, co-doping of additional species is required in order for such isoelectronic HMAs to function with the desired carrier concentration. An alternative approach of forming nonisoelectronic HMAs may provide a solution. Historically, nitrogen has proven to be a controllable *p*-type dopant in ZnTe [102-104] with hole concentrations of up to $10^{20}$ cm$^{-3}$. Nevertheless, systematic studies of the thermoelectric properties of such nitrogen doped *p*-type ZnTe (ZnTe:N) thin films remain largely unknown in the literature. In this letter, a series of ZnTe:N epitaxial layers with varying N content is studied to examine their temperature dependent thermoelectric properties.

Typical transport properties of five as-grown ZnTe:N films at 300 K are summarized in Table 6-1. These ZnTe:N films with similar thickness (1 – 2 μm) demonstrate hole concentrations that range over approximately an order of magnitude ($0.34 - 2.16 \times 10^{19}$ cm$^{-3}$ at 300 K). While even larger ranges of carrier concentration would be desirable to study, difficulties in controlling nitrogen concentration at lower levels, as well as measuring parameters for lower nitrogen concentration (particularly at low temperature where resistivity is high) prohibited inclusion in this study. Samples are labeled in the order of increasing hole concentration at 300 K to facilitate the following discussion.

Table 6-1 Typical transport coefficients of various ZnTe:N thin films at 300 K, including nitrogen concentration [$N$] from SIMS measurement, Hall coefficient $R_H$, hole concentration $p$, electrical resistivity $\rho$, Seebeck coefficient $\alpha$, thermoelectric power factor $PF$, Hall mobility $\mu_H$, and effective mass $m^*$.

| ID | [$N$] $10^{19}$ cm$^{-3}$ | $R_H$ cm$^3$ C$^{-1}$ | $p$ $10^{19}$ cm$^{-3}$ | $\rho$ μΩ m | $\alpha$ μV K$^{-1}$ | $PF$ μW m$^{-1}$ K$^{-2}$ | $\mu_H$ cm$^2$ V$^{-1}$ s$^{-1}$ | $m^*$ / $m_e$ |
|---|---|---|---|---|---|---|---|---|
| 1 | - | 1.836 | 0.34 | 297 | 380 | 486 | 61.8 | 1.31 |
| 2 | 1.41 | 1.019 | 0.61 | 280 | 338 | 408 | 36.4 | 1.39 |
| 3 | - | 0.470 | 1.33 | 233 | 297 | 379 | 20.2 | 1.68 |
| 4 | - | 0.398 | 1.57 | 157 | 259 | 427 | 25.4 | 1.38 |
| 5 | 4.14 | 0.289 | 2.16 | 107 | 232 | 503 | 27.0 | 1.37 |

Temperature dependent Hall measurements of all samples show unanimously positive Hall coefficient $R_H$ at all temperatures, implying the $p$-type conduction of ZnTe:N. The estimated hole concentration $p$ [$= 1/(e \bullet R_H)$, where $e$ is the elementary charge] for all samples from 5 K to 300 K is plotted in Figure 6.1. The increasing hole concentration from sample 1 to sample 5 is a direct result of increasing nitrogen incorporation, as suggested by the SIMS measurements of nitrogen concentration [$N$] in the films (SIMS tests were limited to only two samples due to the experimental cost and schedule). Approximately a factor of two larger nitrogen concentration is measured by SIMS in comparison to the hole concentration measured by the Hall effect. The apparent doping efficiency of nitrogen in these ZnTe:N samples is therefore estimated to be approximately 50%. The Hall mobility $\mu_H$ [$= R_H/\rho$, see Figure 6.2, with $\rho$ shown in Figure

6.3] of these samples are found to be 20 – 60 cm$^2$ V$^{-1}$ s$^{-1}$ at room temperature, in agreement with literature values [104, 105] for samples with a similar doping level.

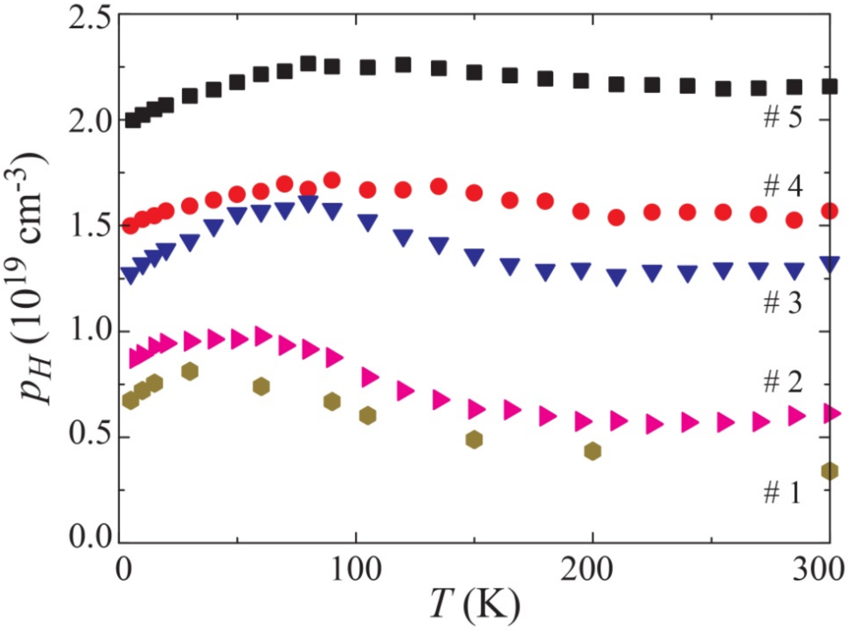

Figure 6.1 Temperature dependent hole concentration $p$ of ZnTe:N MBE thin films with various doping levels.

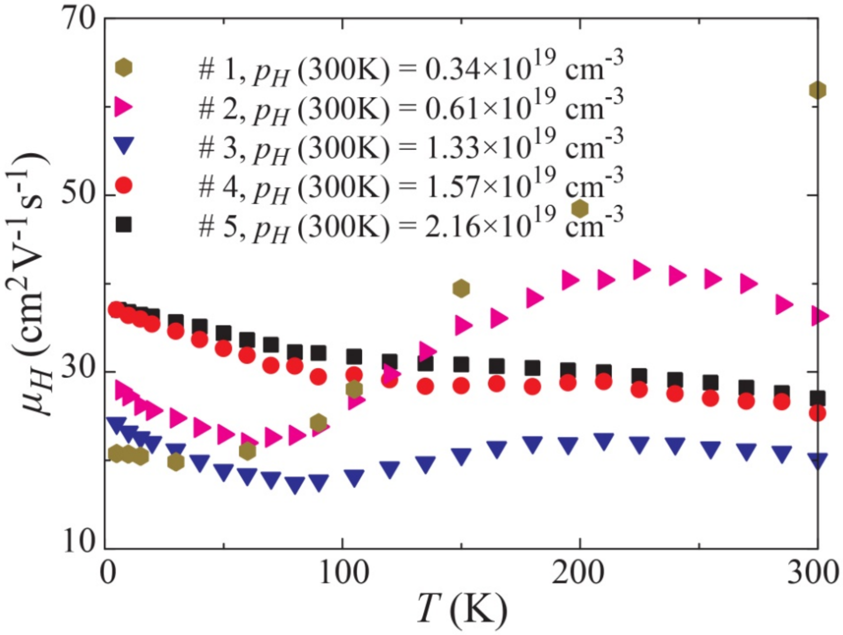

Figure 6.2 Temperature dependent Hall mobility $\mu_H$ of ZnTe:N MBE thin films with various doping levels.

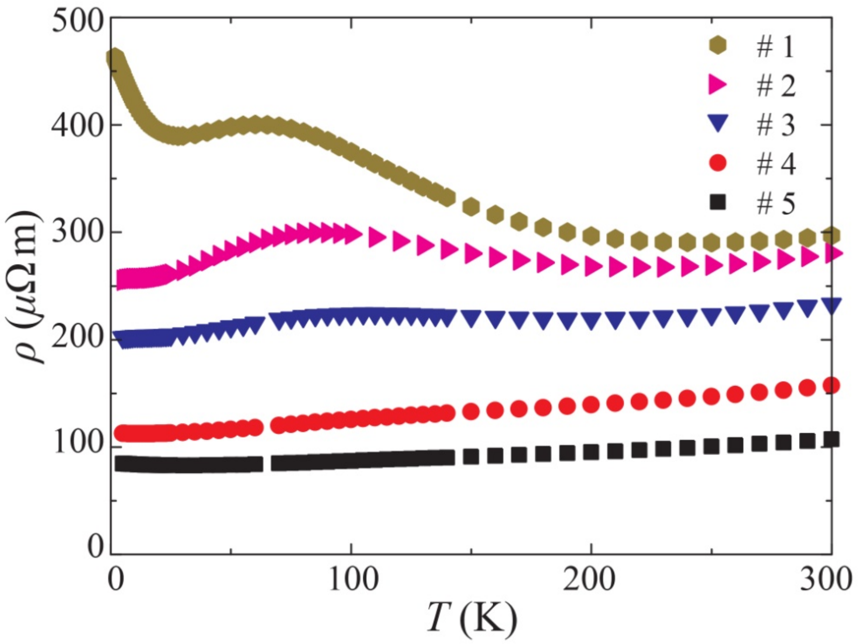

Figure 6.3 Temperature dependent electrical resistivity $\rho$ of ZnTe:N MBE thin films with various doping levels.

As shown in Figure 6.3, the increasing amount of nitrogen incorporation (from sample 1 to 5) improves the overall electrical conductivity due to higher carrier concentration, and also exhibits a surprising qualitative change in the temperature dependence of electrical resistivity. At the highest doping levels (samples 4 and 5, $p > 1.5 \times 10^{19}$ cm$^{-3}$), the electrical resistivity has a positive temperature coefficient over most of the temperature range, i.e., electrical resistivity increases as temperature increases. This is a typical behavior of the heavily-doped degenerate semiconductor. Note that acceptor formation via nitrogen incorporation in ZnTe is typically attributed to the substitution of N on the lattice sites of Te, resulting in an acceptor activation energy of 46 meV [105]. At such high doping levels, acceptor states originated from nitrogen impurity likely form an impurity band, as implied by the nearly temperature independent hole concentration in Figure 6.1. As the nitrogen incorporation is gradually reduced from this highly-doped regime (samples 3, 2, and 1), the electrical resistivity profile deviates from a simple metallic behavior, with a peak observed in the temperature range between 50 K and 100 K. This could be related to the more subtle details of the nitrogen induced impurity level/band in ZnTe, which requires further investigation. To shed more light on the effect of N-doping, Photoluminescence (PL) spectra of various ZnTe:N samples, together with a pure ZnTe sample as reference, were collected at 20 K. They reveal a red shift of the band edge peak upon N-doping, as shown in Figure 6.4. This effect may correspond to the formation and broadening of the nitrogen induced impurity band, as more nitrogen atoms are incorporated into the system.

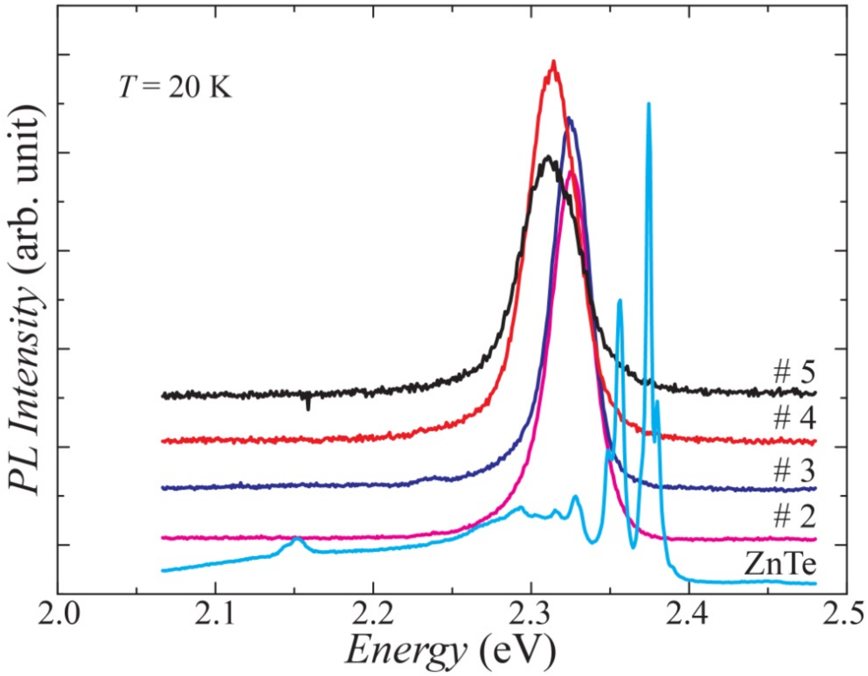

Figure 6.4 PL spectra at 20 K of pure ZnTe and ZnTe:N MBE thin films with various doping levels.

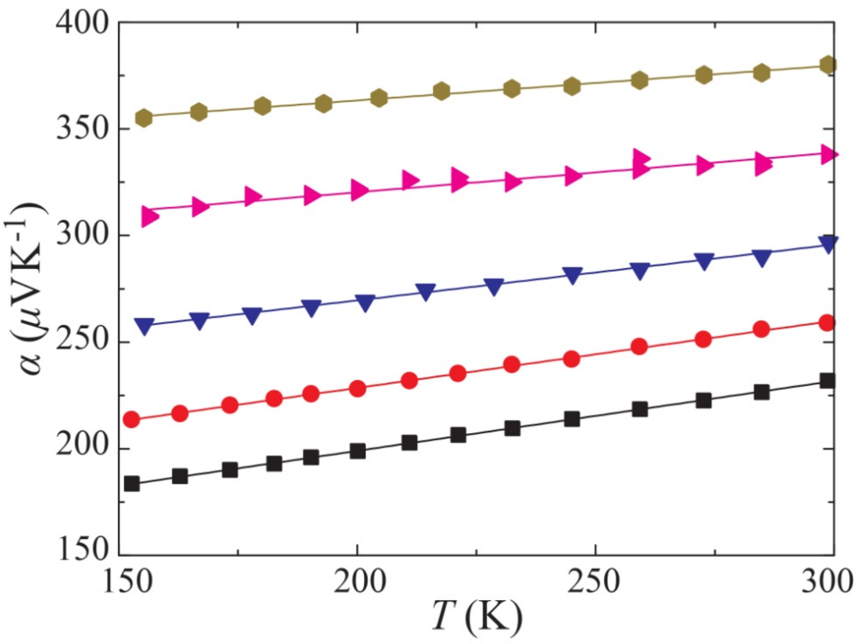

Figure 6.5 Seebeck coefficient of ZnTe:N from 150 K to 300 K.

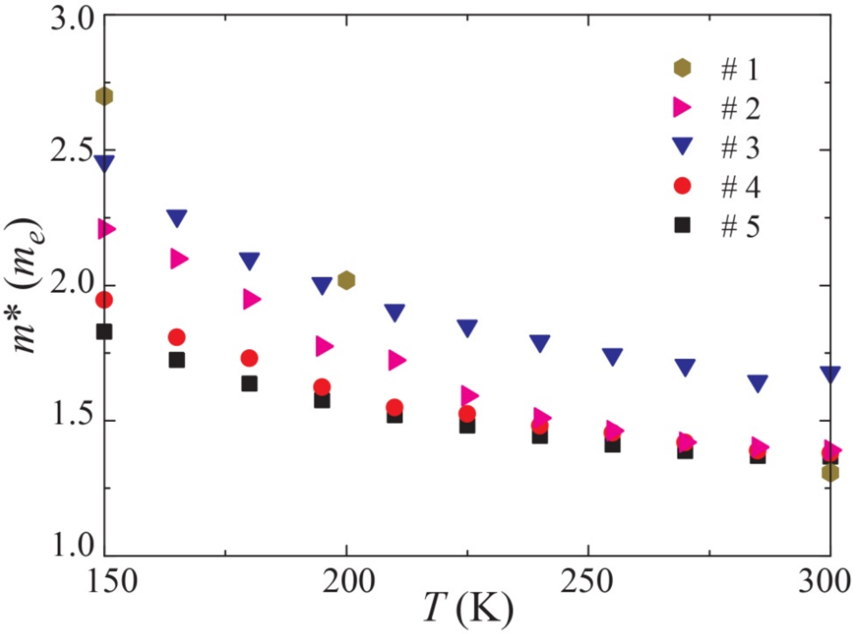

Figure 6.6 The effective mass $m^*$ of ZnTe:N from 150 K to 300 K.

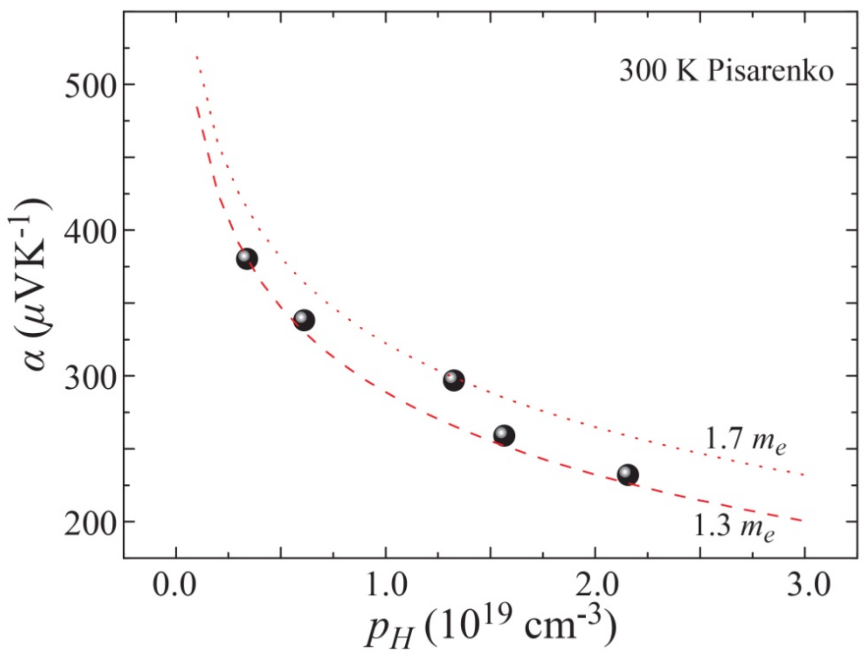

Figure 6.7 Pisarenko plot at 300 K indicating $\alpha$ vs. $p$ relation follows the single parabolic band model.

Figure 6.5 shows a plot of the temperature dependent Seebeck coefficient $\alpha$ of the ZnTe:N films in the temperature range of 150 K to 300 K. $\alpha$ is positive for all samples suggesting $p$-type conduction, in agreement with the Hall effect measurements. The Seebeck coefficient at 300 K decreases as the concentration of holes increases, which agrees with the typical behavior of a degenerate semiconductor. In addition, $\alpha$ increases linearly with $T$ due to carrier diffusion driven by the temperature gradient. For a $p$-type degenerate semiconductor, $\alpha$ can be expressed as follows:

$$\alpha = \frac{k_B}{e}\left[\frac{r+5/2}{r+3/2}\frac{F_{r+3/2}(\eta)}{F_{r+1/2}(\eta)} - \eta\right], \tag{6.1}$$

where $k_B$ is the Boltzmann constant, $e$ the elementary charge, $r$ the index of energy dependent relaxation time $\tau = \tau_0 \varepsilon^r$ (taken to be -1/2 for acoustic phonon scattering),

$\eta = E_F / k_B T$ the reduced Fermi level measured from the top the valence band, and $F_n(\eta)$ the $n$-th Fermi integral given by:

$$F_n(\eta) = \int_0^\infty \frac{\xi^n}{\exp(\xi - \eta) + 1} d\xi, \tag{6.2}$$

The carrier concentration is described by Fermi-Dirac statistics according to

$$p = 4\pi \left( \frac{2m^* k_B T}{h^2} \right)^{3/2} F_{1/2}(\eta), \tag{6.3}$$

where $h$ is the Planck constant and $m^*$ is the effective mass of holes in the valence band. Combining Eq. (6.1) and Eq. (6.3), the effective mass can be estimated from the measured $\alpha$ and $p$ data. The temperature dependent $m^*$ is plotted in Figure 6.6. The observed effective mass (1.3 – 1.7 $m_e$ at 300 K) is significantly larger than the effective mass for intrinsic ZnTe ($m_h^* = 0.2\ m_e$). This observation is consistent with a modified band structure due to the formation of an impurity band via heavy nitrogen doping. The Pisarenko plot of the Seebeck coefficient *versus* hole concentration at 300 K is illustrated in Figure 6.7, where dashed lines are analytical results from Eq. (6.1) and Eq. (6.3) with the effective mass as a parameter. It verifies the suitability of the single parabolic band model for the N-doped ZnTe:N system. In addition, with the N-doping level increased, the power factor (*PF*) improves to 503 μW $m^{-1}$ $K^{-2}$ (see Table 6-1) for the highest doping level explored in this study.

## 6.2 Observation of significant phonon-drag effect in ZnTe

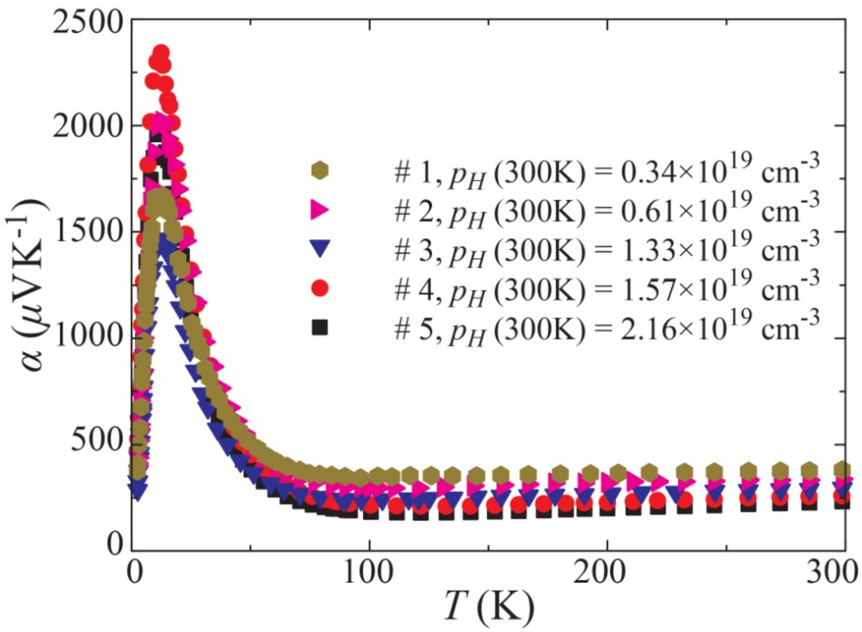

Figure 6.8 Temperature dependent Seebeck coefficient $\alpha$ of ZnTe:N MBE thin films with various doping levels.

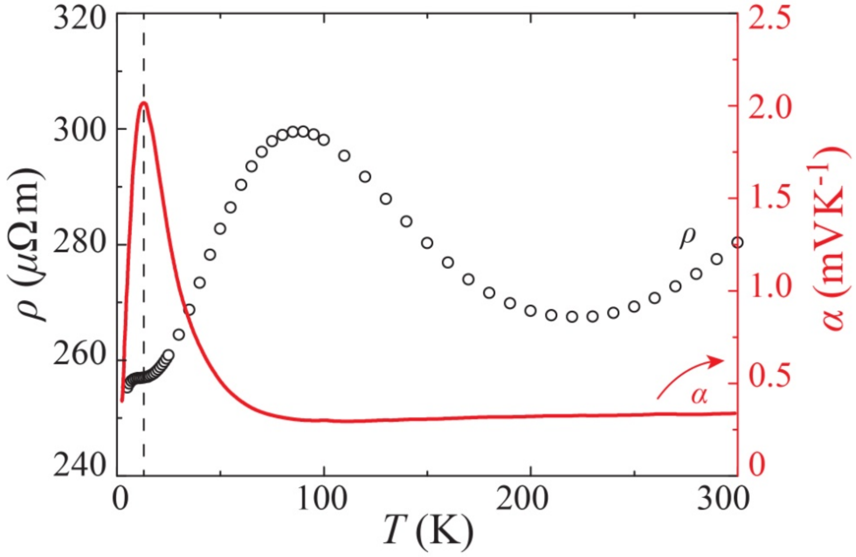

Figure 6.9 The correlation between the Seebeck coefficient peak (~ 13 K) and an electrical resistivity plateau, suggesting that phonon-drag leaves an imprint on the temperature profile of the electrical resistivity.

Figure 6.8 shows a plot of the temperature dependent Seebeck coefficient $\alpha$ of the ZnTe:N films in the full 2– 300 K temperature range. At the lowest temperatures, $\alpha$ increases rapidly to a maximum at ~13 K, and then decreases until ~ 100 K.

The greatly enhanced Seebeck coefficient at low temperatures (as high as 1.5 – 2.5 mV $K^{-1}$) is a manifestation of strong electron-phonon interaction otherwise known as the phonon-drag effect [106]. The peak position of the phonon-drag Seebeck coefficient (~ 13 K) in ZnTe:N coincides with the peak position of the phonon thermal conductivity in bulk crystals of ZnTe [107, 108]. This is in accord with the concept of the phonon-drag effect. In the presence of a thermal gradient, non-equilibrium phonons impart their momentum to electrons, resulting in a momentary electric current just as an applied electric field would do. However, under an open circuit condition (the condition under which the Seebeck coefficient is measured), an electric field is set up that counters such impulsively generated flow of electrons. By the phonon-drag Seebeck coefficient one understands the ratio of this induced electric field to the applied thermal gradient. Unlike the diffusion component of the Seebeck coefficient that is present at all temperatures, the phonon-drag contribution is manifested only at temperatures where phonon-electron processes dominate over all other modes of phonon scattering. Practically, this implies low enough temperatures where phonon-phonon Umklapp processes are infrequent, but temperatures not so low that the population of phonons would be very small. Since these same phonons are responsible for heat conduction, the positions of the phonon-drag peak and the peak in the lattice thermal conductivity essentially coincide. It is worthwhile to note that the thermal conductivity of GaAs substrate peaks at a similar temperature of ~ 10 K [109-111]. Thus, any phonons leaking [112] from the substrate into the film might in principle also contribute to phonon-drag in ZnTe:N grown on GaAs. However, as we shall see later in this chapter, for such leaking phonons to make an appreciable contribution to the phonon drag, the film must be very thin (a few tens of nm) and having a near perfect lattice match with the substrate, a situation difficult to realize in II-VI compounds under current growth conditions.

While examples of significant phonon-drag Seebeck effect are often seen in both metals and semiconductors, it is exceptionally rare to see any signature of phonons dragging charge carriers in the electrical resistivity. The reason why phonon-drag effects are easily detected in the Seebeck coefficient and not in the electrical resistivity lies in the fact that the phonon-drag Seebeck effect is a first-order effect in the interaction between non-equilibrium phonons and electrons while it is a second-order effect as far as the electrical resistivity is concerned. Electrons, accelerated by the applied electric field, lose some of their momentum by being scattered by phonons and thus causing a flow of phonons which then acts back on the electrons.

It is worth to point out that in Figure 6.9, at the lowest temperatures ~ 13 K, there is a local plateau in the electrical resistivity profile which coincides with the position of the phonon-drag Seebeck effect peak. Upon cooling down, instead of decreasing monotonically, the electrical resistivity tends to (quasi-)saturate in the regime where significant phonon-drag Seebeck effect is manifested. This result actually might be one of very rare examples where phonon-drag exerts an influence in the electrical resistivity. Further experimental and theoretical work is needed to ascertain this point.

## 6.3 The phonon-drag effect in thin films

Phonons leaking from a substrate to a thin film have long been recognized as a mechanism contributing to large anomalies in measurements of the Seebeck coefficient at low temperatures. Motivated by the discovery of the quantum Hall effect, numerous studies of the Seebeck coefficient in GaAs/Al$_x$Ga$_{1-x}$As heterostructures [113, 114] and Si-metal-oxide-semiconductor field-effect transistors (MOSFET's) [115-117], have been carried out since the mid-1980s and they often resulted in exceptionally large phonon-drag Seebeck coefficients with values exceeding millivolt/K at liquid helium temperatures. In the case of thin films, it is the nonequilibrium phonons generated in the substrate material (as a result of an imposed thermal gradient) that are leaking into the 2D layer of the heterostructure, interact with the 2D electron system and lead to the enhanced phonon-drag component of Seebeck coefficient (similarly as described in the case of bulk materials in Section 6.2).

Expressions for the phonon-drag thermopower of both bulk [106] and lower-dimensional semiconducting structures, including the temperature dependence of the effect [118, 119], have been worked out and applied to experimental data. Specifically, for 2D heterostructures, the induced phonon-drag electric field can be written in a physically intuitive form [120]:

$$\boldsymbol{E}_{ph} = \sum_s \frac{m^* v_s \Lambda_s}{eT\tau_{e-p}^s} \nabla T \tag{6.4}$$

where $m^*$ is the effective mass, $v_s$ is the velocity of the acoustic phonon mode $s$, $\Lambda_s$ is the phonon mean-free path, $\tau_{e-p}^s$ is the electron-phonon relaxation time for scattering by the mode s and the summation is taken over the appropriate acoustic modes.

In all studies of the low temperature Seebeck effect in lower-dimensional structures [113-117], and even in the recently discovered spin Seebeck effect in Mn-doped GaAs films [11, 121], the active 2D layer had similar composition and structure to the substrate. While this is a desirable feature from the perspective of growing high quality epitaxial layers, the fact that the substrate and the film have essentially the same phonon characteristics curtails a spectrum of information one can gain regarding interactions of substrate phonons with charge carriers of the film. Specifically, issues such as the influence of the Debye temperature and the possibility of tuning the position of the phonon-drag peak are inaccessible in such studies.

It is thus of fundamental interest to study the influence substrate phonons exert on the Seebeck coefficient of films where the substrate and the film are different materials. As a film structure, we have chosen epitaxial films of $Bi_2Te_3$. Beyond the fact that $Bi_2Te_3$ is the best room temperature thermoelectric [8] and the most promising material for studies of topological insulators [122, 123], its distinctly layered structure typified by quintuple layer (QL) of $–Te^1–Bi–Te^2–Bi–Te^1–$ and weak, van der Waals bonds between the neighboring stacks [see Figure 7.1(a)] makes $Bi_2Te_3$ an excellent candidate for the van der Waals-type epitaxy [124]. This ensures that *c*-axis oriented thin films can be grown on many different substrates [125-127]. Specifically, we have chosen $BaF_2$ (111) and sapphire (0001), substrates with vastly different Debye temperatures of 287 and 980 K, respectively. Films with thickness spanning from 6 to 1000 nm were deposited using molecular beam epitaxy [128]. For comparison, data of single crystal $Bi_2Te_3$ (see also CHAPTER 7) have been included.

## 6.4 Tuning the temperature domain of phonon drag in thin films

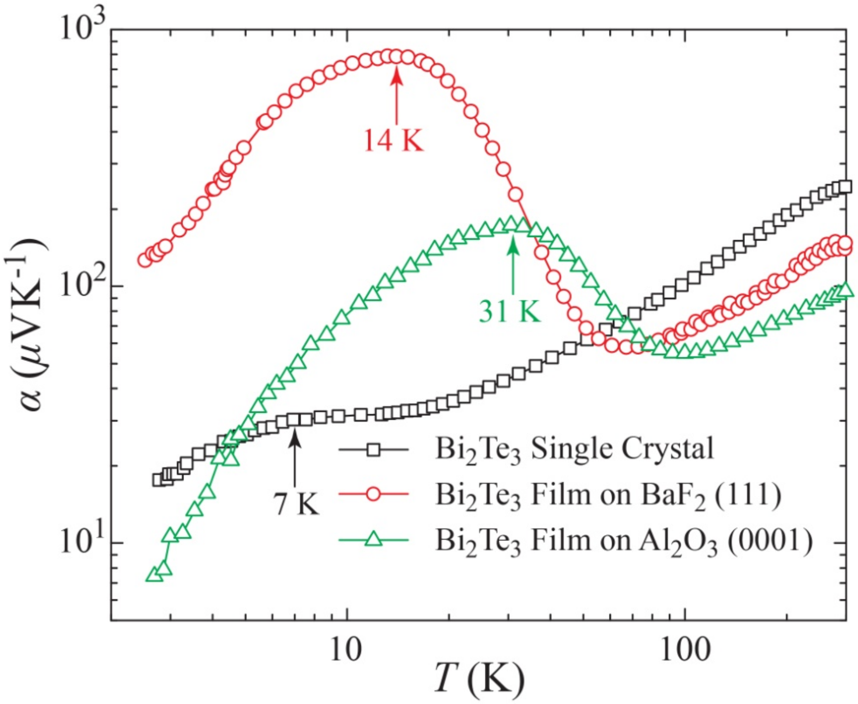

Figure 6.10 Temperature dependent Seebeck coefficient for $Bi_2Te_3$ single crystal, 9 nm $Bi_2Te_3$ films on $BaF_2$ (111), and sapphire (0001) substrates.

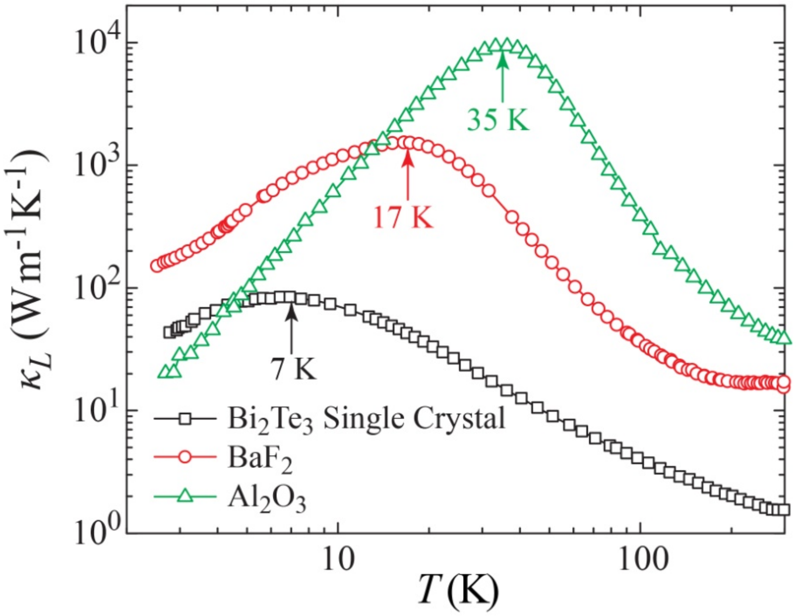

Figure 6.11 The lattice thermal conductivity of bare $BaF_2$ substrate, bare sapphire substrate, and the $Bi_2Te_3$ single crystal, which is obtained by subtracting the electron contribution from the total thermal conductivity via the Wiedemann-Franz law.

The absolute value of temperature dependent Seebeck coefficients for 9 nm films deposited on $BaF_2$ and sapphire, as well as the Seebeck coefficient of a bulk single crystal $Bi_2Te_3$, are shown in Figure 6.10. A small but clearly distinguished phonon-drag contribution observed on the single crystal at 7 K is to be contrasted with an order of magnitude larger phonon-drag in the two film structures with peak positions at 14 K ($BaF_2$ substrate) and 31 K (sapphire substrate). Apart from the same thickness, the two films have also similar carrier densities and mobilities. Consequently, the very different positions of the phonon-drag peak observed in films on $BaF_2$ and on sapphire have nothing to do with the films' electronic properties. One may also consider strain as a potential driving force for the shift of the phonon-drag peak temperature. However, it is well established that the strain in $Bi_2Te_3$ films grown on sapphire substrates is released very fast due to the weak interaction between QLs, and the in-plane lattice parameter attains its normal value of $Bi_2Te_3$ after the growth of only 2 QLs. Therefore, a rebound of the phonon-drag peak position to 7 K would be expected when the film thickness is greater than 10 nm. This does not happen even in films with the thickness of 190 nm. Moreover, the lattice mismatch between $BaF_2$ and $Bi_2Te_3$ is only 0.1% and the difference in the thermal expansion coefficients leads to no more than about 0.1% lattice difference over the range of 300 K; yet a sizable shift in the phonon-drag peak temperature is observed. The above two points effectively rule out the possibility that strain plays a major role in the shifted phonon-drag peak position. Rather, as Figure 6.11 clearly reveals, the position of the phonon-drag peaks closely follows the position of the peak in the lattice thermal conductivity of the respective substrates. This also holds for the bulk $Bi_2Te_3$ single crystal sample. Such agreement between the position of peaks in the

Seebeck coefficient and the thermal conductivity indicates a significant contribution of "leaking" substrate acoustic phonons interacting with charge carriers of the films. The process is most effective at temperatures where there is the largest concentration of heat-carrying phonons that can interact with carriers which is near the peak in the thermal conductivity. At temperatures above the peak in the thermal conductivity, Umklapp processes dissipate phonon momenta. At temperatures much below the peak, the density of available phonons decreases and their favored scattering targets are sample boundaries rather than charge carriers. This general trend is controlled by the Debye temperature of the substrate that specifies temperature regimes where the respective phonon scattering processes dominate. Clearly, the presence of a substrate, through its phonon spectrum, influences the electron-phonon interaction in a deposited semiconducting film which, in turn, governs the strength and the temperature domain of the phonon-drag effect.

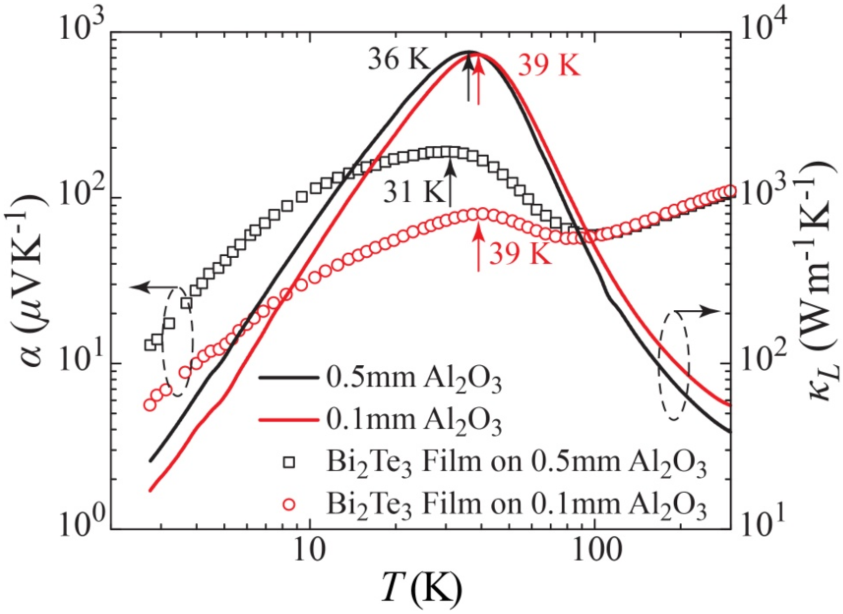

Figure 6.12 Temperature dependence of the Seebeck coefficients (left axis) for two 9 nm films grown on sapphire substrates with thickness of 0.5 mm and 0.1 mm, respectively. The lattice thermal conductivities (right axis) of two substrates are also shown.

Since it is substrate phonons which dominate the phonon-drag process in $Bi_2Te_3$ thin films, any factor that affects substrate phonons should also influence the film's phonon-drag peak. To check this point, we grew 9 nm $Bi_2Te_3$ films simultaneously on two sapphire substrates with thicknesses of 0.5 mm and 0.1 mm, i.e., subject to the exact same growth conditions and component fluxes. Figure 6.12 shows the Seebeck coefficient of the films as well as the lattice thermal conductivity of the two bare substrates with differing thickness as a function of temperature. Note that the thermal conductivity curves overlap at higher temperatures; however, at low temperatures, the boundary scattering of phonons in the thinner substrate is stronger relative to the thicker substrate, and this attenuates the low temperature portion of the lattice thermal conductivity curve in the former. Since boundary scattering of phonons is strong at low temperatures but weak at high temperatures, logically this leads to an effective increase of the peak temperature in lattice thermal conductivity, in our case from 36 K to 39 K. The high temperature Seebeck coefficients (shown) and the electrical resistivity (not shown) also overlap. Additionally, at low temperatures, the stronger phonon boundary scattering in the thinner substrate decreases the momentum that can be transferred from phonons to electrons, and leads to a lower phonon-drag Seebeck effect. For the same reasons mentioned above, the peak temperature of the phonon-drag coefficient also increases with decreasing substrate thickness, in our case from 31 K to 39 K.

In general, one would expect the leaking phonons to be particularly effective in very thin films with the thickness significantly less than the penetration depth of such phonons. As film thickness increases, a smaller fraction of the film volume would be accessible to the leaking phonons before they are scattered and the strength of the phonon-drag should weaken. To test this premise, we deposited $Bi_2Te_3$ films with the thickness in the range of 6–1000 nm on sapphire and measured their transport properties. To minimize the effect of different carrier densities of different films, we normalize the Seebeck coefficient to its value at 200 K, as shown in Figure 6.13. The most striking feature of the data is a strong dependence of the magnitude of the phonon-drag peak on the film thickness while the temperature where the peak occurs is thickness independent. The thinnest $Bi_2Te_3$ sample (6 nm) possesses the peak value an order of magnitude larger than samples with the thickness of 45 mm and 190 nm.

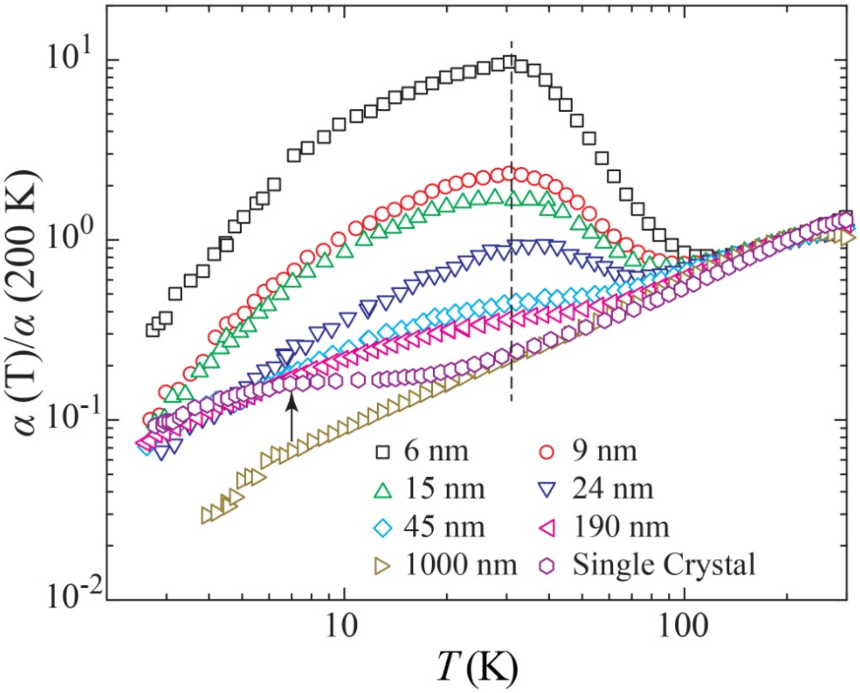

Figure 6.13 Temperature dependent Seebeck coefficient (normalized to the value at 200 K) for $Bi_2Te_3$ single crystal and films with different thickness on sapphire (0001) substrate. The dashed vertical line and arrow indicate the phonon-drag peak position for films and the single crystal, respectively.

## 6.5 Summary

Low temperature thermoelectric characterization on a series of nitrogen doped ZnTe thin films grown by MBE has been performed. Upon tuning the N-doping level, qualitative changes in the temperature dependent electrical resistivity profile develop leading to a marginal improvement of the power factor at the highest doping level. A single parabolic band model proves to be a valid description for the ZnTe:N system at the doping levels we have explored. A significant phonon-drag Seebeck peak (a few mV per K) at ~ 13 K has been observed in all ZnTe:N samples.

Furthermore, in the case of $Bi_2Te_3$ thin films, we have demonstrated that phonons leaking from the substrate strongly affect the carrier dynamics of the film and cause a large phonon-drag peak on the Seebeck curve. The position of this peak correlates with the maximum on the lattice thermal conductivity of the substrate and is governed by the nature of the substrate, namely, by the Debye temperature $\theta_D$. The peak height of this substrate-related phonon drag can be very large for very thin films, but decreases very fast with increasing film thickness. Our research demonstrates that one can manipulate the temperature where the phonon-drag effect dominates by selecting a suitable substrate material. This result provides a way to probe the electron-phonon coupling in thin film structures and demonstrates the influence of substrates on phonon and electronic properties of thin films.

# CHAPTER 7

# FINE TUNING THE FERMI LEVEL IN BISMUTH TELLURIDE VIA THALLIUM DOPING

While the bulk $Bi_2Te_3$ single crystals often exhibit *p*-type metallic conduction due to the $Bi_{Te}$-type antisite defects, doping by thallium ($Bi_{2-x}Tl_xTe_3$, $x = 0 - 0.30$) progressively changes the electrical conduction of $Bi_{2-x}Tl_xTe_3$ from *p*-type ($0 \le x \le 0.08$) to *n*-type ($0.12 \le x \le 0.30$). This is observed via measurements of both the Seebeck coefficient and the Hall effect performed in the crystallographic (0001) plane in the temperature range of 2 − 300 K. At low levels of Tl, $0 \le x \le 0.05$, the temperature dependent in-plane ($I \perp c$) electrical resistivity maintains its metallic character as the hole concentration decreases. Heavier Tl content with $0.08 \le x \le 0.12$ drives the electrical resistivity into a prominent non-metallic regime displaying characteristic metal-insulator transitions upon cooling to below ~100 K. At the highest doping of Tl, $0.20 \le x \le 0.30$, the samples revert back into the metallic state with low resistivity. Thermal conductivity measurements of $Bi_{2-x}Tl_xTe_3$, as examined by the Debye-Callaway phonon conductivity model, reveal a generally stronger point defect scattering of phonons with the increasing Tl content. The systematic evolution of transport properties suggests that the Fermi level of $Bi_2Te_3$, which initially lies in the valence band ($x = 0$), gradually shifts toward the top of the valence band ($0.01 \le x \le 0.05$), then moves into the band gap ($0.08 \le x \le 0.12$), and eventually intersects the conduction band ($0.20 \le x \le 0.30$).

## 7.1 Introduction

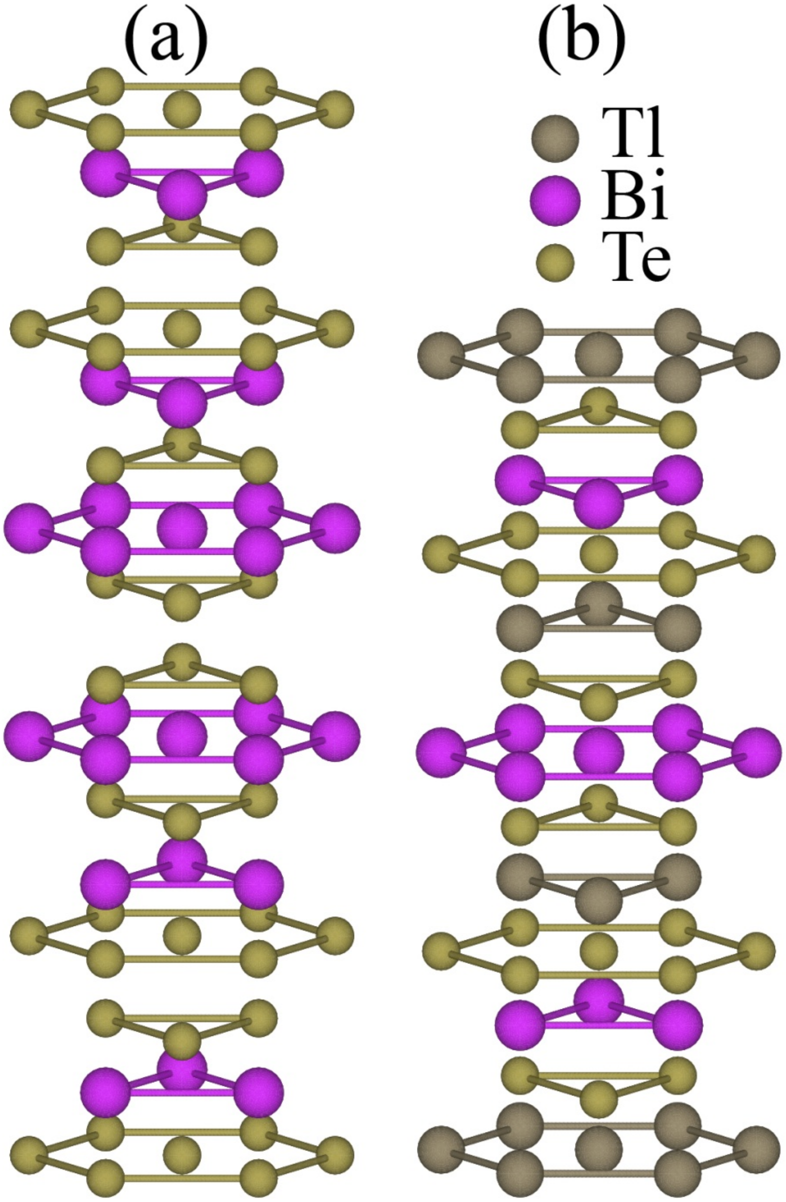

Figure 7.1 Crystal structure of (a) $Bi_2Te_3$ and (b) $TlBiTe_2$ with repeating ($Te^1$–Bi–$Te^2$–Bi–$Te^1$) and (Te–Bi–Te–Tl) layers, respectively. Defected form of $TlBiTe_2$ represented by (Te–Bi–Te–Tl–$V_{Te}^{\bullet\bullet}$) + $2e$ includes an atomic plane of Te vacancies, has nearly identical in-plane lattice parameters as $Bi_2Te_3$, shares the same space group, and donates electrons necessary to explain transport properties.

Single crystals of $Bi_2Te_3$, which have a layered rhombohedral structure [see Figure 7.1(a)] with the space group $R\overline{3}m\,(D_{3d}^{5},\mathrm{S.G.}\#166)$, are narrow band gap ($E_g$ ~ 0.13 eV at 300 K) semiconductors, renowned for excellent thermoelectric properties and efficient cooling applications at and below room temperature [8]. $Bi_2Te_3$, together with its isostructural sister compounds $Bi_2Se_3$ and $Sb_2Te_3$ have recently been also identified as the most promising materials systems with which to realize a three-dimensional (3D) topological insulator (TI) [123]. Such an exotic state of matter possesses a bulk insulator state together with Dirac-like metallic surface states arising from the unique band structure and strong spin-orbit coupling. While angle resolved photoelectron spectroscopy (ARPES) measurements have proved without any doubt the presence of topologically protected surface states [122, 129-131], the spectacular transport properties predicted to be associated with surface states have not yet been fully demonstrated. The primary cause hampering transport measurements is a high conductivity of the bulk state that overshadows the contribution of surface states. This is due to high density of charged antisite defects of the type $\mathrm{Bi}_{\mathrm{Te}}^{-1}$ (an atom of Bi occupying a site on the Te sublattice and carrying charge -1 that is compensated by a hole in the valence band) that drive the system *p*-type and are responsible for high density of holes on the order of $10^{19}$ $cm^{-3}$ at room temperature in $Bi_2Te_3$ crystals grown from stoichiometric melts [132]. Although experimental techniques, such as post-annealing $Bi_2Te_3$ crystals in Te vapors [133, 134], have been developed to compensate such naturally formed acceptor defects in order to achieve a bulk insulator, better and more efficient ways of controlling the carrier density are still highly desirable. In this chapter, our recent attempt of fine tuning *p*-type $Bi_2Te_3$ into the non-metallic regime through elemental Tl-doping is presented. The systematic transport property measurements from 2 K to 300 K have revealed interesting physical phenomena in Tl-doped $Bi_2Te_3$ single crystals as the position of the Fermi level is being altered.

## 7.2 Crystal structure and chemical analyses

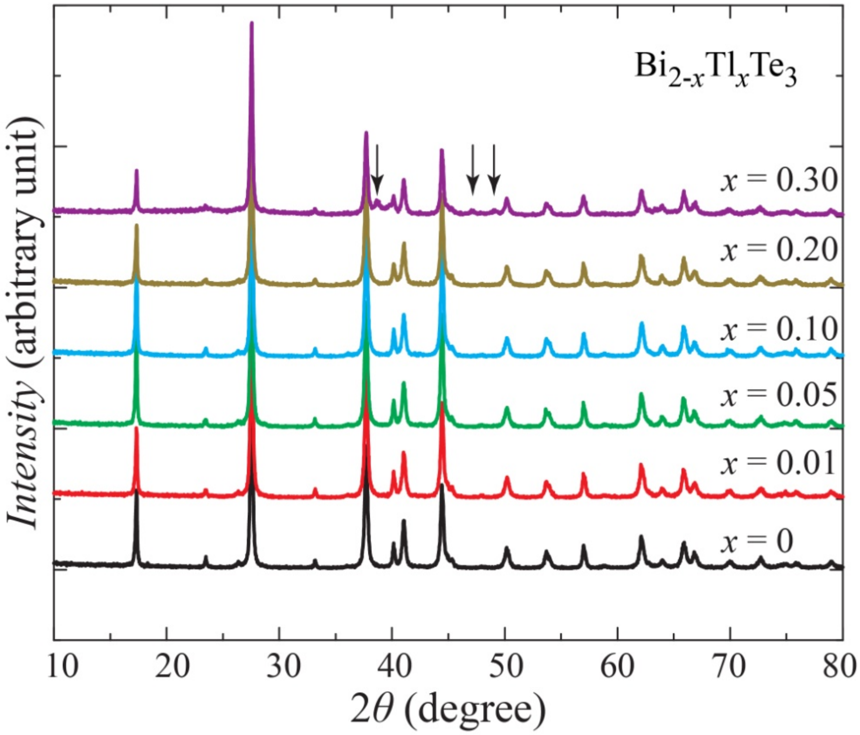

Figure 7.2 XRD patterns of powders made from Tl-doped $Bi_2Te_3$ single crystals, matching the $Bi_2Te_3$ standard (JCPDS 82-0358), with arrows indicating additional peaks of the $TlBiTe_2$ phase.

As shown in Figure 7.1(a), $Bi_2Te_3$ has a layered structure formed by ($Te^1$–Bi–$Te^2$–Bi–$Te^1$) type of quintuple layers (QLs), often referred to as the tetradymite-type lattice. The XRD patterns in Figure 7.2 suggest all samples can be readily indexed to the $Bi_2Te_3$ phase (JCPDS 82-0358) [135], with additional peaks (indicated by arrows) in the $x = 0.30$ sample that can be ascribed to the formation of rhombohedral $TlBiTe_2$ phase

(JCPDS 85-0421) [136]. Figure 7.3(a) and Figure 7.3(b) show the high resolution transmission electron microscopy (HRTEM) image and selected area electron diffraction (SAED) pattern taken from a TEM specimen prepared from the $x = 0.30$ crystal. The measured distance of the neighboring lattice fringes in Figure 7.3(a) is 0.323 nm, in agreement with the $(\bar{1}14)$ lattice spacing for $TlBiTe_2$. The energy dispersive spectrometry (EDS) analysis on the specimen indicates it contains 23.7 at.% Tl, 22.3 at.% Bi, and 54.0 at.% Te, which verifies the chemical composition. The crystal structure of $TlBiTe_2$, as shown in Figure 7.1(b), is typified by (Te–Bi–Te–Tl) type of layers and recently noted as a new family of TI [137].

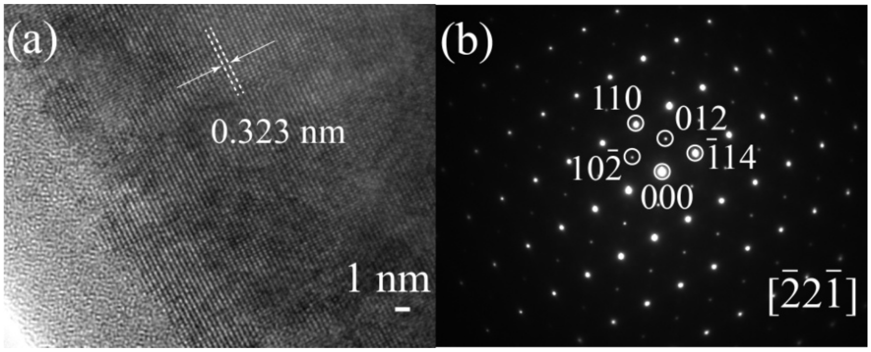

Figure 7.3 (a) HRTEM image and (b) SAED pattern taken from the $x = 0.30$ sample. The distance of the neighboring lattice fringes in (a) is 0.323 nm, in agreement with the $(\bar{1}14)$ lattice spacing for $TlBiTe_2$.

Incorporation of Tl into the tetradymite-type lattice of $Bi_2Te_3$ deserves a comment. One might naively expect the atoms of Tl to substitute for Bi. This to be the case, such doping would enhance the density of holes. As we shall see later, this is contrary to the experimental results that clearly show a crossover from *p*-type to *n*-type dominated transport as the content of Tl increases. A simple scenario in which Tl occupies interstitial sites or is in the van der Waals gap of the $Bi_2Te_3$ structure is also unlikely as this contradicts no changes being observed in the lattice parameters. Finally, arguing that the presence of Tl increases the bond polarity and thus decreases the probability of formation of antisite defects $Bi_{Te}$ that give bulk $Bi_2Te_3$ its *p*-type character, is also unlikely as the content of Tl is very low in these studies. In fact, as the above structural and compositional analysis using XRD, HRTEM and SAED indicates, it is via the formation of $TlBiTe_2$ how Tl enters the $Bi_2Te_3$ lattice. This mechanism was originally suggested in Ref. [138] and we now have an experimental proof of its existence. Since $Bi_2Te_3$ and $TlBiTe_2$ are closely related (the same $D_{3d}^{5}$ space group and nearly identical parameters of the $TeBi_6$ octahedra forming both $Bi_2Te_3$ and $TlBiTe_2$), there is only small energy penalty to be paid by replacing a quintuple layer of ($Te^1$–Bi–$Te^2$–Bi–$Te^1$) by a defected stack of (Te–Bi–Te–Tl–$V_{Te}^{\bullet\bullet}$ ) + 2*e*, where $V_{Te}^{\bullet\bullet}$ represents an atomic plane of Te vacancies. Patches of such empty Te planes will be randomly distributed among the neighboring $Te^1$ sites without forming a continuous layer of unoccupied sites. The most important, the symbiosis of the two structures provides means for supplying electrons in $Bi_2Te_3$ which then compensate holes and, with the increasing content of Tl, eventually take over and dominate the transport, as shown below.

Figure 7.4 presents the X-ray photoelectron spectroscopy (XPS) signals for Bi 4*f* [(a), (d)], Te 3*d* [(b), (e)], and Tl 4*f* [(c), (f)] core levels of various Tl-doped $Bi_2Te_3$ samples, collected from freshly prepared surfaces either perpendicular to the *c*-axis ($\perp c$, i.e. the basal plane) or parallel to the *c*-axis ( $// c$ ), where carbon and oxygen contamination was removed via Ar ion sputtering. The XPS signal was picked up from an analyzed area of approximately ~1.5 mm in diameter. The layered nature of $Bi_2Te_3$ matters in XPS to the extent that the signal from the $// c$ surface (where incident X-rays encounter a cross section of multiple QLs and everything in between) should be more informative than that from the $\perp c$ surface (where incident X-rays see a plane of QLs), in studying the chemical environment between QLs.

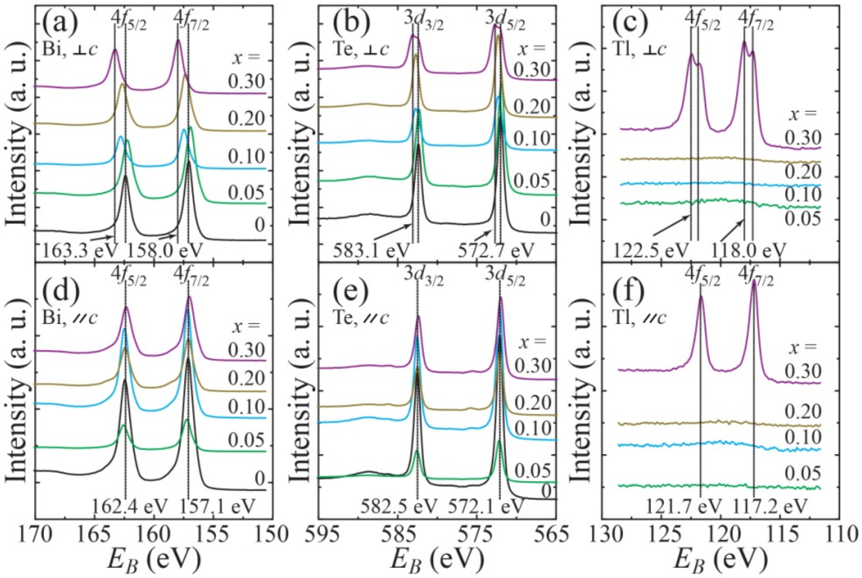

Figure 7.4 XPS analysis performed on various Tl-doped $Bi_2Te_3$ surfaces either perpendicular to the *c*-axis ($\perp c$, i.e. the basal plane) or parallel to the *c*-axis ($// c$) showing core levels for (a) Bi 4*f*, $\perp c$; (b) Te 3*d*, $\perp c$; (c) Tl 4*f*, $\perp c$; (d) Bi 4*f*, $// c$; (e) Te 3*d*, $// c$; (f) Tl 4*f*, $// c$.

Table 7-1 Binding energies $E_B$ in eV observed by XPS.

| | Bi | | Te | | Tl | |
|---|---|---|---|---|---|---|
| | $4f_{5/2}$ | $4f_{7/2}$ | $3d_{3/2}$ | $3d_{5/2}$ | $4f_{5/2}$ | $4f_{7/2}$ |
| $Bi_2Te_3$[a] | 162.5 | 157.2 | 582.3 | 572.0 | - | - |
| Tl[b] | - | - | - | - | 122.17 | 117.73 |
| $x = 0$ | 162.4 | 157.1 | 582.5 | 572.1 | - | - |
| $x = 0.30$ | 163.3 | 158.0 | 583.1 | 572.7 | 122.5,<br>121.7 | 118.0,<br>117.2 |

[a] From Ref. [139].

[b] From Ref. [140].

For sample $x = 0$, the binding energies $E_B$ of Bi and Te determined from both $\perp c$ [Bi, Figure 7.4(a); Te, Figure 7.4(b)] and $// c$ [Bi, Figure 7.4(d); Te, Figure 7.4(e)] surfaces are identical and agree with the literature values for $Bi_2Te_3$ [139], as summarized in Table 7-1. As shown in Figure 7.4(a) and Figure 7.4(b), when $x$ increases from 0 to 0.30, the Bi and Te peaks obtained from the $\perp c$ surface systematically shift toward higher energy, which we interpret as a change of the valence state in Bi and Te due to Tl presence in the lattice. The existence of Tl in the crystal is confirmed by the emergence of peaks corresponding to the Tl 4*f* levels in sample $x = 0.30$ as illustrated in Figure 7.4(c), which are listed in Table 7-1 and compared with literature values for pure Tl [140]. The atomic concentration for Tl is estimated to be 3.83±1.95%, somewhat lower than the nominal value 6% for $x = 0.30$. However, the XPS spectra of sample $x = 0.30$ in the $\perp c$ surface differ from that in the $// c$ surface. Since the Bi and Te $// c$ peaks of the sample $x = 0.30$ do not deviate from that of the sample $x = 0$, as shown in Figure 7.4(d) and Figure 7.4(e), we ascribe the Tl $// c$ peaks of sample $x = 0.30$ in Figure 7.4(f) to some loosely bonded Tl atoms which leave the binding energies of Bi and Te essentially unchanged. Even though Tl peaks were indeed observed in the XPS survey scan of sample $x = 0.20$, no discernible Tl signal in the XPS core scan was picked up for samples with $x \leq 0.20$ (even after several attempts), probably due to the very low concentration of Tl actually incorporated in the crystals (amounts much lower than one would expect based on the nominal $x$), together with the uneven distribution of Tl in the crystal (we have observed a large standard deviation of Tl concentration in the sample of $x = 0.30$). There is no doubt that Tl reveals its presence in $Bi_2Te_3$ on transport properties of the crystals but it is difficult to establish its presence quantitatively by whatever analytical measurement.

## 7.3 Electronic transport properties

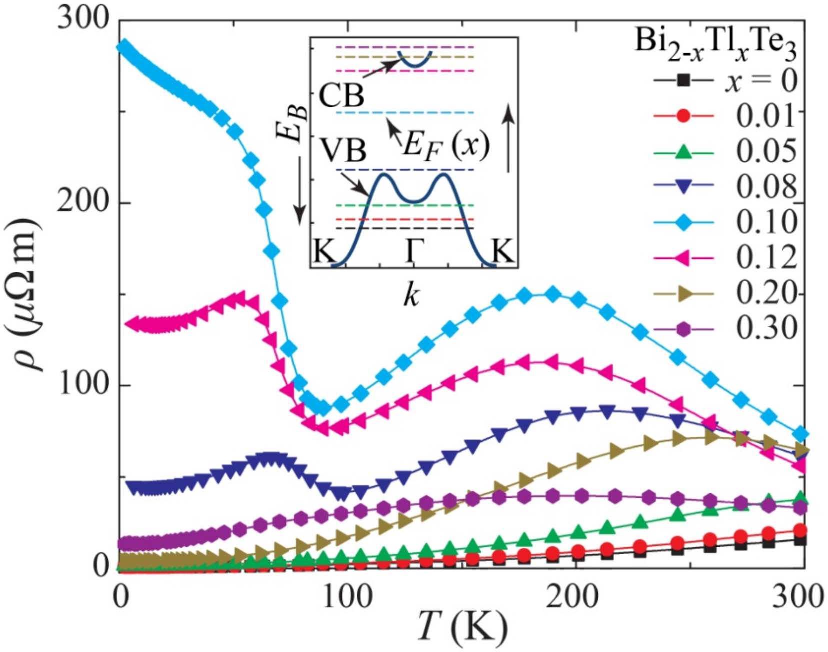

Figure 7.5 Temperature dependent electrical resistivity $\rho$ for Tl-doped $Bi_2Te_3$ single crystals. The inset is a sketch of the band structure (binding energy $E_B$ v.s. wave vector $k$) along the Γ-K direction, where Fermi level $E_F$ for various $x$ are indicated by horizontal dashed lines. With increasing amount of Tl, the $E_F$ is shifted continuously from the valence band (VB) into the conduction band (CB).

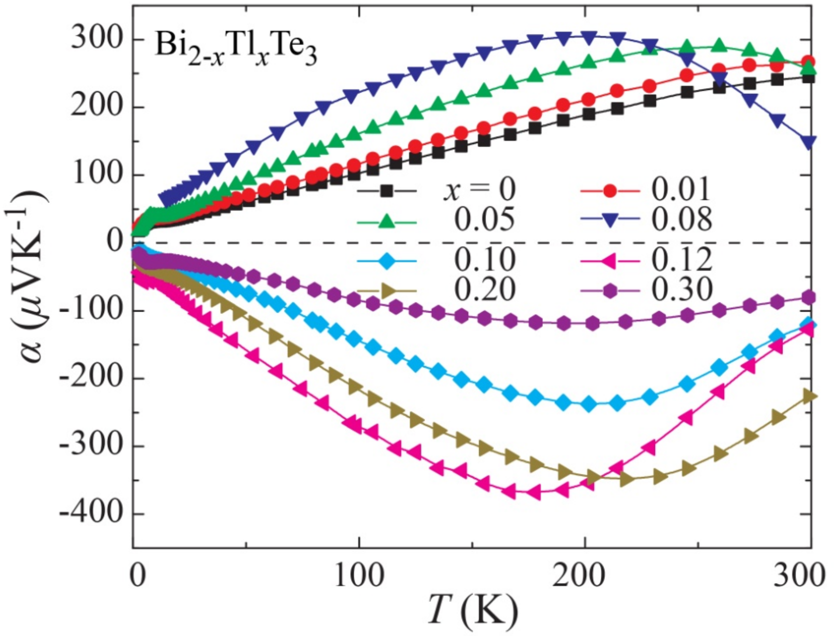

Figure 7.6 Temperature dependent Seebeck coefficient $\alpha$ for Tl-doped $Bi_2Te_3$ single crystals.

The temperature dependent electrical resistivity $\rho$ and Seebeck coefficient $\alpha$ measured in the (0001) plane are shown in Figure 7.5 and Figure 7.6, respectively. The pure $Bi_2Te_3$ ($x = 0$) exhibits a metallic electrical resistivity behavior ($\rho_{300K} = 14.0\ \mu\Omega$ m) and shows a positive Seebeck coefficient ($S_{300K} = +245\ \mu$V K$^{-1}$) in the entire temperature range covered. This *p*-type stoichiometric $Bi_2Te_3$ thus behaves as a highly degenerate semiconductor with the hole concentration $n_{300K} = +1.12\times10^{19}$ cm$^{-3}$ [see Figure 7.8, where positive (negative) $n$ indicates hole (electron)]. The Fermi level $E_F$, in this case, lies in the valence band (VB). With the increasing content of Tl, as shown below, $E_F$ continuously shifts out of VB into the band gap and towards the edge of the conduction band (CB). A sketch of the band model along the Γ-K direction [134, 141, 142], together with the position of $E_F$ (dashed lines) corresponding to various $x$ values, is presented as the inset of Figure 7.5. By properly choosing the content of Tl ($0.08 \leq x \leq 0.12$), one can pin $E_F$ in the band gap, a situation that is potentially favorable for the studies of TIs.

Upon increasing the content of Tl up to $x = 0.05$, the system maintains its metallic conduction characteristics. However, a gradually decreasing density of holes, as shown in Figure 7.8, leads to an increase in the electrical resistivity. This corresponds to a shift of $E_{\rm F}$ toward the VB maximum. Since the density of extrinsic carriers in these lightly Tl-doped samples is decreased, the presence of thermal excitations across the band gap becomes evident on $\rho$ *vs.* $T$ curves before room temperature is reached. Even clearer evidence of intrinsic excitations is seen in the behavior of the Seebeck coefficient where down-turns set in at progressively lower temperatures and are more dramatic as electrons start to compensate extrinsic holes.

Heavier Tl content with $x$ between 0.08 and 0.12 drives the system into a prominent non-metallic regime of conduction. During this transition, the density of extrinsic holes is greatly diminished, the carrier type changes from that of a hole-dominated to an electron-dominated transport [see the behavior of the Seebeck coefficient in Figure 7.6, and the Hall coefficient in Figure 7.7] and $E_F$ shifts from a position close to the top of VB ($x = 0.08$) to a location deep into the band gap ($x = 0.10$), and then approaches the bottom of CB ($x = 0.12$). Very low background carrier concentrations of samples with $0.08 \leq x \leq 0.12$ make thermal excitations across the band gap much more prominent in both the resistivity and Seebeck coefficient data and bi-polar contributions are manifested at even lower temperature ~200 K. Interestingly, when the Tl-doped $Bi_2Te_3$ crystals ($x = 0.08 - 0.12$) are cooled down from ~200 K, a metal-insulator type of transition at ~100 K is always observed in $\rho$. Below ~100 K, the system displays a distinctly insulating behavior (rather than metallic) corresponding to the Fermi level being buried in the band gap. Surprisingly, the insulating behavior peaks near 50 K and is followed by a decreasing resistivity (samples $x = 0.08$ and 0.12) or a tendency to quasi-saturate ($x = 0.10$) that persists down to the lowest temperatures of the experiment. Such unique metallic conduction below ~50 K in the case of $0.08 \leq x \leq 0.12$ could be a manifestation of the dominance of the surface metallic state. However, why the metallic state abruptly ceases to exist near 50 K, the gap opens, and the insulating state takes over is an open question. It is worth noting that a similar transport response was also observed in Tl-doped PbTe [33], where the resonant states introduced by Tl are believed to play an important role in understanding such effect.

The behavior described above regarding $\rho$ maps well onto the trend observed in $\alpha$. In the regime dominated by extrinsic holes ($0 \leq x \leq 0.08$), as $\rho$ increases, the positive $\alpha$ increases. Likewise, in the regime where $\rho$ is governed by electrons ($x = 0.12 - 0.30$), a decreasing $\rho$ leads to a decreasing magnitude of the negative $\alpha$. We also note that a local maximum is seen in the magnitude of $\alpha$ near ~7 K for all samples regardless of Tl-doping level. This is a manifestation of the phonon-drag effect [106] reflecting a strong electron-phonon interaction at low temperatures and high crystalline quality samples.

Results of the Hall coefficient ($R_H$) measurements are shown in Figure 7.7, together with the carrier density $n$ [defined as $n = 1/(e\,R_H)$ and applicable for a single parabolic band approximation, where $e$ is the elementary charge, and positive (negative) $n$ stands for holes (electrons)] and Hall mobility (defined as $\mu_H = R_H/\rho$) in Figure 7.8 and Figure 7.9, respectively. Note that, above ~200 K, where intrinsic excitations start to take place, such simplified experimental determination of the carrier density and mobility is no longer appropriate (see the unphysical sharp turns in $n$ at high temperature for $x > 0.08$). This is also the reason why the $x = 0.10$ sample shows “falsely” large carrier concentration which becomes even more significant at high temperatures, since electrons and holes are compensating each other. We observe systematically varying carrier concentration for $x = 0 - 0.08$, where extrinsic holes dominate the transport process, resulting in positive $R_H$ with density of holes suppressed as $x$ increases. For $x = 0.20 - 0.30$, the negative $R_H$ validates the electron-dominated conduction, where larger $x$ tends to increase the density of electrons as the Fermi level moves deeper into the conduction band. Such tuning of carrier density is in accordance with the increasing content of

$TlBiTe_2$ and therefore progressively higher density of electrons as the nominal amount x of Tl increases.

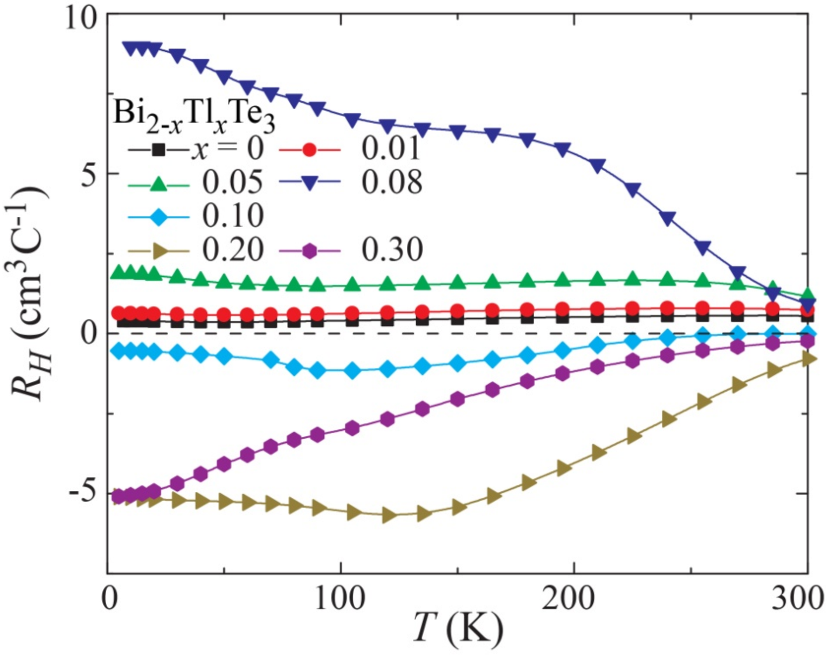

Figure 7.7 Temperature dependent Hall coefficients $R_H$ from 2 K to 300 K.

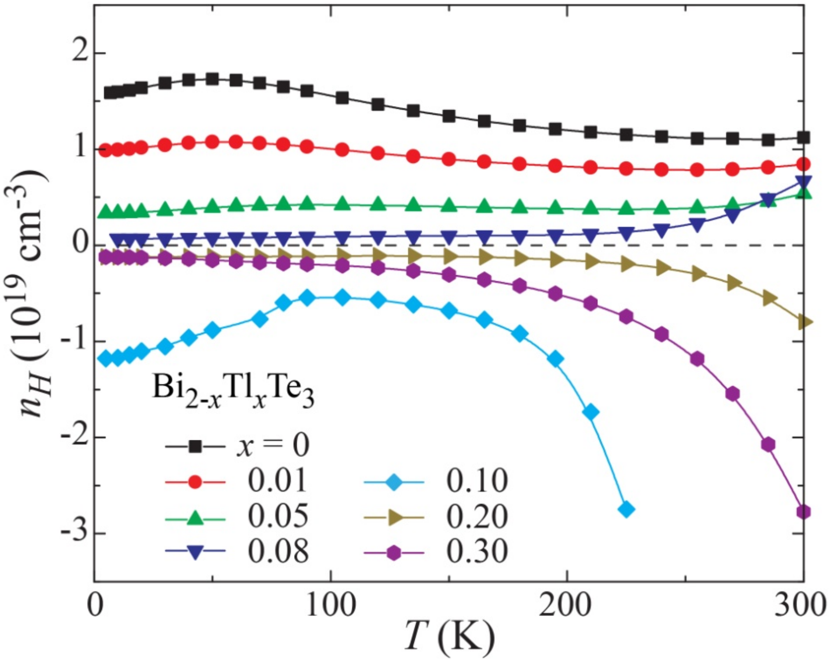

Figure 7.8 Temperature dependent carrier density defined as $n = 1/(e R_H)$, where $e$ is the elementary charge and positive (negative) $n$ stands for hole (electron).

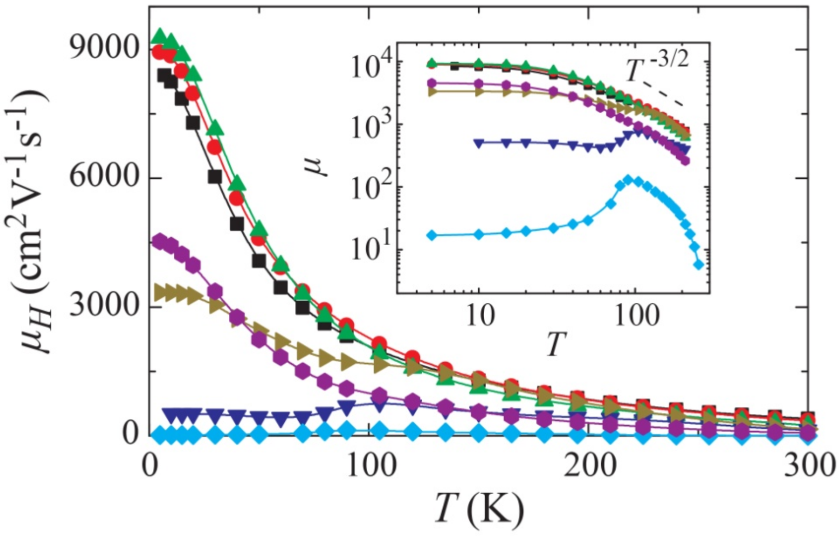

Figure 7.9 Temperature dependent Hall mobility defined as $\mu_H = R_H/\rho$. The inset is $\mu_H$ vs. $T$ plotted on a log-log scale indicating the $T^{-3/2}$ acoustic phonon temperature dependence at temperatures near the ambient.

As shown in Figure 7.9, carriers are clearly classified into three different categories: for $x = 0 – 0.05$, the mobility is high ($\mu_{10K}$ ~ 9000 cm$^2$ V$^{-1}$ s$^{-1}$), while it becomes significantly suppressed (by a factor of ~16) to a low value ($\mu_{10K}$ ~ 560 cm$^2$ V$^{-1}$ s$^{-1}$) for $x = 0.08$; with a further increase in Tl content ($x = 0.20 – 0.30$), the crystal becomes an $n$-type conductor with $\mu_H$ restored to intermediate values ($\mu_{10K}$ ~ 3000 – 4000 cm$^2$ V$^{-1}$ s$^{-1}$). The inset of Figure 7.9 displays a log-log plot of $\mu_H$ vs. $T$, indicating a temperature dependence of $\mu_H \sim T^{-3/2}$ that suggests the acoustic phonon scattering is playing an important role at temperatures near the ambient.

## 7.4 Thermal transport properties

The temperature dependent thermal conductivity $\kappa$ of these Tl-doped $Bi_2Te_3$ samples is shown in Figure 7.10. The resulting dimensionless thermoelectric figure of merit $ZT = S^2\sigma T/\kappa$ is plotted in Figure 7.11, indicating that a trace amount ($x$ ~ 0.01) of Tl may actually help to improve the thermoelectric performance of $Bi_2Te_3$. Higher concentrations of Tl have a clearly negative impact on the thermoelectric performance.

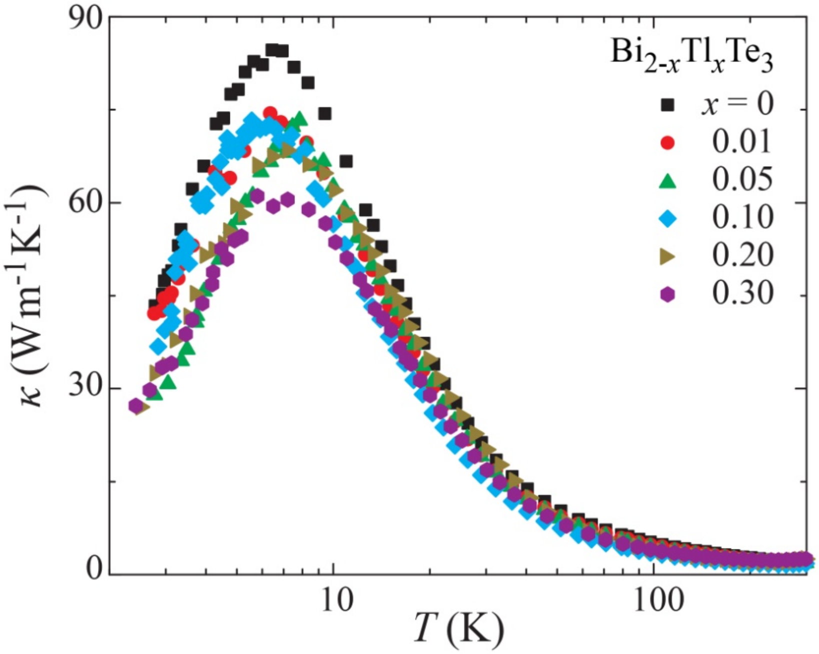

Figure 7.10 The temperature dependence thermal conductivity $\kappa$ for Tl-doped $Bi_2Te_3$ single crystals.

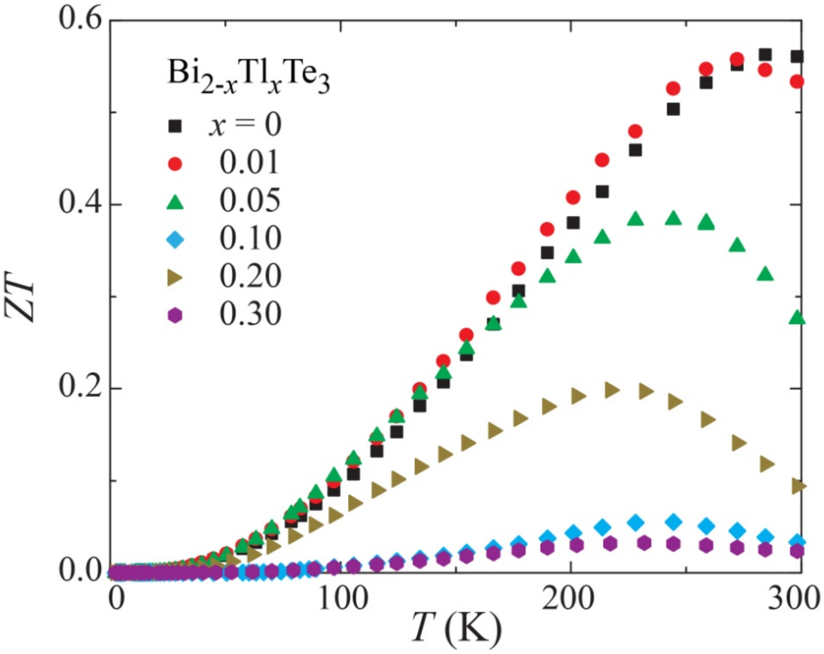

Figure 7.11 The temperature dependence of thermoelectric figure of merit $ZT$ for Tl-doped $Bi_2Te_3$ single crystals.

The total thermal conductivity can be decomposed as $\kappa = \kappa_L + \kappa_e$, where $\kappa_L$ and $\kappa_e$ are the lattice and electronic thermal conductivities, respectively. The $\kappa_L$ is calculated by subtracting $\kappa_e$ obtained from the Wiedemann-Franz law. Here $\kappa_e = L\sigma T$, where $\sigma$ ($=1/\rho$) is the electrical conductivity and $L$ is the Lorenz number. Note that under the single parabolic band approximation with one dominant carrier type, the Seebeck coefficient is given by:

$$\alpha = -\frac{k_B}{q}\left[\eta - \frac{(r+5/2)F_{r+3/2}(\eta)}{(r+3/2)F_{r+1/2}(\eta)}\right], \tag{7.1}$$

where $k_B$ is the Boltzmann constant, $q$ is the charge of carrier [$+e$ ($-e$) for hole (electron)], $r$ is the scattering index in the energy dependent relaxation time $\tau = \tau_0 \varepsilon^r$ (taken to be -1/2 for acoustic phonon scattering), $\eta = E_F / k_B T$ is the reduced Fermi level, and $F_n(\eta)$ is the $n$-th Fermi-Dirac integral defined as:

$$F_n(\eta) = \int_0^\infty \frac{\xi^n}{e^{\xi-\eta}+1} d\xi. \tag{7.2}$$

Using $\eta$ determined from the experimental values of Seebeck coefficient, the Lorenz number $L$ can be estimated via:

$$L = \frac{k_B{}^2}{q^2}\left[\frac{(r+3/2)(r+7/2)F_{r+1/2}(\eta)F_{r+5/2}(\eta) - (r+5/2)^2 F_{r+3/2}(\eta)^2}{(r+3/2)^2 F_{r+1/2}(\eta)^2}\right], \tag{7.3}$$

The resulting temperature dependent phonon conductivity $\kappa_L$ is examined using the Debye-Callaway model [143, 144]:

$$\kappa_L = \frac{k_B}{2\pi^2 v}\left(\frac{k_B}{\hbar}\right)^3 T^3 \int_0^{\theta_D/T} \frac{\tau_c x^4 e^x}{(e^x-1)^2} dx, \tag{7.4}$$

where $x = \hbar\omega / k_B T$, $\omega$ is the phonon frequency, $\hbar$ is the reduced Planck constant, $k_B$ is the Boltzmann constant, $v$ is the averaged velocity of sound, $\theta_D$ is the Debye temperature, and $\tau_c$ is the relaxation time. The overall relaxation rate $\tau_c^{-1}$ is given by:

$$\tau_c^{-1} = v/\ell + A\omega^4 + B\omega^2 T \exp\left(-\theta_D/3T\right) + C\omega T^3, \tag{7.5}$$

where terms on the right hand side correspond to the boundary scattering ($\ell$ is the mean grain size), defect scattering, Umklapp processes[145], and normal phonon scattering [146], respectively. Here $\ell$, $A$, $B$, and $C$ are fitting parameters.

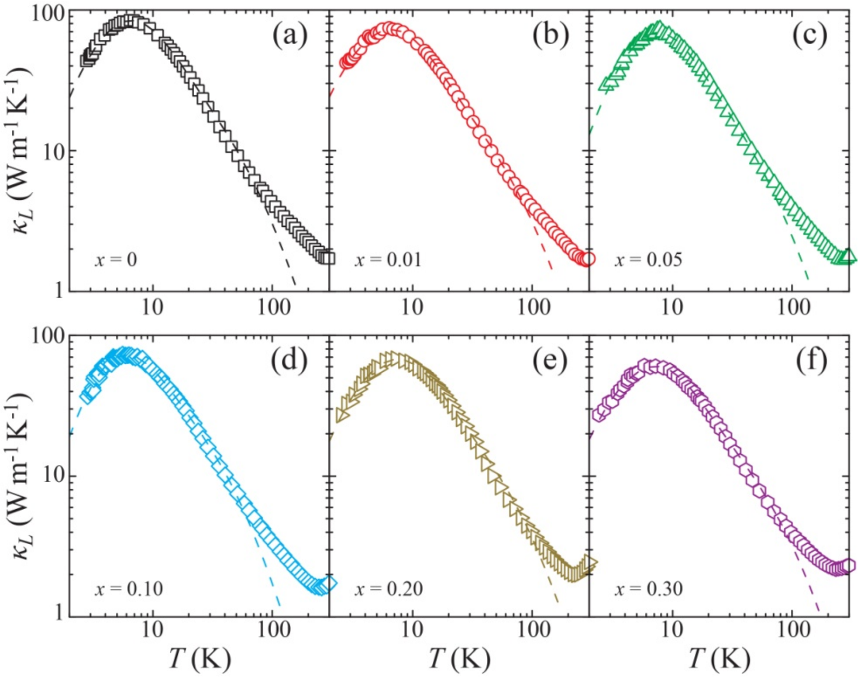

Figure 7.12 The lattice thermal conductivity $\kappa_L$ of Tl-doped $Bi_2Te_3$ single crystals, with the dashed line indicating the numerical fitting result of the Debye-Callaway model for (a) $x$ = 0, (b) $x$ = 0.01, (c) $x$ = 0.05, (d) $x$ = 0.10, (e) $x$ = 0.20, and (f) $x$ = 0.30, which documents a generally enhanced point defect scattering of phonons upon increasing the content of Tl.

Table 7-2 Lattice thermal conductivity fitting parameters for $Bi_{2-x}Tl_xTe_3$ single crystals.

| $x$ | $\ell$ (mm) | $A$ ($10^{-42}$ s$^3$) | $B$ ($10^{-17}$ s K$^{-1}$) | $C$ ($10^{-8}$ K$^{-3}$) |
|---|---|---|---|---|
| 0 | 0.488 | 1.036 | 0.944 | 1.358 |
| 0.01 | 0.593 | 1.765 | 1.018 | 1.078 |
| 0.05 | 0.215 | 0.851 | 1.209 | 1.738 |
| 0.10 | 0.321 | 0.530 | 0.952 | 3.275 |
| 0.20 | 0.382 | 1.703 | 0.746 | 0.968 |
| 0.30 | 0.441 | 2.251 | 0.870 | 1.009 |

Figure 7.12 presents the lattice thermal conductivity for various Tl-doped $Bi_2Te_3$ single crystals. The dashed lines are the numerical fitting result of Eq. (7.4) and Eq. (7.5), with $v = 2.0$ km/s [147], and $\theta_D = 165$ K [148]. Fitting parameters are listed in Table 7-2. Such model depicts the temperature dependence of $\kappa_L$ very well at low temperatures, but starts to underestimate $\kappa_L$ for $T > 100$ K, where effects of radiation loss, temperature dependence of Lorenz number, and bi-polar thermal conductivity all contribute. An attempt to include electron-phonon scattering (e.g. $\tau_{e-p}^{-1} \sim \omega^2$) in the calculations did not improve the overall fit. Note that the increasing content of Tl generally leads to a lower dielectric maximum in $\kappa_L$, a broader peak and its slight shift to higher temperatures, with an enhanced strength of point defect scattering of phonons.

## 7.5 Summary

While it is difficult to establish quantitatively (and even qualitatively at low Tl concentrations) the presence of Tl in the crystal lattice of $Bi_2Te_3$, its systematic effect on the transport behavior leaves no doubt that Tl plays an important role in shifting the Fermi level and thus transport properties of $Bi_2Te_3$. The incorporation of Tl in $Bi_2Te_3$ proceeds via the formation of defected layers of $TlBiTe_2$ that contain charged vacant planes of Te. Such structure is crystallographically akin to $Bi_2Te_3$ and seems randomly distributed. Moreover, it is the source of electrons responsible for an effective way of tuning *p*-type metallic $Bi_2Te_3$ gradually into an *n*-type conductor with the increasing content of Tl, and therefore $TlBiTe_2$, as confirmed by measurements of the Seebeck coefficient and the Hall effect. During the *p*-*n* transition, interesting non-metallic states are present with unique electrical resistivity profile. Samples having the Fermi level in the band gap display a metallic or quasi-saturated conduction below ~50 K. This might be a transport signature of the presence and dominance of the topologically protected surface state. Introducing Tl into the crystal lattice of $Bi_2Te_3$ thus might be of interest in achieving bulk insulating states that then allow detection of surface states. Thermal conductivity of Tl-doped $Bi_2Te_3$ is suppressed on account of enhanced point defect scattering. Very low concentrations of Tl seem to marginally improve the thermoelectric performance of $Bi_2Te_3$.

## CHAPTER 8

# LOW-TEMPERATURE STRUCTURAL AND TRANSPORT ANOMALIES IN DICOPPER SELENIDE

Through systematic examination of symmetrically nonequivalent configurations, first-principles calculations have identified a new ground state of $Cu_2Se$, which is constructed by repeating sextuple layers of Se-Cu-Cu-Cu-Cu-Se. The layered nature is in accord with transport properties, electron and X-ray diffraction studies at and below room temperature. Magnetoresistance measurements at liquid helium temperatures exhibit cusp-shaped field dependence at low fields and evolve into quasi-linear field dependence at intermediate and high fields. These results reveal the existence of weak antilocalization effect, which has been analyzed using a modified Hikami, Larkin, and Nagaoka (HLN) model including a quantum interference term and a classical quadratic contribution. Fitting parameters suggest a quantum coherence length $L$ of 175 nm at 1.8 K. With increasing temperature, the classical parabolic behavior becomes more dominant and $L$ decreases as a power law of $T^{-0.83}$. These surprisingly novel discoveries have improved understanding of $Cu_2Se$-based material systems implying further interesting applications.

## 8.1 Introduction

Transition metal chalcogenides (TMCs) form a fruitful research in contemporary condensed matter physics leading to intriguing discoveries and promising applications [149]. For example, the silver chalcogenides (e.g., $Ag_2Te$) are renowned for their extraordinary large magnetoresistance [150] and have been recently identified as a new class of binary topological insulators (TI) with a highly anisotropic Dirac cone [151]. Additionally, transition metal dichalcogenides (TMDCs) $MX_2$, where M is a transition metal element and X is a chalcogen atom (S, Se, or Te), are well known for their two-dimensional (2D) structures formed by X-M-X layers with strong in-plane bonding and weak out-of-plane interactions. The unique intrinsic 2D nature of TMDCs has facilitated the search for novel states of matter, for instance, by offering a coexistence of superconductivity and the Mott commensurate charge density wave (CCDW) phase in 1T-$TaS_2$ [152]. Furthermore, the electronic band structures of TMDCs are believed to host exotic spin-orbit phenomena exemplified by the systematic crossover from weak localization (WL) to weak anti-localization (WAL) in $WSe_2$ [153, 154].

As an important member of the TMC family, the superionic $Cu_2Se$ has also received heightened attention in the recent developments of thermoelectrics [155] and optoelectronics [156], due to the unique transport properties associated with its structural phase transition occurring at ~ 400 K. The exact transition temperature of this well-known reversible second-order transition from the ordered room temperature (RT) monoclinic $\alpha$-phase to the disordered high temperature (HT) cubic $\beta$-phase depends on the Cu deficiency in the metal sub-lattice [157] and is found to be tunable upon iodine doping on the selenium sites [158]. It is generally accepted that the disordered HT $\beta$-

phase of $Cu_2Se$, space group $Fm\overline{3}m\,(O_h^5, \mathrm{S.G.}\#\,225)$ is constructed by statistically distributing Cu atoms over the 8*c* tetrahedral sites in a face centered cubic (fcc) matrix formed by Se atoms. However the structural determination of the ordered phase(s) still remains controversial [159]. Furthermore, despite some rare reports on samples with quite high Cu deficiency (e.g., $Cu_{2-x}Se$, $0.20 \le x \le 0.25$) [160], detailed study of the transport properties of stoichiometric $Cu_2Se$ at low temperatures is still desirable. In this Letter, we report first-principles determination of the ground state along with several unexpected experimental findings regarding the low-temperature transport properties of $Cu_2Se$, which may indicate an intrinsic 2D quantum behavior.

## 8.2 Ground state of $Cu_2Se$

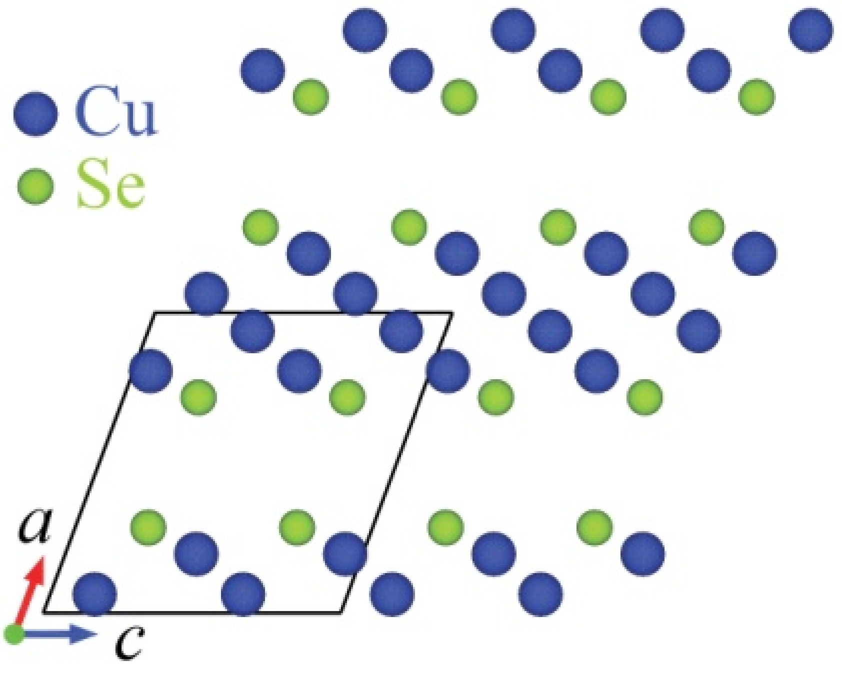

Figure 8.1 Projected (along the monoclinic *b*-axis) *ab inito* ground state structure of $Cu_2Se$ formed by repeating sextuple layers of Se-Cu-Cu-Cu-Cu-Se.

The ground state of $Cu_2Se$ was obtained via structural relaxation of the cubic HT $\beta$-phase. In order to determine the most stable structure, Cu atoms were randomly distributed onto the $32f$ trigonal sites in the fcc Se matrix, which form tetrahedrons around the $8c$ tetrahedral sites. Note that for stoichiometric $Cu_2Se$, only 1/4 of the $32f$ sites are occupied by Cu atoms. Symmetrically distinct configurations with up to 8 Cu atoms have been studied based on the Cu occupancy on the sub-lattice [39]. Subsequent density functional theory (DFT) calculations of the formation energy have allowed us to identify stable configurations of $Cu_2Se$.

The proposed ground state of $Cu_2Se$ crystallizes in space group $P2_1/c\,(C_{2h}^5, \mathrm{S.G.}\#14)$, with optimized lattice parameters: $a$ = 7.453 Å, $b$ = 4.322 Å, $c$ = 6.880 Å, $\alpha$ = 90.00°, $\beta$ = 70.62°, $\gamma$ = 90.00° and atomic occupation: Cu1 (0.06111, 0.58259, 0.15164), Cu2 (0.80599, 0.92292, 0.05310), and Se (0.28070, 0.93855, 0.25485). As shown in Figure 8.1, the ground state of $Cu_2Se$ has quasi-2D characteristics typified by the Se-Cu-Cu-Cu-Cu-Se type of sextuple layers (thickness $t$ = 3.95 Å), which are interconnected via weak Se-Se bonds (gap $\delta$ = 3.08 Å). Comparing with recent literature results using rather different approaches, the monoclinic structure of $Cu_2Se$ obtained here has lower formation energy per unit formula [158, 161]. The proposed structure is also dynamically stable due to the absence of the soft modes in the phonon spectrum, as is evident in Figure 8.2. As shown in Figure 8.3, the monoclinic $Cu_2Se$ is confirmed to be semiconducting and the electronic band gap $E_g$ (using HSE) is found to be 1.03 eV, which agrees very well with the experimental value of 1.20 eV [162] and has been known as the best first-principles result in the literature [163].

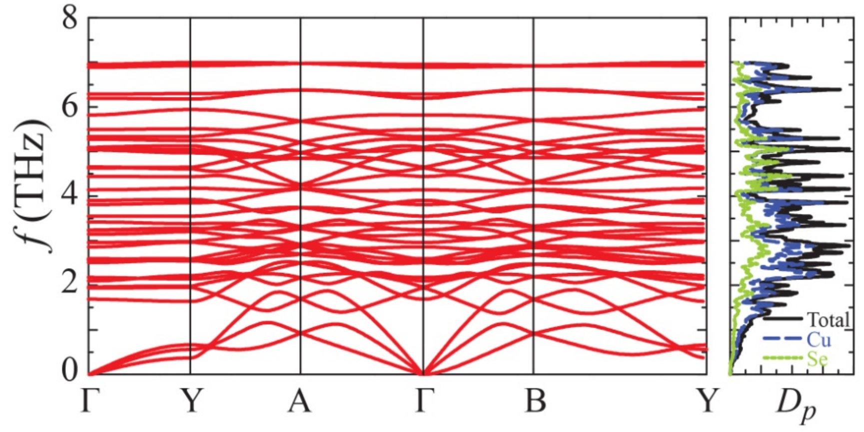

Figure 8.2 The calculated phonon band structure and density of states ($D_p$) indicate the proposed structure is dynamically stable.

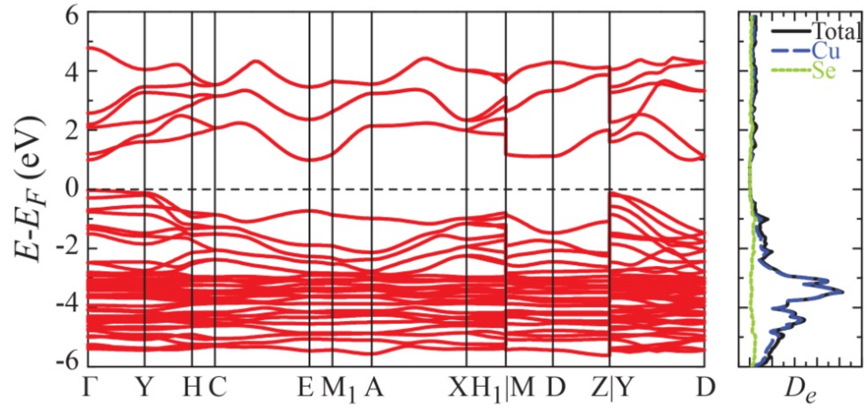

Figure 8.3 The electronic band structure and density of states ($D_e$) calculated using HSE hybrid functional suggests that $Cu_2Se$ is a semiconductor with band gap $E_g$ = 1.03 eV.

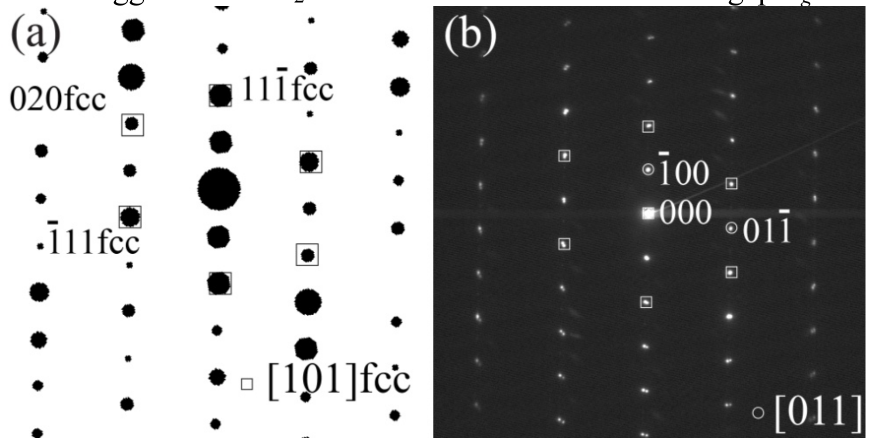

Figure 8.4 (a) Simulated SAED pattern along the zone axis [011] of the monoclinic phase and the $[101]_{fcc}$ with the diffractions from the fcc structure labeled as squares. (b) The experimental SAED pattern along the [011] zone axis of the monoclinic phase.

The EDS analysis on the TEM specimen indicates it contains 66.3 at% Cu and 33.7 at% Se, which verifies the $Cu_2Se$ chemical composition. The simulated SAED pattern along the monoclinic [011] zone axis is presented in Figure 8.4(a), where the monoclinic [011] axis of the proposed ground state is equivalent to an fcc [101] axis. Spots labeled by the square symbols are indexed according to the fcc diffraction pattern, which correspond to the SAED pattern of the HT cubic $\beta$-phase [158]. Figure 8.4(b) displays the experimental SAED pattern along the monoclinic [011] axis. The agreement between the experimental and theoretical pattern has verified the predicted layered structure of the ground state. Additional superstructural diffraction spots/stripes have been also observed along other zone axes. This may result from the different packing order of the sextuple layers and/or Cu-vacancy ordering at finite temperature when thermal energy starts to affect the structure [164].

## 8.3 Another phase transition of $Cu_2Se$

To further understand the structure, low temperature XRD measurements have been performed. In line with earlier reports [160, 164-167], a reversible $\alpha$ to $\alpha'$ superstructure transition is also evident in the sample studied here via an intensity rearrangement of the multiplet of superlattice peaks located in the $Q$-region close to the (400) reflection in cubic notation (Figure 8.5). This is found from assessment of the systematic temperature dependent XRD data, collected in the 100-300 K range upon warming. The transfer of intensity occurs at around 175 K (the upper right inset in Figure 8.5).

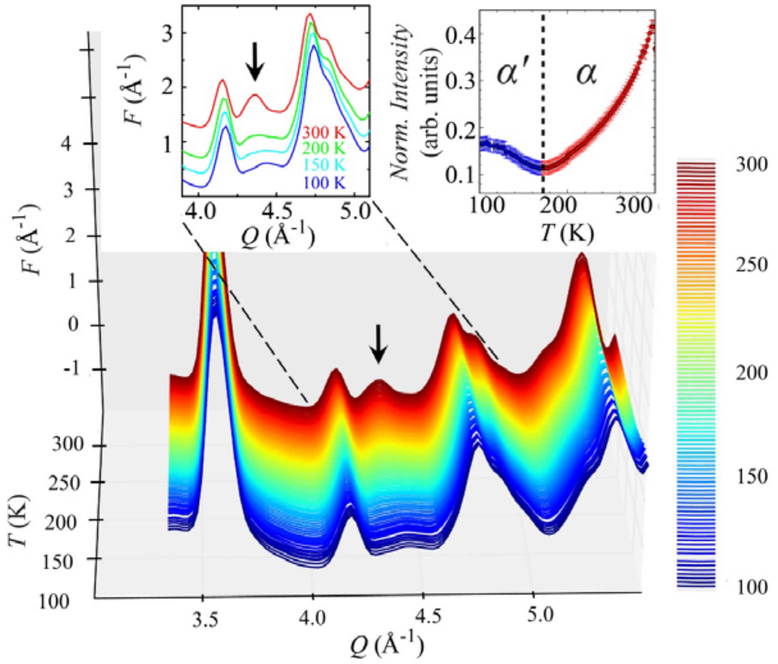

Figure 8.5 Reduced total scattering XRD structure function, $F(Q) = Q[S(Q)-1]$, where $S(Q)$ is the total scattering structure function and $Q$ is the momentum transfer, in 100-300 K range (main panel). Temperature evolution of the normalized intensity around (400) reflection in cubic notation, marked with an arrow in the upper left inset ($Q \sim 4.3$ Å$^{-1}$). This region is sensitive to subtle structural changes, and evidences the $\alpha$□ to $\alpha$ superstructure transition at around 175 K, as denoted by a vertical dashed line (upper right inset). Red symbols denote the evolution with temperature of the intensity peaked at $Q \sim 4.362$ Å$^{-1}$, while the blue symbols show the evolution of the intensity peaked at $Q \sim 4.436$ Å$^{-1}$.

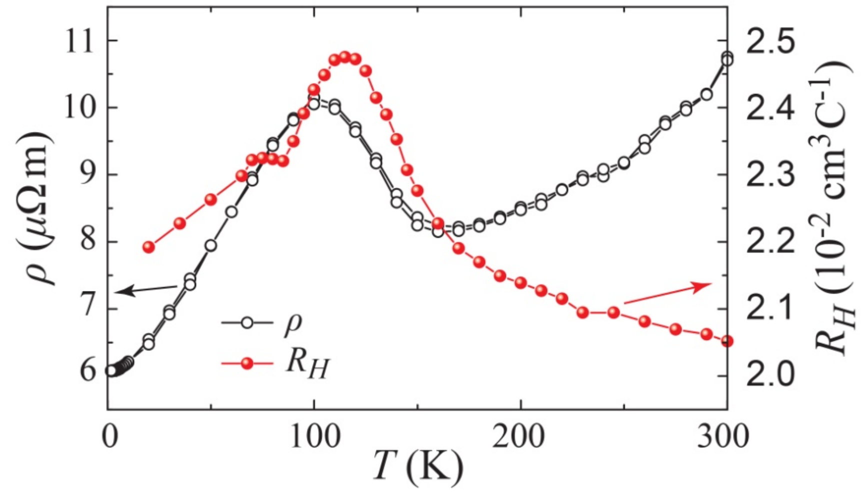

Figure 8.6 Low-temperature electrical resistivity $\rho$ and Hall coefficient $R_H$ of stoichiometric $Cu_2Se$, showing an anomalies at 100–150 K, where $\rho$ measurements overlap upon either warm up or cool down in the temperature.

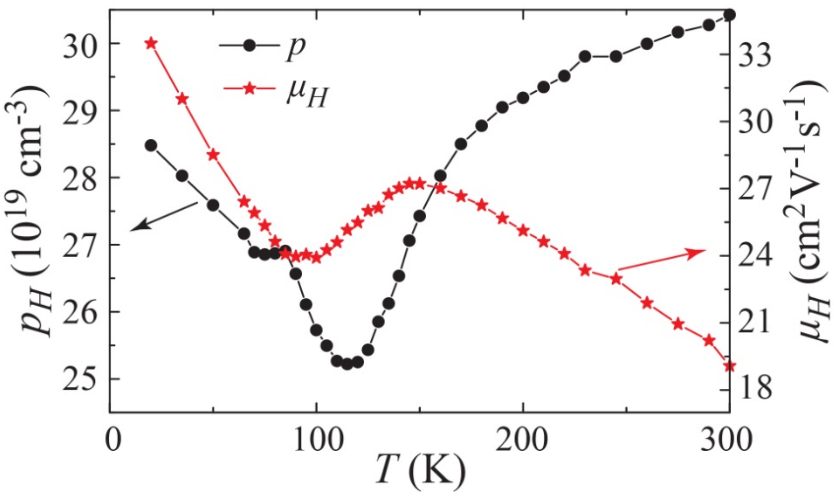

Figure 8.7 Low-temperature Hall density $p$ and Hall mobility $\mu_H$ of stoichiometric $Cu_2Se$.

We were interested to find out what is the impact of such structural changes on the transport properties. As shown in Figure 8.6 and Figure 8.7, the above mentioned $\alpha$ to $\alpha$□-type of transition has a strong imprint on the temperature dependence of the electrical resistivity (20% effect) and the Hall effect. The electrical resistivity of $Cu_2Se$ exhibits a highly anomalous behavior in the 100–150 K temperature range which is also accompanied by a large peak in the Hall effect. We speculate that such features might represent a possible charge density wave (CDW) transition [168], as a result of the distortion/redistribution of the sextuple layers upon temperature change, however, further theoretical and experimental efforts are needed to clarify the issue. We note that, in spite of looking for accompanying anomalies in the Seebeck effect, thermal conductivity and the specific heat, we found none. The anomalous behavior seems to be limited to galvanomagnetic transport only.

## 8.4 The magnetoresistance of $Cu_2Se$

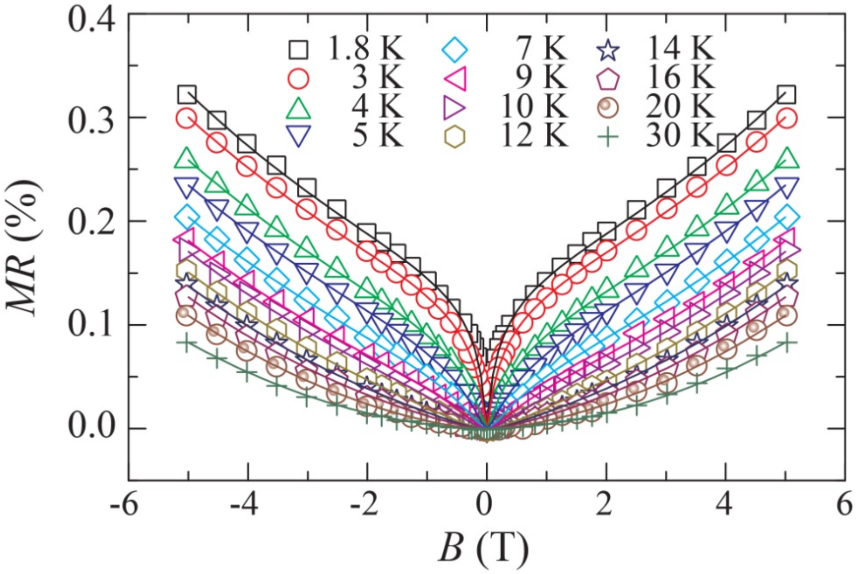

Figure 8.8 Magnetoresistance profile (as a function of magnetic field intensity) of $Cu_2Se$ at various temperatures (1.8–30 K) indicating evolution of weak antilocalization behavior as the temperature is lowered to 1.8 K.

At even lower temperatures (1.8–30 K), the magnetoresistance (MR) of $Cu_2Se$ is extraordinary, as shown in Figure 8.8. The semi-classical transport theory predicts a quadratic field-dependent MR in the low-field range which saturates in high fields. In distinct contrast to the traditional theory, the MR of $Cu_2Se$ at low temperatures exhibits a weak anti-localization (WAL)-like cusp which is suppressed when the temperature increases. In addition, at high fields, the MR increases with the increasing field in a linear fashion with no sign of saturation up to $B = 5$ T.

We account for the field dependence of differential magnetoconductance (MC) over the entire range of fields and temperatures with a modified Hikami, Larkin, and Nagaoka (HLN) quantum interference model [169, 170]:

$$MC \equiv \frac{G(B)-G(0)}{G(0)} = -\alpha\left[\psi\left(\frac{\hbar}{4eL^2B}+\frac{1}{2}\right)-\ln\left(\frac{\hbar}{4eL^2B}\right)\right]+\beta B^2, \tag{8.1}$$

where $\psi$ is the digamma function.

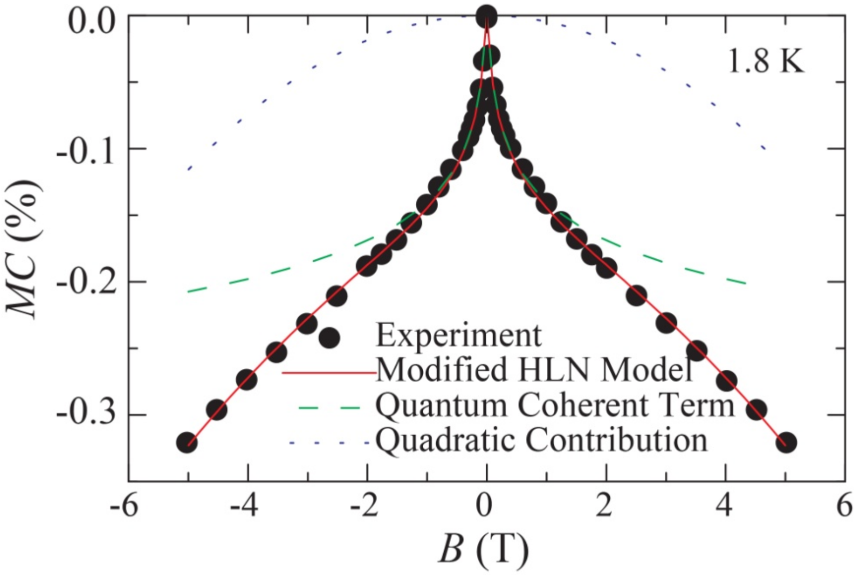

Figure 8.9 Theoretical fitting to differential magnetoconductance using a modified HLN model at 1.8 K.

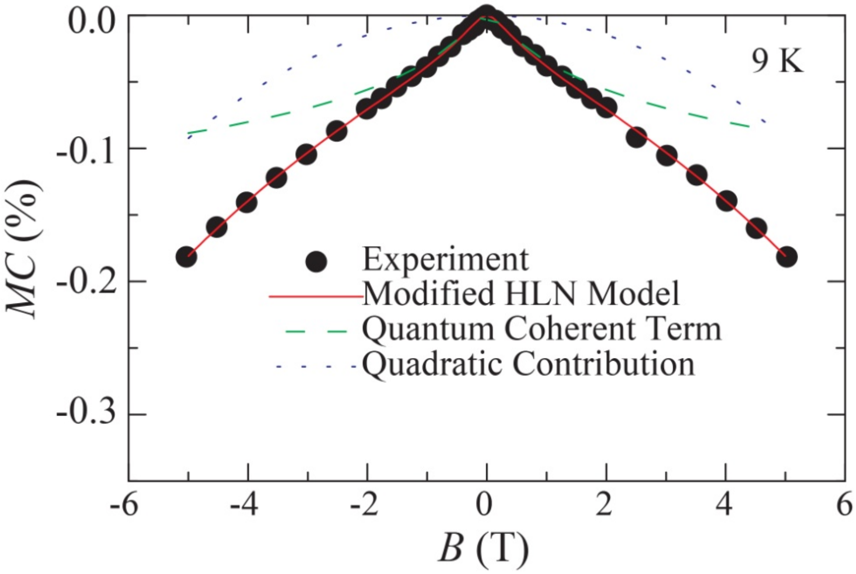

Figure 8.10 Theoretical fitting to differential magnetoconductance using a modified HLN model at 9 K.

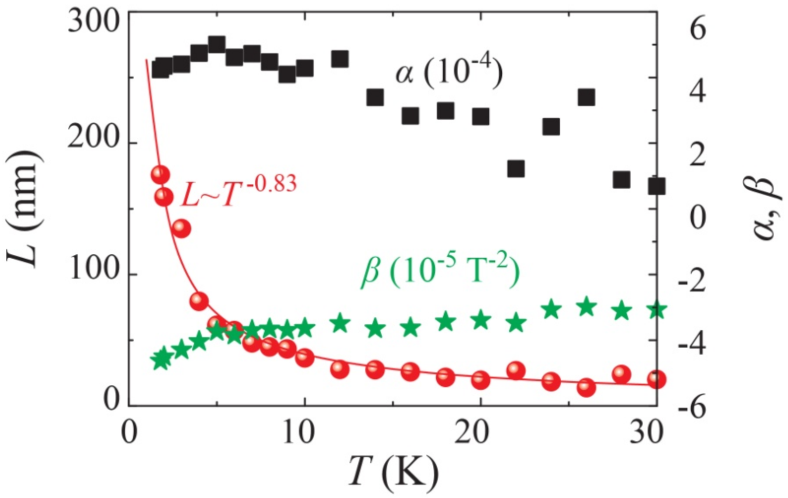

Figure 8.11 the fitting parameters showing a power law behavior (~ $T^{-0.83}$) of the quantum interference length.

The original formalism of the simple HLN model was developed to characterize the transport properties of a 2D system where the conductance quantum ($2e^2/h$) naturally come into play. In order to compensate for the bulk effects of this newly discovered quasi-2D layered structure of $Cu_2Se$, we have normalized the conductance using the zero field value and introduced a dimensionless fitting parameter $\alpha$. Here $L$ is the phase coherence length and $\beta$ is the quadratic coefficient arising from additional scattering terms. The HLN model has been successfully used in explaining the magneto-transport phenomena in various 2D material system, like $Bi_2Se_3$ [171, 172], $Bi_2Se_2Te$ [173], and $Bi_2Te_2Se$ thin films [170]. It is worth to emphasize that such a modified model simultaneously accounts for the quantum phase interference cusp at low fields as well as the linear-like MR at high fields. It is shown that the additional quadratic term compensates the logarithmic dependence of the quantum interference at high fields, leading to an intermediate linear field dependence of MR.

The overall fitting result, along with the corresponding quantum interference term and quadratic term, is shown in Figure 8.9 and Figure 8.10 for $T$ = 1.8 K and 9 K, respectively. In the present sample, the phase coherence length $L$ is 175 nm at 1.8 K and decreases following a power law of $T^{-0.83}$ temperature dependence (Figure 8.11). The successful application of the HLN model in $Cu_2Se$ has advocated the 2D quantum nature of the new phase and likely provided another candidate of bulk materials with monolayer behavior, apart from the newly discovered $ReS_2$ [174].

## 8.5 Summary

The new ground state of $Cu_2Se$, typified by Se-Cu-Cu-Cu-Cu-Se sextuple layers, has been newly identified using *ab initio* calculations. Upon cool down to liquid nitrogen temperatures, the transport property measurements along with the structural analyses have confirmed the existence of yet another phase transition of possible CDW character. The unusual manifestation of the WAL-type of MR profile at liquid helium temperatures indicates the quantum nature of such newly discovered phase of $Cu_2Se$, which may promote further interest in this surprising member system of transition metal chalcogenides.

# CHAPTER 9

# CONCLUDING REMARKS AND OUTLOOK

Combining advanced thermo-galvanomagnetic transport measurement techniques and state-of-the-art *ab initio* theoretical simulation approaches, I have explored fundamental structure-property relations in various condensed matter systems, including $Mg_2Si_{1-x}Sn_x$ solid solutions, Ge/Te double substituted skutterudites, Group III element doped $Bi_2Te_3$ single crystals, ZnTe:N and $Bi_2Te_3$ molecular beam epitaxy (MBE) films, and $Cu_2Se$ based polycrystalline structures. Additional studies concerning the thermoelectric performance of $FeSb_2Te$, GeTe, half Heusler alloys, natural tetrahedrite materials, as well as GaAs based thin films are included in my publication list in APPENDIX B.

I have provided strategies for improving the performance of novel thermoelectric materials. The unique applicability of the single parabolic band (SPB) model in describing the transport properties of $Mg_2Si_{0.3}Sn_{0.7}$ solid solutions has led to a better understanding of the scattering mechanisms governing their excellent power factors. The modeling effort has also resulted in a deeper insight toward further optimization of the thermoelectric performance of *n*-type $Mg_2Si_{1-x}Sn_x$ solid solutions. The Ge/Te double substitution strategy in $CoSb_3$ has been confirmed, both theoretically and experimentally, to be a very effective route of reducing the lattice thermal conductivity of skutterudites which may further enhance their *ZT* values, particularly if successfully combined with the existing paradigm of filling the intrinsic voids in skutterudite structure.

I have investigated the thermoelectric transport properties of various MBE-grown films. The study of electronic properties in ZnTe based MBE films have shown improved power factor upon proper nitrogen doping. Thermopower measurements at liquid helium temperatures have discovered extraordinary large phonon-drag Seebeck peak, leaving also a clear imprint on the electrical resistivity profile, which has rarely been observed before. Furthermore, the understanding of phonon drag phenomena has been deepened via our experimental efforts with $Bi_2Te_3$ MBE thin films grown on sapphire (0001) and $BaF_2$ (111) substrates. For the first time, tunable phonon-drag peak positions have been established via the choice of substrates with different Debye temperatures.

I have proposed the studies of $Bi_{2-x}A_xTe_3$ single crystals using Group III element A (= Tl or In) as a dopant, in line with worldwide efforts of achieving bulk insulating states in such a topological insulator. Low temperature transport measurements have shown that Group III doping can indeed gradually shift the Fermi level. Moreover, proper doping of $x = 0.10$ ($x = 0.20$) for Tl (In) can pin down the Fermi level in the band gap, resulting a predominant non-metallic electrical resistivity profile. These efforts offered means of detection of transport properties associated with the surface states.

I have applied the combined theoretical and experimental tools in the study of low temperature structure and properties of $Cu_2Se$. I predicted a new layered ground state structure which shows unexpected weak anti-localization features in its magnetoresistance.

In summary, I trust the unique approach combining experimental and theoretical techniques will keep providing insights into properties of promising thermoelectric materials. The significant improvement of the crystalline quality of II-VI films should lead to more exciting studies in the future. While the development of novel thermoelectric materials is still very challenging, it is full of surprises, exciting discoveries, and hope that thermoelectric energy conversion will make a meaningful contribution to sustainable utilization of energy.

# APPENDIX A

# ADDITIONAL NOTES ON TRANSPORT COEFFICIENT

## A.1 Kinetic coefficient matrix L

The block kinetic coefficient matrix **L** in Eq. (2.6) can be partitioned,

$$\mathbf{L} \equiv \begin{bmatrix} L_{11} & L_{12} & L_{13} & L_{14} \\ L_{12} & L_{22} & L_{14} & L_{24} \\ -L_{13} & -L_{14} & L_{11} & L_{12} \\ -L_{14} & -L_{24} & L_{12} & L_{22} \end{bmatrix} \equiv \begin{bmatrix} \mathbf{L}_{1,1} & \mathbf{L}_{1,2} \\ -\mathbf{L}_{1,2} & \mathbf{L}_{1,1} \end{bmatrix}, \tag{A.1}$$

where

$$\mathbf{L}_{1,1} = \mathbf{L}_{12;12} = \begin{bmatrix} L_{11} & L_{12} \\ L_{12} & L_{22} \end{bmatrix}, \mathbf{L}_{1,2} = \mathbf{L}_{12;34} = \begin{bmatrix} L_{13} & L_{14} \\ L_{14} & L_{24} \end{bmatrix}, \tag{A.2}$$

are symmetric. The indexes *i* (*j*) in the $\mathbf{L}_{i;j}$ specify the rows (columns) of the **L** matrix that are kept in the submatrix. Such matrix notation may become useful in the further investigation the isotropic assumption is relaxed. Typical matrices are given by

$$\begin{aligned} \det \mathbf{L}_{12;13} &= \det \begin{bmatrix} L_{11} & L_{13} \\ L_{12} & L_{14} \end{bmatrix} = L_{11}L_{14} - L_{12}L_{13}, \\ \det \mathbf{L}_{13;13} &= \det \begin{bmatrix} L_{11} & L_{13} \\ -L_{13} & L_{11} \end{bmatrix} = L_{11}^2 + L_{13}^2, \\ \det \mathbf{L}_{13;14} &= \det \begin{bmatrix} L_{11} & L_{14} \\ -L_{13} & L_{12} \end{bmatrix} = L_{11}L_{12} + L_{13}L_{14}, \\ \det \mathbf{L}_{12;23} &= \det \begin{bmatrix} L_{12} & L_{13} \\ L_{22} & L_{14} \end{bmatrix} = L_{12}L_{14} - L_{13}L_{22}, \end{aligned} \tag{A.3}$$

and

$$\det \mathbf{L}_{22}^{m} = \det \mathbf{L}_{134;134} = \det \begin{bmatrix} L_{11} & L_{13} & L_{14} \\ -L_{13} & L_{11} & L_{12} \\ -L_{14} & L_{12} & L_{22} \end{bmatrix},$$

$$\det \mathbf{L}_{42}^{m} = \det \mathbf{L}_{123;134} = \det \begin{bmatrix} L_{11} & L_{13} & L_{14} \\ L_{12} & L_{14} & L_{24} \\ -L_{13} & L_{11} & L_{12} \end{bmatrix} = -\det \mathbf{L}_{134;123} = -\det \mathbf{L}_{24}^{m}, \qquad \text{(A.4)}$$

$$\det \mathbf{L}_{21}^{m} = \det \mathbf{L}_{134;234} = \det \begin{bmatrix} L_{12} & L_{13} & L_{14} \\ -L_{14} & L_{11} & L_{12} \\ -L_{24} & L_{12} & L_{22} \end{bmatrix} = \det \mathbf{L}_{234;134} = \det \mathbf{L}_{12}^{m}.$$

## A.2 Isothermal and adiabatic boundary conditions

The distinction between the isothermal and adiabatic effects arises because charge carriers do not have exactly the same energy and the applied magnetic field will deflect the faster moving carriers to a lesser extent than the slower moving carriers (recall $mv^2/r = qvB$ leads to $r = mv/qB$). This gives rise to a transverse thermal gradient which is measurable when the sample is thermally isolated, i.e., under adiabatic conditions. On the other hand, if the sample is in contact with a heat reservoir, the heat exchange with the reservoir will compensate for the non-uniformity of heat flow in the sample and the transverse thermal gradient disappears, i.e., isothermal conditions set in.

Let $x$ axis be the direction of the primary electric current density $J_{e,x}$ and/or heat current density $J_{q,x}$. There exist three equations: (1) regardless the definition or the boundary condition, no particle current flow is allowed in the perpendicular direction along the $y$ axis, $J_{e,y} = 0$; (2) since there is only one of the controllable parameters ($J_{e,x}$ and $\nabla_x T$) involved in the definition of a particular effect, set the irrelevant one to zero, i.e. $\nabla_x T = 0$ or $J_{e,x} = 0$; and (3) based on the type of boundary condition, select $\nabla_y T = 0$ (isothermal) or $J_{q,y} = 0$ (adiabatic).

## A.3 Thermo-galvanomagnetic coefficients

### 1. Electrical conductivity

The electrical conductivity $\sigma$ is defined as the electric current density $J_{e,x}$ per unit electrochemical potential gradient $E_x = -\nabla_x \mu / q$,

$$J_{e,x} = \sigma E_x. \tag{A.5}$$

In an isothermal system,

$$J_{e,y} = 0, \nabla_x T = 0, \nabla_y T = 0, \tag{A.6}$$

we have

$$\nabla_x \mu = -\frac{T}{q} \frac{L_{11}}{\det \mathbf{L}_{13;13}} J_{e,x}, \tag{A.7}$$

and

$$\sigma_i = \frac{J_{e,x}}{-\nabla_x \mu / q} = \frac{q^2}{T} \frac{\det \mathbf{L}_{13;13}}{L_{11}}. \tag{A.8}$$

Under adiabatic boundary condition,

$$J_{e,y} = 0, \nabla_x T = 0, J_{q,y} = 0, \tag{A.9}$$

we have

$$\begin{aligned} J_{e,x} &= qL_{11}\left(-\frac{1}{T}\nabla_x \mu\right) + qL_{13}\left(-\frac{1}{T}\nabla_y \mu\right) + qL_{14}\left(\nabla_y \frac{1}{T}\right), \\ 0 &= -L_{13}\left(-\frac{1}{T}\nabla_x \mu\right) + L_{11}\left(-\frac{1}{T}\nabla_y \mu\right) + L_{12}\left(\nabla_y \frac{1}{T}\right), \\ 0 &= -L_{14}\left(-\frac{1}{T}\nabla_x \mu\right) + L_{12}\left(-\frac{1}{T}\nabla_y \mu\right) + L_{22}\left(\nabla_y \frac{1}{T}\right), \end{aligned} \tag{A.10}$$

and

$$\sigma_a = \frac{J_{e,x}}{-\nabla_x \mu / q} = \frac{q^2}{T}\frac{\det \mathbf{L}_{134;134}}{\det \mathbf{L}_{12;12}}. \tag{A.11}$$

## 2. Thermal conductivity

The thermal conductivity $\kappa$ is defined as the heat current density $J_{q,x}$ per unit temperature gradient $-\nabla_x T$ ,

$$J_{q,x} = -\kappa \nabla_x T. \tag{A.12}$$

In an isothermal system,

$$J_{e,y} = 0, J_{e,x} = 0, \nabla_y T = 0, \tag{A.13}$$

we have

$$J_{q,x} = -\frac{1}{T^2}\frac{\det \mathbf{L}_{134;134}}{\det \mathbf{L}_{13;13}} \nabla_x T, \tag{A.14}$$

and

$$\kappa_i = \frac{J_{q,x}}{-\nabla_x T} = \frac{1}{T^2}\frac{\det \mathbf{L}_{134;134}}{\det \mathbf{L}_{13;13}}. \tag{A.15}$$

Under adiabatic boundary condition,

$$J_{e,y} = 0, J_{e,x} = 0, J_{q,y} = 0, \tag{A.16}$$

we have

$$\begin{aligned}
0 &= L_{11}\left(-\frac{1}{T}\nabla_x \mu\right) + L_{12}\left(\nabla_x \frac{1}{T}\right) + L_{13}\left(-\frac{1}{T}\nabla_y \mu\right) + L_{14}\left(\nabla_y \frac{1}{T}\right), \\
J_{q,x} &= L_{12}\left(-\frac{1}{T}\nabla_x \mu\right) + L_{22}\left(\nabla_x \frac{1}{T}\right) + L_{14}\left(-\frac{1}{T}\nabla_y \mu\right) + L_{24}\left(\nabla_y \frac{1}{T}\right), \\
0 &= -L_{13}\left(-\frac{1}{T}\nabla_x \mu\right) - L_{14}\left(\nabla_x \frac{1}{T}\right) + L_{11}\left(-\frac{1}{T}\nabla_y \mu\right) + L_{12}\left(\nabla_y \frac{1}{T}\right), \\
0 &= -L_{14}\left(-\frac{1}{T}\nabla_x \mu\right) - L_{24}\left(\nabla_x \frac{1}{T}\right) + L_{12}\left(-\frac{1}{T}\nabla_y \mu\right) + L_{22}\left(\nabla_y \frac{1}{T}\right),
\end{aligned} \tag{A.17}$$

and

$$\kappa_a = \frac{J_{q,x}}{-\nabla_x T} = \frac{1}{T^2}\frac{\det \mathbf{L}}{\det \mathbf{L}_{134;134}}. \quad \text{(A.18)}$$

### 3. Seebeck effect

The Seebeck coefficient $\alpha$ is defined as the electrochemical potential gradient $E_x = -\nabla_x \mu / q$ per unit temperature gradient $\nabla_x T$ ,

$$E_x = \alpha \nabla_x T. \quad \text{(A.19)}$$

In an isothermal system,

$$J_{e,y} = 0, J_{e,x} = 0, \nabla_y T = 0, \quad \text{(A.20)}$$

we have

$$\nabla_x \mu = -\frac{1}{T}\frac{\det \mathbf{L}_{13;14}}{\det \mathbf{L}_{13;13}}\nabla_x T, \quad \text{(A.21)}$$

and

$$\alpha_i = \frac{-\nabla_x \mu / q}{\nabla_x T} = \frac{1}{qT}\frac{\det \mathbf{L}_{13;14}}{\det \mathbf{L}_{13;13}}. \quad \text{(A.22)}$$

Under adiabatic boundary condition,

$$J_{e,y} = 0, J_{e,x} = 0, J_{q,y} = 0, \quad \text{(A.23)}$$

we have

$$\begin{aligned}
0 &= L_{11}\left(-\frac{1}{T}\nabla_x \mu\right) + L_{12}\left(\nabla_x \frac{1}{T}\right) + L_{13}\left(-\frac{1}{T}\nabla_y \mu\right) + L_{14}\left(\nabla_y \frac{1}{T}\right), \\
J_{q,x} &= L_{12}\left(-\frac{1}{T}\nabla_x \mu\right) + L_{22}\left(\nabla_x \frac{1}{T}\right) + L_{14}\left(-\frac{1}{T}\nabla_y \mu\right) + L_{24}\left(\nabla_y \frac{1}{T}\right), \\
0 &= -L_{13}\left(-\frac{1}{T}\nabla_x \mu\right) - L_{14}\left(\nabla_x \frac{1}{T}\right) + L_{11}\left(-\frac{1}{T}\nabla_y \mu\right) + L_{12}\left(\nabla_y \frac{1}{T}\right), \\
0 &= -L_{14}\left(-\frac{1}{T}\nabla_x \mu\right) - L_{24}\left(\nabla_x \frac{1}{T}\right) + L_{12}\left(-\frac{1}{T}\nabla_y \mu\right) + L_{22}\left(\nabla_y \frac{1}{T}\right),
\end{aligned} \quad \text{(A.24)}$$

and

$$\alpha_a = \frac{-\nabla_x \mu / q}{\nabla_x T} = \frac{1}{qT} \frac{\det \mathbf{L}_{134;234}}{\det \mathbf{L}_{134;134}}. \tag{A.25}$$

**4. Peltier effect**

The Peltier coefficient $\pi$ is defined as the heat current density $J_{q,x}$ per unit electric current density $J_{e,x}$,

$$J_{q,x} = \pi J_{e,x}. \tag{A.26}$$

In an isothermal system,

$$J_{e,y} = 0, \nabla_x T = 0, \nabla_y T = 0, \tag{A.27}$$

we have

$$J_{q,x} = \frac{1}{q} \frac{\det \mathbf{L}_{13;14}}{\det \mathbf{L}_{13;13}} J_{e,x} \tag{A.28}$$

and

$$\pi_i = \frac{J_{q,x}}{J_{e,x}} = \frac{1}{q} \frac{\det \mathbf{L}_{13;14}}{\det \mathbf{L}_{13;13}}. \tag{A.29}$$

Under adiabatic boundary condition,

$$J_{e,y} = 0, \nabla_x T = 0, J_{q,y} = 0, \tag{A.30}$$

we have

$$\begin{aligned}
J_{e,x} &= qL_{11}\left(-\frac{1}{T}\nabla_x \mu\right) + qL_{13}\left(-\frac{1}{T}\nabla_y \mu\right) + qL_{14}\left(\nabla_y \frac{1}{T}\right), \\
J_{q,x} &= L_{12}\left(-\frac{1}{T}\nabla_x \mu\right) + L_{14}\left(-\frac{1}{T}\nabla_y \mu\right) + L_{24}\left(\nabla_y \frac{1}{T}\right), \\
0 &= -L_{13}\left(-\frac{1}{T}\nabla_x \mu\right) + L_{11}\left(-\frac{1}{T}\nabla_y \mu\right) + L_{12}\left(\nabla_y \frac{1}{T}\right), \\
0 &= -L_{14}\left(-\frac{1}{T}\nabla_x \mu\right) + L_{12}\left(-\frac{1}{T}\nabla_y \mu\right) + L_{22}\left(\nabla_y \frac{1}{T}\right),
\end{aligned} \tag{A.31}$$

and

$$\pi_a = \frac{J_{q,x}}{J_{e,x}} = \frac{\det \mathbf{L}_{234;134}}{q \det \mathbf{L}_{134;134}} = \frac{1}{q} \frac{\det \mathbf{L}_{134;234}}{\det \mathbf{L}_{134;134}}. \tag{A.32}$$

The relation $\pi = T\alpha$ naturally holds for both isothermal and adiabatic cases.

The magnetic field dependence in the above mentioned effects come in from that of $L_{ij}$, and in the effects described below, $\boldsymbol{B} = B_z \hat{e}_z$ goes directly into the definition.

**5. Hall effect**

The Hall coefficient $R_H$ is defined as the transverse electrochemical potential gradient $E_y = -\nabla_y \mu / q$ per unit electric current density $J_{e,x}$ in the presence of a perpendicular magnetic field $B_z$,

$$E_y = R_H J_{e,x} B_z. \tag{A.33}$$

In an isothermal system,

$$J_{e,y} = 0, \nabla_x T = 0, \nabla_y T = 0, \tag{A.34}$$

we have

$$\nabla_y \mu = -\frac{T}{q} \frac{L_{13}}{\det \mathbf{L}_{13;13}} J_{e,x}, \tag{A.35}$$

and

$$R_{H,i} = \frac{-\nabla_y \mu / q}{J_{e,x} B_z} = \frac{T}{q^2 B_z} \frac{L_{13}}{\det \mathbf{L}_{13;13}}. \tag{A.36}$$

Under adiabatic boundary condition,

$$J_{e,y} = 0, \nabla_x T = 0, J_{q,y} = 0, \tag{A.37}$$

we have

$$\begin{aligned} J_{e,x} &= qL_{11}\left(-\frac{1}{T}\nabla_x\mu\right) + qL_{13}\left(-\frac{1}{T}\nabla_y\mu\right) + qL_{14}\left(\nabla_y\frac{1}{T}\right), \\ 0 &= -L_{13}\left(-\frac{1}{T}\nabla_x\mu\right) + L_{11}\left(-\frac{1}{T}\nabla_y\mu\right) + L_{12}\left(\nabla_y\frac{1}{T}\right), \\ 0 &= -L_{14}\left(-\frac{1}{T}\nabla_x\mu\right) + L_{12}\left(-\frac{1}{T}\nabla_y\mu\right) + L_{22}\left(\nabla_y\frac{1}{T}\right), \end{aligned} \tag{A.38}$$

and

$$R_{H,a} = \frac{-\nabla_y\mu/q}{J_{e,x}B_z} = \frac{T}{q^2B_z}\frac{-\det\mathbf{L}_{12;23}}{\det\mathbf{L}_{134;134}}. \tag{A.39}$$

## 6. Nernst effect

The Nernst coefficient $N$ is defined as the transverse electrochemical potential gradient $E_y = -\nabla_y\mu/q$ per unit temperature gradient $-\nabla_x T$ in the presence of a perpendicular magnetic field $B_z$,

$$E_y = -N\nabla_x TB_z. \tag{A.40}$$

In an isothermal system,

$$J_{e,y} = 0, J_{e,x} = 0, \nabla_y T = 0, \tag{A.41}$$

we have

$$\nabla_y\mu = \frac{1}{T}\frac{\det\mathbf{L}_{12;13}}{\det\mathbf{L}_{13;13}}\nabla_x T, \tag{A.42}$$

and

$$N_i = \frac{-\nabla_y\mu/q}{-\nabla_x TB_z} = \frac{1}{qTB_z}\frac{\det\mathbf{L}_{12;13}}{\det\mathbf{L}_{13;13}}. \tag{A.43}$$

Under adiabatic boundary condition,

$$J_{e,y} = 0, J_{e,x} = 0, J_{q,y} = 0, \tag{A.44}$$

we have

$$
\begin{aligned}
0 &= L_{11}\left(-\frac{1}{T}\nabla_x\mu\right)+L_{12}\left(\nabla_x\frac{1}{T}\right)+L_{13}\left(-\frac{1}{T}\nabla_y\mu\right)+L_{14}\left(\nabla_y\frac{1}{T}\right),\\
J_{q,x} &= L_{12}\left(-\frac{1}{T}\nabla_x\mu\right)+L_{22}\left(\nabla_x\frac{1}{T}\right)+L_{14}\left(-\frac{1}{T}\nabla_y\mu\right)+L_{24}\left(\nabla_y\frac{1}{T}\right),\\
0 &= -L_{13}\left(-\frac{1}{T}\nabla_x\mu\right)-L_{14}\left(\nabla_x\frac{1}{T}\right)+L_{11}\left(-\frac{1}{T}\nabla_y\mu\right)+L_{12}\left(\nabla_y\frac{1}{T}\right),\\
0 &= -L_{14}\left(-\frac{1}{T}\nabla_x\mu\right)-L_{24}\left(\nabla_x\frac{1}{T}\right)+L_{12}\left(-\frac{1}{T}\nabla_y\mu\right)+L_{22}\left(\nabla_y\frac{1}{T}\right),
\end{aligned}
\tag{A.45}
$$

and

$$
N_a = \frac{-\nabla_y\mu/q}{-\nabla_x TB_z} = \frac{1}{qTB_z}\frac{-\det\mathbf{L}_{134;124}}{\det\mathbf{L}_{134;134}}. \tag{A.46}
$$

The next two effects can only be observed under adiabatic conditions.

### 7. Ettingshausen effect

The Ettingshausen coefficient $P$ is defined as the transverse temperature gradient $-\nabla_y T$ per unit electric current density $J_{e,x}$ in the presence of a perpendicular magnetic field $B_z$,

$$
\nabla_y T = -PJ_{e,x}B_z, \tag{A.47}
$$

under adiabatic boundary condition,

$$
J_{e,y} = 0, \nabla_x T = 0, J_{q,y} = 0, \tag{A.48}
$$

where

$$
\begin{aligned}
J_{e,x} &= qL_{11}\left(-\frac{1}{T}\nabla_x\mu\right)+qL_{13}\left(-\frac{1}{T}\nabla_y\mu\right)+qL_{14}\left(\nabla_y\frac{1}{T}\right),\\
0 &= -L_{13}\left(-\frac{1}{T}\nabla_x\mu\right)+L_{11}\left(-\frac{1}{T}\nabla_y\mu\right)+L_{12}\left(\nabla_y\frac{1}{T}\right),\\
0 &= -L_{14}\left(-\frac{1}{T}\nabla_x\mu\right)+L_{12}\left(-\frac{1}{T}\nabla_y\mu\right)+L_{22}\left(\nabla_y\frac{1}{T}\right),
\end{aligned}
\tag{A.49}
$$

and

$$P = \frac{-\nabla_y T}{J_{e,x} B_z} = \frac{T^2 \det \mathbf{L}_{34;13}}{B_z q \det \mathbf{L}_{134;134}} = \frac{T^2}{qB_z} \frac{\det \mathbf{L}_{12;13}}{\det \mathbf{L}_{134;134}}. \tag{A.50}$$

## 8. Righi-Leduc effect

The Righi-Leduc coefficient $L$ is defined as the transverse temperature gradient $-\nabla_y T$ per unit temperature gradient $-\nabla_x T$ in the presence of a perpendicular magnetic field $B_z$,

$$-\nabla_y T = L(-\nabla_x T)B_z, \tag{A.51}$$

under adiabatic boundary condition,

$$J_{e,y} = 0, J_{e,x} = 0, J_{q,y} = 0, \tag{A.52}$$

where

$$\begin{aligned}
0 &= L_{11}\left(-\frac{1}{T}\nabla_x \mu\right) + L_{12}\left(\nabla_x \frac{1}{T}\right) + L_{13}\left(-\frac{1}{T}\nabla_y \mu\right) + L_{14}\left(\nabla_y \frac{1}{T}\right), \\
J_{q,x} &= L_{12}\left(-\frac{1}{T}\nabla_x \mu\right) + L_{22}\left(\nabla_x \frac{1}{T}\right) + L_{14}\left(-\frac{1}{T}\nabla_y \mu\right) + L_{24}\left(\nabla_y \frac{1}{T}\right), \\
0 &= -L_{13}\left(-\frac{1}{T}\nabla_x \mu\right) - L_{14}\left(\nabla_x \frac{1}{T}\right) + L_{11}\left(-\frac{1}{T}\nabla_y \mu\right) + L_{12}\left(\nabla_y \frac{1}{T}\right), \\
0 &= -L_{14}\left(-\frac{1}{T}\nabla_x \mu\right) - L_{24}\left(\nabla_x \frac{1}{T}\right) + L_{12}\left(-\frac{1}{T}\nabla_y \mu\right) + L_{22}\left(\nabla_y \frac{1}{T}\right),
\end{aligned} \tag{A.53}$$

and

$$L = \frac{-\nabla_y T}{-\nabla_x T B_z} = \frac{1}{B_z} \frac{\det \mathbf{L}_{134;123}}{\det \mathbf{L}_{134;134}}. \tag{A.54}$$

By examining the above 14 coefficients, we have the 8 relations, with the first two being the Kelvin relation connecting Peltier effect and Seebeck effect,

$$\begin{aligned}
\pi_i &= T\alpha_i, \\
\pi_a &= T\alpha_a,
\end{aligned} \tag{A.55}$$

the third one is known as the Bridgman relation,

$$TN_i = \kappa_i P, \tag{A.56}$$

and the other five relations first shown by Putley,[6]

$$\begin{aligned} &\sigma_i^{-1} - \sigma_a^{-1} = B_z^2 P N_i, \\ &\kappa_i - \kappa_a = -B_z^2 \kappa_i L^2, \\ &R_{H,i} - R_{H,a} = P\alpha_i, \\ &N_i - N_a = L\alpha_i, \\ &\alpha_i - \alpha_a = -B_z^2 N_i L. \end{aligned} \tag{A.57}$$

All the thermo-galvanomagnetic coefficients are summarized in Table 2-1. This concludes the discussion regarding thermo-galvanomagnetic transport coefficients using the Onsager's kinetic relations.

### A.4 Solution to the Boltzmann transport equation

In order to evaluate the kinetic coefficients $L_{ij}$, we now solve the Boltzmann transport equation under the relaxation time approximation. The equilibrium Fermi-Dirac distribution of electron is given by,

$$f_0 = \frac{1}{e^{(\varepsilon-\mu_c)/k_B T}+1} = \frac{1}{e^x+1}, \ x = (\varepsilon - \mu_c)/k_B T. \tag{A.58}$$

Energy $\varepsilon$ and $\mu_c$ are measured from the band edge [conduction (valence) band minimum (maximum) $E_C$ ($E_V$) for electron (hole)]. This reference system essentially sets $E_C$ ($E_V$) = 0 at different locations (although the absolute value measured from a global reference system varies at different location). The same quantum state $\boldsymbol{k} = (k_x, k_y, k_z)$ has the same energy at different locations,

$$\varepsilon(\boldsymbol{k}) = \tilde{\varepsilon}(\boldsymbol{k}) - E_C = \frac{\hbar^2}{2m_s^*}\left(k_x^2 + k_y^2 + k_z^2\right), \tag{A.59}$$

where $m_s^*$ is the effective mass for a single carrier in a single band/valley.

Hence in such a reference system,

$$\nabla \varepsilon(\boldsymbol{k}) = 0, \tag{A.60}$$

and

$$\nabla x = \nabla\left(\frac{\varepsilon - \mu_c}{k_B T}\right) = \frac{1}{k_B T}\left(\nabla \varepsilon - \nabla \mu_c\right) - \frac{\varepsilon - \mu_c}{k_B T^2}\nabla T = -\frac{1}{k_B T}\nabla \mu_c - \frac{\varepsilon - \mu_c}{k_B T^2}\nabla T. \tag{A.61}$$

Various derivatives of $f_0$ are thus given by,

$$\begin{aligned}
&\frac{\partial f_0}{\partial \varepsilon} = \frac{df_0}{dx}\frac{\partial x}{\partial \varepsilon} = \frac{df_0}{dx}\frac{1}{k_B T}, or\ \frac{df_0}{dx} = k_B T\frac{\partial f_0}{\partial \varepsilon}, \\
&\frac{\partial f_0}{\partial \boldsymbol{r}} = \nabla f_0 = \frac{df_0}{dx}\nabla x = k_B T\frac{\partial f_0}{\partial \varepsilon}\left[-\frac{1}{k_B T}\nabla \mu_c - \frac{\varepsilon - \mu_c}{k_B T^2}\nabla T\right] \\
&= -\frac{\partial f_0}{\partial \varepsilon}\left[\nabla \mu_c + \frac{\varepsilon - \mu_c}{T}\nabla T\right],
\end{aligned} \tag{A.62}$$

and

$$\begin{aligned}
&\frac{\partial f_0}{\partial \boldsymbol{v}} = \nabla_v f_0 = \frac{\partial f_0}{\partial \varepsilon}\nabla_v \varepsilon = \frac{\partial f_0}{\partial \varepsilon} m_s^* \boldsymbol{v}, \\
&\varepsilon = p^2/2m_s^* = m_s^* v^2/2, \nabla_{\vec{v}} \varepsilon = m_s^* \boldsymbol{v}.
\end{aligned} \tag{A.63}$$

There are some additional very useful relations of the Fermi-Dirac distribution function

$$f_0 = \frac{1}{e^{(\varepsilon - \mu_c)/k_B T} + 1} = \frac{1}{e^{\xi - \eta} + 1}, \xi = \varepsilon / k_B T, \eta = \mu_c / k_B T. \tag{A.64}$$

The Fermi-Dirac integral $F_n(\eta)$ is defined as

$$F_n(\eta) = \int_0^\infty f_0(\xi, \eta)\xi^n d\xi = \int_0^\infty \frac{1}{e^{\xi - \eta} + 1}\xi^n d\xi, \tag{A.65}$$

which, for $n = 0$, is simplified to

$$F_0(\eta) = \ln\left(1 + e^\eta\right). \tag{A.66}$$

Note that,

$$\int_{\varepsilon=0}^{\infty} f_0(\varepsilon,\mu_c)\varepsilon^n d\varepsilon = (k_B T)^{n+1}\int_0^{\infty} f_0(\xi,\eta)\xi^n d\xi = (k_B T)^{n+1} F_n(\eta), \tag{A.67}$$

and

$$\int_{\varepsilon=0}^{\infty} \frac{\partial f_0}{\partial \varepsilon}\varepsilon^s d\varepsilon = f_0\varepsilon^s\Big|_{\varepsilon=0}^{\infty} - s\int_{\varepsilon=0}^{\infty} f_0\varepsilon^{s-1}d\varepsilon = -s\int_{\varepsilon=0}^{\infty} f_0\varepsilon^{s-1}d\varepsilon = -s(k_B T)^s F_{s-1}(\eta). \tag{A.68}$$

The Boltzmann transport equation with relaxation time approximation under small electric field, temperature gradient, and concentration gradient (chemical potential gradient), i.e., $|f - f_0| << f_0$, is given by

$$\frac{\partial f}{\partial t} + \boldsymbol{v}\cdot\frac{\partial}{\partial \boldsymbol{r}} f + \frac{q}{m_s^*}(\boldsymbol{E} + \boldsymbol{v}\times\boldsymbol{B})\cdot\frac{\partial f}{\partial \boldsymbol{v}} = -\frac{f - f_0}{\tau}, \tag{A.69}$$

where the scattering mean-free time $\tau$ generally depends on energy,

$$\tau = \tau_0\varepsilon^r = \tau_0(k_B T)^r \xi^r. \tag{A.70}$$

In cases where the mean-free path $\ell$ is independent of energy (MFPIE),

$$\tau^{MFPIE} = \ell / v = \ell / (2\varepsilon / m_s^*)^{1/2} = (m_s^* / 2)^{1/2}\ell\cdot\varepsilon^{-1/2}, \tag{A.71}$$

so $\tau_0 = (m_s^*/2)^{1/2}\ell, r = -1/2$.

For steady state, $\partial f/\partial t \sim 0$, an *ad hoc* solution of $f$ is given by

$$f = f_0 - \boldsymbol{v}\cdot\boldsymbol{C}(\varepsilon)\frac{\partial f_0}{\partial \varepsilon}, \tag{A.72}$$

and

$$\begin{aligned}
&\boldsymbol{v}\cdot\frac{\partial}{\partial \boldsymbol{r}} f = \boldsymbol{v}\cdot\nabla f \approx \boldsymbol{v}\cdot\nabla f_0 = \boldsymbol{v}\cdot\left\{-\left[\nabla\mu_c + \frac{\varepsilon-\mu_c}{T}\nabla T\right]\frac{\partial f_0}{\partial \varepsilon}\right\},\\
&\frac{q}{m_s^*}\boldsymbol{E}\cdot\frac{\partial f}{\partial \boldsymbol{v}} \approx \frac{q}{m_s^*}\boldsymbol{E}\cdot\frac{\partial f_0}{\partial \boldsymbol{v}} = \frac{q}{m_s^*}\boldsymbol{E}\cdot\left[\frac{\partial f_0}{\partial \varepsilon}m_s^*\boldsymbol{v}\right] = \boldsymbol{v}\cdot\left\{q\boldsymbol{E}\frac{\partial f_0}{\partial \varepsilon}\right\},\\
&\frac{q}{m_s^*}(\boldsymbol{v}\times\boldsymbol{B})\cdot\frac{\partial f}{\partial \boldsymbol{v}} = \frac{q}{m_s^*}(\boldsymbol{v}\times\boldsymbol{B})\cdot\left[-\boldsymbol{C}(\varepsilon)\frac{\partial f_0}{\partial \varepsilon}\right] = \boldsymbol{v}\cdot\left\{-\frac{q}{m_s^*}[\boldsymbol{B}\times\boldsymbol{C}(\varepsilon)]\frac{\partial f_0}{\partial \varepsilon}\right\}.
\end{aligned} \tag{A.73}$$

Hence

$$\boldsymbol{v}\cdot\left\{-\left[\nabla\mu_c+\frac{\varepsilon-\mu_c}{T}\nabla T\right]+q\boldsymbol{E}-\frac{q}{m_s^*}\left[\boldsymbol{B}\times\boldsymbol{C}(\varepsilon)\right]\right\}=\frac{1}{\tau}\boldsymbol{v}\cdot\boldsymbol{C}(\varepsilon). \tag{A.74}$$

Considering the arbitrary choice of ***v***,

$$-\left[\nabla\mu_c+\frac{\varepsilon-\mu_c}{T}\nabla T\right]+q\boldsymbol{E}-\frac{q}{m_s^*}\left[\boldsymbol{B}\times\boldsymbol{C}(\varepsilon)\right]=\frac{1}{\tau}\boldsymbol{C}(\varepsilon). \tag{A.75}$$

If all electric fields and temperature gradients are in the *x*, *y* plane and the applied magnetic field is in *z*-direction $\boldsymbol{B}=B_z\hat{e}_z$, we have

$$\begin{aligned}-\tau\left[\nabla_x\mu+\frac{\varepsilon-\mu_c}{T}\nabla_x T\right]+\tau qE_x+\frac{q\tau}{m_s^*}B_zC_y&=C_x,\\ -\tau\left[\nabla_y\mu+\frac{\varepsilon-\mu_c}{T}\nabla_y T\right]+\tau qE_y-\frac{q\tau}{m_s^*}B_zC_x&=C_y,\end{aligned} \tag{A.76}$$

which is, noting electrochemical potential $\mu=\mu_c+q\varphi_e$,

$$\begin{aligned}C_x-\frac{q\tau}{m_s^*}B_zC_y&=-\tau\left[\nabla_x\mu+\frac{\varepsilon-\mu_c}{T}\nabla_x T\right],\\ \frac{q\tau}{m_s^*}B_zC_x+C_y&=-\tau\left[\nabla_y\mu+\frac{\varepsilon-\mu_c}{T}\nabla_y T\right].\end{aligned} \tag{A.77}$$

Thus,

$$\begin{aligned}C_x&=\frac{\alpha+\gamma\cdot\beta}{1+\gamma^2},\\ C_y&=\frac{\beta-\gamma\cdot\alpha}{1+\gamma^2},\end{aligned} \tag{A.78}$$

where

$$
\begin{aligned}
\alpha &\equiv -\tau\left(\nabla_x\mu + \frac{\varepsilon-\mu_c}{T}\nabla_x T\right), \\
\beta &\equiv -\tau\left(\nabla_y\mu + \frac{\varepsilon-\mu_c}{T}\nabla_y T\right), \\
\gamma &\equiv \frac{q\tau}{m_s^*}B_z = \pm\omega_c\tau,\ \omega_c \equiv \frac{eB_z}{m_s^*}.
\end{aligned}
\tag{A.79}
$$

Overall, the distribution function of electron *f*,

$$f = f_0 - \left(v_x C_x + v_y C_y\right)\frac{\partial f_0}{\partial\varepsilon}. \tag{A.80}$$

and the number of electron per unit volume with energy between $\varepsilon$ and $\varepsilon + d\varepsilon$ is

$$dn = fD(\varepsilon)d\varepsilon. \tag{A.81}$$

The electron density of states per unit volume $D(\varepsilon)$ for a three dimensional (3D) crystal with $N_v$ fold degenerated parabolic band (thus the density-of-states effective mass $m_d^* = N_v^{2/3}m_s^*$) is given by, in various equivalent forms,

$$
\begin{aligned}
D(\varepsilon) &= \frac{m_d^*}{\pi^2\hbar^3}\left(2m_d^*\varepsilon\right)^{1/2} = \frac{\left(2m_d^*\right)^{3/2}}{2\pi^2\hbar^3}\varepsilon^{1/2} = 4\pi\left(\frac{2m_d^*}{h^2}\right)^{3/2}\varepsilon^{1/2} \\
&= \frac{4\pi\left(2m_d^*\right)^{3/2}}{h^3}\varepsilon^{1/2} = \frac{8\pi}{h^3}m_d^{*3/2}(2\varepsilon)^{1/2},
\end{aligned}
\tag{A.82}
$$

where $\hbar$ (= $h/2\pi$) is the Planck constant. It is derived from the following relation, for a single band designated as *s*,

$$
\begin{aligned}
dN_s &= \widetilde{D}_s(\boldsymbol{k})d\boldsymbol{k} = 2\cdot\frac{V}{(2\pi)^3}\cdot 4\pi k^2 dk = \frac{V}{\pi^2}\sqrt{\frac{2m_s^*\varepsilon}{\hbar^2}}\frac{m_s^*}{\hbar^2}d\varepsilon = \widetilde{D}_s(\varepsilon)d\varepsilon, \\
D_s(\varepsilon) &= \widetilde{D}_s(\varepsilon)/V,
\end{aligned}
\tag{A.83}
$$

noting

$$\frac{\hbar^2 k^2}{2m_s^*} = \varepsilon \rightarrow \begin{cases} \dfrac{\hbar^2}{m_s^*} k dk = d\varepsilon \\ k = \sqrt{\dfrac{2m_s^* \varepsilon}{\hbar^2}} \end{cases} . \tag{A.84}$$

The density-of-states effective mass $m_d^* = N_v^{2/3} m_s^*$, since

$$D = N_v D_s(\varepsilon) \propto N_v \left(m_s^*\right)^{3/2} \varepsilon^{1/2} = \left(N_v^{2/3} m_s^*\right)^{3/2} \varepsilon^{1/2} \equiv \left(m_d^*\right)^{3/2} \varepsilon^{1/2}. \tag{A.85}$$

Thus, the electron number current density $J_{n,x}$ is given by, noting $m_s^* v_x^2 / 2 = \varepsilon / 3$,

$$\begin{aligned} J_{n,x} &= \int_{\varepsilon=0}^{\infty} v_x f D(\varepsilon) d\varepsilon = \int_{\varepsilon=0}^{\infty} v_x \left[ f_0 - \left(v_x C_x + v_y C_y\right) \frac{\partial f_0}{\partial \varepsilon} \right] D(\varepsilon) d\varepsilon \\ &= -\int_{\varepsilon=0}^{\infty} v_x^2 C_x \frac{\partial f_0}{\partial \varepsilon} D(\varepsilon) d\varepsilon = \frac{2}{3m_s^*} \int_{\varepsilon=0}^{\infty} \frac{\partial f_0}{\partial \varepsilon} D(\varepsilon) \varepsilon (-C_x) d\varepsilon, \end{aligned} \tag{A.86}$$

the kinetic energy current density $J_{\varepsilon,x}$ is

$$\begin{aligned} J_{\varepsilon,x} &= \int_{0}^{\infty} \varepsilon v_x f D(\varepsilon) d\varepsilon = \int_{\varepsilon=0}^{\infty} \varepsilon v_x \left[ f_0 - \left(v_x C_x + v_y C_y\right) \frac{\partial f_0}{\partial \varepsilon} \right] D(\varepsilon) d\varepsilon \\ &= -\int_{\varepsilon=0}^{\infty} \varepsilon v_x^2 C_x \frac{\partial f_0}{\partial \varepsilon} D(\varepsilon) d\varepsilon = \frac{2}{3m_s^*} \int_{\varepsilon=0}^{\infty} \frac{\partial f_0}{\partial \varepsilon} D(\varepsilon) \varepsilon^2 (-C_x) d\varepsilon, \end{aligned} \tag{A.87}$$

the total energy current density $J_{u,x}$ is

$$J_{u,x} = \frac{2}{3m_s^*} \int_{\varepsilon=0}^{\infty} \frac{\partial f_0}{\partial \varepsilon} D(\varepsilon) (\varepsilon + q\varphi_e) \varepsilon (-C_x) d\varepsilon, \tag{A.88}$$

and the heat current density $J_{q,x}$ ($= J_{u,x} - \mu J_{n,x} = J_{\varepsilon,x} - \mu_c J_{n,x}$)is given by

$$J_{q,x} = \frac{2}{3m_s^*} \int_{\varepsilon=0}^{\infty} \frac{\partial f_0}{\partial \varepsilon} D(\varepsilon) \varepsilon (\varepsilon - \mu_c)(-C_x) d\varepsilon. \tag{A.89}$$

Combining similar expressions along $y$ axis,

$$\begin{aligned} J_{n,x} &= \frac{2}{3m_s^*}\int_{\varepsilon=0}^{\infty}\frac{\partial f_0}{\partial \varepsilon}D(\varepsilon)\varepsilon(-C_x)d\varepsilon, \\ J_{q,x} &= \frac{2}{3m_s^*}\int_{\varepsilon=0}^{\infty}\frac{\partial f_0}{\partial \varepsilon}D(\varepsilon)\varepsilon(\varepsilon-\mu_c)(-C_x)d\varepsilon, \\ J_{n,y} &= \frac{2}{3m_s^*}\int_{\varepsilon=0}^{\infty}\frac{\partial f_0}{\partial \varepsilon}D(\varepsilon)\varepsilon(-C_y)d\varepsilon, \\ J_{q,y} &= \frac{2}{3m_s^*}\int_{\varepsilon=0}^{\infty}\frac{\partial f_0}{\partial \varepsilon}D(\varepsilon)\varepsilon(\varepsilon-\mu_c)(-C_y)d\varepsilon. \end{aligned} \tag{A.90}$$

Using the ***C*** coefficients, we have

$$\begin{aligned} J_{n,x} &= L_{11}\left(-\frac{1}{T}\nabla_x\mu\right)+L_{12}\left(\nabla_x\frac{1}{T}\right)+L_{13}\left(-\frac{1}{T}\nabla_y\mu\right)+L_{14}\left(\nabla_y\frac{1}{T}\right), \\ J_{q,x} &= L_{12}\left(-\frac{1}{T}\nabla_x\mu\right)+L_{22}\left(\nabla_x\frac{1}{T}\right)+L_{14}\left(-\frac{1}{T}\nabla_y\mu\right)+L_{24}\left(\nabla_y\frac{1}{T}\right), \\ J_{n,y} &= -L_{13}\left(-\frac{1}{T}\nabla_x\mu\right)-L_{14}\left(\nabla_x\frac{1}{T}\right)+L_{11}\left(-\frac{1}{T}\nabla_y\mu\right)+L_{12}\left(\nabla_y\frac{1}{T}\right), \\ J_{q,y} &= -L_{14}\left(-\frac{1}{T}\nabla_x\mu\right)-L_{24}\left(\nabla_x\frac{1}{T}\right)+L_{12}\left(-\frac{1}{T}\nabla_y\mu\right)+L_{22}\left(\nabla_y\frac{1}{T}\right), \end{aligned} \tag{A.91}$$

where

$$\begin{aligned} &L_{11}=\mathcal{K}_1, L_{12}=\mathcal{K}_2-\mu_c\mathcal{K}_1, L_{13}=\mathcal{H}_1, L_{14}=\mathcal{H}_2-\mu_c\mathcal{H}_1, \\ &L_{22}=\mathcal{K}_3-2\mu_c\mathcal{K}_2+\mu_c^2\mathcal{K}_1, L_{24}=\mathcal{H}_3-2\mu_c\mathcal{H}_2+\mu_c^2\mathcal{H}_1, \end{aligned} \tag{A.92}$$

and

$$\begin{aligned} \mathcal{H}_i &\equiv \frac{2T}{3m_s^*}\int_{\varepsilon=0}^{\infty}\left(-\frac{\partial f_0}{\partial \varepsilon}\right)D(\varepsilon)\frac{\varepsilon^i\gamma\tau}{1+\gamma^2}d\varepsilon, \\ \mathcal{K}_i &\equiv \frac{2T}{3m_s^*}\int_{\varepsilon=0}^{\infty}\left(-\frac{\partial f_0}{\partial \varepsilon}\right)D(\varepsilon)\frac{\varepsilon^i\tau}{1+\gamma^2}d\varepsilon. \end{aligned} \tag{A.93}$$

In the low field approximation, $\gamma \ll 1$,

$$\begin{aligned}
\mathcal{H}_i \overset{\gamma<<1}{\rightarrow} H_i &\equiv \frac{2T}{3m_s^*}\int_{\varepsilon=0}^{\infty}\left(-\frac{\partial f_0}{\partial \varepsilon}\right)D(\varepsilon)\varepsilon^i\gamma\tau d\varepsilon \\
&= \frac{2T}{3m_s^*}\frac{4\pi\left(2m_d^*\right)^{3/2}}{h^3}\frac{qB_z}{m_s^*}\tau_0^2\left(i+2r+\tfrac{1}{2}\right)\left(k_BT\right)^{i+2r+\frac{1}{2}}F_{i+2r-\frac{1}{2}}(\eta), \\
\mathcal{K}_i \overset{\gamma<<1}{\rightarrow} K_i &\equiv \frac{2T}{3m_s^*}\int_{\varepsilon=0}^{\infty}\left(-\frac{\partial f_0}{\partial \varepsilon}\right)D(\varepsilon)\varepsilon^i\tau d\varepsilon \\
&= \frac{2T}{3m_s^*}\frac{4\pi\left(2m_d^*\right)^{3/2}}{h^3}\tau_0\left(i+r+\tfrac{1}{2}\right)\left(k_BT\right)^{i+r+\frac{1}{2}}F_{i+r-\frac{1}{2}}(\eta).
\end{aligned} \tag{A.94}$$

Now, using Fermi-Dirac statistics and all the thermo-galvanomagnetic transport coefficients defined from Onsager's relations, we can explicitly express them in terms of Fermi-Dirac integrals.

**Carrier density**

The carrier density *n* is given by

$$n = \int_{\varepsilon=0}^{\infty} f_0(\varepsilon)D(\varepsilon)d\varepsilon = \frac{4\pi\left(2m_d^*\right)^{3/2}}{h^3}\int_{\varepsilon=0}^{\infty} f_0(\varepsilon)\varepsilon^{1/2}d\varepsilon = \frac{4\pi\left(2m_d^*k_BT\right)^{3/2}}{h^3}F_{\frac{1}{2}}(\eta). \tag{A.95}$$

**Hall efffect**

The isothermal Hall coefficient $R_H$ is given by

$$\begin{aligned}
R_H &= \frac{T}{q^2B_z}\frac{L_{13}}{\det \mathbf{L}_{13;13}} = \frac{T}{q^2B_z}\frac{\mathcal{H}_1}{\mathcal{K}_1^2+\mathcal{H}_1^2} \overset{\gamma<<1}{\approx} \frac{T}{q^2B_z}\frac{H_1}{K_1^2} \\
&= \frac{3}{2q}\frac{h^3}{4\pi\left(2m_d^*k_BT\right)^{3/2}}\frac{\left(2r+\frac{3}{2}\right)}{\left(r+\frac{3}{2}\right)^2}\frac{F_{2r+\frac{1}{2}}(\eta)}{F_{r+\frac{1}{2}}^2(\eta)} \\
&= \frac{3}{2q}\frac{1}{n}\frac{\left(2r+\frac{3}{2}\right)}{\left(r+\frac{3}{2}\right)^2}\frac{F_{2r+\frac{1}{2}}(\eta)F_{\frac{1}{2}}(\eta)}{F_{r+\frac{1}{2}}^2(\eta)},
\end{aligned} \tag{A.96}$$

and the Hall (carrier) density $n_H$ is defined as

$$n_H \equiv \frac{1}{qR_H} = \frac{2}{3}\frac{\left(r+\frac{3}{2}\right)^2}{\left(2r+\frac{3}{2}\right)}\frac{4\pi\left(2m_d^*k_BT\right)^{3/2}}{h^3}\frac{F_{r+\frac{1}{2}}^2(\eta)}{F_{2r+\frac{1}{2}}(\eta)}. \tag{A.97}$$

Since the Hall coefficient $R_H$ (and thus the Hall density $n_H$) is an experimentally measurable quantity, we can practically estimate the “real” carrier density $n$ via Hall factor $r_H$,

$$n = r_H n_H, \tag{A.98}$$

with

$$r_H \equiv \frac{3}{2}\frac{\left(2r+\frac{3}{2}\right)}{\left(r+\frac{3}{2}\right)^2}\frac{F_{2r+\frac{1}{2}}(\eta)F_{\frac{1}{2}}(\eta)}{F_{r+\frac{1}{2}}^2(\eta)}. \tag{A.99}$$

If the mean-free path is independent of energy, recall that $\tau_0 = \ell\left(m^*/2\right)^{1/2}, r = -1/2$,

$$r_H^{MFPIE} \equiv \frac{3}{4}\frac{F_{-\frac{1}{2}}(\eta)F_{\frac{1}{2}}(\eta)}{F_0^2(\eta)}. \tag{A.100}$$

**Electrical conductivity**

The isothermal electrical conductivity $\sigma$ (reversely proportional to the electrical resistivity $\rho$, $\rho = 1/\sigma$) is given by

$$\begin{aligned}\sigma &= \frac{q^2}{T}\frac{\det \mathbf{L}_{13;13}}{L_{11}} = \frac{q^2}{T}\frac{\mathcal{K}_1^{\ 2}+\mathcal{H}_1^{\ 2}}{\mathcal{K}_1} \overset{\gamma<<1}{\approx} \frac{q^2}{T}K_1 \\ &= \frac{8\pi\left(2m_d^*\right)^{3/2}}{3h^3}\frac{q^2\tau_0}{m_s^*}\left(r+\tfrac{3}{2}\right)\left(k_BT\right)^{r+\frac{3}{2}}F_{r+\frac{1}{2}}(\eta) \\ &= \frac{2}{3}\frac{nq^2\tau_0}{m_s^*}\left(r+\tfrac{3}{2}\right)\left(k_BT\right)^{r}\frac{F_{r+\frac{1}{2}}(\eta)}{F_{\frac{1}{2}}(\eta)},\end{aligned} \tag{A.101}$$

If the mean-free path is independent of energy, recall that $\tau_0 = \ell\left(m_s^*/2\right)^{1/2}, r = -1/2$,

$$\begin{aligned}\sigma^{MFPIE} &= \frac{8\pi\left(2m_d^*\right)^{3/2}}{3h^3}\frac{q^2\tau_0}{m_s^*}\left(r+\tfrac{3}{2}\right)\left(k_BT\right)^{r+\frac{3}{2}}F_{r+\frac{1}{2}}(\eta) \\ &= N_v\frac{16\pi}{3}\frac{m_s^*q^2\ell}{h^3}k_BTF_0(\eta) = N_v\frac{16\pi}{3}\frac{m_s^*q^2\ell}{h^3}k_BT\ln\left(1+e^{\eta}\right).\end{aligned} \tag{A.102}$$

**Mobility**

The drift mobility $\mu_d$ is defined in accordance with electrical conductivity,

$$\mu_d = \frac{\sigma}{nq} = \frac{2}{3}\frac{q\tau_0}{m_s^*}\left(r+\tfrac{3}{2}\right)\left(k_B T\right)^r \frac{F_{r+\frac{1}{2}}(\eta)}{F_{\frac{1}{2}}(\eta)}. \tag{A.103}$$

Another formalism of mobility one can get from typical galvanomagnetic transport measurement is the Hall mobility $\mu_H$,

$$\begin{aligned}\mu_H &= R_H/\rho = R_H\sigma = \frac{1}{B_z}\frac{L_{13}}{L_{11}} = \frac{1}{B_z}\frac{\mathcal{H}_1}{\mathcal{K}_1} \overset{\gamma<<1}{\approx} \frac{1}{B_z}\frac{H_1}{K_1} \\ &= \frac{q}{m_s^*}\tau_0\left(k_B T\right)^r \frac{\left(2r+\frac{3}{2}\right)F_{2r+\frac{1}{2}}(\eta)}{\left(r+\frac{3}{2}\right)F_{r+\frac{1}{2}}(\eta)}.\end{aligned} \tag{A.104}$$

It can be shown that

$$\mu_H = r_H \mu_d, \tag{A.105}$$

where the Hall factor $r_H$ is the link between various formalism of densities and mobilities

$$r_H = \frac{\mu_H}{\mu_d} = \frac{\sigma R_H}{\frac{\sigma}{nq}} = \frac{nq}{n_H q} = \frac{n}{n_H}. \tag{A.106}$$

**Thermal conductivity**

The isothermal electronic thermal conductivity $\kappa_e$ is given by

$$\begin{aligned}\kappa_e &= \frac{1}{T^2}\frac{\det \mathbf{L}_{134;134}}{\det \mathbf{L}_{13;13}} = \frac{1}{T^2}\left(\mathcal{K}_3 - \frac{\mathcal{K}_1\mathcal{K}_2^2 + 2\mathcal{H}_1\mathcal{H}_2\mathcal{K}_2 - \mathcal{K}_1\mathcal{H}_2^2}{\mathcal{K}_1^2+\mathcal{H}_1^2}\right) \overset{\gamma<<1}{\approx} \frac{1}{T^2}\left(K_3 - \frac{K_2^2}{K_1}\right) \\ &= \frac{4\pi\left(2m_d^*\right)^{3/2}}{h^3}\tau_0 \frac{2}{3m_s^* T}\left(k_B T\right)^{r+\frac{7}{2}}\left[\left(r+\tfrac{7}{2}\right)F_{r+\frac{5}{2}}(\eta) - \frac{\left(r+\frac{5}{2}\right)^2 F_{r+\frac{3}{2}}^2(\eta)}{\left(r+\frac{3}{2}\right)F_{r+\frac{1}{2}}(\eta)}\right],\end{aligned} \tag{A.107}$$

whence the Lorenz Number in the Wiedemann–Franz law is,

$$L = \frac{\kappa_e}{\sigma T} = \left(\frac{k_B}{q}\right)^2\left[\frac{\left(r+\frac{7}{2}\right)F_{r+\frac{5}{2}}(\eta)}{\left(r+\frac{3}{2}\right)F_{r+\frac{1}{2}}(\eta)} - \frac{\left(r+\frac{5}{2}\right)^2 F_{r+\frac{3}{2}}^2(\eta)}{\left(r+\frac{3}{2}\right)^2 F_{r+\frac{1}{2}}^2(\eta)}\right]. \tag{A.108}$$

**Seebeck effect**

The Seebeck coefficient $\alpha$ is given by

$$\begin{aligned}\alpha &= \frac{1}{qT}\frac{\det\mathbf{L}_{13;14}}{\det\mathbf{L}_{13;13}} = -\frac{1}{qT}\left[\mu_c - \frac{\mathcal{K}_1\mathcal{K}_2 + \mathcal{H}_1\mathcal{H}_2}{\mathcal{K}_1^2 + \mathcal{H}_1^2}\right] \overset{\gamma \ll 1}{\approx} -\frac{1}{qT}\left[\mu_c - \frac{K_2}{K_1}\right] \\ &= -\frac{1}{qT}\left[\mu_c - k_B T\frac{\left(r+\tfrac{5}{2}\right)F_{r+\frac{3}{2}}(\eta)}{\left(r+\tfrac{3}{2}\right)F_{r+\frac{1}{2}}(\eta)}\right] = -\frac{k_B}{q}\left[\eta - \frac{\left(r+\tfrac{5}{2}\right)F_{r+\frac{3}{2}}(\eta)}{\left(r+\tfrac{3}{2}\right)F_{r+\frac{1}{2}}(\eta)}\right].\end{aligned} \tag{A.109}$$

For a mixed conduction, both electron and hole contribute to the Seebeck coefficient,

$$\alpha = \frac{n\mu_e\alpha_e + p\mu_h\alpha_h}{n\mu_e + p\mu_h}, \tag{A.110}$$

where $n$ ($p$) is the carrier density, $\mu_e$ ($\mu_h$) is the mobility for electron (hole).

### Nernst effect

The isothermal Nernst coefficient $N$ is given by,

$$\begin{aligned}N &= \frac{1}{qTB_z}\frac{\det\mathbf{L}_{12;13}}{\det\mathbf{L}_{13;13}} = \frac{1}{qTB_z}\frac{\mathcal{K}_1\mathcal{H}_2 - \mathcal{K}_2\mathcal{H}_1}{\mathcal{K}_1^2 + \mathcal{H}_1^2} \overset{\gamma \ll 1}{\approx} \frac{1}{qTB_z}\frac{K_1H_2 - K_2H_1}{K_1^2} \\ &= \frac{\tau_0\left(k_BT\right)^{r+1}}{m_s^*T}\left[\frac{\left(2r+\tfrac{5}{2}\right)F_{2r+\frac{3}{2}}(\eta)}{\left(r+\tfrac{3}{2}\right)F_{r+\frac{1}{2}}(\eta)} - \frac{\left(r+\tfrac{5}{2}\right)\left(2r+\tfrac{3}{2}\right)F_{r+\frac{3}{2}}(\eta)F_{2r+\frac{1}{2}}(\eta)}{\left(r+\tfrac{3}{2}\right)^2F_{r+\frac{1}{2}}^2(\eta)}\right].\end{aligned} \tag{A.111}$$

The transport coefficients derived so far hold for general degenerate semiconductors. Useful results can often be obtained for two extreme cases, namely the non-degenerate limit and the highly degenerate (metallic) limit, by taking proper limit of $F_n(\eta)$ in the formula.

### The highly-degenerate (metallic) limit

In the highly degenerate, or metallic, limit, $\eta = \mu_c/k_BT \gg 0$,

$$
\begin{aligned}
F_n(\eta) &= \int_0^\infty f_0(\xi,\eta)\xi^n d\xi = -\frac{1}{n+1}\int_0^\infty \frac{\partial f_0}{\partial \xi}\xi^{n+1} d\xi \\
&= -\frac{1}{n+1}\int_0^\infty \frac{\partial f_0}{\partial \xi}\left\{ \xi^{n+1}\Big|_{\xi=\eta} + \sum_{m=1}^{\infty} \frac{d^m \xi^{n+1}}{d\xi^m}\bigg|_{\xi=\eta} \frac{(\xi-\eta)^m}{m!} \right\} d\xi \\
&= -\frac{1}{n+1}\int_0^\infty \frac{\partial f_0}{\partial \xi}\left\{ \eta^{n+1} + (n+1)\eta^n(\xi-\eta) + (n+1)n\eta^{n-1}\frac{(\xi-\eta)^2}{2} + \cdots \right\} d\xi \\
&\approx \frac{\eta^{n+1}}{n+1} + n\eta^{n-1}\frac{\pi^2}{6},
\end{aligned}
\tag{A.112}
$$

where

$$
\begin{aligned}
&f_0 = \frac{1}{e^{\xi-\eta}+1}, \frac{\partial f_0}{\partial \xi} = -\frac{e^x}{\left(e^x+1\right)^2}, x = \xi - \eta, \\
&\int_{-\infty}^{\infty} \frac{e^x}{\left(e^x+1\right)^2} x dx = 0, \int_0^{\infty} \frac{e^x}{\left(e^x+1\right)^2} x^2 dx = \frac{\pi^2}{6}.
\end{aligned}
\tag{A.113}
$$

For example,

$$
F_1(\eta) \overset{metal}{\approx} \tfrac{1}{2}\eta^2 + \tfrac{\pi^2}{6}; F_{\frac{1}{2}}(\eta) \overset{metal}{\approx} \tfrac{2}{3}\eta^{\frac{3}{2}}; F_0(\eta) \overset{metal}{\approx} \eta \tag{A.114}
$$

The highly-degenerate carrier density $n_\infty$ (the subscript "$\infty$" designates the highly-degenerate limit) is given by,

$$
n_\infty = \frac{8\pi\left(2m_d^* k_B T\right)^{3/2}}{3h^3}\eta^{3/2}, \tag{A.115}
$$

and the chemical potential

$$
\mu_{c,\infty} = \frac{h^2}{8m_d^*}\left(\frac{3n_\infty}{\pi}\right)^{2/3}. \tag{A.116}
$$

The highly-degenerate electrical conductivity $\sigma_\infty$ is given by, for mean free path independent of energy,

$$
\sigma_\infty^{MFPIE} = \frac{16\pi}{3}\frac{m^* q^2 \ell}{h^3} k_B T \eta. \tag{A.117}
$$

The highly-degenerate Seebeck coefficient $\alpha_\infty$ is given by,

$$\alpha_\infty = \frac{\pi^2}{3}\left(r+\frac{3}{2}\right)\frac{k_B}{q}\eta^{-1}. \tag{A.118}$$

hence for mean free path independent of energy, where $r = -1/2$,

$$\alpha_\infty^{MFPIE} = \frac{\pi^2}{3}\frac{k_B}{q}\frac{1}{\eta} = \frac{8\pi^2 k_B^2}{3qh^2} m_d^* T\left(\frac{\pi}{3n_\infty}\right)^{2/3}. \tag{A.119}$$

Since $\eta = \mu_c/k_BT$, we have (simplifying the notation by dropping all the sub/superscription)

$$\frac{d\ln\sigma}{d\mu_c} = \frac{1}{\eta}\frac{1}{k_BT}, \tag{A.120}$$

and

$$\begin{aligned}\alpha &= \frac{\pi^2}{3}\frac{k_B}{q}k_BT\left\{\frac{d\ln[\sigma(\varepsilon)]}{d\varepsilon}\right\}\Bigg|_{\varepsilon=\mu_c}\\ &= \frac{\pi^2}{3}\frac{k_B}{q}k_BT\left\{\frac{1}{n}\frac{dn(\varepsilon)}{d\varepsilon}+\frac{1}{\mu}\frac{d\mu(\varepsilon)}{d\varepsilon}\right\}\Bigg|_{\varepsilon=\mu_c},\end{aligned} \tag{A.121}$$

which is often cited as the Mott formula.

## The non-degenerate limit

In the non-degenerate limit (the Fermi-Dirac distribution would essentially become the Maxwell-Boltzmann distribution, see below for $f_0$), $\mu_c$ is located in the bandgap with a distance from the conduction or valence band edges larger than ~$3k_BT$, so that

$$\begin{aligned}
&\frac{\varepsilon-\mu_c}{k_B T}=\xi-\eta>3,\\
&f_0=\frac{1}{e^{(\varepsilon-\mu_c)/k_B T}+1}\approx e^{-(\varepsilon-\mu_c)/k_B T},\\
&\frac{\partial f_0}{\partial\varepsilon}\approx-\frac{1}{k_B T}e^{-(\varepsilon-\mu_c)/k_B T}.
\end{aligned}\tag{A.122}$$

Thus the Fermi-Dirac integral becomes, in the non-degenerate limit,

$$\begin{aligned}
F_n(\eta)&=\int_0^\infty f_0(\xi,\eta)\xi^n d\xi=\int_0^\infty\frac{1}{\exp(\xi-\eta)+1}\xi^n d\xi\\
&\approx\int_0^\infty\frac{\xi^n d\xi}{\exp(\xi-\eta)}=e^\eta\int_0^\infty e^{-\xi}\xi^n d\xi=e^\eta\Gamma(n+1),
\end{aligned}\tag{A.123}$$

where the Γ-function is defined as follows

$$\begin{aligned}
&\Gamma(z)\equiv\int_0^\infty e^{-t}t^{z-1}dt,\\
&\Gamma(z+1)=z\Gamma(z),\\
&\Gamma(1/2)=\sqrt{\pi},\,\Gamma(1)=1.
\end{aligned}\tag{A.124}$$

The non-degenerate carrier density $n_0$ (the subscript "0" designates the non-degenerate limit) is given by,

$$n_0=\frac{2\left(2\pi m_d^* k_B T\right)^{3/2}}{h^3}e^\eta,\tag{A.125}$$

and the chemical potential

$$\mu_{c,0}=k_B T\ln\frac{n_0 h^3}{2\left(2\pi m_d^* k_B T\right)^{3/2}}.\tag{A.126}$$

Thus, the integrals $H_i$ and $K_i$ can be further simplified to $H_{i,0}$ and $K_{i,0}$,

$$\begin{aligned}
H_{i,0}&=\frac{2T}{3m_s^*}\frac{2}{\pi^{1/2}}\frac{qB_z}{m_s^*}\tau_0^2 n_0\left(k_B T\right)^{i+2r-1}\Gamma\left(i+2r+\tfrac{3}{2}\right),\\
K_{i,0}&=\frac{2T}{3m_s^*}\frac{2}{\pi^{1/2}}\tau_0 n_0\left(k_B T\right)^{i+r-1}\Gamma\left(i+r+\tfrac{3}{2}\right).
\end{aligned}\tag{A.127}$$

The non-degenerate Hall coefficient $R_{H,0}$ is given by,

$$R_{H,0} = \frac{3\pi^{1/2}}{4}\frac{1}{n_0 q}\frac{\Gamma\left(2r+\frac{5}{2}\right)}{\Gamma^2\left(r+\frac{5}{2}\right)}. \tag{A.128}$$

For mean-free path that is independent of energy, $r = -1/2$,

$$R_{H,0}^{MFPIE} = \frac{3\pi}{8}\frac{1}{n_0 q} = \frac{1}{n_{H,0} q}. \tag{A.129}$$

The non-degenerate electrical conductivity $\sigma_0$ is given by,

$$\sigma_0 = \frac{4}{3\pi^{1/2}}\frac{n_0 q^2 \tau_0}{m_s^*}\left(k_B T\right)^r \Gamma\left(r+\tfrac{5}{2}\right). \tag{A.130}$$

For mean-free path that is independent of energy, i.e., $\tau_0 = \ell\left(m_s^*/2\right)^{1/2}, r = -1/2$,

$$\sigma_0^{MFPIE} = \frac{4}{3}\frac{n_0 q^2 \ell}{\left(2\pi m_s^* k_B T\right)^{1/2}} = \frac{n_0 e^2 \bar{\tau}}{m_s^*}. \tag{A.131}$$

The non-degenerate drift mobility $\mu_{d,0}$ and Hall mobility $\mu_{H,0}$ are given by

$$\mu_{d,0} = \frac{4}{3\pi^{1/2}}\frac{q\tau_0}{m_s^*}\left(k_B T\right)^r \Gamma\left(r+\tfrac{5}{2}\right), \tag{A.132}$$

and

$$\mu_{H,0} = \frac{q\tau_0}{m_s^*}\left(k_B T\right)^r \frac{\Gamma\left(2r+\frac{5}{2}\right)}{\Gamma\left(r+\frac{5}{2}\right)}, \tag{A.133}$$

respectively. For mean-free path that is independent of energy, i.e., $\tau_0 = \ell\left(m_s^*/2\right)^{1/2}, r = -1/2$,

$$\mu_{d,0}^{MFPIE} = \frac{4}{3}\frac{q\ell}{\left(2\pi m_s^* k_B T\right)^{1/2}}, \tag{A.134}$$

and

$$\mu_{H,0}^{MFPIE} = \frac{\pi^{1/2}}{2} \frac{q\ell}{\left(2m_s^* k_B T\right)^{1/2}}, \tag{A.135}$$

The non-degenerate Hall factor $r_{H,0}$ is given by,

$$r_{H,0} = \frac{3\pi^{1/2}}{4} \frac{\Gamma\left(2r + \frac{5}{2}\right)}{\Gamma^2\left(r + \frac{5}{2}\right)}, \tag{A.136}$$

and for mean-free path that is independent of energy, $r = -1/2$,

$$r_{H,0}^{MFPIE} = \frac{\mu_{H,0}^{MFPIE}}{\mu_{d,0}^{MFPIE}} = \frac{3\pi}{8}. \tag{A.137}$$

Since the non-degenerate drift mobility $\mu_{d,0}$ for various scattering mechanisms (different $\tau_0$ and $r$) can usually be derived with proper analysis, it is often advantageous to revise the degenerate mobility formulae to utilize the existing literature results, so that the degenerate drift mobility $\mu_d$ and Hall mobility $\mu_H$ are given by,

$$\mu_d \equiv \mu_{d,0} \frac{\mu_d}{\mu_{d,0}} = \mu_{d,0} \frac{\Gamma\left(\frac{3}{2}\right)}{\Gamma\left(r + \frac{3}{2}\right)} \frac{F_{r+\frac{1}{2}}(\eta)}{F_{\frac{1}{2}}(\eta)}, \tag{A.138}$$

and

$$\mu_H \equiv \mu_{d,0} \frac{\mu_H}{\mu_{d,0}} = \mu_{d,0} \frac{3}{2} \frac{2r + \frac{3}{2}}{\left(r + \frac{3}{2}\right)^2} \frac{\Gamma\left(\frac{3}{2}\right)}{\Gamma\left(r + \frac{3}{2}\right)} \frac{F_{2r+\frac{1}{2}}(\eta)}{F_{r+\frac{1}{2}}(\eta)} \equiv \mu_{d,0} \Psi_r(\eta), \tag{A.139}$$

with $\Psi_r(\eta)$ defined as a combination of Hall factor $r_H$ and Fermi-Dirac integrals,

$$\Psi_r(\eta) = r_H \frac{\sqrt{\pi}}{2} \frac{1}{\Gamma\left(r + \frac{3}{2}\right)} \frac{F_{r+\frac{1}{2}}(\eta)}{F_{\frac{1}{2}}(\eta)}. \tag{A.140}$$

For scattering mechanisms with a mean-free path independent of energy, $r = -1/2$,

$$\mu_H^{MFPIE} = \mu_{d,0}^{MFPIE} \frac{3\sqrt{\pi}}{8} \frac{F_{-\frac{1}{2}}(\eta)}{F_0(\eta)}. \tag{A.141}$$

With these formulas, the overall $\mu_H$ can be given, by the Matthiessen's rule,

$$\frac{1}{\mu_H} = \sum_s \frac{1}{\mu_H^s}, \tag{A.142}$$

where $s$ stands for various scattering mechanisms whose mean-free path $\ell$ in the non-degenerate drift mobility $\mu_{d,0}$ can be properly acquired.

The acoustic phonon (AP) scattering is one of such mechanism with mean-free path independent of energy, as first calculated by Bardeen and Shockley [6, 175, 176],

$$\ell_{d,0}^{AP} = \frac{\pi \hbar^4 c_{ii}}{E_{def}^2 \left(m_s^*\right)^2 k_B T}, \tag{A.143}$$

hence

$$\mu_{d,0}^{AP} = \frac{\left(8\pi\right)^{1/2} e\hbar^4 c_{ii}}{3E_{def}^2 \left(m_s^*\right)^{5/2} \left(k_B T\right)^{3/2}}, \tag{A.144}$$

where $c_{ii}$ ($= \rho\, v_i^2$, $\rho$ is the mass density, $v_i$ is the sound velocity) is the elastic constant for longitudinal strain in the direction of propagation of the wave and $E_{def}$ is the deformation potential.

The alloy scattering (AS) is another such example described by a widely accepted Brooks' formula. Although the original derivation was embed in some private communications, more recent derivations have been provided in the literature,[55, 177, 178]

$$\mu_{d,0}^{AS} = \frac{64 e\hbar^4 N_0}{9\left(2\pi\right)^{3/2} x\left(1-x\right) E_{alloy}^2 \left(m_s^*\right)^{5/2} \left(k_B T\right)^{1/2}}, \tag{A.145}$$

where $N_0$ is the number of atoms per unit volume, $x$ is the fractional concentration of one of the species, and $E_{alloy}$ is an energy parameter characterizing the alloy potential fluctuations.

The non-degenerate electronic thermal conductivity $\kappa_{e,0}$ is given by

$$\kappa_e = \frac{4}{3\pi^{1/2}}\frac{n_0\tau_0}{m_s^* T}\left(k_B T\right)^{r+2}\Gamma\left(r+\tfrac{7}{2}\right), \tag{A.146}$$

For mean-free path that is independent of energy, i.e., $\tau_0 = \ell\left(m_s^*/2\right)^{1/2}$, $r = -1/2$,

$$\kappa_e^{MFPIE} = \frac{2k_B^2 T}{q} n_0 \mu_{d,0}^{MFPIE}. \tag{A.147}$$

where

$$\mu_{d,0}^{MFPIE} = \frac{4}{3}\frac{q\ell}{\left(2\pi m_s^* k_B T\right)^{1/2}} \equiv \frac{e\bar{\tau}}{m_s^*}. \tag{A.148}$$

The non-degenerate Lorenz Number in the Wiedemann-Franz law is

$$L_0 = \left(r+\tfrac{5}{2}\right)\left(\frac{k_B}{q}\right)^2. \tag{A.149}$$

The non-degenerate Seebeck coefficient $S_0$ is given by,

$$S_0 = -\frac{k_B}{q}\left[\eta - \left(r+\tfrac{5}{2}\right)\right] = -\frac{1}{qT}\left[\mu_c - k_B T\left(r+\tfrac{5}{2}\right)\right], \tag{A.150}$$

where $\mu_c$ is measured from the conduction band minimum $E_C$ for electron and valence band maximum $E_V$ for hole. Located within the bandgap, $\mu_c$ is negative for both electron and hole. In a global energy reference system

$$\begin{aligned} S_{0,e} &= -\frac{1}{-eT}\left[\mu_c - E_C - k_B T\left(r+\tfrac{5}{2}\right)\right] = -\frac{1}{eT}\left[E_C - \mu_c + k_B T\left(r+\tfrac{5}{2}\right)\right], \\ S_{0,h} &= -\frac{1}{eT}\left[E_V - \mu_c - k_B T\left(r+\tfrac{5}{2}\right)\right] = \frac{1}{eT}\left[\mu_c - E_V + k_B T\left(r+\tfrac{5}{2}\right)\right]. \end{aligned} \tag{A.151}$$

The non-degenerate Nernst coefficient $N_0$ is given by,

$$N_0 = \frac{\tau_0\left(k_B T\right)^{r+1}}{m_s^* T}\frac{r\Gamma\left(2r+\tfrac{5}{2}\right)}{\Gamma\left(r+\tfrac{5}{2}\right)}. \tag{A.152}$$

For mean-free path that is independent of energy, i.e., $\tau_0 = \ell\left(m_s^*/2\right)^{1/2}$, $r = -1/2$,

$$N_0^{MFPIE} = -\frac{\ell}{4}\left(\frac{\pi k_B}{2m_s^* T}\right)^{1/2}. \tag{A.153}$$

# APPENDIX B

## PUBLICATION LIST

1. *"Highly efficient* $(In_2Te_3)_x(GeTe)_{3-3x}$ *thermoelectric materials: a substitute for TAGS"*, H. Sun, X. Lu, **Hang Chi,** D. T. Morelli, and C. Uher, Phys. Chem. Chem. Phys. **16**, 15570-15575 (2014).
2. *"Low-temperature structural and transport anomalies in* $Cu_2Se$*"*, **Hang Chi,** H. Kim, J. C. Thomas, G. Shi, K. Sun, M. Abeykoon, E. S. Bozin, X. Shi, Q. Li, X. Shi, E. Kioupakis, A. Van der Ven, M. Kaviany, and C. Uher, Phys. Rev. B **89**, 195209-5 (2014).
3. *"Donor and acceptor impurity-driven switching of magnetic ordering in* $MnSb_{2-x}Sn_xSe_4$*"*, H. Djieutedjeu, X. Zhou, **Hang Chi,** N. Haldolaarachchige, K. Ranmohotti, C. Uher, D. Young, and P. F. P. Poudeu, J. Mater. Chem. C **2**, 6199-6210 (2014).
4. *"Electronic and phonon transport in Sb-doped* $Ti_{0.1}Zr_{0.9}Ni_{1+x}Sn_{0.975}Sb_{0.025}$ *nanocomposites"*, Y. Liu, A. Page, P. Sahoo, **Hang Chi,** C. Uher, and P. F. P. Poudeu, Dalton Trans. **43**, 8094-8101 (2014).
5. *"Advanced thermoelectrics governed by single parabolic band:* $Mg_2Si_{0.3}Sn_{0.7}$*, a canonical example"*, W. Liu,† **Hang Chi,†** H. Sun, Q. Zhang, K. Yin, X. Tang, Q. Zhang, and C. Uher, Phys. Chem. Chem. Phys. **16**, 6893-6897 (2014).
6. *"Realization of high thermoelectric performance in p-type unfilled ternary skutterudites* $FeSb_{2+x}Te_{1-x}$ *via band structure modification and significant point defect scattering"*, G. Tan, W. Liu, **Hang Chi,** X. Su, S. Wang, Y. Yan, X. Tang, W. Wong-Ng, and C. Uher, Acta Mater. **61**, 7693-7704 (2013).
7. *"Ultrahigh Thermoelectric Performance by Electron and Phonon Critical Scattering in* $Cu_2Se_{1-x}I_x$*"*, H. Liu, X. Yuan, P. Lu, X. Shi, F. Xu, Y. He, Y. Tang, S. Bai, W. Zhang, L. Chen, Y. Lin, L. Shi, H. Lin, X. Gao, X. Zhang, **Hang Chi,** and C. Uher, Adv. Mater. **25**, 6607-6612 (2013).
8. *"Thermoelectric properties of Ag-doped* $Cu_2Se$ *and* $Cu_2Te$*"*, S. Ballikaya, **Hang Chi,** J. R. Salvador, and C. Uher, J. Mater. Chem. A **1**, 12478-12484 (2013).
9. *"Enhancing thermopower and hole mobility in bulk p-type half-Heuslers using full-Heusler nanostructures"*, P. Sahoo, Y. Liu, J. P. A. Makongo, X. Su, S. Kim, N. Takas, **Hang Chi,** C. Uher, X. Pan, and P. F. P. Poudeu, Nanoscale **5**, 9419-9427 (2013).
10. *"Tuning the Temperature Domain of Phonon Drag in Thin Films by the Choice of Substrate"*, G. Wang, L. Endicott, **Hang Chi,** P. Lošt'ák, and C. Uher, Phys. Rev. Lett. **111**, 046803-5 (2013).
11. *"Transport properties of ZnTe:N thin films"*, **Hang Chi,** C. Chen, J. D. Phillips, and C. Uher, Appl. Phys. Lett. **103**, 042108-5 (2013).

12. *"Influence of embedded indium nanocrystals on GaAs thermoelectric properties"*, M. V. Warren, J. C. Canniff, **Hang Chi,** E. Morag, F. Naab, V. A. Stoica, R. Clarke, C. Uher, and R. S. Goldman, *J. Appl. Phys.* **114**, 043704-4 (2013).
13. *"Low-temperature transport properties of Tl-doped* $Bi_2Te_3$ *single crystals"*, **Hang Chi,** W. Liu, K. Sun, X. Su, G. Wang, P. Lošt'ák, V. Kucek, Č. Drašar, and C. Uher, *Phys. Rev. B* **88**, 045202-7 (2013).
14. *"Lower Thermal Conductivity and Higher Thermoelectric Performance of Fe-Substituted and Ce, Yb Double-Filled p-Type Skutterudites"*, S. Ballikaya, N. Uzar, S. Yildirim, **Hang Chi,** X. Su, G. Tan, X. Tang, and C. Uher, *J. Electron. Mater.* **42**, 1622-1627 (2013).
15. *"High figure of merit and thermoelectric properties of Bi-doped* $Mg_2Si_{0.4}Sn_{0.6}$ *solid solutions"*, W. Liu, Q. Zhang, K. Yin, **Hang Chi,** X. Zhou, X. Tang, and C. Uher, *J. Solid State Chem.* **203**, 333-339 (2013).
16. *"Large Enhancements of Thermopower and Carrier Mobility in Quantum Dot Engineered Bulk Semiconductors"*, Y. Liu, P. Sahoo, J. P. A. Makongo, X. Zhou, S.-J. Kim, **Hang Chi,** C. Uher, X. Pan, and P. F. P. Poudeu, *J. Am. Chem. Soc.* **135**, 7486-7495 (2013).
17. *"Thermoelectric performance of nanostructured p-type* $Zr_{0.5}Hf_{0.5}Co_{0.4}Rh_{0.6}Sb_{1-x}Sn_x$ *half-Heusler alloys"*, P. Maji, J. P. A. Makongo, X. Zhou, **Hang Chi,** C. Uher, and P. F. P. Poudeu, *J. Solid State Chem.* **202**, 70-76 (2013).
18. *"High Performance Thermoelectricity in Earth-Abundant Compounds Based on Natural Mineral Tetrahedrites"*, X. Lu, D. T. Morelli, Y. Xia, F. Zhou, V. Ozolins, **Hang Chi,** X. Zhou, and C. Uher, *Adv. Energy Mater.* **3**, 342-348 (2013).
19. *"Configuring pnicogen rings in skutterudites for low phonon conductivity"*, **Hang Chi,** H. Kim, J. C. Thomas, X. Su, S. Stackhouse, M. Kaviany, A. Van der Ven, X. Tang, and C. Uher, *Phys. Rev. B* **86**, 195209-7 (2012).
20. *"The role of Ga in* $Ba_{0.30}Ga_xCo_4Sb_{12+x}$ *filled skutterudites"*, X. Su, H. Li, Y. Yan, **Hang Chi,** X. Tang, Q. Zhang, and C. Uher, *J. Mater. Chem.* **22**, 15628-15634 (2012).
21. *"Microstructure and thermoelectric properties of* $CoSb_{2.75}Ge_{0.25-x}Te_x$ *prepared by rapid solidification"*, X. Su, H. Li, Y. Yan, G. Wang, **Hang Chi,** X. Zhou, X. Tang, Q. Zhang, and C. Uher, *Acta Mater.* **60**, 3536-3544 (2012).
22. *"Thermoelectric Performance of Sb- and La-Doped* $Mg_2Si_{0.5}Ge_{0.5}$*"*, X. Zhou, G. Wang, **Hang Chi,** X. Su, J. R. Salvador, W. Liu, X. Tang, and C. Uher, *J. Electron. Mater.* **41**, 1589-1594 (2012).
23. *"Enhanced thermoelectric properties of Ba-filled skutterudites by grain size reduction and Ag nanoparticle inclusion"*, X. Zhou, G. Wang, L. Zhang, **Hang Chi,** X. Su, J. Sakamoto, and C. Uher, *J. Mater. Chem.* **22**, 2958-2964 (2012).
24. *"Structure and Transport Properties of Double-Doped* $CoSb_{2.75}Ge_{0.25-x}Te_x$ $(x=0.125\text{-}0.20)$ *with in Situ Nanostructure"*, X. Su, H. Li, G. Wang, **Hang Chi,** X. Zhou, X. Tang, Q. Zhang, and C. Uher, *Chem. Mater.* **23**, 2948-2955 (2011).

# REFERENCE

[1] H. B. Callen, The Application of Onsager's Reciprocal Relations to Thermoelectric, Thermomagnetic, and Galvanomagnetic Effects. Phys. Rev. **73**, 1349-1358 (1948).

[2] H. B. Callen, *Thermodynamics and an introduction to thermostatistics* (John Wiley & Sons, New York, 1985).

[3] N. W. Ashcroft and N. D. Mermin, *Solid State Physics* (Saunders College, Philadelphia, 1976).

[4] Lord Kelvin (Sir W. Thomson), Mathematical and Physical Papers Volume I (University Press, Cambridge, 1882), pp. 232-291

[5] A. Sommerfeld and N. H. Frank, The Statistical theory of thermoelectric, galvano- and thermomagnetic phenomena in metals. Rev. Mod. Phys. **3**, 1-42 (1931).

[6] E. H. Putley, *The Hall Effect and Related Phenomena* (Butterworths, London, 1960).

[7] I. M. Tsidil'kovskii, *Thermomagnetic Effects in Semiconductors* (Infosearch Limited, London, 1962).

[8] H. J. Goldsmid, *Electronic Refrigeration* (Pion, London, 1986).

[9] K. Uchida, S. Takahashi, K. Harii, J. Ieda, W. Koshibae, K. Ando, S. Maekawa, and E. Saitoh, Observation of the spin Seebeck effect. Nature **455**, 778-781 (2008).

[10] K. Uchida, J. Xiao, H. Adachi, J. Ohe, S. Takahashi, J. Ieda, T. Ota, Y. Kajiwara, H. Umezawa, H. Kawai, G. E. W. Bauer, S. Maekawa, and E. Saitoh, Spin Seebeck insulator. Nature Materials **9**, 894-897 (2010).

[11] C. M. Jaworski, J. Yang, S. Mack, D. D. Awschalom, J. P. Heremans, and R. C. Myers, Observation of the spin-Seebeck effect in a ferromagnetic semiconductor. Nature Materials **9**, 898-903 (2010).

[12] C. M. Jaworski, R. C. Myers, E. Johnston-Halperin, and J. P. Heremans, Giant spin Seebeck effect in a non-magnetic material. Nature **487**, 210-213 (2012).

[13] Z. Wang, *Thermodynamics and statistical physics (in Chinese)* (Higher Education Press, Beijing, 2000).

[14] L. Onsager, Reciprocal Relations in Irreversible Processes. I. Phys. Rev. **37**, 405-426 (1931).

[15] L. Onsager, Reciprocal Relations in Irreversible Processes. II. Phys. Rev. **38**, 2265-2279 (1931).

[16] J. M. Sanchez, F. Ducastelle, and D. Gratias, Generalized cluster description of multicomponent systems. Physica A **128**, 334-350 (1984).

[17] G. Kresse and J. Furthmüller, Efficient iterative schemes for ab initio total-energy calculations using a plane-wave basis set. Phys. Rev. B **54**, 11169 (1996).

[18] J. P. Perdew, K. Burke, and M. Ernzerhof, Generalized Gradient Approximation Made Simple. Phys. Rev. Lett. **77**, 3865-3868 (1996).

[19] P. E. Bl□chl, Projector augmented-wave method. Phys. Rev. B **50**, 17953 (1994).

[20] G. Kresse and D. Joubert, From ultrasoft pseudopotentials to the projector augmented-wave method. Phys. Rev. B **59**, 1758 (1999).

[21] J. Heyd, G. E. Scuseria, and M. Ernzerhof, Hybrid functionals based on a screened Coulomb potential. The Journal of Chemical Physics **118**, 8207-8215 (2003).

[22] A. V. Krukau, O. A. Vydrov, A. F. Izmaylov, and G. E. Scuseria, Influence of the exchange screening parameter on the performance of screened hybrid functionals. The Journal of Chemical Physics **125**, 224106 (2006).

[23] K. Parlinski, PHONON software package (Cracow, 2008).

[24] D. M. Rowe, *CRC Handbook of Thermoelectrics* (CRC Press, Boca Raton, FL, 1995).

[25] D. M. Rowe, *Thermoelectrics Handbook: Macro to Nano* (CRC Press, Boca Raton, FL, 2006).

[26] V. K. Zaitsev, M. I. Fedorov, E. A. Gurieva, I. S. Eremin, P. P. Konstantinov, A. Y. Samunin, and M. V. Vedernikov, Highly effective Mg_{2}Si_{1−x}Sn_{x} thermoelectrics. Phys. Rev. B **74**, 045207 (2006).

[27] W. Liu, X. Tan, K. Yin, H. Liu, X. Tang, J. Shi, Q. Zhang, and C. Uher, Convergence of Conduction Bands as a Means of Enhancing Thermoelectric Performance of n-Type Mg2Si1-xSnx Solid Solutions. Phys. Rev. Lett. **108**, 166601 (2012).

[28] K. Kutorasiński, J. Tobola, and S. Kaprzyk, Calculating electron transport coefficients of disordered alloys using the KKR-CPA method and Boltzmann approach: Application to Mg_{2}Si_{1−x}Sn_{x} thermoelectrics. Phys. Rev. B **87**, 195205 (2013).

[29] B. Poudel, Q. Hao, Y. Ma, Y. Lan, A. Minnich, B. Yu, X. Yan, D. Wang, A. Muto, D. Vashaee, X. Chen, J. Liu, M. S. Dresselhaus, G. Chen, and Z. Ren, High-Thermoelectric Performance of Nanostructured Bismuth Antimony Telluride Bulk Alloys. Science **320**, 634-638 (2008).

[30] W. Xie, J. He, H. J. Kang, X. Tang, S. Zhu, M. Laver, S. Wang, J. R. D. Copley, C. M. Brown, Q. Zhang, and T. M. Tritt, Identifying the Specific Nanostructures Responsible for the High Thermoelectric Performance of (Bi,Sb)2Te3 Nanocomposites. Nano Lett **10**, 3283-3289 (2010).

[31] R. J. Mehta, Y. Zhang, C. Karthik, B. Singh, R. W. Siegel, T. Borca-Tasciuc, and G. Ramanath, A new class of doped nanobulk high-figure-of-merit thermoelectrics by scalable bottom-up assembly. Nat Mater **11**, 233-240 (2012).

[32] H. Chi, W. Liu, K. Sun, X. Su, G. Wang, P. Lošt'ák, V. Kucek, Č. Drašar, and C. Uher, Low-temperature transport properties of Tl-doped Bi2Te3 single crystals. Phys. Rev. B **88**, 045202-7 (2013).

[33] J. P. Heremans, V. Jovovic, E. S. Toberer, A. Saramat, K. Kurosaki, A. Charoenphakdee, S. Yamanaka, and G. J. Snyder, Enhancement of Thermoelectric Efficiency in PbTe by Distortion of the Electronic Density of States. Science **321**, 554-557 (2008).

[34] Y. Z. Pei, X. Y. Shi, A. LaLonde, H. Wang, L. D. Chen, and G. J. Snyder, Convergence of electronic bands for high performance bulk thermoelectrics. Nature **473**, 66-69 (2011).

[35] K. Biswas, J. He, I. D. Blum, C.-I. Wu, T. P. Hogan, D. N. Seidman, V. P. Dravid, and M. G. Kanatzidis, High-performance bulk thermoelectrics with all-scale hierarchical architectures. Nature **489**, 414-418 (2012).

[36] C. Uher, "Chapter 5 Skutterudites: Prospective novel thermoelectrics" in Semiconductors and Semimetals, Volume 69, p139-253 (Elsevier, 2001)

[37] M. M. Koza, M. R. Johnson, R. Viennois, H. Mutka, L. Girard, and D. Ravot, Breakdown of phonon glass paradigm in La- and Ce-filled Fe4Sb12 skutterudites. Nature Mater. **7**, 805-810 (2008).

[38] X. Shi, J. Yang, J. R. Salvador, M. Chi, J. Y. Cho, H. Wang, S. Bai, J. Yang, W. Zhang, and L. Chen, Multiple-Filled Skutterudites: High Thermoelectric Figure of Merit through Separately Optimizing Electrical and Thermal Transports. J. Am. Chem. Soc. **133**, 7837-7846 (2011).

[39] H. Chi, H. Kim, J. C. Thomas, X. Su, S. Stackhouse, M. Kaviany, A. Van der Ven, X. Tang, and C. Uher, Configuring pnicogen rings in skutterudites for low phonon conductivity. Phys. Rev. B **86**, 195209-7 (2012).

[40] C. Uher, J. Yang, S. Hu, D. T. Morelli, and G. P. Meisner, Transport properties of pure and doped MNiSn (M=Zr, Hf). Phys. Rev. B **59**, 8615-8621 (1999).

[41] Y. Liu, P. Sahoo, J. P. A. Makongo, X. Zhou, S.-J. Kim, H. Chi, C. Uher, X. Pan, and P. F. P. Poudeu, Large Enhancements of Thermopower and Carrier Mobility in Quantum Dot Engineered Bulk Semiconductors. J. Am. Chem. Soc. **135**, 7486-7495 (2013).

[42] J.-H. Lee, J. Wu, and J. C. Grossman, Enhancing the Thermoelectric Power Factor with Highly Mismatched Isoelectronic Doping. Phys. Rev. Lett. **104**, 016602 (2010).

[43] H. Chi, C. Chen, J. D. Phillips, and C. Uher, Transport properties of ZnTe:N thin films. Appl. Phys. Lett. **103**, 042108-5 (2013).

[44] L. D. Crossman and G. C. Danielson, Piezoresistance of n-Type Magnesium Stannide. Phys. Rev. **171**, 867-875 (1968).

[45] X. Liu, T. Zhu, H. Wang, L. Hu, H. Xie, G. Jiang, G. J. Snyder, and X. Zhao, Low Electron Scattering Potentials in High Performance Mg2Si0.45Sn0.55 Based Thermoelectric Solid Solutions with Band Convergence. Adv. Energy Mater. **3**, 1238-1244 (2013).

[46] A. Chandra and L. F. Eastman, A study of alloy scattering in Ga1−xAlxAs. J. Appl. Phys. **51**, 2669-2677 (1980).

[47] D. C. Look, D. K. Lorance, J. R. Sizelove, C. E. Stutz, K. R. Evans, and D. W. Whitson, Alloy scattering in p-type AlxGa1−xAs. J. Appl. Phys. **71**, 260-266 (1992).

[48] E. Bellotti, F. Bertazzi, and M. Goano, Alloy scattering in AlGaN and InGaN: A numerical study. J. Appl. Phys. **101**, - (2007).

[49] V. W. L. Chin, Calculations of the electron mobility of InAsxP1−x. J. Phys. Chem. Solids **52**, 1193-1195 (1991).

[50] S. Krishnamurthy, A. Sher, and A.-B. Chen, Generalized Brooks' formula and the electron mobility in SixGe1-x alloys. Appl. Phys. Lett. **47**, 160-162 (1985).

[51] Y. I. Ravich, B. A. Efimova, and I. A. Smirnov, *Semiconducting Lead Chalcogenides* (Plenum Press, New York, 1970).

[52] H. Wang, Y. Pei, A. D. LaLonde, and G. J. Snyder, Weak electron–phonon coupling contributing to high thermoelectric performance in n-type PbSe. Proceedings of the National Academy of Sciences **109**, 9705-9709 (2012).

[53] H. Wang, A. D. LaLonde, Y. Pei, and G. J. Snyder, The Criteria for Beneficial Disorder in Thermoelectric Solid Solutions. Adv. Funct. Mater. **23**, 1586-1596 (2013).

[54] D. Chattopadhyay, Electron mobility in Cd0.8Zn0.2Te. Solid State Communications **91**, 149-151 (1994).

[55] J. W. Harrison and J. R. Hauser, Alloy scattering in ternary III-V compounds. Phys. Rev. B **13**, 5347-5350 (1976).

[56] A. Atanassov and M. Baleva, On the band diagram of Mg2Si/Si heterojunction as deduced from optical constants dispersions. Thin Solid Films **515**, 3046-3051 (2007).

[57] M. Schoijet, Possibilities of new materials for solar photovoltaic cells. Solar Energy Materials **1**, 43-57 (1979).

[58] W. Liu, X. Tang, H. Li, K. Yin, J. Sharp, X. Zhou, and C. Uher, Enhanced thermoelectric properties of n-type Mg2.16(Si0.4Sn0.6)1-ySby due to nano-sized Sn-rich precipitates and an optimized electron concentration. J. Mater. Chem. **22**, 13653-13661 (2012).

[59] I.-H. Jung, D.-H. Kang, W.-J. Park, N. J. Kim, and S. Ahn, Thermodynamic modeling of the Mg–Si–Sn system. Calphad **31**, 192-200 (2007).

[60] G. A. Slack, in CRC Handbook of Thermoelectrics, (CRC Press, Boca Raton, FL, 1995)

[61] D. T. Morelli and G. P. Meisner, Low-Temperature Properties of the filled Skutterudite CeFe4Sb12. J. Appl. Phys. **77**, 3777-3781 (1995).

[62] C. Uher, "Skutterudites: Prospective novel thermoelectrics" in Recent Trends in Thermoelectric Materials Research I, 69, p139-253 (Academic Press Inc, San Diego, 2001)

[63] H. Li, X. F. Tang, Q. J. Zhang, and C. Uher, High performance InxCeyCo4Sb12 thermoelectric materials with in situ forming nanostructured InSb phase. Appl. Phys. Lett. **94**, 102114 (2009).

[64] I. Oftedal, The crystal structure of skutterudite and smaltine chloanthite. Z Kristallogr **A66**, 517-546 (1928).

[65] J. L. Feldman and D. J. Singh, Lattice dynamics of skutterudites: First-principles and model calculations for CoSb3. Phys. Rev. B **53**, 6273 (1996).

[66] I. K. Dimitrov, M. E. Manley, S. M. Shapiro, J. Yang, W. Zhang, L. D. Chen, Q. Jie, G. Ehlers, A. Podlesnyak, J. Camacho, and Q. Li, Einstein modes in the phonon density of states of the single-filled skutterudite Yb_{0.2}Co_{4}Sb_{12}. Phys. Rev. B **82**, 174301 (2010).

[67] X. Y. Li, L. D. Chen, J. F. Fan, W. B. Zhang, T. Kawahara, and T. Hirai, Thermoelectric properties of Te-doped CoSb3 by spark plasma sintering. J. Appl. Phys. **98**, 083702-6 (2005).

[68] W. S. Liu, B. P. Zhang, L. D. Zhao, and J. F. Li, Improvement of Thermoelectric Performance of CoSb3-xTex Skutterudite Compounds by Additional Substitution of IVB-Group Elements for Sb. Chem. Mater. **20**, 7526-7531 (2008).

[69] X. Su, H. Li, G. Wang, H. Chi, X. Zhou, X. Tang, Q. Zhang, and C. Uher, Structure and Transport Properties of Double-Doped CoSb2.75Ge0.25-xTex (x = 0.125-0.20) with in Situ Nanostructure. Chemistry of Materials **23**, 2948-2955 (2011).

[70] X. Su, H. Li, Y. Yan, G. Wang, H. Chi, X. Zhou, X. Tang, Q. Zhang, and C. Uher, Microstructure and thermoelectric properties of CoSb2.75Ge0.25-xTex prepared by rapid solidification. Acta Mater. **60**, 3536-3544 (2012).

[71] P. Vaqueiro, G. G. Sobany, and A. V. Powell, A synchrotron powder X-ray diffraction study of the skutterudite-related phases AB(1.5)Te(1.5) (A = Co, Rh, Ir; B = Ge, Sn). Dalton T **39**, 1020-1026 (2010).

[72] S. V. Barabash, V. Ozolins, and C. Wolverton, First-Principles Theory of Competing Order Types, Phase Separation, and Phonon Spectra in Thermoelectric AgPbmSbTem+2 Alloys. Phys. Rev. Lett. **101**, 155704 (2008).

[73] S. V. Barabash, V. Ozolins, and C. Wolverton, First-principles theory of the coherency strain, defect energetics, and solvus boundaries in the PbTe-AgSbTe2 system. Phys. Rev. B **78**, 214109 (2008).

[74] J. W. Cahn, Coherent fluctuations and nucleation in isotropic solids. Acta Metallurgica **10**, 907-913 (1962).

[75] P. W. Voorhees and W. C. Johnson, "The thermodynamics of elastically stressed crystals" in Solid State Physics, Volume 59, p1-201 (Academic Press, 2004)

[76] A. Van der Ven, K. Garikipati, S. Kim, and M. Wagemaker, The Role of Coherency Strains on Phase Stability in Li(x)FePO(4): Needle Crystallites Minimize Coherency Strain and Overpotential. Journal of the Electrochemical Society **156**, A949-A957 (2009).

[77] B. C. Sales, B. C. Chakoumakos, D. Mandrus, and J. W. Sharp, Atomic Displacement Parameters and the Lattice Thermal Conductivity of Clathrate-like Thermoelectric Compounds. J Solid State Chem **146**, 528-532 (1999).

[78] G. S. Nolas, D. T. Morelli, and T. M. Tritt, SKUTTERUDITES: A Phonon-Glass-Electron Crystal Approach to Advanced Thermoelectric Energy Conversion Applications. Annual Review of Materials Science **29**, 89-116 (1999).

[79] T. Caillat, A. Borshchevsky, and J. P. Fleurial, Properties of single crystalline semiconducting CoSb[sub 3]. J. Appl. Phys. **80**, 4442-4449 (1996).

[80] G. P. Meisner, D. T. Morelli, S. Hu, J. Yang, and C. Uher, Structure and Lattice Thermal Conductivity of Fractionally Filled Skutterudites: Solid Solutions of Fully Filled and Unfilled End Members. Phys. Rev. Lett. **80**, 3551-3554 (1998).

[81] L. Zhang, G. Rogl, A. Grytsiv, S. Puchegger, J. Koppensteiner, F. Spieckermann, H. Kabelka, M. Reinecker, P. Rogl, W. Schranz, M. Zehetbauer, and M. A. Carpenter, Mechanical properties of filled antimonide skutterudites. Materials Science and Engineering: B **170**, 26-31 (2010).

[82] J. Dong, O. F. Sankey, G. K. Ramachandran, and P. F. McMillan, Chemical trends of the rattling phonon modes in alloyed germanium clathrates. J. Appl. Phys. **87**, 7726-7734 (2000).

[83] M. Beekman, R. P. Hermann, A. Mochel, F. Juranyi, and G. S. Nolas, A study of low-energy guest phonon modes in clathrate-II Na x Si 136 ( x = 3, 23, and 24). J. Phys. Condens. Matter **22**, 355401 (2010).

[84] X. Shi, W. Zhang, L. D. Chen, J. Yang, and C. Uher, Thermodynamic analysis of the filling fraction limits for impurities in CoSb3 based on ab initio calculations. Acta Mater. **56**, 1733-1740 (2008).

[85] M. Ibanez, R. Zamani, A. LaLonde, D. Cadavid, W. H. Li, A. Shavel, J. Arbiol, J. R. Morante, S. Gorsse, G. J. Snyder, and A. Cabot, Cu2ZnGeSe4 Nanocrystals: Synthesis and Thermoelectric Properties. J. Am. Chem. Soc. **134**, 4060-4063 (2012).

[86] H. Kim, M. Kaviany, J. C. Thomas, A. Van der Ven, C. Uher, and B. L. Huang, Structural Order-Disorder Transitions and Phonon Conductivity of Partially Filled Skutterudites. Phys. Rev. Lett. **105**, 265901 (2010).

[87] P. G. Klemens, Thermal Resistance due to Point Defects at High Temperatures. Phys. Rev. **119**, 507-509 (1960).

[88] J. Callaway and H. C. von Baeyer, Effect of Point Imperfections on Lattice Thermal Conductivity. Phys. Rev. **120**, 1149-1154 (1960).

[89] B. Abeles, Lattice Thermal Conductivity of Disordered Semiconductor Alloys at High Temperatures. Phys. Rev. **131**, 1906-1911 (1963).

[90] G. S. Nolas, J. L. Cohn, and G. A. Slack, Effect of partial void filling on the lattice thermal conductivity of skutterudites. Phys. Rev. B **58**, 164-170 (1998).

[91] S. Stackhouse, L. Stixrude, and B. B. Karki, Thermal Conductivity of Periclase (MgO) from First Principles. Phys. Rev. Lett. **104**, 208501 (2010).

[92] M. Kaviany, *Heat Transfer Physics* (Cambridge, New York, 2008).

[93] B. Huang and M. Kaviany, Filler-reduced phonon conductivity of thermoelectric skutterudites: Ab initio calculations and molecular dynamics simulations. Acta Mater. **58**, 4516-4526 (2010).

[94] E. F. Steigmeier and B. Abeles, Scattering of Phonons by Electrons in Germanium-Silicon Alloys. Phys. Rev. **136**, A1149-A1155 (1964).

[95] M. Murabayashi, Thermal Conductivity of Ceramic Solid Solutions. Journal of Nuclear Science and Technology **7**, 559-563 (1970).

[96] R. Berman, *Thermal Conduction in Solids* (Oxford University Press, Oxford, 1979).

[97] F. Muller-Plathe, A simple nonequilibrium molecular dynamics method for calculating the thermal conductivity. The Journal of Chemical Physics **106**, 6082-6085 (1997).

[98] C. Nieto-Draghi and J. B. Avalos, Non-equilibrium momentum exchange algorithm for molecular dynamics simulation of heat flow in multicomponent systems. Molecular Physics **101**, 2303-2307 (2003).

[99] S. Adachi, *Properties of Group-IV, III-V and II-VI Semiconductors* (John Wiley & Sons, West Sussex, UK, 2005).

[100] K. Sato, M. Hanafusa, A. Noda, A. Arakawa, M. Uchida, T. Asahi, and O. Oda, ZnTe pure green light-emitting diodes fabricated by thermal diffusion. Journal of Crystal Growth **214/215**, 1080-1084 (2000).

[101] W. Wang, A. S. Lin, and J. D. Phillips, Intermediate-band photovoltaic solar cell based on ZnTe:O. Appl. Phys. Lett. **95**, 011103-3 (2009).

[102] J. Han, T. S. Stavrinides, M. Kobayashi, R. L. Gunshor, M. M. Hagerott, and A. V. Nurmikko, Heavy p-doping of ZnTe by molecular beam epitaxy using a nitrogen plasma source. Appl. Phys. Lett. **62**, 840-842 (1993).

[103] I. W. Tao, M. Jurkovic, and W. I. Wang, Doping of ZnTe by molecular beam epitaxy. Appl. Phys. Lett. **64**, 1848-1849 (1994).

[104] T. Baron, K. Saminadayar, and N. Magnea, Nitrogen doping of Te-based II-VI compounds during growth by molecular beam epitaxy. J. Appl. Phys. **83**, 1354-1370 (1998).

[105] Y. Fan, J. Han, L. He, J. Saraie, R. L. Gunshor, M. Hagerott, and A. V. Nurmikko, Electrical transport characterizations of nitrogen doped ZnSe and ZnTe films. J. Electron. Mater. **23**, 245-249 (1994).

[106] C. Herring, Theory of the Thermoelectric Power of Semiconductors. Phys. Rev. **96**, 1163-1187 (1954).

[107] G. A. Slack, Thermal Conductivity of II-VI Compounds and Phonon Scattering by Fe^{2+} Impurities. Phys. Rev. B **6**, 3791 (1972).

[108] A. Noguera and S. M. Wasim, Lattice thermal conductivity of II-VI compounds. Solid State Communications **50**, 483-486 (1984).

[109] A. I. Ivanov, A. N. Luk'yanov, B. A. Merisov, A. V. Sologubenko, and G. Y. Khadjai, Thermal conductivity of a GaAs single crystal grown in microgravity. Low Temperature Physics **28**, 462-464 (2002).

[110] T. Dannecker, Y. Jin, H. Cheng, C. F. Gorman, J. Buckeridge, C. Uher, S. Fahy, C. Kurdak, and R. S. Goldman, Nitrogen composition dependence of electron effective mass in GaAs1-xNx. Phys. Rev. B **82**, 125203 (2010).

[111] M. V. Warren, A. W. Wood, J. C. Canniff, F. Naab, C. Uher, and R. S. Goldman, Evolution of structural and thermoelectric properties of indium-ion-implanted epitaxial GaAs. Appl. Phys. Lett. **100**, 102101-4 (2012).

[112] M. A. Zudov, I. V. Ponomarev, A. L. Efros, R. R. Du, J. A. Simmons, and J. L. Reno, New Class of Magnetoresistance Oscillations: Interaction of a Two-Dimensional Electron Gas with Leaky Interface Phonons. Phys. Rev. Lett. **86**, 3614-3617 (2001).

[113] R. Fletcher, M. D'Iorio, A. S. Sachrajda, R. Stoner, C. T. Foxon, and J. J. Harris, Evidence of phonon drag in the thermopower of a GaAs-Ga0.68Al0.32As heterojunction. Phys. Rev. B **37**, 3137-3140 (1988).

[114] R. Fletcher, J. J. Harris, C. T. Foxon, M. Tsaousidou, and P. N. Butcher, Thermoelectric properties of a very-low-mobility two-dimensional electron gas. Phys. Rev. B **50**, 14991-14998 (1994).

[115] R. Fletcher, V. M. Pudalov, Y. Feng, M. Tsaousidou, and P. N. Butcher, Thermoelectric and hot-electron properties of a silicon inversion layer. Phys. Rev. B **56**, 12422-12428 (1997).

[116] S. Agan, O. A. Mironov, E. H. C. Parker, and T. E. Whall, The phonon-drag thermopower in Si:B and Si:Sb δ-doped samples. Semiconductor Science and Technology **15**, 551 (2000).

[117] N. V. Zavaritsky, Phonon drag in two-dimensional electron systems. Physica **126B**, 369-376 (1984).

[118] H. L. Stormer, L. N. Pfeiffer, K. W. Baldwin, and K. W. West, Observation of a Bloch-Grüneisen regime in two-dimensional electron transport. Phys. Rev. B **41**, 1278-1281 (1990).

[119] S. K. Lyo, Low-temperature phonon-drag thermoelectric power in heterojunctions. Phys. Rev. B **38**, 6345-6347 (1988).

[120] A. Miele, R. Fletcher, E. Zaremba, Y. Feng, C. T. Foxon, and J. J. Harris, Phonon-drag thermopower and weak localization. Phys. Rev. B **58**, 13181-13190 (1998).

[121] C. M. Jaworski, J. Yang, S. Mack, D. D. Awschalom, R. C. Myers, and J. P. Heremans, Spin-seebeck effect: a phonon driven spin distribution. Phys. Rev. Lett. **106**, 186601-186601 (2011).

[122] Y. L. Chen, J. G. Analytis, J.-H. Chu, Z. K. Liu, S.-K. Mo, X. L. Qi, H. J. Zhang, D. H. Lu, X. Dai, Z. Fang, S. C. Zhang, I. R. Fisher, Z. Hussain, and Z.-X. Shen, Experimental Realization of a Three-Dimensional Topological Insulator, Bi2Te3. Science **325**, 178-181 (2009).

[123] H. Zhang, C.-X. Liu, X.-L. Qi, X. Dai, Z. Fang, and S.-C. Zhang, Topological insulators in Bi2Se3, Bi2Te3 and Sb2Te3 with a single Dirac cone on the surface. Nat Phys **5**, 438-442 (2009).

[124] A. Koma, K. Sunouchi, and T. Miyajima, Summary Abstract: Fabrication of ultrathin heterostructures with van der Waals epitaxy. Journal of Vacuum Science & Technology B **3**, 724-724 (1985).

[125] R. Venkatasubramanian, E. Siivola, T. Colpitts, and B. O'Quinn, Thin-film thermoelectric devices with high room-temperature figures of merit. Nature **413**, 597-602 (2001).

[126] S. Cho, Y. Kim, A. DiVenere, G. K. Wong, J. B. Ketterson, and J. R. Meyer, Antisite defects of Bi2Te3 thin films. Appl. Phys. Lett. **75**, 1401-1403 (1999).

[127] L. W. da Silva, M. Kaviany, and C. Uher, Thermoelectric performance of films in the bismuth-tellurium and antimony-tellurium systems. J. Appl. Phys. **97**, 114903 (2005).

[128] G. Wang, L. Endicott, and C. Uher, Recent Advances in the Growth of Bi-Sb-Te-Se Thin Films. Science of Advanced Materials **3**, 539-560 (2011).

[129] D. Hsieh, Y. Xia, D. Qian, L. Wray, J. H. Dil, F. Meier, J. Osterwalder, L. Patthey, J. G. Checkelsky, N. P. Ong, A. V. Fedorov, H. Lin, A. Bansil, D. Grauer, Y. S. Hor, R. J. Cava, and M. Z. Hasan, A tunable topological insulator in the spin helical Dirac transport regime. Nature **460**, 1101-1105 (2009).

[130] Y. Xia, D. Qian, D. Hsieh, L. Wray, A. Pal, H. Lin, A. Bansil, D. Grauer, Y. S. Hor, R. J. Cava, and M. Z. Hasan, Observation of a large-gap topological-insulator class with a single Dirac cone on the surface. Nat Phys **5**, 398-402 (2009).

[131] Y. L. Chen, J.-H. Chu, J. G. Analytis, Z. K. Liu, K. Igarashi, H.-H. Kuo, X. L. Qi, S. K. Mo, R. G. Moore, D. H. Lu, M. Hashimoto, T. Sasagawa, S. C. Zhang, I. R. Fisher, Z. Hussain, and Z. X. Shen, Massive Dirac Fermion on the Surface of a Magnetically Doped Topological Insulator. Science **329**, 659-662 (2010).

[132] C. B. Satterthwaite and R. W. Ure, Jr., Electrical and Thermal Properties of Bi2Te3. Phys. Rev. **108**, 1164-1170 (1957).

[133] Y. S. Hor, D. Qu, N. P. Ong, and R. J. Cava, Low temperature magnetothermoelectric effect and magnetoresistance in Te vapor annealed Bi2Te3. J. Phys. Condens. Matter **22**, 375801 (2010).

[134] Y. S. Hor, J. G. Checkelsky, D. Qu, N. P. Ong, and R. J. Cava, Superconductivity and non-metallicity induced by doping the topological insulators Bi2Se3 and Bi2Te3. J. Phys. Chem. Solids **72**, 572-576 (2011).

[135] Y. Feutelais, B. Legendre, N. Rodier, and V. Agafonov, A study of the phases in the bismuth - tellurium system. Mat. Res. Bull. **28**, 591-596 (1993).

[136] E. F. Hockings and J. G. White, The crystal structures of TlSbTe2 and TlBiTe2. Acta Cryst. **14**, 328-328 (1961).

[137] Y. L. Chen, Z. K. Liu, J. G. Analytis, J. H. Chu, H. J. Zhang, B. H. Yan, S. K. Mo, R. G. Moore, D. H. Lu, I. R. Fisher, S. C. Zhang, Z. Hussain, and Z. X. Shen, Single Dirac Cone Topological Surface State and Unusual Thermoelectric Property of Compounds from a New Topological Insulator Family. Phys. Rev. Lett. **105**, 266401 (2010).

[138] P. Lošťák, P. Bezdička, J. Horák, and J. Šrámková, Electrical and optical properties of Tl-doped Bi2Te3 crystals. Radiation Effects and Defects in Solids **138**, 251-260 (1996).

[139] H. Bando, K. Koizumi, Y. Oikawa, K. Daikohara, V. A. Kulbachinskii, and H. Ozaki, The time-dependent process of oxidation of the surface of Bi 2 Te 3 studied by x-ray photoelectron spectroscopy. J. Phys. Condens. Matter **12**, 5607 (2000).

[140] N. Martensson, A. Berndtsson, and R. Nyholm, Core-level binding energies of solid thallium. J. Electron. Spectrosc. **19**, 299-301 (1980).

[141] D.-X. Qu, Y. S. Hor, J. Xiong, R. J. Cava, and N. P. Ong, Quantum Oscillations and Hall Anomaly of Surface States in the Topological Insulator Bi2Te3. Science **329**, 821-824 (2010).

[142] J. Zhang, C.-Z. Chang, Z. Zhang, J. Wen, X. Feng, K. Li, M. Liu, K. He, L. Wang, X. Chen, Q.-K. Xue, X. Ma, and Y. Wang, Band structure engineering in (Bi1-xSbx)2Te3 ternary topological insulators. Nat Commun **2**, 574 (2011).

[143] J. Yang, G. P. Meisner, D. T. Morelli, and C. Uher, Iron valence in skutterudites: Transport and magnetic properties of Co1-xFexSb3. Phys. Rev. B **63**, 014410 (2000).

[144] D. T. Morelli, J. P. Heremans, and G. A. Slack, Estimation of the isotope effect on the lattice thermal conductivity of group IV and group III-V semiconductors. Phys. Rev. B **66**, 195304 (2002).

[145] C. J. Glassbrenner and G. A. Slack, Thermal Conductivity of Silicon and Germanium from 3K to the Melting Point. Phys. Rev. **134**, A1058-A1069 (1964).

[146] R. Berman and J. C. F. Brock, The Effect of Isotopes on Lattice Heat Conduction. I. Lithium Fluoride. Proc. R. Soc. London, Ser. A **289**, 46-65 (1965).

[147] J. O. Jenkins, J. A. Rayne, and R. W. Ure, Jr., Elastic Moduli and Phonon Properties of Bi2Te3. Phys. Rev. B **5**, 3171-3184 (1972).

[148] G. E. Shoemake, J. A. Rayne, and R. W. Ure, Jr., Specific Heat of n- and p-Type Bi2Te3 from 1.4 to 90 K. Phys. Rev. **185**, 1046-1056 (1969).

[149] Q. H. Wang, K. Kalantar-Zadeh, A. Kis, J. N. Coleman, and M. S. Strano, Electronics and optoelectronics of two-dimensional transition metal dichalcogenides. Nat Nano **7**, 699-712 (2012).

[150] R. Xu, A. Husmann, T. F. Rosenbaum, M. L. Saboungi, J. E. Enderby, and P. B. Littlewood, Large magnetoresistance in non-magnetic silver chalcogenides. Nature **390**, 57-60 (1997).

[151] W. Zhang, R. Yu, W. X. Feng, Y. G. Yao, H. M. Weng, X. Dai, and Z. Fang, Topological Aspect and Quantum Magnetoresistance of beta-Ag2Te. Phys. Rev. Lett. **106**, 156808 (2011).

[152] B. Sipos, A. F. Kusmartseva, A. Akrap, H. Berger, L. Forro, and E. Tutis, From Mott state to superconductivity in 1T-TaS2. Nat Mater **7**, 960-965 (2008).

[153] H. Yuan, M. S. Bahramy, K. Morimoto, S. Wu, K. Nomura, B.-J. Yang, H. Shimotani, R. Suzuki, M. Toh, C. Kloc, X. Xu, R. Arita, N. Nagaosa, and Y. Iwasa, Zeeman-type spin splitting controlled by an electric field. Nat Phys **9**, 563-569 (2013).

[154] H.-Z. Lu, W. Yao, D. Xiao, and S.-Q. Shen, Intervalley Scattering and Localization Behaviors of Spin-Valley Coupled Dirac Fermions. Phys. Rev. Lett. **110**, 016806 (2013).

[155] H. Liu, X. Shi, F. Xu, L. Zhang, W. Zhang, L. Chen, Q. Li, C. Uher, T. Day, and G. J. Snyder, Copper ion liquid-like thermoelectrics. Nat Mater **11**, 422-425 (2012).

[156] S. C. Riha, D. C. Johnson, and A. L. Prieto, Cu2Se Nanoparticles with Tunable Electronic Properties Due to a Controlled Solid-State Phase Transition Driven by Copper Oxidation and Cationic Conduction. J. Am. Chem. Soc. **133**, 1383-1390 (2010).

[157] X. Xiao, W. Xie, X. Tang, and Q. Zhang, Phase transition and high temperature thermoelectric properties of copper selenide Cu 2− x Se (0 ≤ x ≤ 0.25). Chin. Phys. B **20**, 087201 (2011).

[158] H. Liu, X. Yuan, P. Lu, X. Shi, F. Xu, Y. He, Y. Tang, S. Bai, W. Zhang, L. Chen, Y. Lin, L. Shi, H. Lin, X. Gao, X. Zhang, H. Chi, and C. Uher, Ultrahigh Thermoelectric Performance by Electron and Phonon Critical Scattering in Cu2Se1-xIx. Adv. Mater. **25**, 6607-6612 (2013).

[159] SpringerMaterials - The Landolt-Börnstein Database (http://www.springermaterials.com).

[160] T. Ohtani, Y. Tachibana, J. Ogura, T. Miyake, Y. Okada, and Y. Yokota, Physical properties and phase transitions of β Cu2−xSe (0.20≤x≤0.25). J Alloy Compd **279**, 136-141 (1998).

[161] M. C. Nguyen, J.-H. Choi, X. Zhao, C.-Z. Wang, Z. Zhang, and K.-M. Ho, New Layered Structures of Cuprous Chalcogenides as Thin Film Solar Cell Materials: Cu2Te and Cu2Se. Phys. Rev. Lett. **111**, 165502 (2013).

[162] G. K. Padam, The properties of chemically deposited Cu2−xSe thin films. Thin Solid Films **150**, L89-L92 (1987).

[163] M. Råsander, L. Bergqvist, and A. Delin, Density functional theory study of the electronic structure of fluorite Cu 2 Se. J. Phys. Condens. Matter **25**, 125503 (2013).

[164] N. Frangis, C. Manolikas, and S. Amelinckx, Vacancy-Ordered Superstructures in Cu2Se. Phys. Status Solidi A **126**, 9-22 (1991).

[165] A. L. N. Stevels and F. Jellinek, Phase transitions in copper chalcogenides: I. The copper-selenium system. Recueil **90**, 273-283 (1971).

[166] M. A. Korzhuev, V. F. Bankina, B. F. Gruzinov, and G. S. Bushmarina, Electrophysical properties of superionic Cu2-xSe. Sov. Phys. Semicond. **23**, 959 (1989).

[167] S. A. Danilkin, M. Avdeev, T. Sakuma, R. Macquart, and C. D. Ling, Neutron diffraction study of diffuse scattering in Cu2−δSe superionic compounds. J Alloy Compd **509**, 5460-5465 (2011).

[168] J. S. Rhyee, K. H. Lee, S. M. Lee, E. Cho, S. Il Kim, E. Lee, Y. S. Kwon, J. H. Shim, and G. Kotliar, Peierls distortion as a route to high thermoelectric performance in In(4)Se(3-delta) crystals. Nature **459**, 965-968 (2009).

[169] S. Hikami, A. I. Larkin, and Y. Nagaoka, Spin-Orbit Interaction and Magnetoresistance in the Two Dimensional Random System. Progress of Theoretical Physics **63**, 707-710 (1980).

[170] B. A. Assaf, T. Cardinal, P. Wei, F. Katmis, J. S. Moodera, and D. Heiman, Linear magnetoresistance in topological insulator thin films: Quantum phase coherence effects at high temperatures. Appl. Phys. Lett. **102**, 012102-4 (2013).

[171] J. Chen, H. J. Qin, F. Yang, J. Liu, T. Guan, F. M. Qu, G. H. Zhang, J. R. Shi, X. C. Xie, C. L. Yang, K. H. Wu, Y. Q. Li, and L. Lu, Gate-Voltage Control of Chemical Potential and Weak Antilocalization in Bi_{2}Se_{3}. Phys Rev Lett **105**, 176602 (2010).

[172] M. Liu, J. Zhang, C.-Z. Chang, Z. Zhang, X. Feng, K. Li, K. He, L.-l. Wang, X. Chen, X. Dai, Z. Fang, Q.-K. Xue, X. Ma, and Y. Wang, Crossover between Weak Antilocalization and Weak Localization in a Magnetically Doped Topological Insulator. Phys. Rev. Lett. **108**, 036805 (2012).

[173] L. Bao, L. He, N. Meyer, X. Kou, P. Zhang, Z. Chen, A. V. Fedorov, J. Zou, T. M. Riedemann, T. A. Lograsso, K. L. Wang, G. Tuttle, and F. Xiu, Weak Anti-localization and Quantum Oscillations of Surface States in Topological Insulator Bi2Se2Te. Sci. Rep. **2**, 726 (2012).

[174] S. Tongay, H. Sahin, C. Ko, A. Luce, W. Fan, K. Liu, J. Zhou, Y.-S. Huang, C.-H. Ho, J. Yan, D. F. Ogletree, S. Aloni, J. Ji, S. Li, J. Li, F. M. Peeters, and J. Wu, Monolayer behaviour in bulk ReS2 due to electronic and vibrational decoupling. Nat Commun **5**, 3252 (2014).

[175] J. Bardeen and W. Shockley, Deformation Potentials and Mobilities in Non-Polar Crystals. Phys. Rev. **80**, 72-80 (1950).

[176] V. I. Fistul, *Heavily Doped Semiconductors* (Plenum Press, New York, 1969).

[177] L. Makowski and M. Glicksman, Disorder scattering in solid solutions of III–V semiconducting compounds. J. Phys. Chem. Solids **34**, 487-492 (1973).

[178] S. Krishnamurthy, A. Sher, and A.-B. Chen, Generalized Brooks' formula and the electron mobility in Si[sub x]Ge[sub 1 - x] alloys. Appl. Phys. Lett. **47**, 160-162 (1985).